# Electronic Excitation Induced Effects on the Structural and Electrical Properties of HfO<sub>2</sub> thin films

A thesis submitted by

#### KARRA VINOD KUMAR

in the partial fulfillment of the requirement for the award of the degree of

#### DOCTOR OF PHILOSOPHY IN PHYSICS



Under the supervision of

Prof. S.V.S. Nageswara Rao

School of Physics
University of Hyderabad
Hyderabad-500046
Telangana
India

*April - 2022* 

### **Declaration**

I, Karra Vinod Kumar, hereby declare that this thesis titled "Electronic Excitation Induced Effects on the Structural and Electrical Properties of HfO<sub>2</sub> thin films" submitted to the University of Hyderabad in partial fulfillment for the award of Doctor of Philosophy (Ph.D.) in Physics is an original research work carried out by me under the supervision of Prof. S. V. S. Nageswara Rao in the School of Physics, University of Hyderabad, Telangana, India. I also declare that this work has not been submitted for any other degree either in part or in full to this University or to any other University or Institution.

A report on plagiarism statistics from the University librarian is enclosed.

Place: Hyderabad

Date: 12-04-2022

(K Vinod Kumar)

(Reg. No. 15PHPH08)

### **Certificate**

This is to certify that the work embodied in this thesis entitled "Electronic Excitation Induced Effects on the Structural and Electrical Properties of HfO<sub>2</sub> thin films" has been carried out by Mr. Karra Vinod Kumar (Reg. No. 15PHPH08), in partial fulfilment of the requirements for award of Doctor of Philosophy (Ph.D.) in Physics, is a bonafide work carried out by him under my supervision and guidance.

This thesis is free from plagiarism and has not been submitted previously, in part or in full to this or any other University or Institution, for an award of any degree or diploma. Further, the student has the following publications before the submission of the thesis for adjudication.

- [1].**K. Vinod Kumar**, J. Pundareekam Goud, Kanaka Ravi Kumar, K. C. James Raju, S. V. S. Nageswara Rao, "Laser Annealing of Au/HfO<sub>2</sub> bi-layers to Fabricate Au Nanoparticles without altering the Phase of HfO<sub>2</sub> for Applications in SERS and Memory Devices", *Journal of Materials Science: Materials in Electronics* **2022**, 33, 6657-6669 (part of Chapter 6).
- [2].K. Vinod Kumar, N. Arun, A. Mangababu, Sunil Ojha, S. V. S. Nageswara Rao, A. P. Pathak "120 MeV Ag ion irradiation induced intermixing, grain fragmentation in HfO<sub>2</sub>/GaO<sub>x</sub> thin films and consequent effects on the electrical properties of HfO<sub>2</sub>/GaO<sub>x</sub>/Si-based MOS capacitors", *Rad. Eff. Deff. In Sol.* **2020**, 175 (1-2), 150-159 (part of Chapter 5).
- [3].**K. Vinod Kumar**, N. Arun, A. Mangababu, Sunil Ojha, A. P. Pathak, S.V.S. Nageswara Rao, "Swift Heavy Ion irradiation induced modifications of HfO<sub>2</sub> thin films deposited on GaAs", (Submitted JMSE-D-22-01194) (part of Chapter 4).

#### **Conference Proceedings**

[1].K. Vinod Kumar, N. Arun, A. P. Pathak, S. V. S. Nageswara Rao, "Effects of Thermal Annealing and Gamma Irradiation on HfO<sub>2</sub> Thin Films deposited on GaAs", AIP Conference Proceedings 2019, 2115, 030021-1–030021-4 (part of Chapter 3).

Prof. S.V.S. NAGESWARA RAO
School of Physics
School of Hyderabad
University of Hyderabad
Hyderabad-500 046, INDIA.

Further, the student has passed the following courses towards fulfilment of coursework requirement for Ph.D.:

| Course Code                | Name of the Course                | Credits | Pass/Fail |
|----------------------------|-----------------------------------|---------|-----------|
| PY801                      | Advanced Quantum Mechanics        | 4       | Pass      |
| PY803                      | 03 Advanced Statistical Mechanics |         | Pass      |
| PY804                      | Advanced Electromagnetic Theory   | 4       | Pass      |
| PY821 Research Methodology |                                   | 4       | Pass      |

Prof. S. V. S. Nageswara Rao 12/04/2022.
(Supervisor)

Prof. S.V.S. NAGESWARA RAO
School of Physics
University of Hyderabad
Hyderabad-500 046, INDIA.

Dean

(School of Physics)

DEAN
- School of Physics
University of Hyderabad

HYDERABAD - 500 046

iii

### <u>Acknowledgements</u>

First and foremost, I would like to express my sincere thanks and gratitude to my thesis supervisor Prof. S. V. S. Nageswara Rao, School of Physics, University of Hyderabad for his esteemed supervision, inspiration, constant encouragement, support and help throughout my research carrier. I personally and individually thank my supervisor. His best teaching skills with logical consistency and composure levels in numerous aspects have an enormous impact on my life at various stages. I feel proud to be trained under one of the best teachers in my life as he comes down to our stage to explain some of the basic and preliminary insights of the subject. I owe him a lot for all of his consistent, instructive suggestions and help during my difficult times.

I thank Prof. K. C. James Raju, Dean, School of Physics and former Deans Prof. Ashok Chatterjee, Prof. V. Seshubai, Prof. Bindu A Bambha, Prof. Rajendra Singh and Prof. S. Chaturvedi for their co-operation in providing facilities and infrastructure in School of Physics. I am very privileged to have Prof. Ashok Chatterjee and Prof. S Srinath as my Doctoral committee members whose suggestions, encouragement and insights have improved the understanding of our results. I express my sincere gratitude to Prof. A. P. Pathak for his valuable suggestions during my research work.

I express my sincere thanks to Dr. D. K. Avasthi for technical discussions and help during beam time experiments at Inter University Accelerator Center (IUAC), New Delhi and during his visits to of University of Hyderabad. I thank Dr. D. Kanjilal, former Director, IUAC for his useful suggestions during discussions. I express my sincere thanks to Dr. S. A. Khan (Our local experiment collaborator at IUAC) for technical discussions and help during beam time. I thank Dr. D. Kabiraj and Mr. Abhilash for allowing us to utilize the facilities in target lab. I would like to thank Mr. Sunil Ojha for his help during RBS measurements and analysis. I am also thankful to the members of Pelletron Accelerator group and other scientists at IUAC for necessary support during experiments. I thank Dr. Saumithra Vajandar for his help in performing HRBS measurements at NUS, Singapore.

I sincerely thank Prof. K. C. James Raju, School of Physics for his suggestions and Dr. J. Pundareekam Goud for extending his help during laser annealing experiments. I sincerely thank Prof. S. Venugopal Rao, ACRHEM and his students for their help during SERS measurements.

I would like to thank UGC, New Delhi for providing fellowship as JRF and SRF.

I also thank personally the technical staff Mr. Naresh, Ms. Sunitha, Ms. Jyothi, Mr. Santosh and Mr. Prashanth for their help during the experiments. I would like to thank Mr. Abraham, Mr. Prasad, Mr. Sudarshan Mrs. Shailaja, Mrs. Deepika and all non-teaching staff in school of physics and nano center for their help over these years.

I personally thank my friends Dr. Murali, Mr. Shivanarayana and Mr. Srikanth Karan for sharing their experiences, views and fun times. I would like to thank my Ph.D. batch mates Mr. Avisek Das, Mr. Abu Taher, Mr. Bappaditya, Ms. Leelashree, Ms. Manasa, Mr. Naresh, Mr. Nilanjan, Mrs. Praneetha, Mr. Rajesh, Mr. Rashmi Ranjan, Mr. Rasi, Dr. Sujai and Mr. Zahid Malik for their love and support. I thank all my friends who have helped me when I was in struggle. I would like to thank my seniors Dr. Vendamani, Dr. Manikanthababu, Dr. Dhanujaya and Dr. Arun for sharing their knowledge and lab experiences. I would like to thank to Mr. Mangababu, Mr. Sai Prasad and Mr. Ravi Kumar for their help in various aspects.

I convey my sincere thanks to all my teachers right after my childhood till date for their consistent encouragement who have taught me the basic concepts and given me the opportunity to learn and lead a successful life and career.

It wouldn't be enough to say simply thanks to my parents Mr. Chandya Nayak and Mrs. Anthi Bai who brought me where I am now. This wouldn't have happened without the contiguous and tireless support of my wife Jayasri. I would like to express my sincere thanks to all other family members for their timely support. I would like to thank all of them who are involved either directly or indirectly for the completion of my Ph.D. successfully.

K Vinod Kumar

### <u>Glossary</u>

AC Alternative Current

ALD Atomic Layer Deposition

BE Bottom electrode

BRIT Board of Radiation and Isotope Technology

BLC Bulk Limited Conduction

C-V Capacitance-Voltage

CFN Center for Nano Technology

CVD Chemical Vapor Deposition

CMOS Complementary Metal Oxide Semiconductor

DC Direct Current

DIW De Ionized Water

DT Direct Tunneling

EB e-beam evaporation

ECM Electro Chemical Mechanism

EDX Energy Dispersive x-ray Spectroscopy

EHPs Electron Hole Pairs

ELC Electrode-Limited Conduction

EOT Equivalent Oxide Thickness

FC Faraday Cup

FESEM Field Emission Scanning Electron Microscopy

FET Field Effect Transistor

FN Fowler Nordheim

FS Femtosecond

GB Grain Boundaries

GIXRD Glancing Incidence X-Ray Diffraction

HRTEM High Resolution Transmission Electron Microscope

IC's Integrated Circuits

I-V Current-Voltage

IUAC Inter University Accelerator Centre

JCPDS Joint Committee on Powder Diffraction Standards

MBE Molecular Beam epitaxy

MCSNICS Multi Cathode Source of Negative Ions by Cesium Sputtering

MOS Metal Oxide Semiconductor

MOSCAPs Metal oxide semiconductor capacitors

MOSFET Metal Oxide Semiconductor Field Effective Transistor

NIR Near infra-red

NS Nanosecond

NVM Non-Volatile Memory

PF Poole Frenkel

PL Photo Luminescence

PnA Particle nanoAmpere

PVD Physical Vapor Deposition

RAM Random Access Memory

RBS Rutherford Backscattering Spectrometry

RCA Radio Corporation of America

RF Radio Frequency

ROM Read Only Memory

RRAM Resistive Random-Access Memory

SCCM Standard Cubic Centimeters per Minute

SCLC Space-Charge-Limited Conduction

SDA Semiconductor Device Analyzer

SE Schottky Emission

SEAD Selective Area Electron Diffraction

SF6 Sulphur Hexa-Fluoride

SHI Swift Heavy Ion

SIMNRA Simulation of Ions in Matter and Nuclear Reaction Analysis

SNICS Source of Negative Ions by Cesium Sputtering

SPR Surface Plasmon Resonance

SRIM Stopping and Ranging of Ions in Matter

TAT Trap-Assisted Tunneling

TE Top Electrode

TEM Transmission Electron Microscope

TID Total Ionizing Dose
UHV Ultra-High Vacuum

UoH University of Hyderabad

UV-Vis-IR Ultra-Violet Visible and Infra-Red

XRD X-Ray Diffraction XRR X-Ray Reflectivity

## Table of Contents

| Declaration   | 1    |
|---|------|
| Certificate   | ii   |
| Acknowledgements  | iv   |
| Glossary  | vi   |
| Table of content  | ix   |
| Abstract  | xiv  |
| Chapter 1: Introduction and Motivation                                | 1-38 |
| 1.1. Introduction   | 02   |
| 1.2. Development of semiconductor based devices                       | 03   |
| 1.3. Significance of high-k gate dielectrics in microelectronics      | 05   |
| 1.4. Requirements for suitable advanced dielectric constant materials | 06   |
| 1.5. High-k dielectric materials                                      | 06   |
| 1.6. The MOS capacitor/diode  | 10   |
| 1.6.1. Leakage current – Voltage (I-V) characteristics                | 12   |
| 1.6.2. Capacitance – Voltage (C-V) characteristics                    | 16   |
| 1.6.3. Effects of defects   | 17   |
| 1.7. Fundamentals of ion-solid interactions                           | 19   |
| 1.7.1. Radiation induced damage                                       | 21   |
| 1.7.2. Swift Heavy Ion (SHI) irradiation                              |      |
| 1.7.3. Thermal spike model  | 23   |
| 1.8. SHI irradiation induced crystallization                          | 24   |
| 1.9. Floating gate based flash memory devices                         | 24   |
| 1.10. Laser Annealing   | 26   |
| 1.11. The objective and framework of the thesis                       | 26   |
| 1.12. References  | 30   |

| Chapter 2: Experimental Details and Characterization Techniques  |       |  |  |
|--|-------|--|--|
| 2.1. Introduction  | 40    |  |  |
| 2.2. Physical Vapor Deposition systems   | 41    |  |  |
| 2.2.1. RF/DC magnetron sputtering technique  | 41    |  |  |
| 2.2.2. e-beam evaporation and thermal evaporation techniques   | 43    |  |  |
| 2.3. Irradiation facilities and Ion beam analysis  | 45    |  |  |
| 2.3.1. Gamma irradiation   | 45    |  |  |
| 2.3.2. Swift Heavy Ion (SHI) Irradiation   | 46    |  |  |
| 2.3.3. Rutherford Backscattering Spectroscopy  | 48    |  |  |
| 2.4. Characterization Techniques   | 50    |  |  |
| 2.4.1. Profilometer  | 50    |  |  |
| 2.4.2. Field Emission Scanning Electron Microscopy (FESEM) technique and   |       |  |  |
| Energy Dispersive X-ray Spectroscopy (EDX) technique   | 51    |  |  |
| 2.4.3. X-Ray Diffraction (XRD)   | 52    |  |  |
| 2.4.4. Photoluminescence Spectroscopy (PL)   | 55    |  |  |
| 2.4.5. Raman spectroscopy  | 56    |  |  |
| 2.4.6. Ultra Violet-Vis-Near Infrared Spectroscopy   | 58    |  |  |
| 2.4.7. Electrical characterizations  | 59    |  |  |
| 2.5. Conclusions   | 60    |  |  |
| 2.6. References  | 61    |  |  |
| Chapter 3: Effects of Thermal Annealing and Gamma Irradiation<br>on the structural and electrical properties of HfO <sub>2</sub> thin<br>films deposited on GaAs | 63-86 |  |  |
| 3.1. Introduction  | 64    |  |  |
| 3.2. Experimental Details  | 67    |  |  |
| 3.2.1. Synthesis of HfO <sub>2</sub> thin films  | 67    |  |  |
| 3.2.2. Sample Characterization   | 68    |  |  |
| 3.2.3. Thermal Annealing   | 68    |  |  |
| 3.2.4. Gamma irradiation   | 68    |  |  |

| 3.2.5. Fabrication and electrical characterization of MOS structures          | 69     |
|---|--------|
| 3.3. Results and discussions  | 69     |
| 3.3.1. Effects of growth parameters   | 69     |
| 3.3.2. Effects of thermal annealing   | 75     |
| 3.3.2. Effects of Gamma irradiation   | 81     |
| 3.4. Conclusions  | 82     |
| 3.5. References   | 83     |
| Chapter 4: Effects of Swift Heavy Ion (SHI) irradiation on the                |        |
| structural and electrical properties of HfO <sub>2</sub> thin-films           | 0= 442 |
| deposited on GaAs   | 87-113 |
| 4.1. Introduction   | 88     |
| 4.2. Experimental Methods   | 90     |
| 4.2.1. Synthesis of HfO <sub>2</sub> thin films                               | 90     |
| 4.2.2. SHI irradiation  | 90     |
| 4.2.3. Sample Characterization  | 91     |
| 4.2.4. Fabrication and characterization of MOS structures                     | 92     |
| 4.3. Results and discussions  | 93     |
| 4.3.1. Characterization of thickness and stoichiometry of pristine thin films | 93     |
| 4.3.2. Impact of SHI irradiation  | 94     |
| a) Surface structure and Grain agglomeration                                  | 94     |
| b) SHI irradiation induced phase transformations                              | 97     |
| c) SHI irradiation induced defect dynamics                                    | 99     |
| d) SHI irradiation induced mixing and surface roughness                       | 102    |
| e) Electrical characteristics   | 104    |
| 4.4. Conclusions  | 108    |
| 4.5. References   | 110    |

| on the structural and electrical properties of HfO <sub>2</sub> /GaO <sub>x</sub> |         |
|---|---------|
| thin films  | 114-140 |
| 5.1. Introduction   | 115     |
| 5.2. Experimental details   | 116     |
| 5.2.1. Synthesis of thin films  | 116     |
| 5.2.2. SHI irradiation  | 117     |
| 5.2.3. Gamma irradiation  | 118     |
| 5.2.4. Sample Characterization  | 118     |
| 5.2.5. Fabrication and electrical characterization of MOS capacitors              | 119     |
| 5.3. Results and discussions  | 120     |
| 5.3.1. Characterization of thickness and stoichiometry of pristine thin films     | 120     |
| A. Characterization of GaOx thin films  | 120     |
| B. Characterization of HfO2/GaOx bi-layer thin films                              | 122     |
| 5.3.2. Effects of SHI irradiation   | 124     |
| a) Surface structure and Grain fragmentation                                      | 124     |
| b) Electrical characteristics   | 130     |
| 5.3.3. Effects of Gamma irradiation   | 132     |
| 5.4. Conclusions  | 135     |
| 5.5. References   | 136     |
| Chapter 6: Effects of Laser Annealing on the structural and electrical            | l       |
| properties of HfO <sub>2</sub> and Au/HfO <sub>2</sub> thin films deposited on Si | 141-176 |
| 6.1. Introduction   | 142     |
| 6.2. Experimental details   | 144     |
| 6.2.1. Synthesis of thin films  | 144     |
| 6.2.2. Laser Annealing  | 145     |
| 6.2.3. Sample Characterization  | 145     |
| 6.2.4. Fabrication and electrical characterization of MOS capacitors              | 146     |
| 6.3. Results and discussions  | 148     |
| A. Effects of laser annealing on the structural and electrical properties of      |         |

| HfO <sub>2</sub> thin films  | 148     |
|--|---------|
| B. Effects of laser annealing on Au/HfO <sub>2</sub> bi-layer thin films | 156     |
| 6.3.1. Morphology and Optical properties of Au NPs                       | 157     |
| 6.3.2. Crystal structure of Au/HfO <sub>2</sub> bi-layers                | 161     |
| 6.3.3. SERS studies of R6G dye on Au NPs                                 | 163     |
| 6.3.4. Electrical characteristics of MOS capacitors                      | 165     |
| 6.4. Conclusions   | 170     |
| 6.5. References  | 172     |
| Chapter 7: Conclusions and Scope of future work                          | 177-181 |
| 7.1. Conclusions   | 178     |
| 7.2. Future Scope  | 181     |
| 7.3. References  | 181     |
| List of publications and conferences attended                            | 182-185 |

### **Abstract**

In this thesis, the effects of electronic excitation induced by Gamma irradiation, Swift Heavy Ion (SHI) irradiation and Laser annealing on the structural and electrical properties of HfO<sub>2</sub> thin films have been studied. Further, an array of high density gold nanoparticles have been produced on the surface of HfO<sub>2</sub> thin films, without modifying the phase of HfO<sub>2</sub> using a non-thermal laser annealing technique. HfO<sub>2</sub> thin films used in this study were deposited on high mobility and/or wide bandgap semiconductor substrates by using Radio Frequency (RF) magnetron sputtering and e-beam evaporation techniques.

As expected, thermal annealing has introduced monoclinic phase in otherwise amorphous HfO<sub>2</sub> thin films which resulted in an increase in the leakage current density of the HfO2 based Metal Oxide Semiconductor (MOS) structures. A systematic increase in leakage current density indicates the production of defects in HfO<sub>2</sub> thin films with increasing gamma irradiation dose. SHI (120 MeV Ag) irradiation resulted in a systematic increase in the grain size and increase in the roughness of the HfO<sub>2</sub> films. As-grown HfO<sub>2</sub> thin films are amorphous in nature. Ion induced phase transformation of HfO<sub>2</sub> thin films from amorphous to monoclinic and tetragonal phases have been observed. The influence of Poole-Frenkel (PF) and Fowler-Nordheim (FN) tunneling processes have been investigated by examining the Leakage current-Voltage (I-V) characteristics. The tunneling mechanisms revealed the existence of defects in the as-grown HfO<sub>2</sub> films. Ion induced defect annealing has been observed below the critical fluence (5x1012 ions/cm2) which resulted in decrease of the leakage current density. Whereas ion induced defect creation and radiation damage have been observed above the critical fluence, which resulted in an increase in the leakage current density. Further, an array of high density gold nanoparticles has been produced on the surface of HfO<sub>2</sub> thin films without modifying the phase of HfO<sub>2</sub> by subjecting the Au/HfO<sub>2</sub> bi-layers to laser annealing. Applications of these Au nanoparticles to Surface Enhanced Raman Spectroscopy (SERS) and floating gate type memory devices have been discussed in detail.

This study will provide useful information for understanding the effects of electronic excitation on the structural and electrical properties of HfO<sub>2</sub> thin films deposited on various technologically important semiconductor substrates for fabricating tunable and radiation harsh electronic devices.

### **Introduction and Motivation**

This chapter outlines the introduction, motivation and aim of the present thesis work. We explain here the significance of the choice of materials which are presently used and suggest the research requirements in the cutting edge of the current research field. The literature survey offers comprehensive information about the current knowledge in this area. This chapter concisely elucidates the importance of the present work and promising areas in which this thesis is to build up.

#### 1.1. Introduction

The enormous development in the microelectronic technology to enhance the performance of integrated circuits, predominantly in recent Metal Oxide Semiconductor Field Effect Transistor (MOSFET) based microelectronic devices, and the consequent down-scaling of transistor size has led to an exponential growth in the transistor count per chip to follow the law predicted in 1965 by the cofounder of Intel, Gorden E. Moore [1, 2]. On the other hand, this increase in the number of transistors and device scaling may result in several problems due to various issues associated with heat generation within the device and extreme power consumptions by the integrated circuits [3-6]. Hence, the modern microelectronic device technology is searching for the alternative materials to boost-up the device performance, particularly by replacing gate oxide and semiconductor materials and novel device structural design in place of standard silicon based CMOS devices. In order to overcome these difficulties, more than a decade of research and improvement has been accompanied by many research groups to be ready with the alternate possibilities to carry on downscaling. The diverse methodologies such as replacing standard gate oxide by the high - k dielectric, as well as replacing the silicon substrates with advanced high mobility channel semiconductors like III-V group and III-VI group compound semiconductors such as GaAs, GaN, GaSb, InAs and Ga<sub>2</sub>O<sub>3</sub> etc. have been proposed [7, 8]. In standard Silicon CMOS technology, reduction of SiO<sub>2</sub> layer thickness leads to an increase in the leakage current density by some orders of magnitude which may be objectionable for low power device applications [9, 10]. To avoid the leakage current due to tunneling, thicker gate oxide layers are mandatory. As the oxide layer becomes thicker, the electrical characteristics of a transistor have to be maintained by introducing new gate oxide materials with higher dielectric constant (k) which is directly proportional to the capacitance density (C/A), whereas capacitance density is inversely propositional to the dielectric layer thickness. SiO<sub>2</sub> had been replaced by HfO<sub>2</sub> (dielectric constant 18-25 and band gap 5.8 eV) as the gate oxide in some advanced CMOS transistors for the first time by Intel in 2007. It is important to note that, in Silicon CMOS technology, use of Si as the standard semiconductor was encouraged because it has outstanding interface properties with the dielectric SiO<sub>2</sub> [11]. However, in microelectronics community, standard gate oxide SiO<sub>2</sub> has been replaced by HfO<sub>2</sub> [12]. As discussed above, for further device scaling, it is presently followed by an attempt to replace the Si with superior high mobility semiconductors. Among the many compound semiconductors GaAs attracted the attention in recent years due to its higher electron mobility. The electron mobility of GaAs is around six times greater than that of Si, which makes it an attractive substrate for the future high-speed applications in CMOS devices [13].

#### 1.2. Development of semiconductor based devices

The invention of the bipolar transistor by William Shockley, Walter Houser Brattain and John Bardeen in the year of 1947 and invention of the solid-state based amplifier, created a revolution in the semiconductor-based device technology. Later in 1958, the first demonstration of integrated circuits by Jack Kilby and in 1960, the first fabrication of MOSFET by Dawon Kahng and Mohamed M. Atalla have provided the origin for the development of microelectronic devices. After that, the MOSFET became the heart of every integrated circuit in the application of memory devices and micro-processors. Furthermore, the down-scaling of transistor size improved the device performance with cost effectiveness and efficiency in power consumption. The transistor size feature has scaled-down from 10 µm to ~5 nm in the last five decades as an outcome of scaling by the micro-electronics community [4, 5, 9, 14] to follow the Moore's law (the transistor count on a chip would double for every two years) predicted in 1965 by Gorden E. Moore [1]. Moore's law plot of transistor count per chip and transistor size feature as a function of year are shown in Fig. 1.1 and Fig. 1.2 respectively [15].

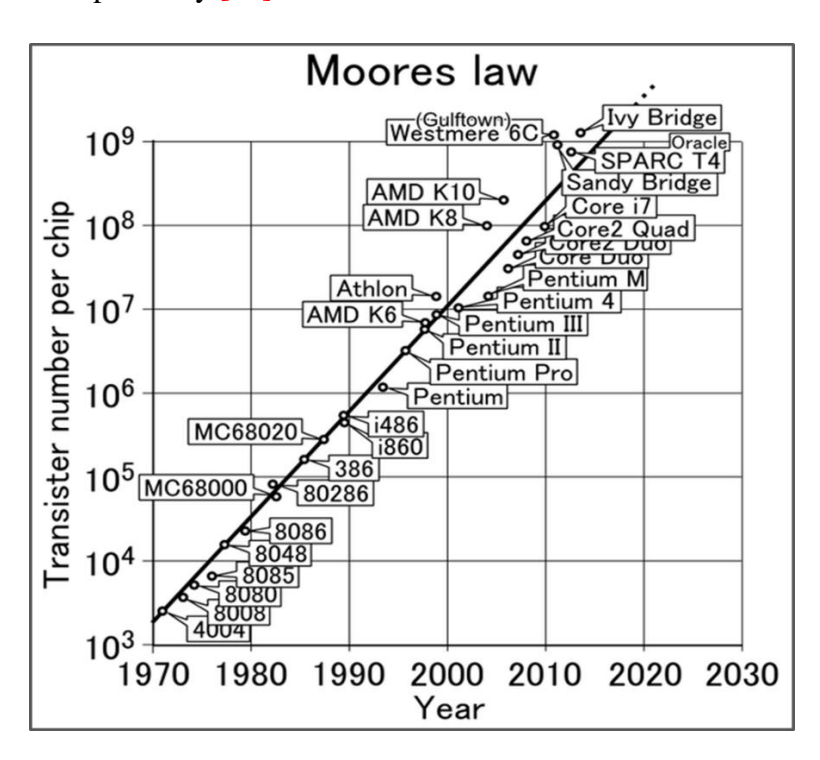


Fig. 1.1: Moore's law plot of transistor count per chip as a function of year [1].

Intel introduced the first 10 µm technology micro-processor – 4004 with transistor count of only 2300 in the year of 1971. In 1972, the transistor count per chip increased to 3500 for micro-processor 8008 and it increased to 42 x 10<sup>5</sup> in the year 2000 for Pentium 4. Further, Intel has showed numerous developments such as 90nm technology in 2002 [16]. Up to a transistor count per chip of 188 x 10<sup>6</sup>, the microelectronics community was able to follow the Moore's law with 60 nm feature transistor size. In 1980's the microelectronics community moved from existing bipolar Si based transistor to complementary Metal Oxide Semiconductor (CMOS) based planar transistor technology. CMOS based planar transistor technology has continued more than three decades as a leading technology. Now, the major challenge is that the CMOS based transistor size scaled down to few nm, which results physical complications like poor reliability and high leakage currents due to tunneling. This high leakage currents can cause high power consumption and damage the device due to joule-heating [3, 5, 6].

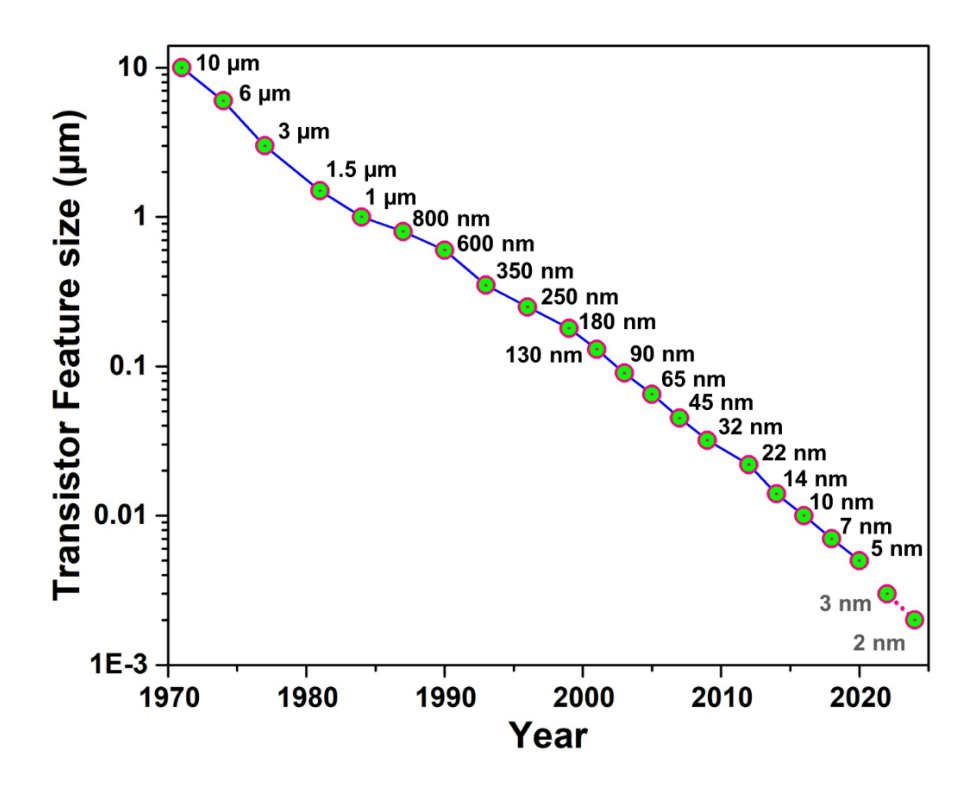


Fig. 1.2: Transistor feature size as a function of year [15].

In 2007, the introduction of hafnium oxide (HfO<sub>2</sub>) as gate oxide in some advanced CMOS transistors and fabrication of 45 nm technology processors by Intel, encouraged the microelectronics community to attempt further device scaling.

#### 1.3. Significance of high-k gate dielectrics in microelectronics

The extreme improvements in the performance of microelectronics memory devices have been possible by scaling down the feature size of the devices, which results in physical complications like poor reliability and high leakage currents due to tunneling. In standard Silicon CMOS technology, for every 0.2 nm reduction of SiO<sub>2</sub> layer thickness, the leakage current will increase by around one order of magnitude [9, 10]. To avoid the leakage current due to tunneling, thicker gate oxide layers are mandatory. As the oxide layer becomes thicker, the electrical characteristics of the transistor have to be maintained by introducing new gate oxide materials with advanced dielectric constant (k) which is directly proportional to the capacitance density (C/A), whereas capacitance density is inversely propositional to the dielectric layer thickness. The performance of a memory device is measured in terms of capacitance density (C/A) as given by the equation 1.1.

Capacitance density 
$$\binom{C}{A} = \frac{\varepsilon_0 k}{d_{ox}}$$
 (1.1)

In this equation,  $d_{ox}$  is the thickness of high-k dielectric oxide layer,  $\epsilon_0$  is permittivity in vacuum and area of the top metal electrode is A.

This scaling down of the device size demanded radical reduction of the standard gate oxide  $SiO_2$  layer thickness to realize advanced capacitance densities. This reduction of the gate oxide layer thickness has now reached the limit with arising of severe problems like higher leakage current due to quantum tunneling. At this basic minimum thickness, the gate oxide will no longer be capable to efficiently resist the leakage current. In addition to the leakage current, reliability is also a severe problem due to down-scaling. The reliability requirements are much challenging than the requirements for leakage current density. To overcome these problems due to down-scaling, the ultimate solution is to replace the standard gate oxide  $SiO_2$  (k ~ 3.9) with a advanced dielectric material which can offer the lower Equivalent Oxide Thickness (EOT – the required thickness of the standard  $SiO_2$  gate oxide to attain the capacitance density equivalent to that of high-k dielectric material) with increased layer thickness given by,

Equivalent Oxide Thickness (EOT) = 
$$\frac{3.9 d_{ox}}{k}$$
 (1.2)

In past few years, researchers have made several efforts to find some capable high-k dielectric constant materials such as TiO<sub>2</sub>, ZrO<sub>2</sub>, Al<sub>2</sub>O<sub>3</sub>, Ta<sub>2</sub>O<sub>5</sub>, HfO<sub>2</sub>, Gd<sub>2</sub>O<sub>3</sub>, La<sub>2</sub>O<sub>3</sub>, Y<sub>2</sub>O<sub>3</sub>, Nb<sub>2</sub>O<sub>5</sub> etc. to replace the standard gate oxide SiO<sub>2</sub> [17, 18]. Another advantage of SiO<sub>2</sub> was that it can be grown conveniently by oxidizing the Si. In contrast, the high-k dielectric layer must be grown by one of the physical vapor deposition techniques only.

#### 1.4. Requirements for suitable advanced dielectric constant materials

The major material and electrical requirements [5, 19, 20] for suitable advanced dielectric constant materials to replace the standard gate oxide  $SiO_2$  are:

- ➤ High dielectric constant (k)
- ➤ Higher energy band gap with good barrier height to semiconductor and metal gate to ease the leakage current density
- ➤ Good kinetic and thermal stability
- ➤ Lower oxygen diffusion coefficients
- Lower defect densities in bulk high-k dielectric films
- ➤ Good reliability with extended life time.
- ➤ Compatible with existing CMOS device fabrication method

#### 1.5. High-k dielectric materials

The choice of a high-k dielectric oxide with greater 'k' value than that of standard gate oxide SiO<sub>2</sub> can offer the EOT with increased layer thickness. A number of high-k dielectric materials were recognized as possible appropriate materials to replace the standard gate oxide SiO<sub>2</sub>. However many high-k materials did not have all the required material properties. It was realized that each high-k dielectric material has one or the other drawback with its material properties. Searching for the good high-k dielectric material with all desired material properties is not an easy task. Various leading advanced dielectric constant materials and their material properties are listed in Table 1.1.

After a thorough investigation of these high-k dielectric materials, the observed disadvantages inherited by each high-k candidate have resulted in choice of HfO<sub>2</sub> with dielectric constant of 18-25 and band gap of 5.8 eV as capable with advanced material properties to replace standard gate oxide SiO<sub>2</sub> in the new generation advanced MOS devices [21]. HfO<sub>2</sub> has numerous advantages

over SiO<sub>2</sub> such as significant heat of formation i.e. 271 kcal/mol, high refractive index of around 2, UV to IR transparent range and considerable thermal stability etc. [22]. These advantageous material properties made HfO<sub>2</sub> as a considerably superior high-k dielectric material to be used as a gate oxide in advanced MOS devices [23]. The balancing factors like low band offset of 1.5 eV and high dielectric constant of 18-25 have conceded HfO<sub>2</sub> as an evolving material [24, 25]. As a result, in microelectronics community, standard gate oxide SiO<sub>2</sub> has been replaced by HfO<sub>2</sub> as the gate oxide in some advanced CMOS transistors by Intel in 2007 [26].

| Material                       | Eg (eV) | Dielectric<br>constant (k) | Crystal Structure                           |              |
|--------------------------------|---------|----------------------------|---|--------------|
| SiO <sub>2</sub>               | 9       | 3.9                        | Amorphous                                   | [5]          |
| TiO <sub>2</sub>               | 3-3.5   | 30-100                     | Tetragonal                                  | [5,14,27-29] |
| ZrO <sub>2</sub>               | 5.8     | 25                         | Monoclinic, Tetragonal, Cubic               | [30-32]      |
| Al <sub>2</sub> O <sub>3</sub> | 8.7     | 8.5-10.5                   | Amorphous                                   | [33-36]      |
| Ta <sub>2</sub> O <sub>5</sub> | 4-4.5   | 20-35                      | Orthorhombic                                | [37-40]      |
| Gd <sub>2</sub> O <sub>5</sub> | 5.4     | 12-23                      | Amorphous                                   |              |
| La <sub>2</sub> O <sub>3</sub> | 4.3     | 27                         | Hexagonal, Cubic                            | [5,41]       |
| Y <sub>2</sub> O <sub>3</sub>  | 5.6     | 12-20                      | Cubic                                       | [5,42]       |
| Nb <sub>2</sub> O <sub>5</sub> | -       | 50-200                     | -   | [43-45]      |
| Si <sub>3</sub> N <sub>4</sub> | 5       | 7.5                        | Amorphous                                   | [5]          |
| HfO <sub>2</sub>               | 5.8     | 18-25                      | Amorphous, Monoclinic,<br>Tetragonal, Cubic | [30]         |

Table 1.1: Leading advanced dielectric constant materials and their material properties.

HfO<sub>2</sub> is mainly known to exist in three crystallographic phases at ambient pressure depending on the temperature. It exists in monoclinic phase (m-HfO<sub>2</sub>) in the temperature range of room temperature (RT) to 1700 °C, transforms to tetragonal (t-HfO<sub>2</sub>) at higher temperatures greater than 1700 °C and at very high temperatures greater than 2600 °C, it becomes cubic (c-HfO<sub>2</sub>). The crystallographic phases of HfO<sub>2</sub> and phase diagram are shown in Fig. 1.3 and Fig. 1.4 respectively

and corresponding lattice parameters are listed in Table 1.2. Some important material properties of  $HfO_2$  are listed in Table 1.3.

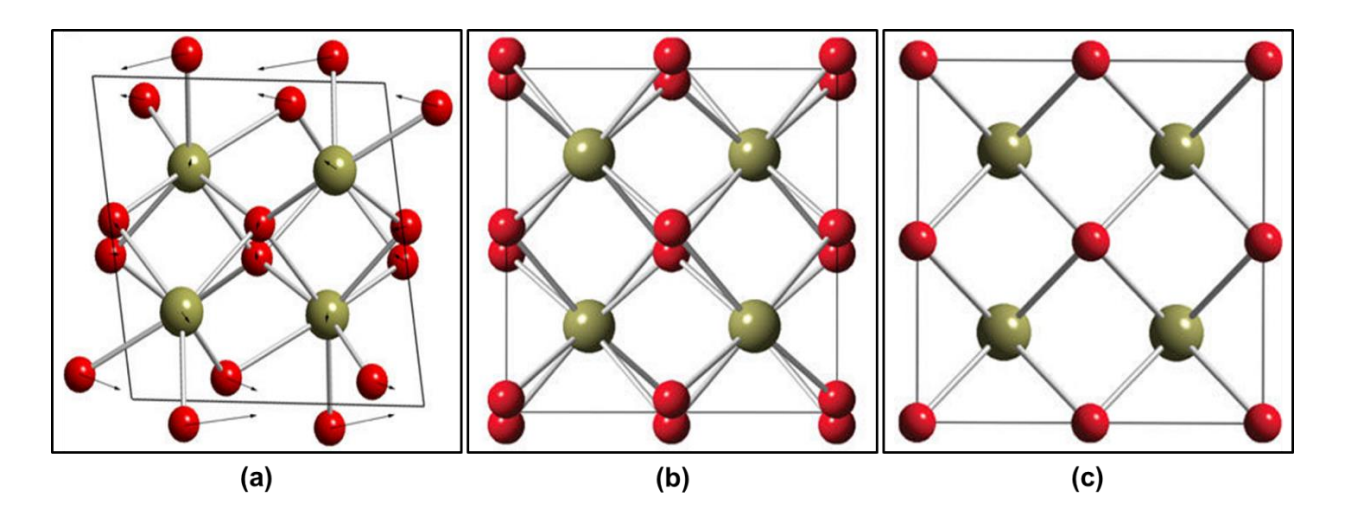


Fig. 1.3: HfO<sub>2</sub> crystallographic phases (a) Monoclinic, (b) Tetragonal and (c) Cubic [46].

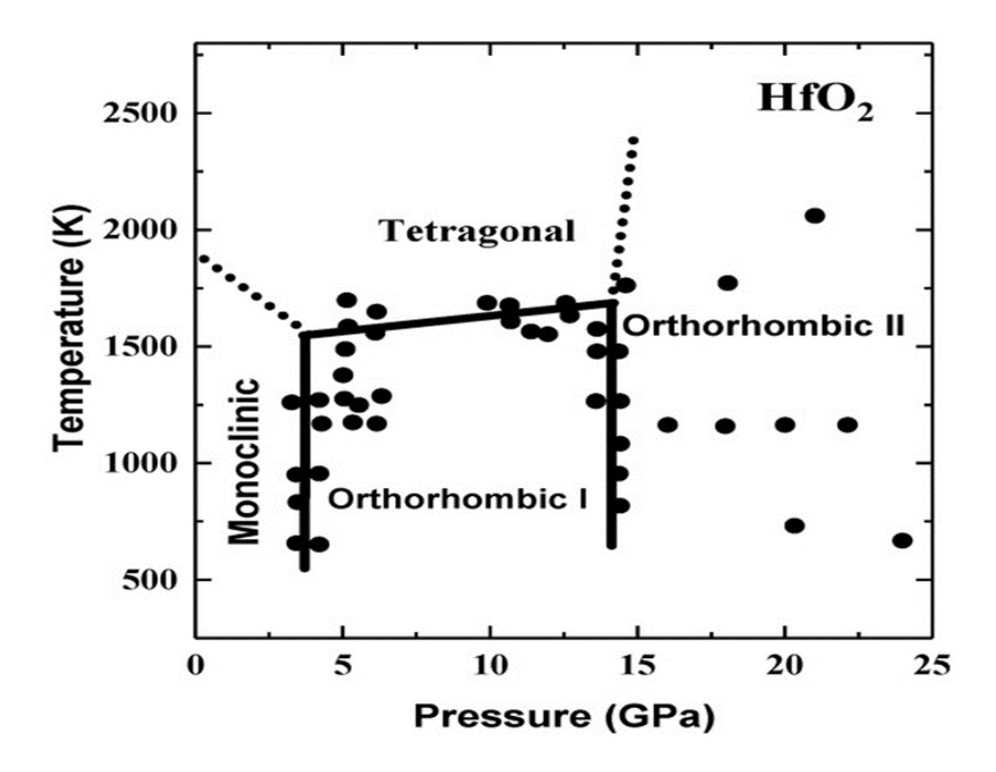


Fig. 1.4: HfO<sub>2</sub> Phase diagram [47].

| HfO <sub>2</sub> crystallographic phase | Temperature   | Lattice<br>parameters                          | Space<br>group       | Ref.     |
|---|---------------|--|----------------------|----------|
| Monoclinic                              | RT to 1700 °C | a=5.117 Å<br>b=5.175 Å<br>c=5.290 Å<br>β=99.77 | P2 <sub>1</sub> /c   | [48]     |
| Tetragonal                              | >1700 °C      | a=5.14 Å<br>c=5.25 Å                           | P4 <sub>2</sub> /nmc | [49, 50] |
| Cubic                                   | >2600 °C      | 5.08 Å   | Fm-3m                | [51]     |

Table 1.2: Phase transition temperatures and corresponding lattice parameters of HfO<sub>2</sub>.

| Dielectric constant (k) | (18-25)                     |
|-------------------------|-----------------------------|
| Density                 | 9.68 g/cm <sup>3</sup>      |
| Energy Band gap (Eg)    | 5.7 eV                      |
| Specific Heat Capacity  | 120 J/kg-K                  |
| Refractive Index        | ~ 2                         |
| Electron mean free path | 9.2 nm                      |
| Melting point           | 3000° K                     |
| Boiling point           | 5500° K                     |
| Thermal Conductivity    | 1.1 W/m K                   |
| Youngs module           | 57 GPa                      |
| Thermal Expansion       | 6.0 μm/m-K                  |
| Linear expansion        | 5.8X10 <sup>-6</sup> /k     |
| Thermal Diffusivity     | $0.95 \text{ m}^2/\text{s}$ |

Table 1.3: Some important material properties of HfO<sub>2</sub> [21].

It is important to note that, in Silicon CMOS technology, use of Si as the standard semiconductor was encouraged because it has outstanding interface properties with the dielectric SiO<sub>2</sub> [52]. However, in microelectronics community, standard gate oxide SiO<sub>2</sub> has been replaced by HfO<sub>2</sub> [53]. For further device scaling, it is presently followed by an attempt to replace the Si with superior high mobility semiconductors. Among the many superior semiconductor materials, III-V group and III-VI group compound semiconductors such as GaAs, GaN, GaSb, InAs and Ga<sub>2</sub>O<sub>3</sub> etc. are capable to attain the future high speed devices with good electrical characteristics [54, 55]. These compound semiconductors attracted the attention in current years owing to their higher electron mobility and wide band gap which makes them an attractive substrates for the new generation high-speed applications in CMOS devices [56].

#### 1.6. The MOS capacitor/diode

MOS diode/capacitor is the key structure of the MOSFET technology. It has the following structure as shown in Fig. 1.5. MOS structure consists of a semiconductor substrate on which a layer of dielectric material is deposited with thickness 'd'. On top of this dielectric layer, metal electrodes are deposited as top contact and another metal electrode like conductive Ag paste used underneath the semiconductor substrate as bottom contact.

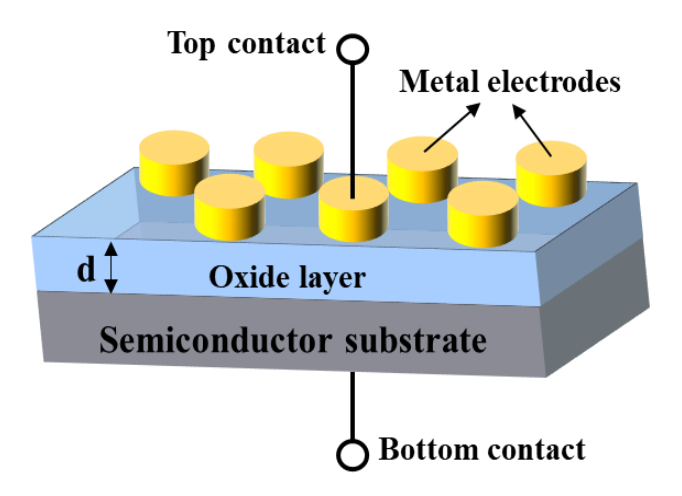


Fig. 1.5: The schematic structure of the MOS capacitor/diode.

As mentioned in the previous section 1.3, the memory performance of MOS capacitor is measured in terms of capacitance density (C/A) as given by the equation 1.1.

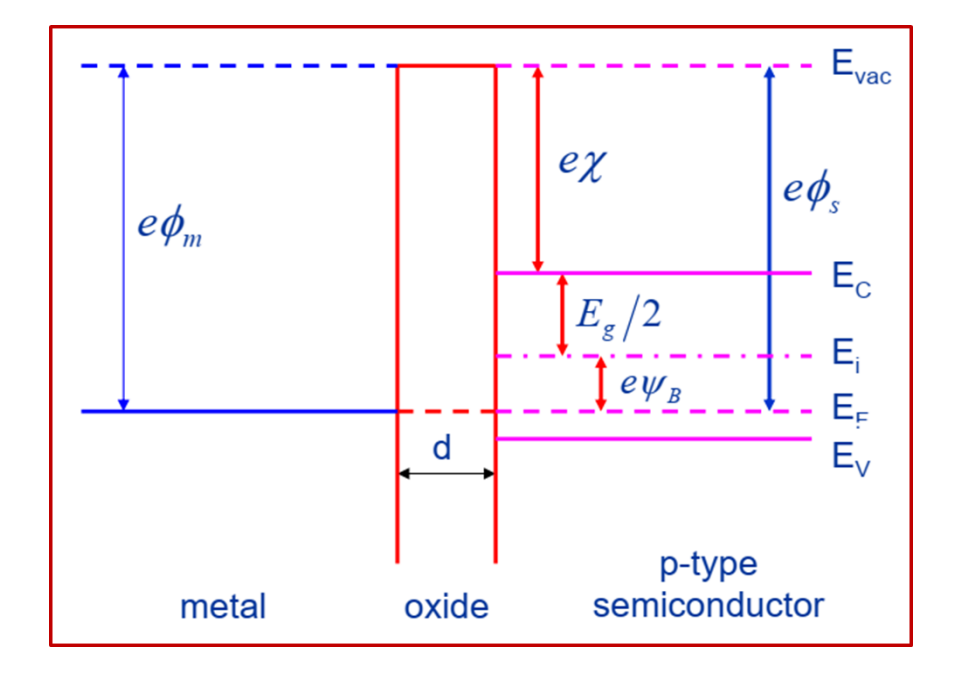


Fig. 1.6: The band diagram of an ideal MOS capacitor/diode [57].

The band diagram of an ideal MOS diode at equilibrium condition is shown in Fig. 1.6 where  $e\phi_m$  and  $e\phi_s$  are work functions of metal and semiconductor respectively.  $e\chi$  is electron affinity and d is thickness of the dielectric oxide layer. At the thermal equilibrium state, without any bias applied, the Fermi levels of both materials (the metal and the semiconductor) are aligned.

#### For an ideal MOS diode:

- Without any bias applied, the difference in the energy between the metal work function and the semiconductor work function is zero (called as flat-band state).
- The only charges which present in the structure at any applied bias are on the metal surface and in the semiconductor.

In general, there are three types of conditions that are known in MOS structure, depending on the positive or negative applied bias as shown in Fig. 1.7. Here, a MOS capacitor/diode is fabricated using a p-type semiconductor. When a negative bias is applied to the MOS diode, no current runs so that the semiconductor Fermi level is constant. In this situation, the bands bend upwards and extra holes are prompted at the interface between semiconductor and oxide. Since  $E_i$ - $E_F$  increases at the surface of semiconductor, holes accumulate (see Fig. 1.7(a)). This is known as the accumulation condition. With a minor applied positive bias, the majority carriers (holes) are depleted and the bands bend in downward direction (see Fig. 1.7(b)). This is known as the

depletion condition. With further increasing applied positive bias, the intrinsic fermi level (E<sub>i</sub>) crosses the fermi level by further bending of bands (see Fig. 1.7(c)). This is identified as the inversion condition.

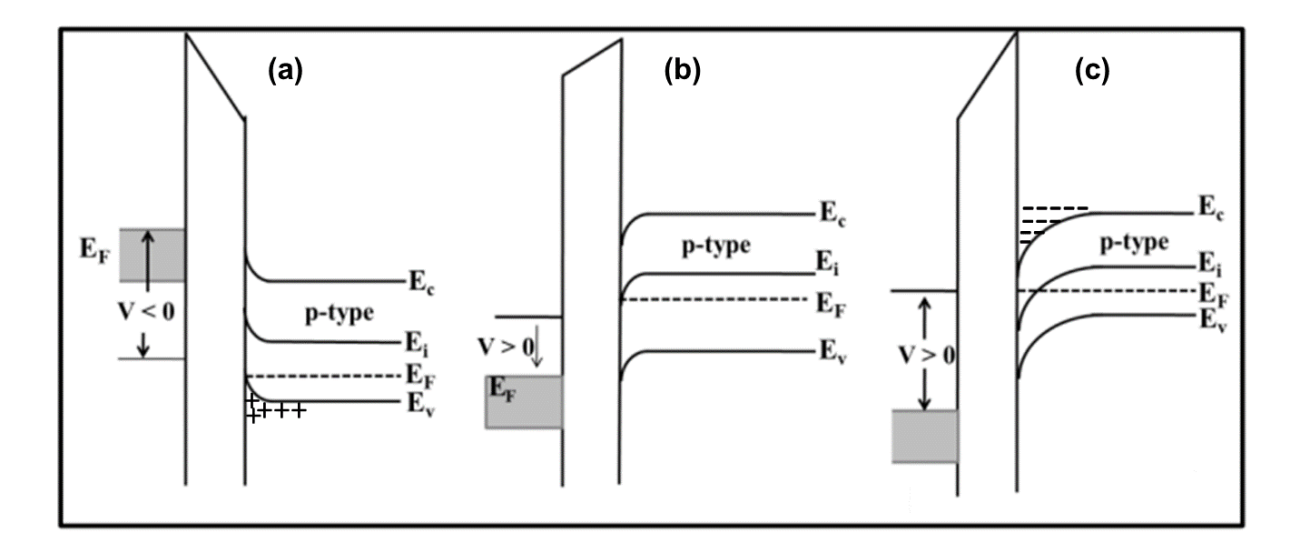


Fig. 1.7: Band diagrams of an ideal MOS capacitor/diode under negative and positive applied bias (a) accumulation condition, (b) depletion condition and (c) inversion condition [57].

#### 1.6.1. Leakage current – Voltage (I-V) characteristics

Examination of I-V characteristics is used to study the leakage current conduction mechanisms of MOS capacitor/diode through the gate oxide. The choice of gate dielectric material depends on the quantity of leakage current density through the MOS device, which decides its capability for practical applications. Although the dielectric oxide is an insulating material, it conducts minor leakage current depending on the applied voltage. With increase in the applied voltage above the breakdown of the corresponding dielectric oxide layer, it turns into conducting layer which results in an increase in the leakage current density. However, it is essential to know the cause of conductivity in dielectric oxide materials. Mostly, the conduction mechanisms in the dielectric oxide materials are classified as Electrode and Bulk Limited Conduction mechanisms (ELC and BLC respectively). The ELC is due to Schottky Emission (SE) mechanism, Direct Tunneling (DT) mechanism, Fowler-Nordheim tunneling (FN) mechanism and Thermionic Field-Emission mechanism, whereas BLC is due to Ohmic conduction, Ionic conduction, Poole-Frenkel tunneling (PF) mechanism, Space Charge (SC) limited conduction mechanism, Trap Assisted tunneling (TAT) mechanism or Hopping conduction mechanism and Grain Boundary (GB) limited

conduction mechanism (see Fig. 1.8). The ELC and BLC are dependent on the metal-oxide interface electrical properties and oxide material dielectric properties respectively.

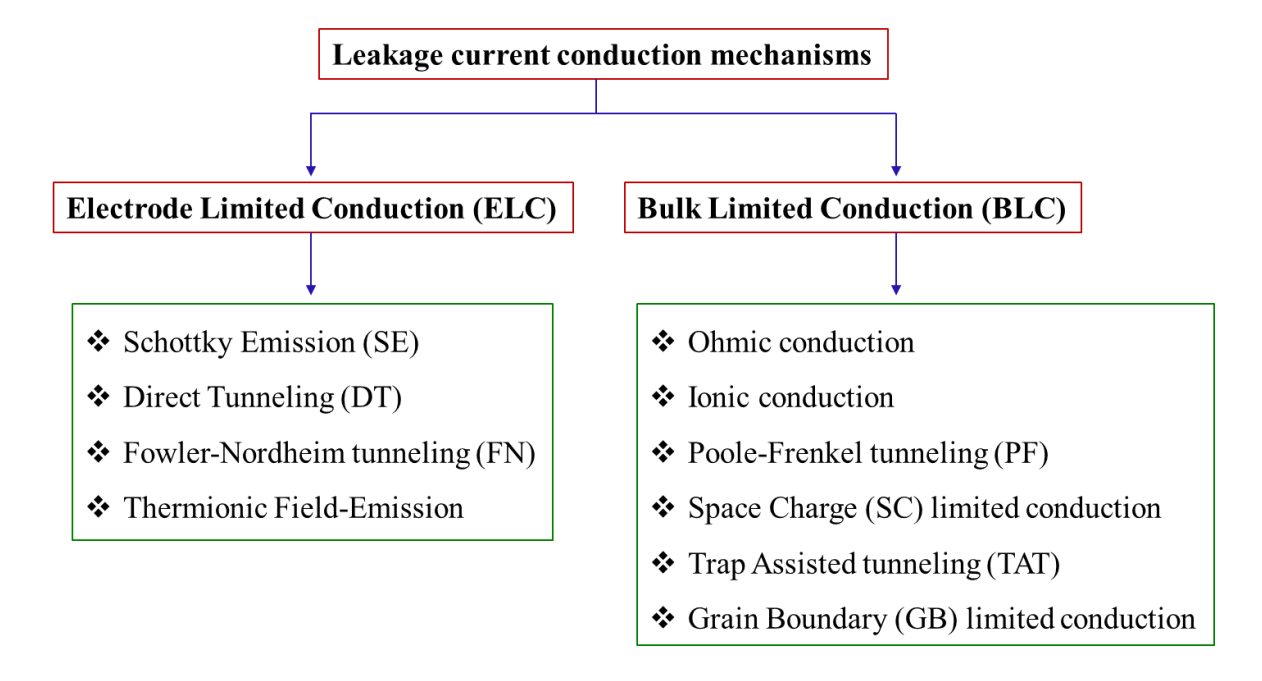


Fig. 1.8: Leakage current conduction mechanisms [57].

#### **Direct Tunneling:**

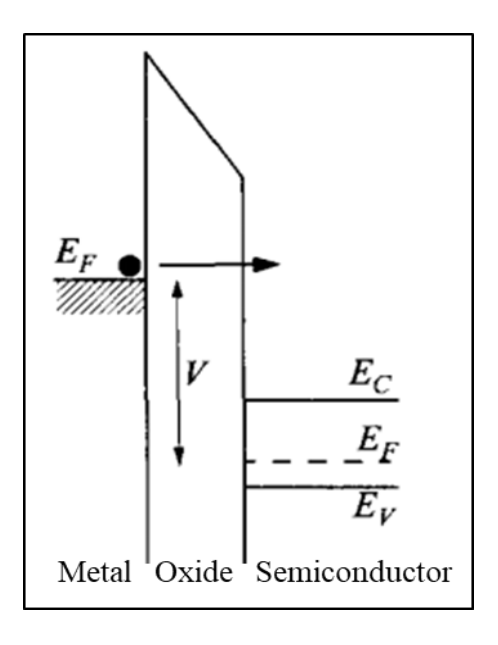


Fig. 1.9: Band diagram of DT conduction mechanism [59].

The leakage current conduction due to direct tunneling is responsible when the electrons directly tunnel through the dielectric layer and is relevant to the high-k gate oxides with thickness of less than 6 nm [58]. Band diagram of direct tunneling conduction mechanism is shown in Fig. 1.9 and expression for leakage current density due to direct tunneling is given by [59],

$$J_{DT} = \frac{q^3}{16\pi^2\hbar\Phi_b} F_{ox}^2 \exp\left\{-\frac{4}{3} \frac{\sqrt{2m_{ox}^*}\Phi_b^{3/2}}{\hbar q} \frac{1}{F_{ox}} \left[1 - \left(1 - \frac{qV_{ox}}{\Phi_b}\right)^{3/2}\right]\right\}$$
(1.3)

#### **\*** Fowler-Nordheim tunneling:

The leakage current due to FN tunneling is observed, when the applied bias is effectually more so that the barrier of dielectric oxide becomes triangular in shape and at the edge of the triangle the barrier becomes thinner than the original barrier. At this high applied voltage, the electrons can tunnel easily through this thinner triangular barrier and leakage current increases exponentially. Band diagram of FN tunneling conduction mechanism is shown in Fig. 1.10 and expression for leakage current density due to FN tunneling is given by equation 1.4 [60].

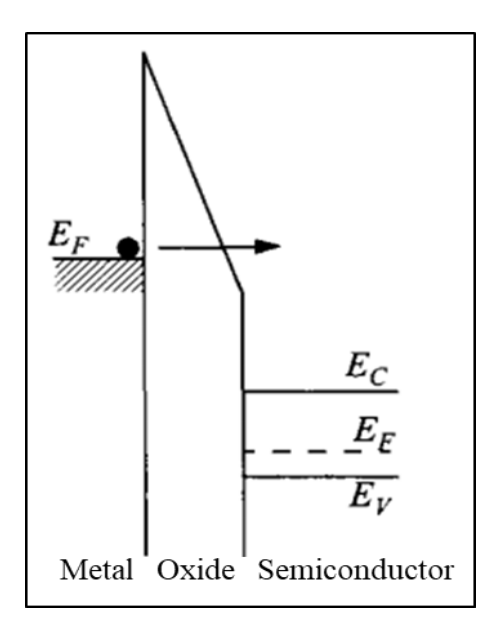


Fig. 1.10: Band diagram of FN tunneling conduction mechanism [60].

$$J_{FN} = \frac{q^3}{16\pi^2 \hbar \Phi_b} F_{ox}^2 \exp\left[ -\frac{4}{3} \frac{\sqrt{2m_{ox}^*} \Phi_b^{3/2}}{\hbar q} \frac{1}{F_{ox}} \right]$$
(1.4)

#### **❖** Poole-Frenkel tunneling:

The leakage current in dielectric oxides due to PF tunneling is mainly attributed to the presence of defects in the dielectric oxide layers. These defects in the dielectric oxide layers act as charge trapping centers and confine the charges by creating potential wells. In this mechanism, conduction is mainly due to the emission of confined electrons from the trap to the conduction band of the dielectric oxide. Band diagram of PF tunneling conduction mechanism is shown in Fig. 1.11 and expression for leakage current density due to PF tunneling is given by equation 1.5 [61].

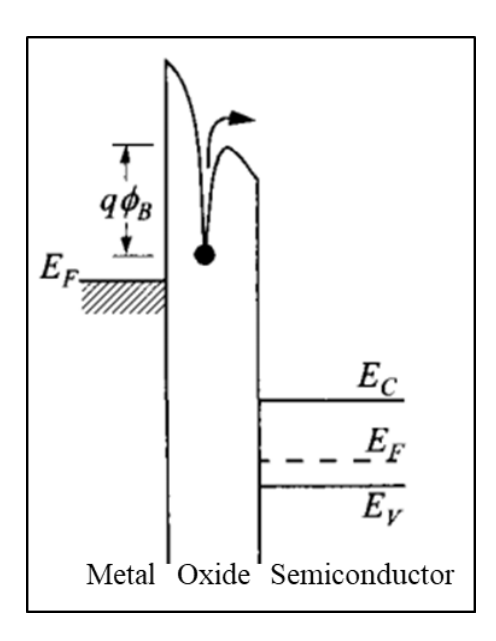


Fig. 1.11: Band diagram of PF tunneling conduction mechanism [61].

$$J_{PF} = EF_{ox} \exp\left[-\frac{q\Phi - \beta\sqrt{F_{ox}}}{\xi KT}\right]$$
 (1.5)

In these equations,  $F_{ox}$  is the electric field through the dielectric layer  $HfO_2$  and  $\xi$  (value in between 1 and 2 which is constant) is the factor obtained by acceptor compensation. Other well-known constants are like Boltzmann's constant (K), Charge of electron (q), Temperature (T) and reduced Planck constant (ħ). Here,  $\Phi_b$  is the barrier height among the conduction bands at the semiconductor-gate oxide interface,  ${m_{ox}}^*$  is the effective mass of electrons in the dielectric layer and  $V_{ox}$  is the applied voltage through the dielectric oxide.

#### **1.6.2.** Capacitance – Voltage (C-V) characteristics

As discussed above, In MOS structure there are three types of conditions: accumulation, depletion and inversion. These are known to be operative depending on the positive or negative applied bias. Variation in the applied frequency (low-high) results in difference in C-V curve in these conditions. When a negative bias is applied to the MOS diode, accumulation of holes takes place which results in maximum capacitance. With decreasing negative bias (small positive bias), formation of a depletion layer takes place which results in a decrease in the capacitance. With further increasing applied positive bias, weak/strong inversion takes place depending on the surface concentration of electrons. This inversion can be observed only at lower frequencies as the generation rate of electrons is fast at this frequency and deep depletion can be observed at higher frequencies as shown in Fig. 1.12.

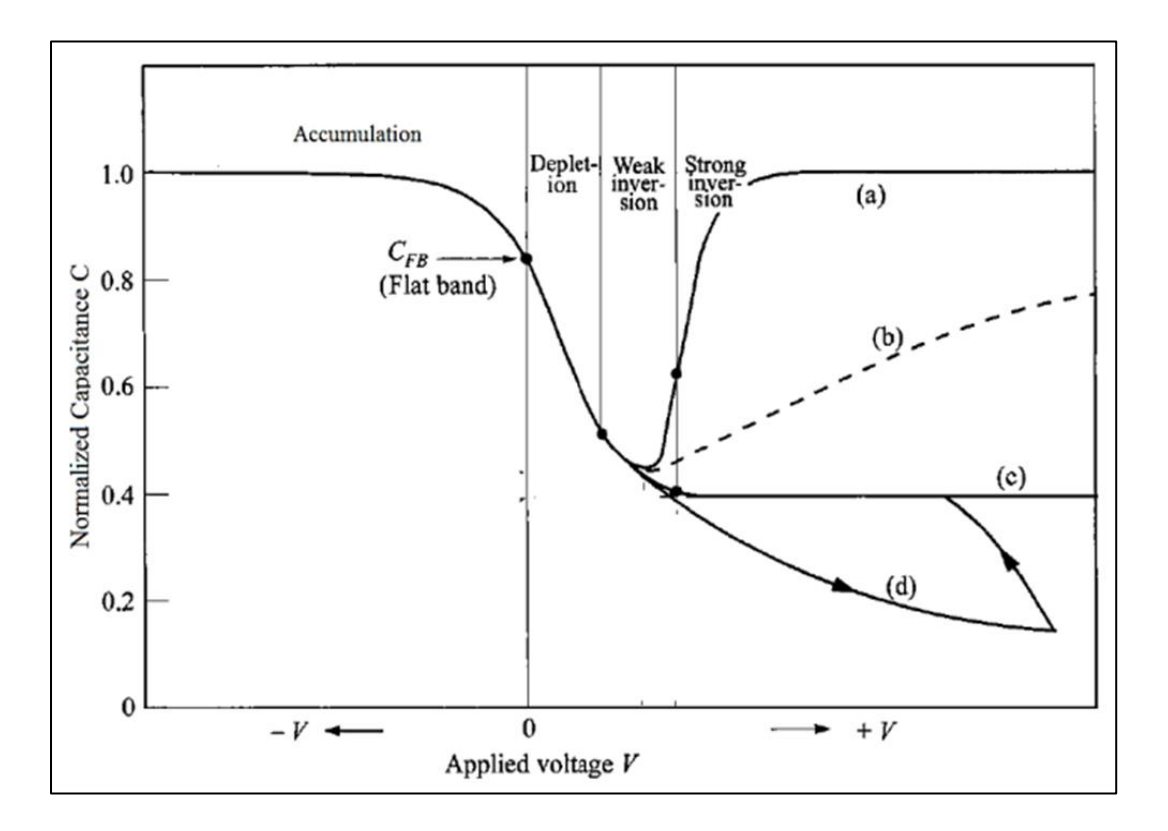


Fig. 1.12: MOS capacitor (p-type) C-V characteristics with flat-band voltage (V) = 0 at different frequencies (a) lower frequency, (b) intermediate frequency, (c) higher frequency and (d) higher frequency with a fast sweep [57].

#### 1.6.3. Effects of defects

In MOS structure, the interfaces between metal-oxide and oxide-semiconductor play an important role in the electrical performance of the MOS device. These interfaces are expected to contain interface trapped charges and oxide charges. Four kinds of charges namely mobile ionic  $(Q_m)$ , fixed oxide  $(Q_f)$ , oxide trapped  $(Q_{ot})$  and interface trapped  $(Q_{it})$  charges are known in MOS structures as shown in Fig. 1.13.

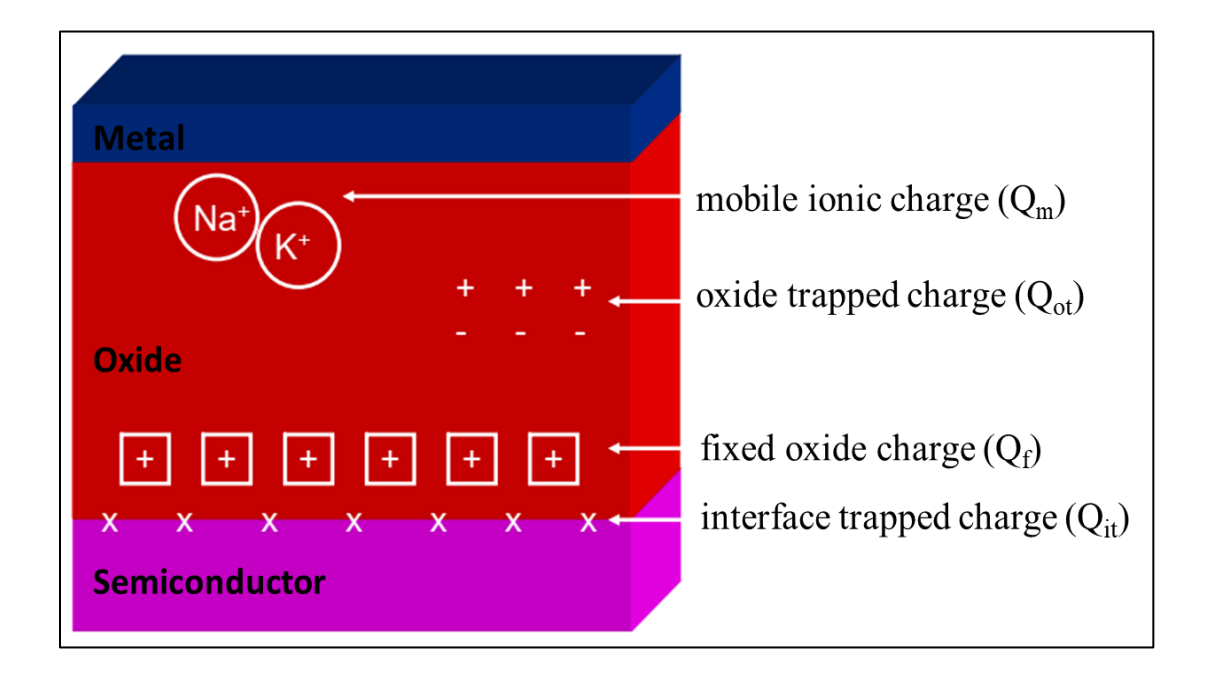


Fig. 1.13: Charges related with the MOS structure [57].

The mobile ionic charges  $(Q_m)$  are observed because of alkali ions and heavy metal ions. With a applied bias to the metal gate, these charges transport through the dielectric oxide which result in flat band voltage shift in the C-V hysteresis curve of the MOS capacitor. Fixed oxide charges  $(Q_f)$  typically originate from the dangling bonds which are positive charges and found nearby the oxide/semiconductor interface. These charges are fixed and immovable with applied voltage bias. These charges also result in the flat band voltage  $(V_{fb})$  shift depending on the positive or negative charges as shown in Fig.1.14.

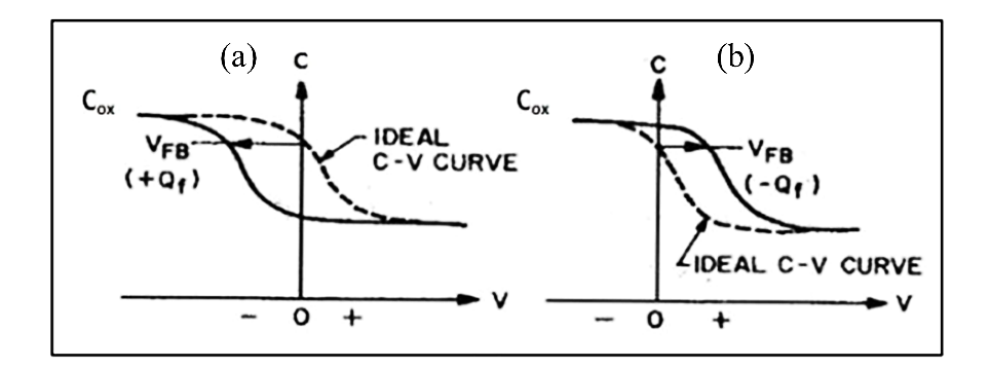


Fig. 1.14: C-V curves of the MOS capacitor due to

(a) positive and (b) negative fixed oxide charges [57].

Oxide trapped Charges ( $Q_{ot}$ ) are defects that are present in the dielectric oxide layer which can confine the holes/electrons or both. These charges may be minimized by annealing the dielectric oxide layer. These charges can affect the threshold voltage ( $V_{th}$ ) of the MOS capacitor by trapping the charge carriers. The interface trapped charges (Qit) are positive or negative. When the interface loses electrons, the positive charges are observed while negative charges are observed with gaining of electrons. These charges have the electrical communication with the semiconductor. Depending on the surface potential, these traps can be dis-charged or charged. With the applied voltage, variation of charge of the interface traps takes place which results in variation in the C-V characteristics as shown in Fig. 1.15.

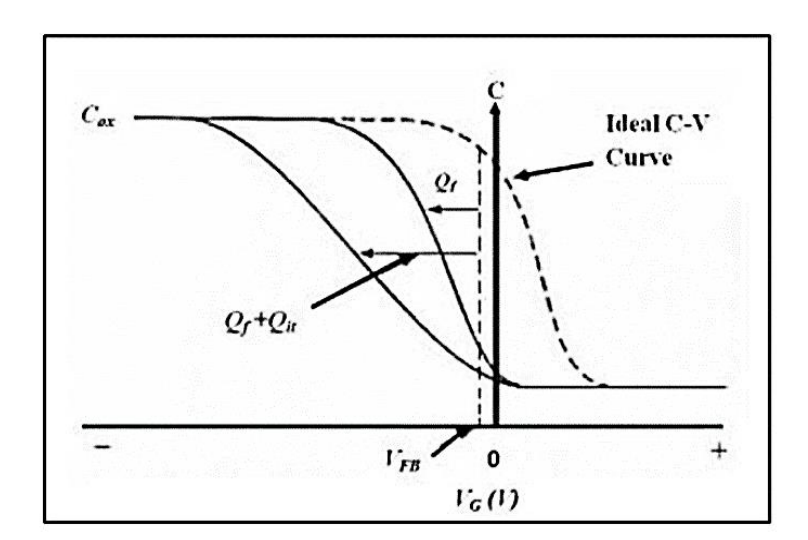


Fig. 1.15: C-V characteristics of MOS capacitor with fixed oxide charges and interface trapped charges [57].

It may be possible to generate or anneal the interface/oxide trapped charges inside the dielectric oxide by ionizing radiations. As discussed earlier, high-k dielectric HfO<sub>2</sub> has gained some importance in modern integrated circuit (IC) technology [12, 17, 26]. However, some of its material properties are still under investigation for better understanding as it has found numerous applications not only in advanced microelectronics but also in other fields [62, 63]. Furthermore, the detailed studies on the effects of ionizing radiations, low/high energy ion irradiation, gamma irradiation and device reliability are essential for long-term device usages, especially when these devices are used in radiation harsh environments. Moreover, ion irradiation studies also help to obtain the necessary data to improve the electrical properties of these high-k dielectric based MOS devices. Some transitory discussions about the fundamentals of ion-solid interactions and studies on ion beam irradiation of solid-state devices are summarized below.

#### 1.7. Fundamentals of ion-solid interactions

In Physics, the research related to energetic ion-beams ages back since more than a hundred years. In the year of 1911, the ion-beam related study started with Rutherford's well-known gold-foil experiment [64]. In the year of 1932, development of the Cockcroft-Walton accelerator by John Cockroft and Ernest Walton and studies on the transformation of Lithium to Helium due to energetic proton irradiation [65] attracted the attention of researchers towards understanding the fundamentals of ion-matter interactions. When an accelerated ion with high/low energy is incident on a solid material (target material), the interaction between the ion-nuclei or ion-electrons contingent on the energy. The interaction between the ions and electrons is significant when the velocity of incident ion is equivalent or greater than Bohr velocity of the electrons [66, 67]. The interaction between the ions of low energy and the target material (nuclei) is generally by elastic collisions. In this case, the energy lost by incident ions in this collisions is termed as nuclearenergy loss  $\left[S_n \text{ or } \left(\frac{dE}{dx}\right)_{nuc}\right]$ . The interaction between the ions of high energy and the target material (electrons) is generally by inelastic collisions and the energy lost by incident ions in these collisions is called electronic energy loss  $\left[S_e \text{ or } \left(\frac{dE}{dx}\right)_{ele}\right]$  which results in the ionization and excitation of electrons in the target material. The projected range (Rp) of the ion in solid, Sn and Se depend on the accelerated ion and target solid material. The projectile ion energy, its mass and

charge as well as the density and charge of the target material play important role in these ionsolid interactions as illustrated here:

$$\left(\frac{dE}{dx}\right)_{total} = \left(\frac{dE}{dx}\right)_{elec} + \left(\frac{dE}{dx}\right)_{nuc} = -N\varepsilon(E)$$
 (1.6)

The actual values of  $R_p$ ,  $S_n$  and  $S_e$  due to interactions between the known ion and target materials can be estimated by using a well-known numerical simulation program called Stopping & Range of Ions in Matter (SRIM) [68]. The energy of the backscattered ions from the bulk of the target material deep below the surface will be less as compared to that of backscattered ions from the surface of target material owing to the  $S_e$ . The  $S_n$  is governed by the elastic collisions between the accelerated ion and atoms of the solid target material (see equation 1.7). The kinetic energy and momenta before and after the interaction are conserved in elastic collisions.

$$\left(\frac{dE}{dx}\right)_{nuc} = \left(\frac{4\pi Z_1^2 Z_2^2 e^4 N}{v^2 M_2}\right) * \left(\frac{b_{max}}{b_{min}}\right)$$
(1.7)

Where  $M_1$ , v and  $Z_1$  e are the incident ion mass, velocity and charge respectively.  $Z_2$  and  $M_2$  e are the charge and mass of the target atom respectively. The  $S_e$  is ruled by the inelastic collisions (see equation 1.8). In this process, the energy of the incident ion is shared to electronic subsystem of the target material. This process results in ionization and excitation of electrons in the target material according to

$$\left(-\frac{dE}{dX}\right)_{ele} = \left(\frac{4\pi Z_1^2 e^4 n}{v^2 m}\right) * \left(ln \frac{b_{max}}{b_{min}}\right)$$
(1.8)

- ❖ If energy is in the range of few eV, it may possibly be absorbed into the target or it may bounce off from the surface of the target material. In this energy range, momentum of the accelerated ion is not sufficient to affect the atomic bindings of the target material.
- ❖ If energy is in the range of ~ 5 eV to ~ 5 keV, subsequent momentum transfer between the ion and target material results in the desorption, ionization of electrons and sputtering of the target surface. The atoms at the surface are ejected from the surface when the kinetic energy of the incident ion is sufficiently more than the binding energy. Mostly, the elastic collision results in sputtering, whereas inelastic result in the charge exchange and ionization.

- If energy of the incident ion is in between ~ 5 keV to few MeV, it passes into the bulk of target material and shares the energy by elastic or inelastic scattering. In this energy range, the scattering results in production of secondary electrons and phonons. The projected range (R<sub>p</sub>) of accelerated ion be governed by the energy of the accelerated ion and density of objective material. Usually ion projected range varies from few nm to μm. This results in Ion Implantation which is most important phenomena in the fabrication of semiconductor devices.
- ❖ The accelerated energetic ions shares the energy to the target atoms by two main processes
  - 1) Nuclear energy loss (Sn): energy transferred to the atoms of the target.
  - 2) Electronic energy loss (Se): energy transferred to the electrons of the target.

Ion irradiation results in sputtering of the target surface atoms, ionization, creation of defects and modification of vacancy/charge states.

#### 1.7.1. Radiation induced damage

- **Displacement:** In low energy ion irradiation, the atoms of the target are relocated to several lattice sites away from their original lattice sites which affects the electrical properties. This results in the formation of several types of point defects. This displacement damage due to ion irradiation can be estimated using SRIM analysis.
- Ionization: Depending on the energy, the energetic ions ionization occurs which results in charge carriers. These mobile charges travel around the material and get trapped which results in regions of the intense charges and consequently dependent fields. This effect is independent of radiation type. For creating EHPs in a piece of silicon by photon, its energy must be greater than the silicon energy band gap. Hence, the energy depends on the material properties as Si Eg > 1.1 eV and SiO<sub>2</sub> Eg > 9 eV. The damage due to ionizing radiation in insulators is indicated as total dose [69, 70]. The total dose is an amount of energy deposited in the target material by ionizing process which is estimated in the units of Gray or Rad (1 Gray = 100 Rad). The number of EHPs created through ionization is directly proportional to the total dose of radiation.

#### 1.7.2. Swift Heavy Ion irradiation (SHI)

SHI irradiation has imperious impact on electrical and structural properties. SHI irradiation can be used for the synthesis and characterization and modification of materials [71-79]. This is a well-established procedure, used for material characterization and modification in the nanometer region due to its spatial selectivity [80-82]. This technique is more useful because of good control of irradiation fluence and energy of incident ion. SHI irradiation can achieve energies in the range of MeV/u and these energetic ions can travel with 15% of light velocity.

As discussed, in SHI irradiation, the interaction of heavy ions with target material results in energy loss to both atomic nuclei and electrons in the target material. At lower energies (< 0.5 MeV/u), nuclear energy loss (energy transfers to atomic nuclei) dominates, which leads to the displacement of target atoms via elastic scattering. For higher energies (> 0.5 MeV/u), electronic energy loss dominates, which leads to local ionization [83] and damage production [84] in the target material.

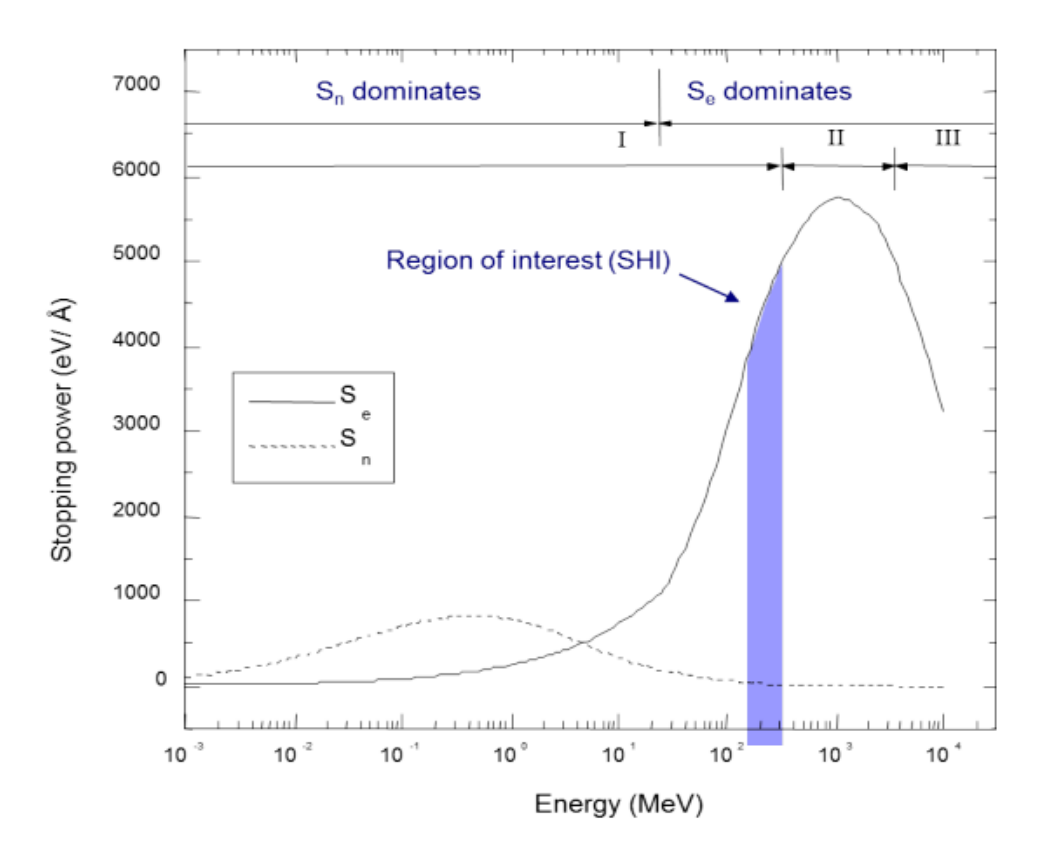


Fig. 1.16: Stopping power calculations of ions using the Monte-Carlo software (SRIM) [68].

The consequent energy losses produce damage in the cylindrical zone all through the ion path which is known as ion track. The formation of ion tracks depends on the material and energy of the ion and the diameter of the tracks ranges between few nm to several nm. The ion tracks with nanometer diameters formed due to SHI irradiation has been used in wide range of nanoscience applications [85, 86].

In the process of SHI irradiation, when an ion passes through the target material, it deposits a very huge amount of energy to the target atoms in the form of electronic and nuclear energy losses, which results in inter-diffusion/inter-mixing at the interface [87, 88]. Stopping power calculations of ions using the Monte-Carlo software (SRIM) with the energy ranging from 10 keV to 10 GeV is shown in Fig. 1.16.

There are few models explaining the mechanism of energy transfer in between the ion and solid material and the key prominence in these models is on describing the transfer of energy from the incident ion to the target material. Thermal spike model explains about the lattice heating, which results in melting of target material along the ion path, vaporization of the target material and subsequent thermal quenching via formation of ion tracks as shown in Fig. 1.17.

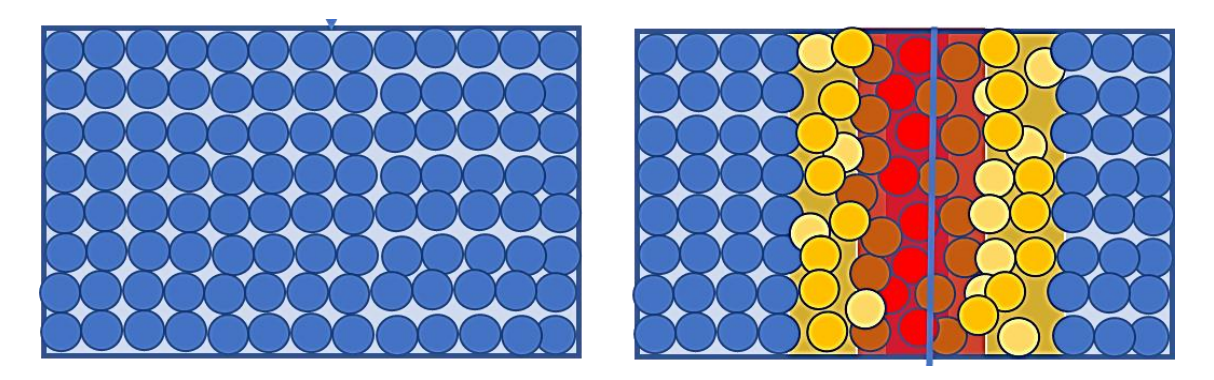


Fig. 1.17: The schematic of the formation of the latent track due to SHI irradiation [84].

#### 1.7.3. Thermal spike model

Thermal spike model [89] is known to elucidate the structural changes and track formation in the target materials. This model is also responsible for the ion induced annealing/creation of defects and ion induced phase transformations of the target material. These are explained by considering the atomic and electronic systems separately. It describes the transitory energy converted in to the thermal energy. The high energetic ions initially share their energy with the electrons of the target

material by the prominent ionization process. The electronic energy loss deposited through ion irradiation can bring the material up to melting temperatures within timescales of picosecond within the effective region [90-94].

In this model, two coupled differential equations given below are used to estimate the evolution of electronic and lattice temperatures.

$$C_e \frac{\partial T_e}{\partial t} = \frac{1}{r} \frac{\partial}{\partial r} \left[ r K_e \frac{\partial T_e}{\partial r} \right] - g (T_e - T_\alpha) + A(r, t)$$
 (1.9)

$$C_a \frac{\partial T_a}{\partial t} = \frac{1}{r} \frac{\partial}{\partial r} \left[ r K_a \frac{\partial T_a}{\partial r} \right] \mp g (T_e - T_\alpha)$$
 (1.10)

In these equations,  $C_e$  and  $C_a$  are the electronic and atomic specific heats respectively.  $K_e$ ,  $K_a$  are the thermal conductivities.  $T_e$  and  $T_a$  are temperatures of the electronic and atomic systems. r and g are the radial distance and electron phonon coupling parameter respectively.

## 1.8. SHI irradiation induced crystallization

Ion beam irradiation technique is known to crystallize the high-k dielectric materials in the nm region by raising its temperature up to melting point. The defects (O-vacancies) that are created through the irradiation, generate strain field in the target material and this generated strain field is responsible for the phase transformations in high-k dielectrics [95]. Some studies suggest that SHI induced phase transition depends on the primary phase of the target material and irradiation conditions like energy and radiation fluence. SHI irradiation induced amorphous to monoclinic and then monoclinic to tetragonal phase transformations of ZrO<sub>2</sub> and HfO<sub>2</sub> dielectric oxides have been reported [96, 97]. ZrO<sub>2</sub> and HfO<sub>2</sub> exhibit various crystallographic phases at ambient pressure depending on the temperature.

# 1.9. Floating gate based flash memory devices

In flash memory devices, an electrically floating metal gate is there within the gate oxide [98]. In 1967, a polysilicon-based floating gate type flash memory was invented by D. Kahng and S. M. Sze [99]. This will certainly increase the dielectric loss and leakage current as compared to that of an oxide without an embedded floating metal gate. However this gate is essential for getting the memory feature. In current flash memory devices, a metal floating gate within the gate oxide and

a common gate on the top of the gate oxide are there. When a high V<sub>GS</sub> is applied, a huge avalanche current flows during the set operation. This will induce a charge on the embedded floating gate. Now this charge on the floating gate cannot escape even if the V<sub>GS</sub> is removed. This charge will turn the device ON and hence it is non-volatile. This charge can be removed only by applying reverse voltage or by subjecting it to UV for erasing the memory. So an embedded floating metal gate is required for fabricating these memory devices. Now this continuous floating gate is being replaced by "isolated metal nanoparticles (NPs)" [100]. The dielectric loss will be less for the device with isolated metal NPs based floating gate memory devices than that of a device with continuous floating metal gate [101]. The floating gate based memory devices with embedded metal NPs have the benefits of extensive range of work-functions, unconventional efficiency and low operating voltages as compared to the memory devices with embedded semiconductor NPs [102]. When an array of isolated NPs is used as a floating gate, then each isolated gate will store the charge. This gate will hold the total charge even if few gates lose their charge over some unwanted leakage paths. Hence, such a memory device will have superior retention characteristics as compared to that of the devices which use continuous metal layer as an embedded floating gate [101].

To increase the storage capacity and to improve the retention properties of these floating gate based memory devices, integration of large work-functional metal NPs like Silver (Ag), Gold (Au) and Platinum (Pt) in-between the two oxide layers has been reported [103]. Among these large work-function metal NPs, Au NPs gained the consideration because they are easily produced, greater density of states and large work function (5.1 eV), which produces deep potential well that avoids retention loss of the devices and improves carrier confinement [104, 105]. For producing an array of high density Au NPs, several thin film deposition techniques such as RF/DC Sputtering, electron beam (e-beam) evaporation, Chemical Vapor Deposition (CVD) and Atomic Layer deposition (ALD) have been used [106-109]. To achieve the uniform spherical NPs, post deposition Thermal Annealing (TA), Rapid Thermal Annealing (RTA) and Ion beam irradiation methods have been used [110, 111]. Floating gate type memory devices with high density metal NPs will have large charge storage capacity. On the other hand floating gate type memory devices with good uniform metal NPs will help in enhancing the reproducibility of device properties [112]. TA and RTA procedures have been widely used to produce Au NPs in-between two HfO<sub>2</sub> thin-film layers [113, 114]. However, the usual TA and Ion beam irradiation procedures are known to crystallize the

tunneling oxide layer which results in an increase in the leakage currents due to tunneling and can deteriorate the device properties, in particular for modern alternate high-k dielectric oxides like HfO<sub>2</sub> [115-117]. Now, the main challenge is to produce an array of high density metal NPs without affecting the phase of the underneath tunneling oxide layer. Non-thermal methods such as Laser Annealing (LA) offer alternate technique to anneal layers of interest without altering the phase of the substrates and/or the surrounding medium.

## 1.10. Laser Annealing

In recent years, the effects of electronic excitation by laser annealing/irradiation on various properties has attracted significant attention [118, 119]. Laser irradiation/annealing induced defect creation in oxides, crystallization and inter-diffusion/inter-mixing by using ultrafast lasers have been reported [120-122]. Rittman et al. [123] reported the phase transition in ZrO<sub>2</sub> from monoclinic to tetragonal phase by employing ultrafast laser irradiation and the results are consistent with the phase transformations due to SHI irradiation [124]. Laser annealing is a capable technique to produce metal NPs because it offers a high degree of control over the formation of NPs and it has a benefit of defect minimization in the underneath tunneling oxide layer [125]. Furthermore, the laser annealing method can be used for producing some uniform high density metal NPs in-between the gate oxide layers without modifying the phase of high-k dielectric oxides. In 2016, Nikolaos Kalfagiannis et al. [126] suggested this method of Modifying NP Arrays by Laser Induced Self Assembly (MONA-LISA) to yield the pre-determined patterns of metal nanostructures. In 2018, L. Kastanis et al. [127] used laser annealing method to achieve uniformly spaced Au nanocrystals (NCs) and developed n-Si/SiO<sub>2</sub>/Au-NCs/Y<sub>2</sub>O<sub>3</sub>/Au structured floating gate type memory devices.

# 1.11. The objective and framework of the thesis

The main aim of this thesis is to report on the Thermal Annealing, Gamma irradiation, SHI irradiation and Laser annealing effects on the structural, optical and electrical properties of high-k dielectric HfO<sub>2</sub> thin films. In brief, the main motivations are:

1) To optimize the thickness of HfO<sub>2</sub> thin films on GaAs, GaOx/Si and Si substrates using RF magnetron sputtering.

- 2) To study the effects of Thermal annealing, Gamma irradiation, SHI irradiation and Laser annealing on the structural changes and subsequent effects on the electrical characteristics of HfO<sub>2</sub> thin films deposited on high mobility and wide bandgap semiconductors.
- 3) To fabricate a high density array of Au nanoparticles on the surface of HfO<sub>2</sub> without altering the phase of HfO<sub>2</sub> by using laser annealing technique for SERS substrate and floating gate type memory device applications.

This study will offer worthwhile information about the effects of electronic excitation on the structural changes and subsequent effects on the electrical properties of HfO<sub>2</sub> thin films deposited on high mobility and/or wide bandgap semiconductors for fabricating tunable and radiation harsh electronic devices, as HfO<sub>2</sub> based MOS structures are expected to be used in many devices in space, medical applications (radiological treatment equipment's) and physics experiments associated to high energy such as nuclear power plants.

#### **Chapter-1: Introduction and Motivation**

This chapter outlines the introduction, motivation and aim of the current thesis work. We explain here the significance of the choice of materials which are presently used and suggest the research requirements in the cutting edge of the current research field. The literature survey offers comprehensive information about the current knowledge in this area. This chapter concisely elucidates the importance of the present work and promising areas in which this thesis is to build up.

#### **Chapter-2: Experimental Details and Characterization Techniques**

Chapter 2 explains the fabrication of the thin films, various material characterization techniques and experimental facilities employed to investigate the present thesis work. HfO<sub>2</sub> thin films, HfO<sub>2</sub>/GaO<sub>x</sub>, Au/HfO<sub>2</sub> bilayer films and Au metal contacts were deposited by using RF magnetron sputtering, e-beam and thermal evaporation techniques in our department. Few as-deposited thin-films of HfO<sub>2</sub> were annealed in the temperature range of 200° C to 600° C in N<sub>2</sub> atmosphere for 60 min. Furthermore, a set of samples were irradiated by <sup>60</sup>Co gamma (1.25 MeV) rays with dose 2 KGy - 64 KGy and another set of samples were subjected to SHI irradiation with 120 MeV Ag ions using a Pelletron accelerator (15 UD tandem) at Inter University Accelerator Centre (IUAC),

New Delhi, India. These samples were examined by Surface Profilometer, FESEM, GIXRD, XRR, PL and optical spectroscopy available at University of Hyderabad while RBS measurements (using 2 MeV He<sup>2+</sup> ions at 165° of scattering angle at IUAC, New Delhi, India) have been performed on these samples to estimate the thickness and elemental composition This chapter also explains the working principle of 15 MV Pelletron accelerator. Electrical characteristics such as Leakage current – Voltage (I-V) and Capacitance – Voltage (C-V) of HfO<sub>2</sub> thin films based MOS structures have been performed by using Agilent B1500A semiconductor device analyzer at CFN, University of Hyderabad. In principle, the specifications of the experimental facilities, fundamentals of experimental techniques and characterization methods are discussed in detail.

# Chapter-3: Effects of Thermal Annealing and Gamma Irradiation on the structural and electrical properties of HfO<sub>2</sub> films deposited on GaAs

Chapter 3 embodies the discussion about the optimization of film thickness deposited under various deposition times to synthesize reproducible HfO<sub>2</sub> films with good quality using RF magnetron sputtering deposition technique. Thin films of HfO<sub>2</sub> were synthesized on Semi-Insulating GaAs substrates and the role of deposition time on the HfO<sub>2</sub> films have been studied. Further, thin films of HfO<sub>2</sub> synthesized using optimized growth parameters were exposed to thermal annealing and gamma irradiation. Effects of post deposition thermal annealing and gamma irradiation on the structural changes and subsequent effects on the electrical properties of HfO<sub>2</sub> films have been discussed.

# Chapter-4: Effects of Swift Heavy Ion (SHI) irradiation on the structural and electrical properties of HfO<sub>2</sub> thin-films deposited on GaAs

Chapter 4 provides a brief report on the SHI irradiation induced effects on grain agglomeration and introduction of crystalline phases in otherwise amorphous HfO<sub>2</sub> thin films deposited on GaAs substrates. These modifications in the films due to SHI irradiation were observed by performing FESEM, PL, RBS, XRR and GIXRD measurements. An orderly increase in the size of spherical grains and increase in the roughness of the films have been noticed. As-grown HfO<sub>2</sub> thin films exhibit amorphous nature. Ion irradiation has introduced monoclinic and tetragonal phases in otherwise amorphous thin films of HfO<sub>2</sub>. Further, Au/HfO<sub>2</sub>/GaAs based MOS structures have been fabricated to study the effects of SHI irradiation on the electrical properties of these devices. The leakage current conduction through the gate oxide has been studied using the Poole-Frenkel and

Fowler-Nordheim tunneling mechanisms by examining the leakage current-voltage characteristics.

# Chapter-5: Effects of Swift Heavy Ion (SHI) and Gamma irradiation on the structural and electrical properties of HfO<sub>2</sub>/GaO<sub>x</sub> thin films

Chapter 5 provides a brief report on the SHI irradiation induced effects on HfO<sub>2</sub>/GaO<sub>x</sub> bi-layered films synthesized on p-type Silicon (100) substrates. These modifications in the films due to SHI irradiation were observed by performing FESEM, RBS and GIXRD measurements. As-grown films contain highly strained inhomogeneous large grains. The average grain size decreases with increasing fluence which is attributed to SHI induced grain fragmentation. Ion-induced inter-diffusion/inter-mixing of Hf and Ga elements has been observed which leads to the development of inter-mixing of layers at the interfaces. Further, HfO<sub>2</sub>/GaO<sub>x</sub>/Si based Metal Oxide Semiconductor (MOS) capacitors have been fabricated and the effects of SHI irradiation and Gamma irradiation on the electrical properties of these devices have been discussed in detail.

# Chapter-6: Effects of Laser Annealing on the structural and electrical properties of HfO<sub>2</sub> and Au/HfO<sub>2</sub> bi-layered films deposited on Si

The main aim of this chapter is to report on fabrication of high-density arrays of gold nanoparticles on the surface of HfO<sub>2</sub> thin films without altering the phase of HfO<sub>2</sub> using an athermal laser annealing technique. HfO<sub>2</sub> (~ 30 nm) thin films synthesized on Si substrates by e-beam evaporation technique were exposed to Laser Annealing. Structural and electrical properties of pristine and laser annealed HfO<sub>2</sub> thin films have been studied as a function of the number of laser pulses incident on the sample. It is observed that pristine and laser annealed films are predominantly amorphous in nature, though there are observable changes in their morphology. Further, Au (~ 5 nm) and amorphous HfO<sub>2</sub> (~ 10 nm) films deposited on Si by thermal evaporation and e-beam evaporation methods respectively were subjected to Laser Annealing to produce an array of Au nanoparticles. Here, it is necessary to note that the usual thermal annealing methods would modify the phase of the HfO<sub>2</sub>. The structural modifications and optical properties of as-grown and laser annealed gold nanoparticles have been studied by using FESEM, GIXRD and UV-Vis absorption measurements. The leakage current conduction through the gate oxide with and without embedded Au nanoparticles has been studied by several tunneling mechanisms by investigating the Leakage

current – Voltage (I-V) characteristics. Memory performance of MOS structures with and without embedded Au nanoparticles has been studied by Capacitance – Voltage (C-V) measurements. Applications of these high-density Au nanoparticles in the fabrication of SERS substrates for molecular detection and floating gate type memory devices have been discussed in detail.

#### **Chapter-7: Conclusions and Scope of future work**

This chapter encapsulates the total work done in this thesis and provides the scope and outlook for the possible future investigations in this field.

#### 1.12. References

- [1] G. E. Moore, *Electronics*. **1965**, 38, 114-118.
- [2] B. Hoeneisen, C. A. Mead, MOS technology. *Solid State Electron.* **1972**, 15, 819-829.
- [3] S. Chen, Y. Y. Zhu, R. Xu, Y. Q. Wu, X. J. Yang, Y. L. Fan, F. Lu, Z. M. Jiang, J. Zou, *Appl. Phys. Lett.* **2006**, 88, 222902.
- [4] M. L Green, E. P Gusev, R. Degraeve, E. L Garfunkel, J. Appl. Phys. 2001, 90, 2057.
- [5] G. D. Wilk, R.M. Wallace, J.M. Anthony, J. Appl. Phys. **2001**, 89, 5243.
- [6] L. Yan, C. M. Lopez, R. P. Shrestha, E. A. Irene, A. A. Suvorova, M. Saunders, *Appl. Phys. Lett.* 2006, 88, 142901.
- [7] Y. C. Wang, M. Hong, J. M. Kuo, J. P. Mannaerts, J. Kwo, H. S. Tsai, J. J. Krajewski, Y. K. Chen, A. Y. Cho, *IEEE Electron Device Lett.* **1999**, 20, 9, 457-459.
- [8] R. B. Brown, B. Bernhardt, M. La Macchia, J. Abrokwah, P. N. Parakh, T. D. Basso, S. M. Gold, S. Stetson, C. R. Gauthier, D. Foster, B. Crawforth, T. K. McQuire, K. Sakallah, R. J. Lomax, T. N. Mudge, *IEEE Trans. Very Large Scale Integr. Syst.* 1998, 6, 1, 47-51.
- [9] Semiconductor Industry Association International Technology Roadmap for Semiconductors, **2001**.
- [10] D. A. Muller, T. Sorsch, S. Moccio, F. H. Baumann, K. Evans-Lutterodt, G. Timp, *Nature* 1999, 399, 758–761.
- [11] K. K. Hung, Y. C. Cheng, J. Appl. Phys. **1987**, 62, 4204.

- [12] J. Robertson, Eur. Phys. J. Appl. Phys. **2004**, 28, 265-29.
- [13] T. Mimura, K. Odani, N. Yokoyama, Y. Nakayama, M. Fukuta, *IEEE Trans. Electron Devices* **1978**, 25, 6, 573-579.
- [14] S. Wolf, Silicon Processing for the VLSI Era: Deep-Submicron Process Technology, 4, Lattice Press, Sunset Beach, CA **2002**.
- [15] D. Burg, J. H. Ausubel, *Moore's Law revisited through Intel chip density*, PLoS ONE **2021**, 16(8), e0256245.
- [16] Www.zdnet.com/zdnn/special/javascript/futurecpu/futurecpu.html, Processors: Past, Present and Future.
- [17] Huang et al., "Hf-based high-k dielectrics", Advances in Solid State Technologies, P. K. Chu (Ed.)
- [18] Zhenjie Tang, Ma Dongwei, Zhang Jing, Jiang Yunhong, Wang Guixia, Zhao Dongqiu, *IEEE Electron Device Letters* **2014**, 15, 241-244.
- [19] M. Houssa, *High-k Gate Dielectrics*, Institute of Physics Publishing, Bristol, UK **2004**.
- [20] T. Hori, *Gate Dielectrics and MOS ULSIs: Principles, Technologies and Applications*, Springer, Berlin, Germany **1997**.
- [21] Byoung Hun Lee, Laegu Kang, Renee Nieh, Jack C. Lee, Appl. Phys. Lett. 2000, 76, 1926.
- [22] L.V. Goncharova, M. Dalponte, T. Feng, T. Gustafsson, E. Garfunkel, P.S. Lysaght, G. Bersuker, *Phys. Rev. B* **2011**, 83, 115329.
- [23] Tzu-Ray Shan, Bryce D. Devine, Travis W. Kemper, Susan B. Sinnott, Simon R. Phillpot, *Phys. Rev. B* **2010**, 81, 125328.
- [24] R. K. Nahar, V. Singh, A. Sharma, J. Mater. Sci. Mater. Elec. 2007, 18, 615.
- [25] B. Aguirre, R. S. Vemuri, D. Zubia, M. H. Engelhard, V. Shutthananadan, K. K. Bharathi, C. V. Ramana, Appl. Surf. Sci. 2011, 257, 2197.
- [26] J. Robertson, Eur. Phys. J. Appl. Phys. **2004**, 28, 265-29.
- [27] M. Ritala, M. Leskela, *Atomic layer deposition*. *In Handbook of Thin Film Materials* **2001**, 1, Ed. H.S. Nawla, Academic Press, San Diego, CA, 103.

- [28] R. Singh, R.K. Ulrich, *Electrochem. Soc. Interface* **1999**, 8, 26-30.
- [29] K. Kukli, M. Ritala, M. Leskela, R. Lappalainen, *Chem. Vap. Depos.* **1998**, 4, 29-34.
- [30] Y. Kim, B. Gebara, M. Freiler, , J. Barnett, D. Riley, J. Chen, K.Torres, J. Lim, B. Foran, F. Shaapur, A. Agarwal, P. Lysaght, G. Brown, C. Young, S. Borthakur, H. Li, B. Nguyen, P. Zeitzoff, G. Bersuker, D. Derro, R. Bergmann, R. Murto, A. Hou, H. Huff, E. Shero, C. Pomarede, M. Givens, M. Mazanec, C. Werkhoven, *IEDM Tech. Digest* 2001, 20.2.1-20.2.4.
- [31] K. Kukli, M. Ritala, M. Leskela, Chem. Vap. Depos. 2000, 6, 297-302.
- [32] C. M Perkins, B. B Triplett, P. C McIntyre, K. C Saraswat, S. Haukka, M. Tuominen, *Appl. Phys. Lett.* **2001**, 78, 2357-2359.
- [33] O. Sneh, R. B Clark-Phelps, A. R Londergan, J. Winkler, T.E Seidel, *Thin Solid Films* **2002**, 402, 248–261.
- [34] M. Ritala, M. Leskela, *Atomic layer deposition. In Handbook of Thin Film Materials* (Ed. H.S. Nawla), Academic Press, San Diego, CA, 103, **2001**.
- [35] J. Robertson, J. Vac. Sci. Technol. B **2000**, 18, 1785–1791.
- [36] M. D Groner, J.W Elam, F.H Fabreguette, S.M George, *Thin Solid Films* **2002**, 413, 186–197.
- [37] Y.S Kim, J.S Kang, S.J Yun, K.I Cho, *J. Korean Phys. Soc.* **1999**, 35, S216–S220.
- [38] Y.S Kim, S.H.K Park, S.J Yun, J.S. Kang, *J. Korean Phys. Soc.* **2000**, 37, 975–979.
- [39] K. Kukli, M. Ritala, M. Leskela, J. Electrochem. Soc. 1995, 142, 1670–1675.
- [40] K Kukli, M. Ritala, M. Leskela, *Chem. Mater.* **2000**, 12, 1914–1920.
- [41] M. Nieminen, M. Putkonen, L. Niinisto, *Appl. Surf. Sci.* **2001**, 174, 155–165.
- [42] M. Putkonen, T. J. W Sajavaara, *Chem. Vap. Depos.* **2001**, 7, 44–50.
- [43] K. Kukli, M. Ritala, M. Leskela, R. Lappalainen, Chem. Vap. Depos. 1998, 4, 29–34.

- [44] M. Stromme, G. Niklasson, M. Ritala, M. Leskela, K. Kukli, *J. Appl. Phys.* **2001**, 90, 4532–4542.
- [45] K. Kukli, M. Ritala, M. Leskela, J. Electrochem. Soc. 2001, 148, F35–F41.
- [46] O. Ohtaka, H. Fukui, T. Kunisada, T. Fujisawa, K. Funakoshi, W. Utsumi, T. Irifune, K. Kuroda, T. Kikegawa, *J. Am. Ceram. Soc.* **2001**, *84*, 1369–1373.
- [47] Bethany M. Hudak, Sean W. Depner, Gregory R. Waetzig, Anjana Talapatra, Raymundo Arroyave, Sarbajit Banerjee, Beth S. Guiton, *Nature Communications*, **2017**, 8, 15316.
- [48] J. Adam, M. D. Rodgers, Acta. Crystallogr. 1959, 12951.
- [49] R. E. Hann, P. R. Suttch, J. L. Pentecost, J. Am. Ceram. Soc. 1985, 68C-285.
- [50] G. B. Bokiy, *Introduction into Crystallochemistry* Moscow State University, **1954**.
- [51] Hong Jiang, Ricardo I. Gomez-Abal, Patrick Rinke, Matthias Scheffler, *Phys. Rev. B* 2010, 81, 085119.
- [52] K. K. Hung, Y. C. Cheng, J. Appl. Phys. 1987, 62, 4204.
- [53] J. Robertson, Eur. Phys. J. Appl. Phys. **2004**, 28, 265-29.
- [54] Y. C. Wang, M. Hong, J. M. Kuo, J. P. Mannaerts, J. Kwo, H. S. Tsai, J. J. Krajewski, Y. K. Chen, A. Y. Cho, *IEEE Electron Device Lett.* 1999, 20, 9, 457-459.
- [55] R. B. Brown, B. Bernhardt, M. La Macchia, J. Abrokwah, P. N. Parakh, T. D. Basso, S. M. Gold, S. Stetson, C. R. Gauthier, D. Foster, B. Crawforth, T. K. McQuire, K. Sakallah, R. J. Lomax, T. N. Mudge, *IEEE Trans. Very Large Scale Integr. Syst.* 1998, 6, 1, 47-51.
- [56] T. Mimura, K. Odani, N. Yokoyama, Y. Nakayama, M. Fukuta, *IEEE Trans. Electron Devices* **1978**, 25, 6, 573-579.
- [57] S. M. Sze, Kwok K.Ng, "Physics of Semiconductor Devices, 3rd Edition," John Wiley & Sons, Inc, 2007.
- [58] Khairurrijal, W. Mizubayashi, S. Miyazaki, M. Hirose, J. Appl. Phys. 2000, 87, 3000.
- [59] K. Y. Cheong, J. H. Moon, H. J. Kim, W. Bahng, N. K. Kim, J. Appl. Phys. 2008, 103, 084113.

- [60] C. Ranuarez, M. J. Deen, C. H. Chen, *Microelectron. Reliab.* **2006**, 46, 1939.
- [61] A. Paskaleva, A. J. Bauer, M. Lemberger, S. Zucher, J. Appl. Phys. 2004, 95, 5583.
- [62] Zengtao Liu, Chungho Lee, Venkat Narayanan, Gen Pei, Edwin Chihchuan Kan, *IEEE Electron Device Letters* **2002**, 49, 1606-1613.
- [63] Paolo Pavan, Roberto Bez, Piero Olivo, Enrico Zanoni, *Proceedings of IEEE* **1997**, 85, 1248-1271.
- [64] E. Rutherford. "The Scattering of α and β Particles by Matter and the Structure of the Atom". Philosophical Magazine. Series **1911**, 6. 21, 669–688.
- [65] J.D. Cockcroft, E.T.S. Walton. *Nature* **1932**, 129, 242-649.
- [66] Anand P. Pathak, *Phy. Rev. B* **1976**, 13, 460-463.
- [67] Anand P. Pathak, *Radiation Effects & Defects in Solids* **1979**, 43, 55-59.
- [68] J. F. Ziegler, "SRIM-2003". Nucl. Instr. Meth. B 2004, 1027, 219-220.
- [69] Z. Ye, R. Liu, J. L. Taggart, H. J. Barnaby, S. Yu, *IEEE Trans. Nucl. Sci.* **2019**, 66, 1, 97–103.
- [70] S. Mohapatra, Y. K. Mishra, Jay Ghatak, D. K. Avasthi, Adv. Mat. Lett. 2013, 4, 444.
- [71] Y. K. Mishra, Fouran Singh, D. K. Avasthi, *Appl. Phys. Lett.* **2007**, 91, 063103.
- [72] Fouran Singh, P. K. Kulriya, J. C. Pivin, *Solid State Communications* **2010**, 150, 1751–1754.
- [73] T. Cesca, P. Calvelli, G. Battaglin, P. Mazzoldi, G. Mattei, *Opt. Express* 2012, 20, 4537-4547.
- [74] A. P. Gnana Prakash, S. C. Ke, K. Siddappa, Semicond. Sci. Technol. 2003, 18, 1037.
- [75] L. C. Feldman, J. W. Mayer "Fundamentals of surface and thin film analysis" Elsevier Science Publisher.
- [76] Utpal S. Joshi, Radiation Effects and Defects in Solids 2011, 166:8-9, 724-733.

- [77] P. Dash, P. Mallick, H. Rath, A. Tripathi, Jai Prakash, D.K. Avasthi, S. Mazumder, S. Varma, P.V. Satyam, N.C. Mishra, *Applied Surface Science* **2009**, 256, 558–561.
- [78] K. R. Mavania, D. S. Ranaa, S. Rayaprola, R. N. Parmar, D. G. Kuberkar, Ravi Kumar, M. Tonouchi, J. John, R. Nagarajan, *Solid State Communications* **2007**, 142, 462–465.
- [79] S. Chandramohan, R. Sathyamoorthy, P. Sudhagar, D. Kanjilal, D. Kabiraj, K. Asokan, *Nuclear Instruments and Methods in Physics Research B* **2007**, 254, 236–242.
- [80] Y. K. Mishra, A. Kumar, D. K. Avasthi, J. Polym. Mater. 2008, 25, 303.
- [81] D. K. Avasthi, Y. K. Mishra, F. Singh, J. P. Stoquert, *Nucl. Instr. and Meth. in Phys. Res. B* **2010**, 268 (19), 3027.
- [82] D. K. Avasthi, Def. Sci. J. 2009, 59, 401-412.
- [83] J. Zhang, M. Lang, R. C. Ewing, R. Devanathan, W. J. Weber, M. Toulemonde, *J. Mater. Res.* **2010**, 25, 1344-51.
- [84] M. Toulemonde, W. J. Weber, G. Li, V. Shutthanandan, P. Kluth, T. Yang, Y. Wang, Y. Zhang, *Phys. Rev. B* **2011**, 83, 054106.
- [85] R. Hellborg, H. Whitlow, Y. Zhang, "Ion beams in nanoscience and technology". Berlin Heidelberg: Springer-Verlag. **2009**, 369-87.
- [86] R, Neumann, Nucl. Instrum. Methods Phys. Res. B 2013, 3, 14, 4-10.
- [87] K. Xiong, J. Robertson, M. Gibson, S. J. Clark, *Appl. Phys. Lett.* **2005**, 87, 183505.
- [88] J. Kim, K. Yong, J. Electrochem. Soc. **2005**, 152(4), F45.
- [89] A. Benyagoub, Eur. Phys. J. B **34**, 395–398 (2003).
- [90] M. Toulemonde, C. Dufour, A. Meftah, E. Paumier, *Nucl. Instr. Meth. B Beam. Interact. Atoms.* **2000**, 166–167, 903–912.
- [91] G. Szenes, Nucl. Instr. Meth. B Beam. Interact. Atoms. **1996**, 2, 1–4.
- [92] M. Toulemonde, J.M. Costantini, C. Dufour, A. Meftah, E. Paumier, F. Studer, *Nucl. Instr. Meth. B Beam. Interact. Atoms.* **1996**, 116, 37–42.
- [93] A. Benyagoub, *Phys. Rev. B* **2005**, 72, 094114.

- [94] N. Itoh, D.M. Duffy, S. Khakshouri, and M. Stoneham, J. Phys. Condens. Matter. 2009, 21, 474205.
- [95] P. Balasaritha, S. Amirthapandian, P. Magudapathy, R.M. Sarguna, S. K. Srivastava, B. K. Panigrahi, *Journal of Nuclear Materials* **2018**, 508, 385-394.
- [96] Aleksi A. Leino, Flyura Djurabekova, Kai Nordlund, Eur. Phys. J. B 2014, 87, 242.
- [97] A. V. Krasheninnikov, K. Nordlund, *J. Appl. Phys.* **2010**, 107, 071301.
- [98] S. M. Sze, "Physics of semiconductor devices", New York: Wiley 1981.
- [99] D. Kahng, S. M. Sze, Bell Syst. Tech. J. 1967, 46, 1288-1295.
- [100] Jaswant S. Rathore, RajveerFandan, Shalini Srivastava, Krista R. Khiangte, Sudipta Das, Udayan Ganguly, Apurba Laha, Suddhasatta Mahapatra, ACS Appl. Electron. Mater. 2019, 1, 1852-1858.
- [101] G. Chakraborty, A. Sengupta, F. G. Requejo, C. K. Sarkar, J. Appl. Phys. 2011, 109, 064504.
- [102] Terry Tai-Jui Wang, Chang-Lung Chu, Ing-Jar Hsieh, Wen-Shou Tseng, Appl. Phys. Lett. 2010, 97, 143507.
- [103] Ch. Sargentis, K. Giannakopoulos, A. Travlos, D. Tsamakis, *Physica E* **2007**, 38, 85-88.
- [104] S. A. Ng, K. A. Razak, K. Y. Cheong, K. C. Aw, *Thin Solid Films* **2016**, 615, 84-90.
- [105] C. W. Tseng, D. C. Huang, Y. T. Tao, ACS Appl. Mater. Interfaces 2013, 5, 9528-9536.
- [106] S. Horikoshi, N. Matsumoto, Y. Omata, T. Kato, J. Appl. Phys. **2014**, 115, 193506.
- [107] M. Mederos, S. N. M. Mestanza, R. Lang, I. Doi, J. A. Diniz, *Thin Solid Films* **2016**, 611, 39-45.
- [108] Ch. Sargentis, K. Giannakopoulos, A. Travlos, D. Tsamakis, *Superlattices and Microstructures* **2008**, 44, 483-488.
- [109] Y. K. Mishra, S. Mohapatra, D. Kabiraj, B. Mohanta, N. P. Lalla, J. C. Pivin, D. K. Avasthi, *Scripta Materialia* **2007**, 56, 629-632.
- [110] S. Zhu, T. P. Chen, Y. C. Liu, S. F. Yu, Y. Liu, Electrochemical and Solid-State Letters

- **2010**, 13(12), K96-K99.
- [111] Y. K. Mishra, D. K. Avasthi, P. K. Kulriya, F. Singh, D. Kabiraj, A. Tripathi, J. C. Pivin, I. S. Bayer, A. Biswas, *Appl. Phys. Lett.* **2007**, 90, 073110.
- [112] Raju Kumar Gupta, Damar Yoga Kusuma, P.S. Lee, M.P. Srinivasan, *ACS Appl. Mater. Interfaces* **2011**, 3, 4619-4625.
- [113] V. Mikhelashvili, B. Meyler, S. Yoffis, J. Salzman, M. Garbrecht, T. Cohen-Hyams, W. D. Kaplan, G. Eisenstein, *Appl. Phys. Lett.* **2009**, 95, 023104.
- [114] Xuan Feng, Shurong Dong, Hei Wong, Danqun Yu, K. L. Pey, K. Shubhakar, W. S. Lau, *Microelectronics Reliability* **2016**, 61, 78-81.
- [115] M. Dhanunjaya, S. A. Khan, A. P. Pathak, D. K. Avasthi, S. V. S. Nageswara Rao, J. Phys. D: Appl. Phys. 2017, 50, 505301.
- [116] N. Manikanthababu, S. Vajandar, N. Arun, A. P. Pathak, K. Asokan, T. Osipowicz, T. Basu, S. V. S. Nageswara Rao, Appl. Phys. Lett. 2018, 112, 131601.
- [117] Arun Vinod, Mahendra Singh Rathore, Srinivasa Rao Nelamarri, *Superlattices and Microstructures* **2018**, 120, 616-628.
- [118] Ayman M. Mostafa, Journal of Molecular Structure 2021, 1226, 129407.
- [119] Aswin Asaithambi, Roland Kozubek, M. Günther, Prinz, Francesco Reale, Erik Pollmann, Marcel Ney, Cecilia Mattevi, Marika Schleberger, Axel Lorke, *Phys. Status Solidi RRL* 2021, 15, 2000466.
- [120] E. Majkova, S. Luby, M. Jergel, Y. Chushkin, E. D'Anna, A. Luches, M. Martino, P. Mengucci, G. Majni, Y. Kuwasawa, S. Okayasu, *Applied Surface Science* 2003, 208-209, 394-398.
- [121] P. Darmawan, P. S. Lee, Y. Setiawan, J. Ma, T. Osipowicz, *Appl. Phys. Lett.* **2007**, 91, 092903.
- [122] M. Jergel, A. Anopchenko, E. Majkova, M. Spasova, S. Luby, V. Holy, M. Brunel, A. Luches, M. Martino, *Thin Solid Films* **2000**, 373, 216-221.

- [123] D. R Rittman, C. L.Tracy, A. B.Cusick, M. J.Abere, B. Torralva, R. C. Ewing, S. M. Yalisove, *Appl. Phys. Lett.* 2015, 106, 171914-171918.
- [124] B. Schuster, F. Fujara, B. Merk, R. Neumann, T. Seidl, C. Trautmann, Nucl. *Instruments Methods B* **2012**, 277, 45 52.
- [125] A. Miotello, M. Bonelli, G. De Marchi, G. Mattei, P. Mazzoldi, C. Sada, F. Gonella, *Appl. Phys. Lett.* **2001**, 79, 2456.
- [126] Nikolaos Kalfagiannis, AnastasiosSiozios, Dimitris V. Bellas, Dimosthenis Toliopoulos, Leon Bowen, Nikolaos Pliatsikas, Wayne M. Cranton, Constantinos Kosmidis, Demosthenes C. Koutsogeorgis, Elefterios Lidorikis, Panos Patsalas, *Nanoscale* 2016, 8, 8236-8244.
- [127] L. Kastanis, J. L. Spear, Ch. Sargentis, N. Konofaos, D. Tsamakis, D. C. Koutsogeorgis, E. K. Evangelou, *Solid State Electronics* 2018, 148, 63-69.

# **Experimental Details and Characterization Techniques**

This chapter provides the details of the experimental methods, available facilities, fabrication and characterization techniques that are used to complete the investigations of the current thesis work. Complete experimental details used in various experiments are specified in the relevant chapters.

#### 2.1. Introduction

In this chapter, various Physical Vapor Deposition (PVD) techniques used for deposition of HfO<sub>2</sub> thin films, HfO<sub>2</sub>/GaO<sub>x</sub>, Au/HfO<sub>2</sub> bilayer films and Au metal contacts, post deposition thermal annealing, gamma irradiation, SHI irradiation and laser annealing details and experimental facilities that are mainly used in thesis work, have been discussed briefly. To fabricate thin films, PVD methods such as RF/DC magnetron sputtering, electron-beam evaporation and thermal evaporation were utilized. The working principles of the various characterization techniques are pre-requisites to understand and analyze the data obtained from various characterization techniques. The pre-plan and required irradiation experimental details play an important role in the work. The samples were characterized by Surface Profilometer for estimating film thickness, FESEM for surface morphology, GIXRD for crystal structure, XRR for estimating surface roughness, PL for defect studies and RBS for estimating thickness and elemental composition of the films. Electrical characteristics such as I-V and C-V of MOS structures have been performed by semiconductor device analyzer.

To fabricate thin films, PVD is the most routine and popular method which has many advantages like as good control of the growth parameters and uniformity etc. In PVD method, the solid target material is sputtered/evaporated into the gaseous form by applying external power, and then gets deposited as a film on the substrates in the form of solid. In this process, solid material transforms to atomic species under applied external power. The atomic species with minimal kinetic energy (3 – 15 eV) travel through a distance (source to substrate) and get deposited on the substrate by nucleation process. As the time passes, the nucleation process builds up and leads to the formation of a continuous film of desired thickness. The thickness of the film can be increased by increasing deposition time. The deposition conditions at the time of PVD process like distance between target and substrate, deposition pressure, substrate temperature at the time of deposition, inert gas flow rate, external applied power and target/source material density etc. play an important role in these PVD systems. The Current thesis-work employed the well-known PVD methods such as RF sputtering, e-beam and thermal evaporation to deposit HfO<sub>2</sub> thin films, HfO<sub>2</sub>/GaO<sub>x</sub>, Au/HfO<sub>2</sub> bilayer films and Au metal contacts.

## 2.2. Physical Vapor Deposition systems

#### 2.2.1. RF/DC magnetron sputtering technique

RF Sputtering is one of the most popular PVD process to deposit high quality thin films [1]. The sputtering of target atoms occurs at a high vacuum (~ 10<sup>-6</sup> mbar). Basically, in this process the inert gas (Ar) atoms are converted in to positive ions and electrons by acquiring energy from the applied external power. The ionized Ar ions bombard the target surface and knock out the atoms/molecules of the target material. These ejected atoms/molecules then get deposited as thin film on the substrate by nucleation process. Using this sputtering process, we can deposit a wide range of materials like metals, insulators and plastics (polymers) by choosing the power supply like DC or AC. Usually, DC sputtering is employed to deposit metals and RF sputtering is employed to deposit both metals and insulators. Among all the deposition processes, sputtering is one of the most effective process to fabricate thin films of various materials. The disadvantage of both RF and DC sputtering are the low ionization rate (~ 0.1 %) which results the poor deposition rates. Another disadvantage of conventional sputtering is that it requires high inert gas pressure to develop the plasma, which lowers the film quality.

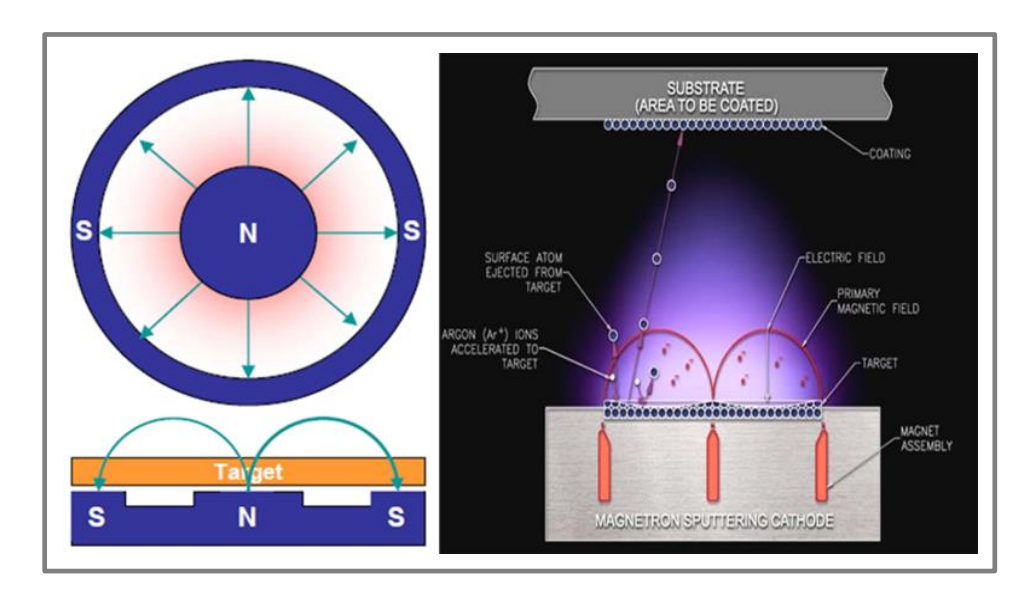


Fig 2.1: The schematic demonstration of RF sputtering [2].

The schematic image of RF sputtering procedure is shown in Fig. 2.1 [2]. The high strength magnets fixed under the target material confine the energetic electrons in a spiral path. The confined electrons lead to increase in the ionization rate ( $\sim 0.1$ -1 %) which increases the deposition

rate even at lower inert gas (Ar) pressures. After ionization, the positively charged Ar ions attain energy in the range of 0.5-1 keV.

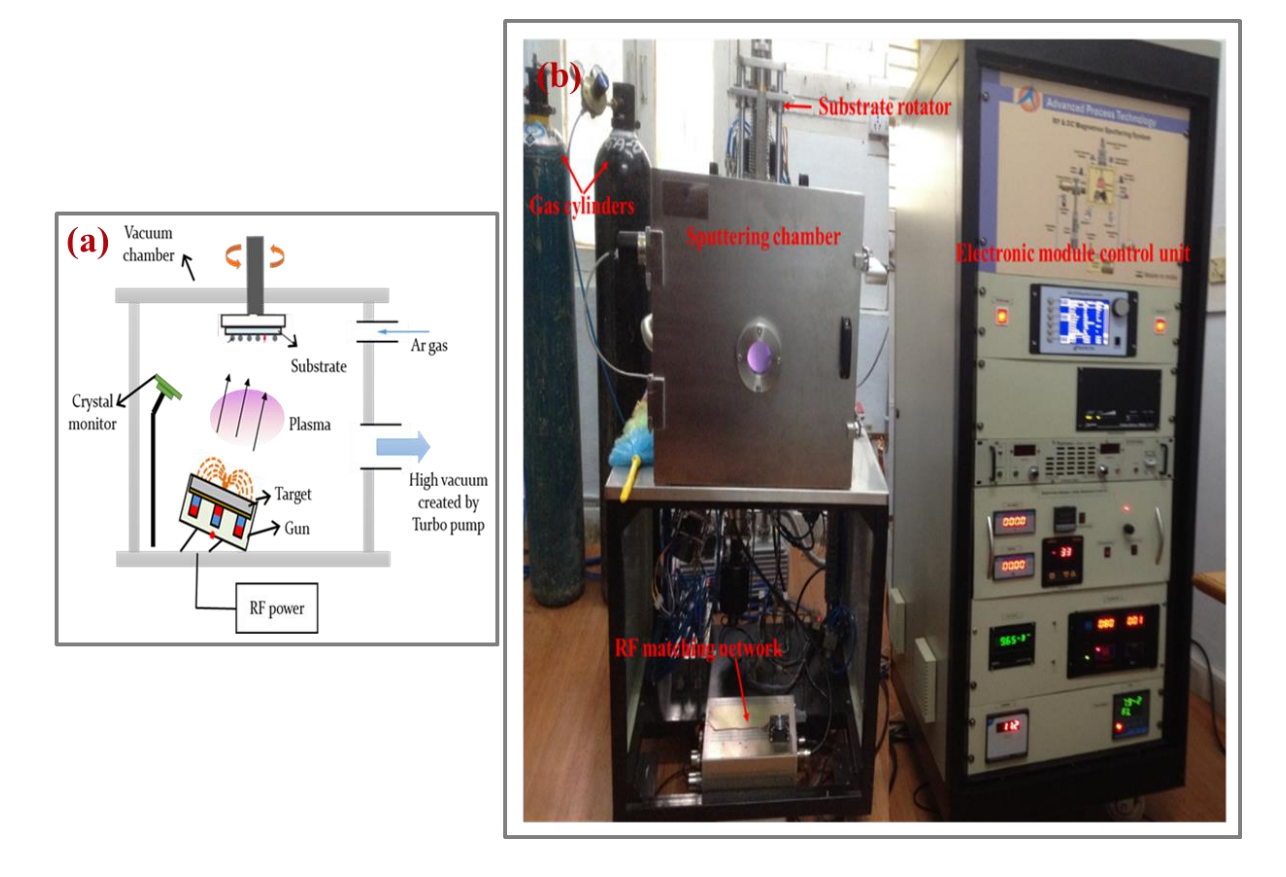


Fig. 2.2: (a) Schematic of RF/DC magnetron sputtering [2] and (b) picture of semi-automatic RF/DC magnetron sputtering system.

The schematic and picture of the semi-automatic RF/DC magnetron sputtering system available at SoP, UoH are shown in Fig. 2.2. As mentioned above, the deposition conditions at the time of PVD process like distance between target and substrate, deposition (Ar) pressure, substrate temperature at the time of deposition, inert gas (Ar) flow rate, and external applied RF power determine and control the deposited thin film properties. Generally in DC sputtering, current is varied from 0.5 Amp to 2 Amp whereas voltage is varied from 0.5 kV to 2 kV. In RF magnetron sputtering, the power is used in the range of 30 W to 250 W depending on the size of the target/source material. Inert gas (Ar) pressure is varied from 5 mtorr to 50 mtorr. Depending on the required thin films both the Ar and O gases can be introduced into the deposition chamber to achieve stoichiometry of the film. The advantages of the RF/DC magnetron sputtering method are: high deposition rate at low deposition pressure, good film quality with enhanced reproducibility

and good control over the deposition while the disadvantage is that it requires a target material with lager diameter (~ 2-inch) and more thickness(~3 mm). For the present thesis work, the RF magnetron sputtering system was initially optimized (w. r. t. deposition parameters) to synthesize high quality reproducible HfO<sub>2</sub> thin films. Using the optimized deposition parameters, HfO<sub>2</sub> thin films of various thickness and HfO<sub>2</sub>/GaO<sub>x</sub> bi-layer thin films were fabricated. These samples were exposed to thermal annealing, gamma irradiation, SHI irradiation and laser annealing to study their effects on the structural changes and subsequent effects on the electrical properties of the films.

#### 2.2.2. e-beam evaporation and thermal evaporation techniques

Electron beam technique as well as thermal evaporation technique are two well-known PVD methods used to deposit thin films of various materials [3]. In both methods the target material is evaporated by applying external energy and the evaporated material travels from the source to substrate and gets deposited as a film. In e-beam evaporation, beam of intensive electrons is focused towards the target material by a strong magnetic field. The melting and evaporation of target material occurs when a huge amount of energy (around several million watts/square inch) is transferred to the target in a high vacuum ( $10^{-5}$  to  $10^{-6}$  mbar). This method is appropriate to deposit materials with high melting point.

Thermal evaporation is one of the most used technique to deposit metal electrodes of various materials like Al, Ag and Au etc. for developing electronics devices [3]. It is one of the modest techniques of all the deposition methods. In thermal evaporation, the target material is placed in a boat of high melting point material (like Molybdenum or Tungsten) and the external applied high voltage/current brings the target material to melting point and then the target material gets evaporated from the source. This method offers high deposition rate and high quality uniform films with the minimal optimized conditions [4]. The schematic diagrams of the e-beam and thermal evaporation are shown in Fig 2.3 [5] and picture of the e-beam and thermal evaporation system available at SoP, UoH are shown in Fig. 2.4.

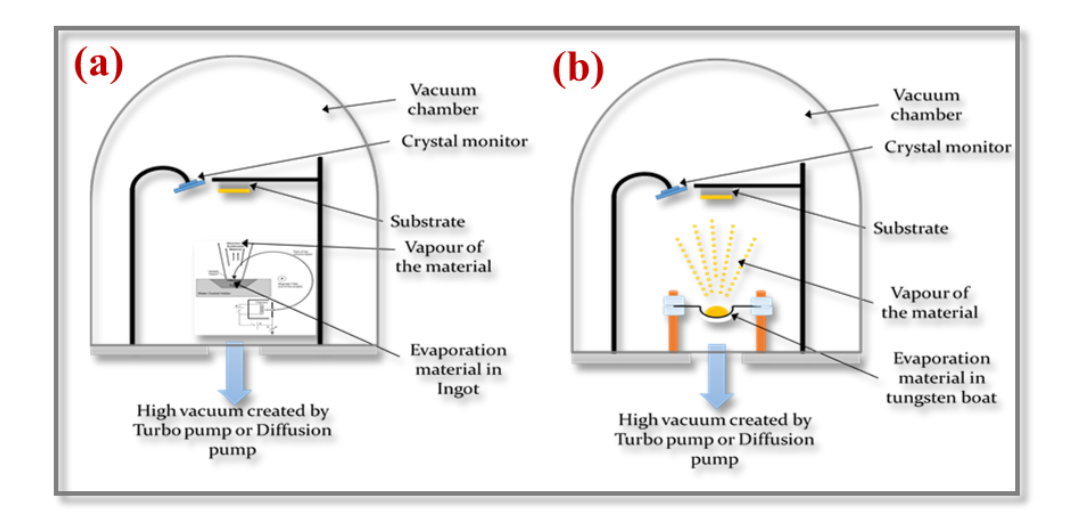


Fig. 2.3: Schematics diagrams of (a) e-beam and (b) thermal evaporation processes [5, 6].



Fig. 2.4: The picture of e-beam/thermal evaporation system at SoP, UoH.

In the present thesis work, e-beam as well as thermal evaporation methods are used to synthesize HfO<sub>2</sub> and Au multilayer thin films on Si substrates as well as Quartz substrates without breaking the vacuum of the deposition chamber. The e-beam evaporation is used to grow HfO<sub>2</sub> thin films,

whereas Au thin films are grown using thermal evaporation. These samples are subjected to laser annealing to study the effects on the structural and electrical properties of the films. The deposition parameters used to grow HfO<sub>2</sub> and Au multilayer thin films and experimental specifications are discussed in detail in the corresponding chapters.

## 2.3. Irradiation facilities and Ion beam analysis

In order to elucidate the effects of irradiation on the structural and electrical properties of HfO<sub>2</sub> thin films, gamma irradiation and SHI irradiation have been employed using the facilities available at IUAC, New Delhi. Rutherford backscattering spectroscopy (RBS) measurements (using 2 MeV He<sup>2+</sup> ions at IUAC, New Delhi, India) have been performed on these samples to estimate the thickness and elemental composition of different layers. Diffusion/inter-mixing of layers at the interfaces has also been studied using RBS spectra.

#### 2.3.1. Gamma irradiation

A gamma chamber GC 1200 of 1.25 MeV Cobalt 60 (Co-60) source manufactured by the Board of Radiation Isotope Technology has been utilized to perform gamma irradiation experiments. The decay mechanism [7] and a picture of gamma chamber are shown in Fig. 2.5(a-b). The sample is placed in the movable (up/down) sample holder inside the irradiation chamber.

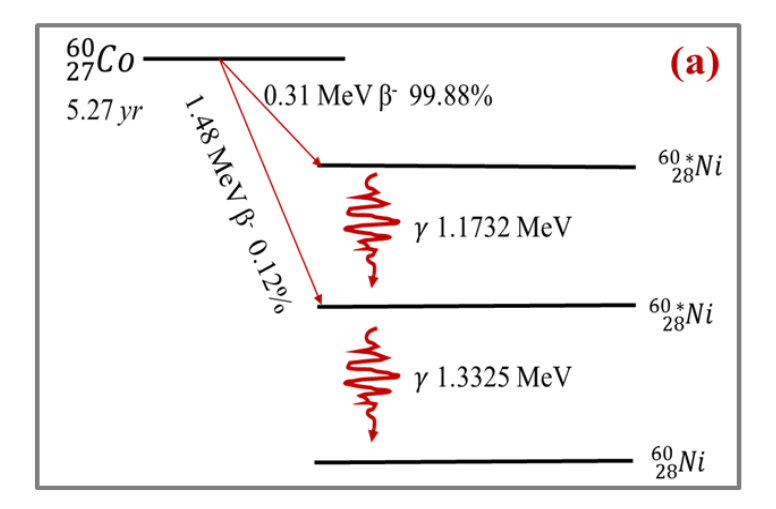




Fig. 2.5: (a) The decay mechanism and (b) picture of gamma chamber at IUAC [7].

#### 2.3.2. Swift Heavy Ion (SHI) Irradiation

SHI irradiation has been performed on the RF sputtered HfO<sub>2</sub> thin films and HfO<sub>2</sub>/GaO<sub>x</sub> bi-layer films using 15 UD Pelletron of tandem Van de Graff accelerator at IUAC New Delhi [8]. The schematic representation of the accelerator manufactured by National Electrostatics Corporation (NEC) is shown in Fig. 2.6. The Pelletron type accelerator can accelerate most ions (keV-MeV) [9]. First of all, the negative ions (SNICS) are pre-accelerated up to 300 keV. The negatively charged ions are then, injected to the main accelerator tank with the assistance of injector magnet. The negatively charged ions are accelerated towards the strong positive electrical field terminal. These negative ions pass through the stripper foil at the middle of the accelerator and get converted in to the positive ions by leaving some of the electrons.

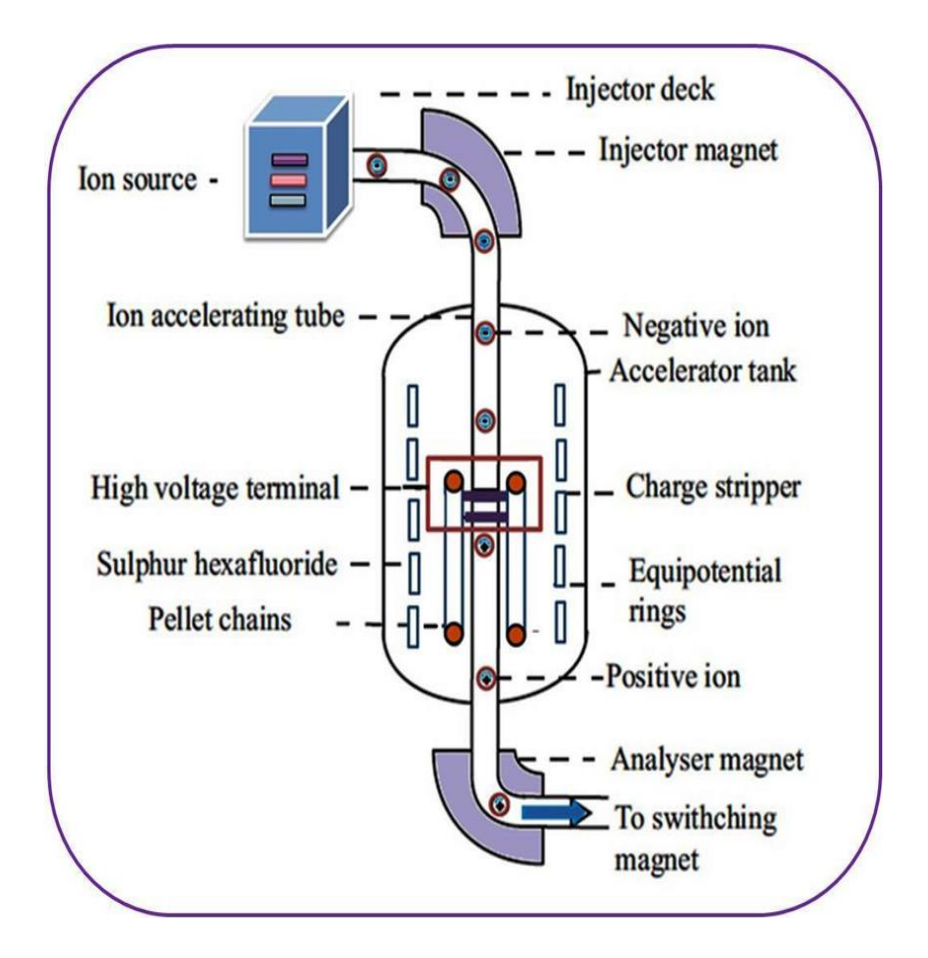


Fig. 2.6: Schematic representation of Pelletron Accelerator at IUAC [8].

Further, the positively charged ions are accelerated from the terminal to the ground potential. Hence, various charge states are produced. Ions procure different energies depending on the charge state given by the following equation 2.1.

$$E_i(MeV) = E_d + (1+q)V_t \cong (1=q)V_t$$
 (2.1)

In this equation,  $E_d$  is the energy of the ion generated from the SNICS source and  $V_t$  is the voltage created at the terminal.

The SHI irradiation fluence depends on the time of irradiation (time that the sample is subjected to high energy ion beam). The time of irradiation required to achieve the fluence is calculated by using the following equation 2.2.

$$Time (sec) = \frac{Flunce (ions/_{cm^2}) X Area (cm^2)}{6.25 X 10^{12} X Beam current (pnA)}$$
(2.2)

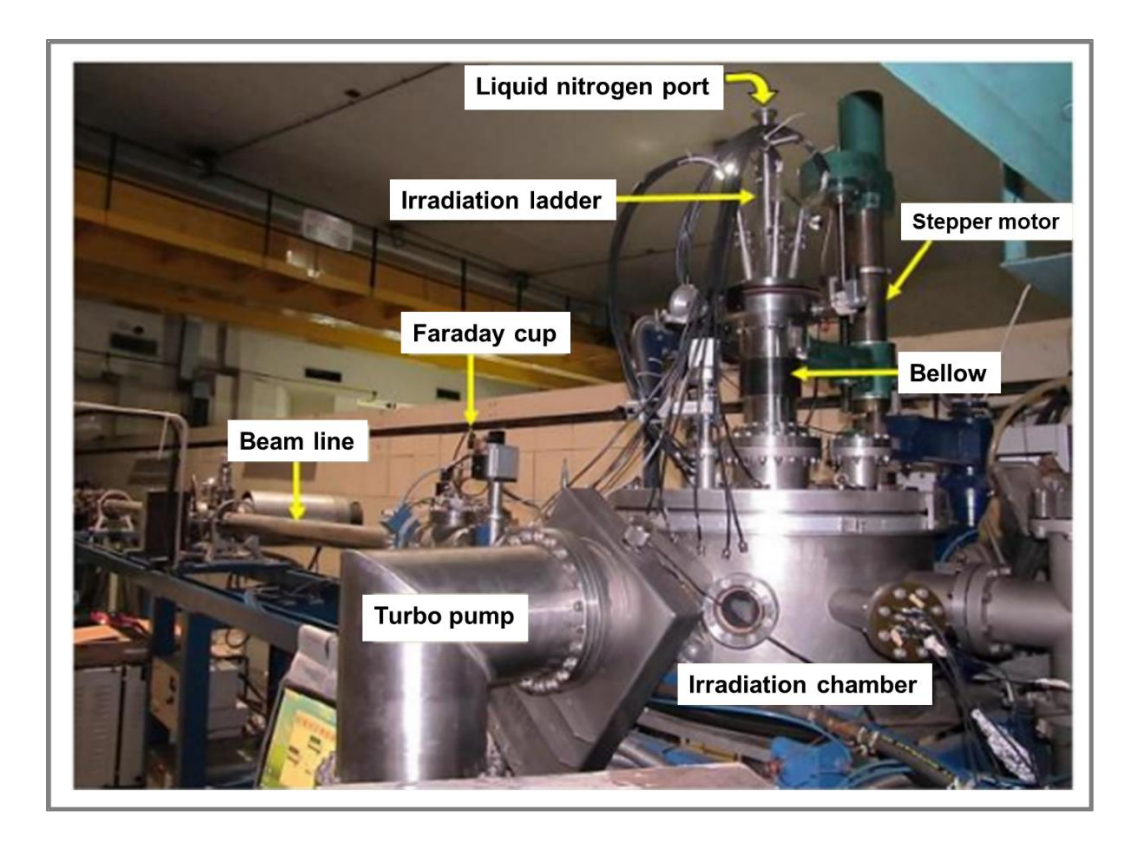


Fig. 2.7: Material science beam line and irradiation chamber at IUAC [9].

In IUAC New Delhi, there are seven beam lines and among these beam lines, materials science beam line is situated at 15° to the switching magnet. The accelerated ion beam can be switched to the desired beam line according to our experimental requirements. The material science irradiation beam line chamber is shown in Fig. 2.7. In the present thesis work, samples of structure HfO<sub>2</sub>/GaAs and HfO<sub>2</sub>/GaO<sub>x</sub>/Si were subjected to SHI irradiation with 120 MeV Ag ions using a Pelletron accelerator (15 UD tandem) at Inter University Accelerator Centre (IUAC), New Delhi, India. To avoid the substrate heating, a constant ion beam current of 0.5 particle nano-Ampere (pnA) was used and scanned over the sample of area 1 x 1 cm<sup>2</sup>. By varying the time of irradiation, the ion fluence ranging from 1 x 10<sup>12</sup> ions/cm<sup>2</sup> to 1 x 10<sup>14</sup> ions/cm<sup>2</sup> was achieved.

#### 2.3.3. Rutherford Backscattering Spectroscopy

Rutherford in 1911 used the backscattering spectroscopy in his revolutionary gold foil experiment to determine the structure of atoms [10]. However, Rubin et al. [11] brought this method to modern material analysis applications. In recent years, RBS turned out to be one of the best and common techniques in material science. RBS measurements are widely used to analyze the composition of

the material, thickness of the films and inter diffusion of layers of thin films. A target is bombarded by a light element (projectile) with MeV energy, which is backscattered at certain angle with a certain energy.

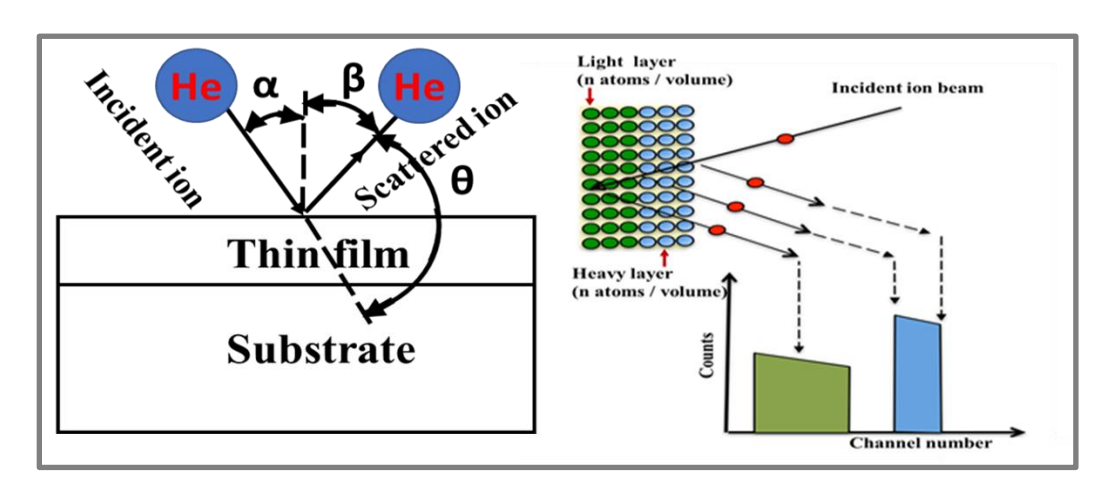


Fig. 2.8: Schematic illustrations of the RBS [12].

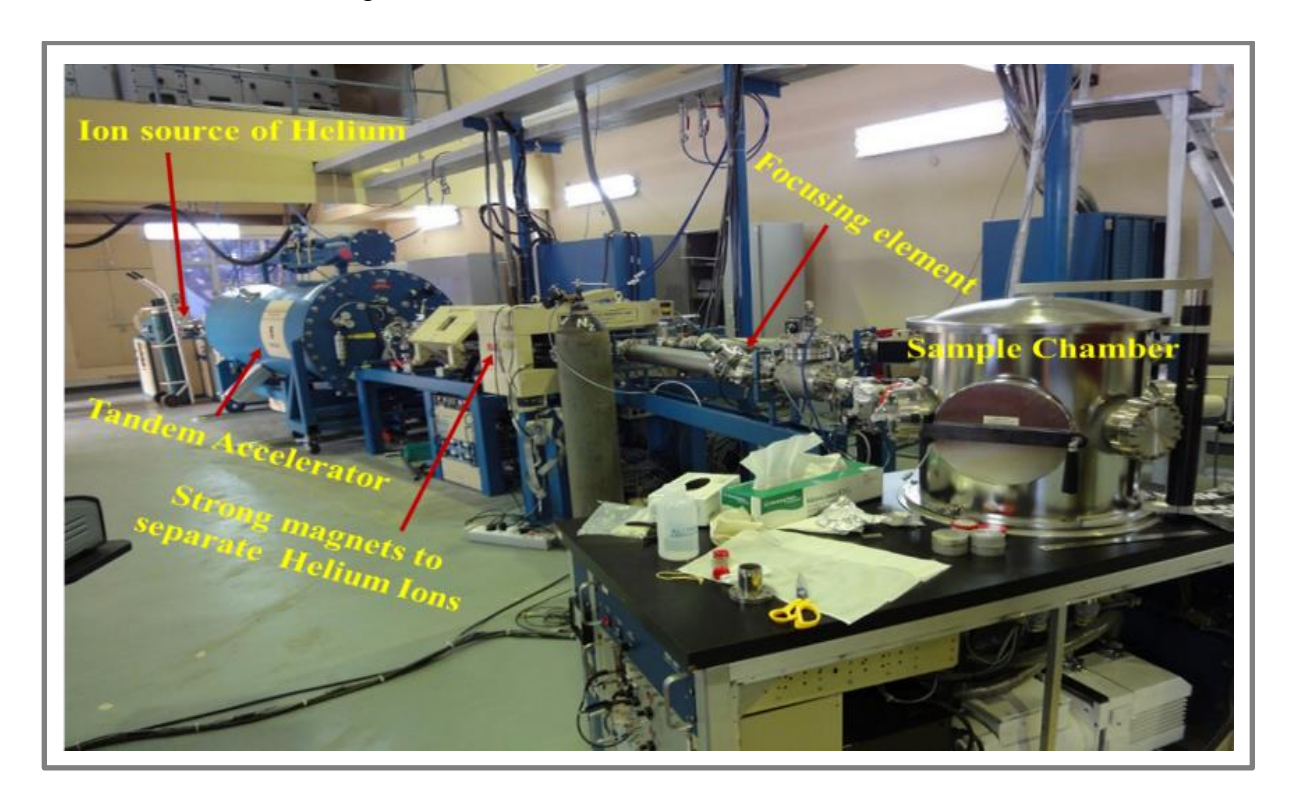


Fig. 2.9: The RBS facility at IUAC [12].

The working principle of RBS is established on elastic collisions among the projectile and target atoms. Based on this principle, by measuring the backscattered momentum and energy, one can

obtain the information about the target elements. The main advantage of the RBS is that it is very sensitive to the higher mass number elements with good depth resolution of several nm while the drawback of the RBS is low sensitivity for the lighter elements. RBS quantitatively determines the composition of the sample.

In the present thesis work, The RBS facility at IUAC is employed for RBS measurements and the setup is shown in Fig. 2.9. We have used 2 MeV He<sup>2+</sup> ions to evaluate the thickness, elemental composition of the film and SHI induced inter-diffusion/inter-mixing of HfO<sub>2</sub> thin films and HfO<sub>2</sub>/GaO<sub>x</sub> bi-layer films.

## 2.4. Characterization Techniques

There are many characterization techniques that are used to study the structural changes, optical properties as well as electrical properties of films. The detailed description of the characterization techniques that are used in this thesis are provided in the following sections.

#### **2.4.1. Profilometer (film thickness study)**

Profilometer is one of the simple device which is used to perceive the surface roughness and to estimate the thickness. The Profilometer (AMBIOS XP 200) can measure up to a maximum step height of 800 µm with a maximum resolution of 1 Å and it offers the 3D profiler of the film surfaces. The stylus is used to detect the film surface which moves physically along the film surface to obtain the height (thickness of the film). A schematic diagram, a picture of the Profilometer setup at CFN, UoH are shown in Fig. 2.10.

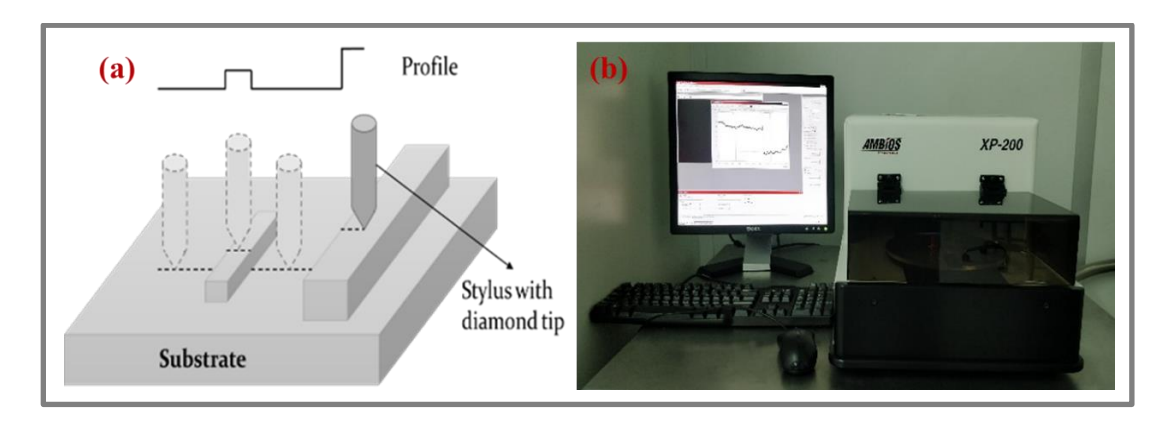


Fig. 2.10: (a) Schematic diagram and (b) picture of the Profilometer setup at CFN, UoH.

# 2.4.2. Field Emission Scanning Electron Microscopy (FESEM) technique and Energy Dispersive X-ray Spectroscopy (EDX) technique

The FESEM technique was invented by Erwin Wilhelm Muller in 1936 [13]. It is one of the multipurpose techniques which is extensively employed to study the surface structure, morphology of thin films and chemical composition of the thin films. FESEM is a non-destructive technique. The conventional microscopes are used to magnify feature size up to certain extent (10x to 100x) in real space. In the case of FESEM, energetic electrons are used to scan the surface beyond the detection lines of conventional microscopes and gives the spatial resolution up to 1 nm. A field emission scanning microscope consists of a sharp tip, usually a tungsten having tip area around 100 nm and high melting point. High energy electrons pass through the tip and can get focused at an area of 1-5 nm with the help of condenser electromagnetic lenses. The focused electron beam scans the whole surface bit by bit. Owing to interaction between electron beam and sample surface, the secondary electrons and back scattered electrons are emitted. These electrons are collected by the detector and give the electronic signal of surface morphology. The schematic diagram and picture of the FESEM setup at SoP, UoH are shown in Fig. 2.11 [14-16].

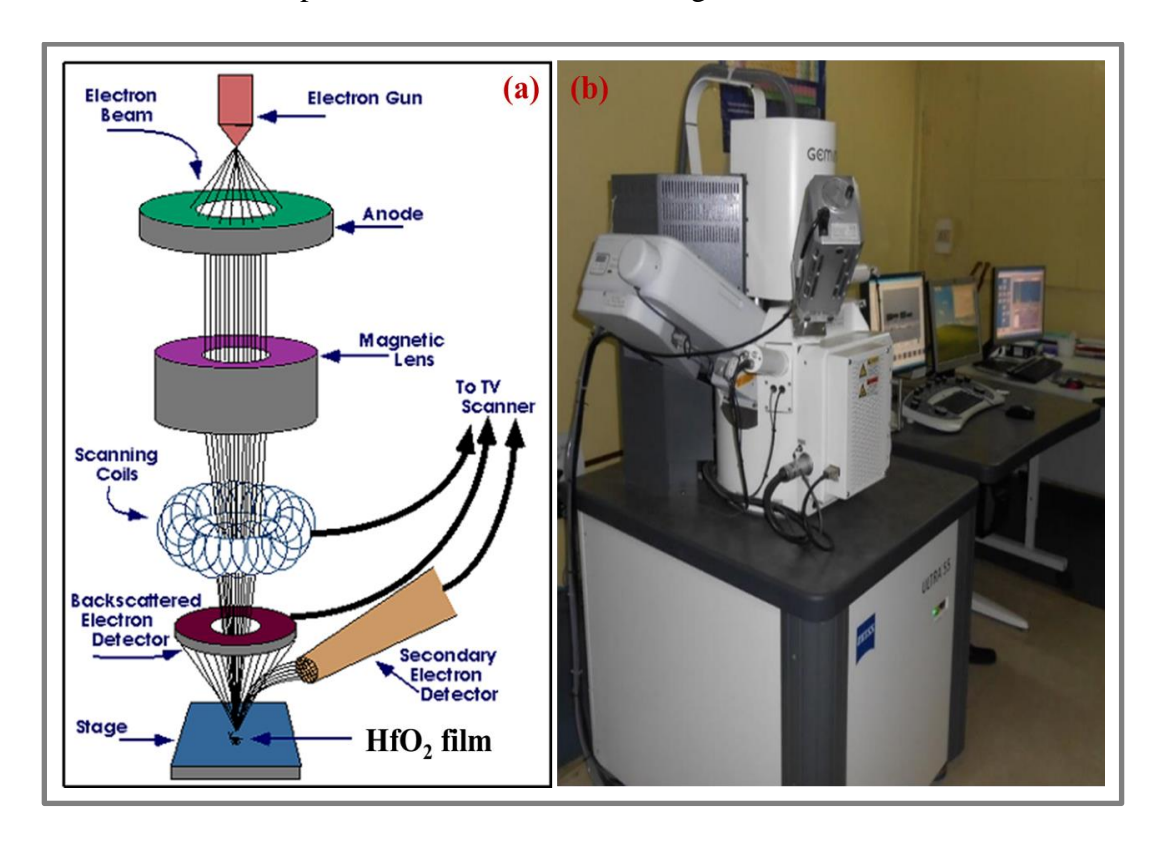


Fig. 2.11: (a) The schematic diagram [14] and (b) The picture of FESEM setup at SoP, UoH.

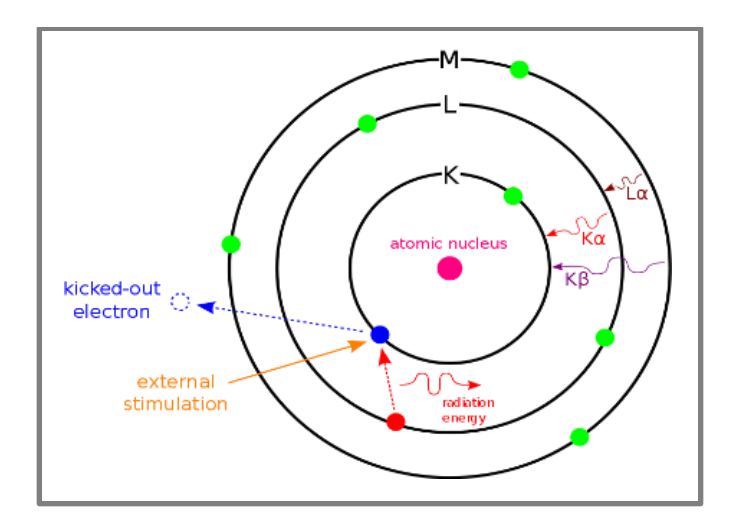


Fig. 2.12: The schematic diagram of the EDX [17].

The EDX technique in combination with FESEM is used to detect elemental composition of the sample. The X-Rays are generated when the energetic electrons interact with the sample along with secondary electrons and back scattered electrons. The electron beam ionizes the inner core shell electrons of each of the elements present in the sample. The inner core shells are filled by the outer electrons via emission of the characteristic X-Rays. These X-Rays are specific to the existing elements. The schematic drawing of EDX is presented in Fig. 2.12 [17].

In the present thesis, FESEM measurements were performed using Carl ZEISS, FEG, ultra-55 at the University of Hyderabad to study the surface morphology, to estimate the grain size of HfO<sub>2</sub> thin films, HfO<sub>2</sub>/GaO<sub>x</sub> bi-layer films, to estimate the uniformity and size distribution of Au NPs formed on the surface of HfO<sub>2</sub>. The elemental composition of the film is determined by EDX technique using an in-built Oxford instruments EDX setup in the FESEM system at SoP, UoH. The obtained spectra is analyzed using INCA software.

#### 2.4.3. X-Ray Diffraction (XRD)

X-ray diffraction is a fundamental and nondestructive method used to characterize the material (thin film or powder form) to identify its phase, crystal structure, strain and crystallite size. X-rays were first discovered by German physicist W. Rontgen in 1895 [18]. After that two English physicists W. L. Bragg and W. H. Bragg in 1913 [19] gave explanation for the appearance of crystallographic structures of various materials when they are subjected to the beam of X-rays at

certain incident angles. This technique works based on the standard Bragg's law of diffraction, given by

$$2d \sin \theta = n\lambda \tag{2.3}$$

The schematic of X-rays incident at an angle  $\theta$  on the material with the atomic spacing of planes d is shown in Fig. 2.13 which reveals the information about lattice spacing, bonding angles and planar directions of the crystal structures [20].

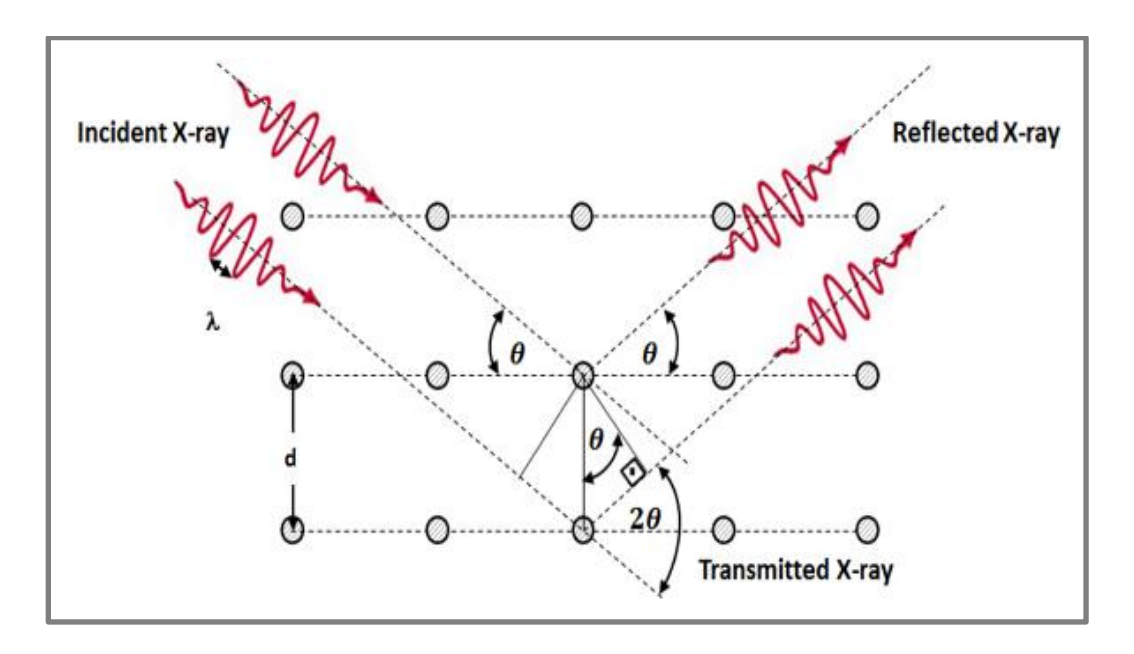


Fig. 2.13: The Schematic diagram of X-Ray Diffraction.

The average crystallite size (D) is predictable from the obtained width of the diffraction peak by using Scherer formula known by the following equation 2.4 [21].

$$D = \frac{0.9\lambda}{\beta \cos \theta} \tag{2.4}$$

Glancing Incident X-Ray Diffraction (GIXRD) is a suitable method to investigate the crystallographic structures of thin films where the incident angle of X-ray is very small to enhance the path length in the thin film. The XRD experimental set up is shown in Fig. 2.14.

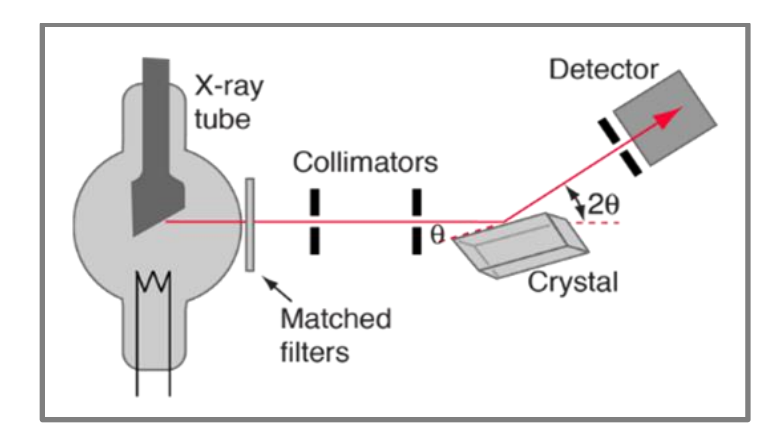


Fig. 2.14: Experimental setup of the XRD [22].



Fig. 2.15: The X-ray diffraction facility at SoP, UoH.

The X-rays are produced in a cathode ray tube by heating a filament made of tungsten (W) to produce electrons. By applying external DC voltage these are accelerated to bombard the target

material [22]. The diffracted rays that are produced from the thin films gives the diffraction patterns. The diffraction peaks were examined by using the PDF-4 software or Joint Committee on Powder Diffraction Standards (JDPDS) [23]. The X-ray diffraction facility at SoP, UoH is shown in Fig. 2.15.

In the present thesis, Grazing incident x-ray diffraction (GIXRD) measurements were performed on HfO<sub>2</sub> films using Bruker D8 Advance diffractometer with Cu K $\alpha$ ,  $\lambda = 1.54$  Å.

#### 2.4.4. Photoluminescence Spectroscopy (PL)

Photoluminescence is a contactless and nondestructive technique which is used to study the defect and electronic states of various materials. The schematic diagram of a standard PL spectroscope is shown in Fig. 2.16 [24] and the picture of a Flourolog-1427C-AU PL spectroscope at SoP, UoH is presented in Fig. 2.17.

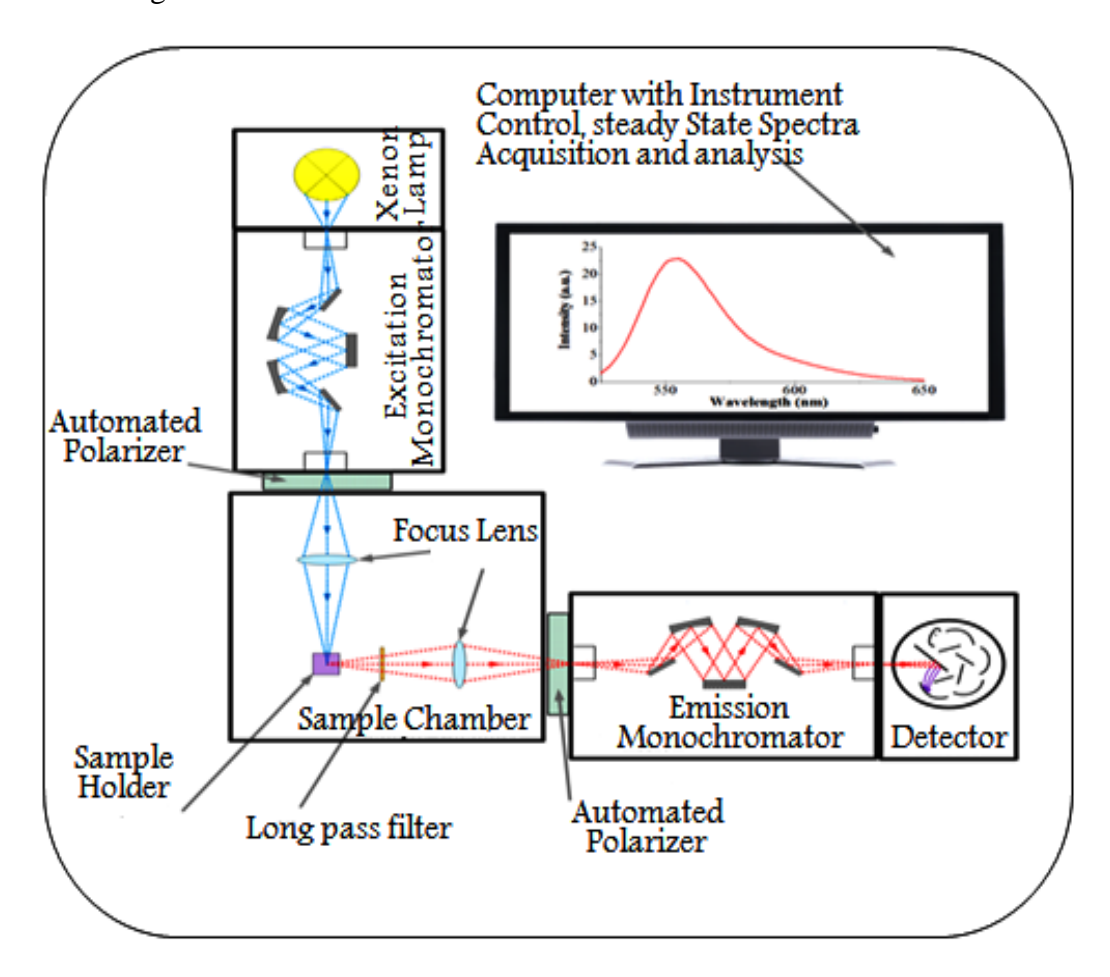


Fig. 2.16: The schematic figure of a standard PL spectroscope [24].

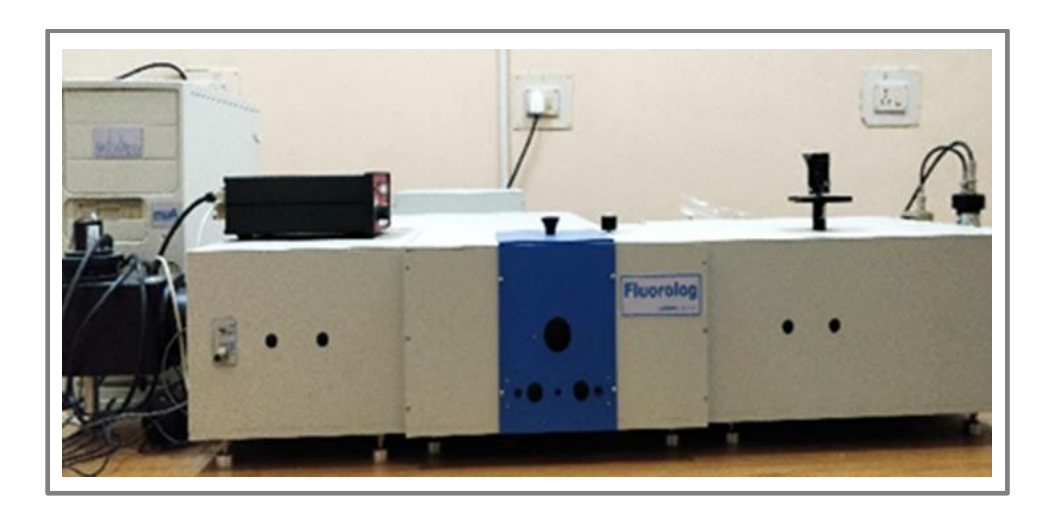


Fig. 2.17: The picture of a PL spectroscope at SoP, UoH.

Flourolog-1427C-AU PL spectroscope at SoP, UoH, a xenon lamp of 450 W used as an excitation source. For counting of the emitted photons, the standard R928P based photo multiplier is used. A monochromatic filter is utilized to select preferred excitation wavelength. The collected photons are passed over the monochromatic filter. The signal is further processed and the output is given in either digital or analog form. In the present thesis, PL measurements were performed using Flourolog-1427C-AU PL spectroscope at SoP, UoH to study the oxygen vacancy related defect dynamics in HfO<sub>2</sub> thin films.

#### 2.4.5. Raman spectroscopy

Raman spectroscopy is a non-destructive technique that can be used to analyze the samples either for quantitative or qualitative information. Raman Effect was fist observed by Prof. C. V. Raman in 1923 [25]. The basic principle of Raman Effect is that when light interacts with a molecule or an atom, most of the light is scattered through elastic scattering process known as Rayleigh scattering. A small portion of light scatters inelastically by excitation process. The inelastically scattered photons have signature of molecule or atom. The first micro-Raman system was introduced by Horiba scientific in 1970. This technique works on the principle of the vibrational agitations within the molecule. Each molecule has a fingerprint region on wave number which indicates the presence of that particular molecule in the material. The schematic diagram of micro Raman spectroscope is shown in Fig. 2.18 [26].

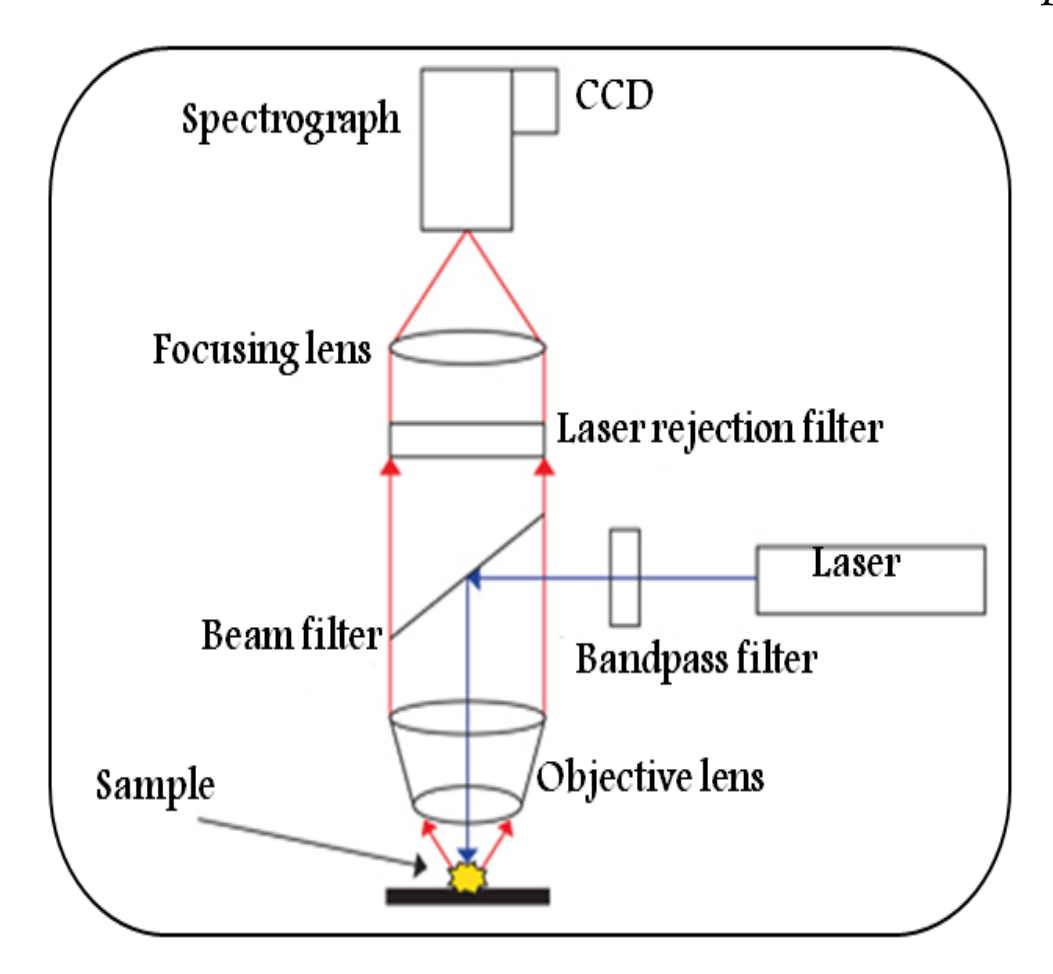


Fig. 2.18. The schematic figure of micro Raman spectroscope [26].



Fig. 2.19: The picture of LabRAM HR Evolution – HORIBA Scientific confocal Raman microscope at UoH.

The Raman signals are detected by the charge couple devices (CCD). To adjust the position of the sample under illumination spot, joystick is used which can move in XY directions. In the present thesis, SERS measurements were performed by drop-casting Rhodamine 6G (R6G) dye on top of as-grown and laser annealed Au/HfO<sub>2</sub> bi-layers. A laser with excitation wavelength of 632 nm and 20 mW power has been used for these measurements using LabRAM HR Evolution – HORIBA Scientific confocal Raman microscope with 100X magnification at UoH as shown in Fig. 2.19.

### 2.4.6. Ultra Violet-Vis-Near Infrared Spectroscopy (UV-Visible-NIR)

UV-Visible-NIR (200 nm to 2600 nm) spectroscopy is one of the elementary characterization procedures which is used to examine the light-matter interaction. The Schematic diagram of UV-Visible-NIR double beam spectrophotometer is presented in Fig. 2.20 [27].

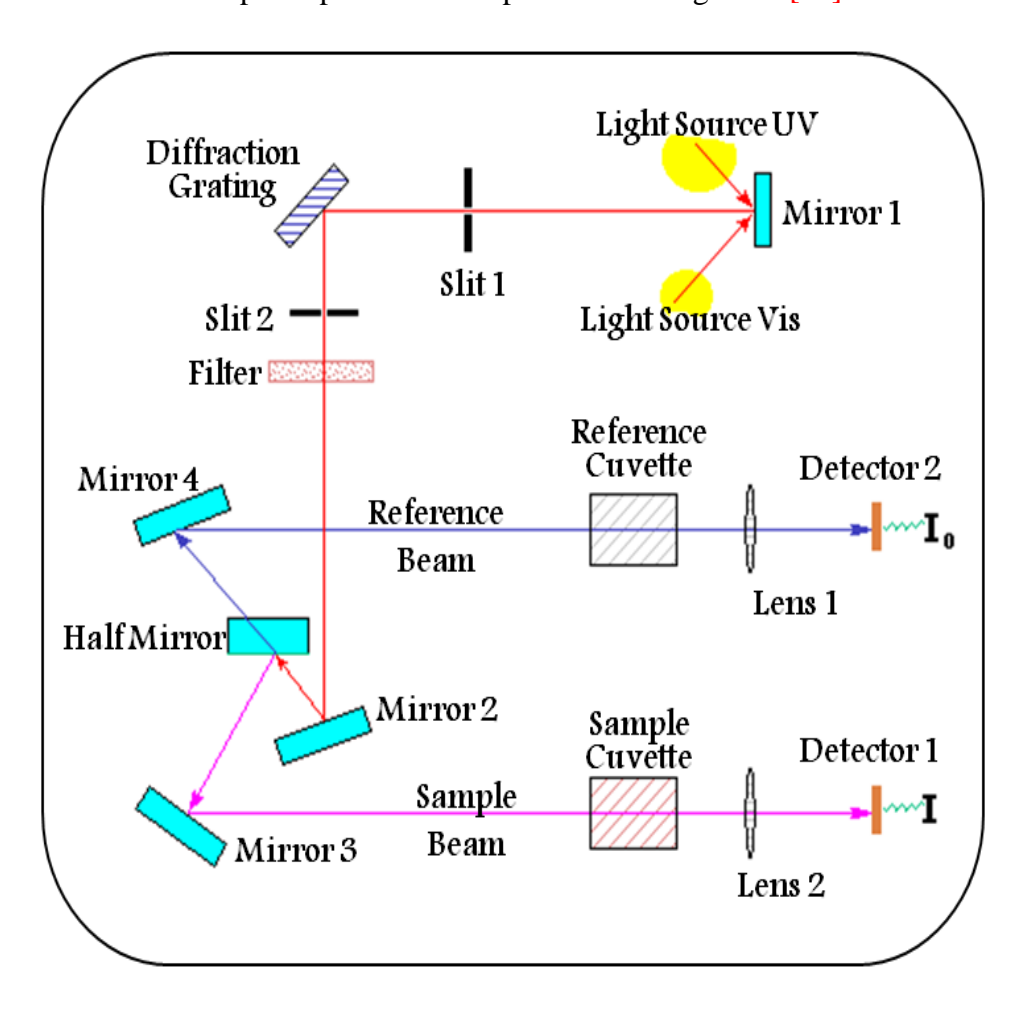


Fig. 2.20: The schematic figure of UV-Vis-NIR double beam spectrophotometer [27].

As shown in the picture, one beam acts as a reference light with light intensity (I) and passes through the reference sample. Another beam passes through the target sample and gives the intensity ( $I_0$ ). The ratio between the intensities of two light beams ( $I/I_0$ ) gives the information about the sample. The absorbance of a sample is defined as logarithm of ratio of two transmitted beams. The reflectance (%R) is defined as the intensity ratio between the two reflected beams from the target sample and the reference sample. The transmittance (%T) is defined as the intensity ratio between the two transmitted beams from the sample and reference.

In the present thesis, UV-visible absorption measurements (in the range of 300 nm – 1000 nm) of Au/HfO<sub>2</sub> bi-layers deposited on quartz substrates as a function of number of laser pulses were performed using a UV-visible spectrometer at CFN, UoH and the picture of JASCO V-570 double beam spectrophotometer is shown in Fig. 2.21. We have used pure quartz (air-medium) sample as the reference.

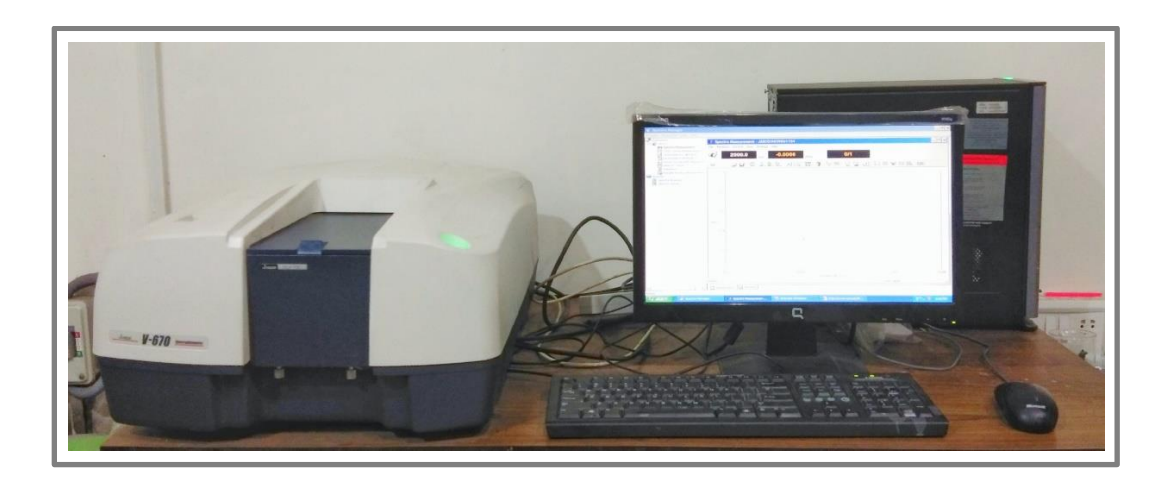


Fig. 2.21: The picture of JASCO V-570 double beam spectrophotometer at CFN, UoH [28].

### 2.4.7. Electrical characterizations

The current conduction mechanisms of the MOS structures have been studied by performing Leakage current – Voltage (I-V) measurements while the High frequency (1 MHz) Capacitance – Voltage (C-V) measurements have been performed to understand the memory performance using an Agilent technologies (B1500A) semiconductor device analyzer with attached Signatone probe station - P1160 at CFN, UoH is shown in Fig. 2.22.

It is a multipurpose Current-Voltage device analyzer which can be used for I-V, C-V and pulse/dynamic I-V etc. measurements. The inclusive determining capabilities of this analyzer

offers the electrical characteristics of the electronic devices with more reliability and high efficiency. The Easy EXPERT - GUI based characterization software associated with this analyzer offers the speed characterization of the devices. The characterization data is instantaneously stored in the corresponding built-in workspace. Agilent technologies B1500A semiconductor device analyzer is equipped with the standard SMU modules which is used for I-V and quasi-Static C-V characteristics. Further high frequency C-V characteristics are performed by MFCMU modules and without using an external switching unit, SCCU modules offers the switching between I-V as well as C-V characteristics.

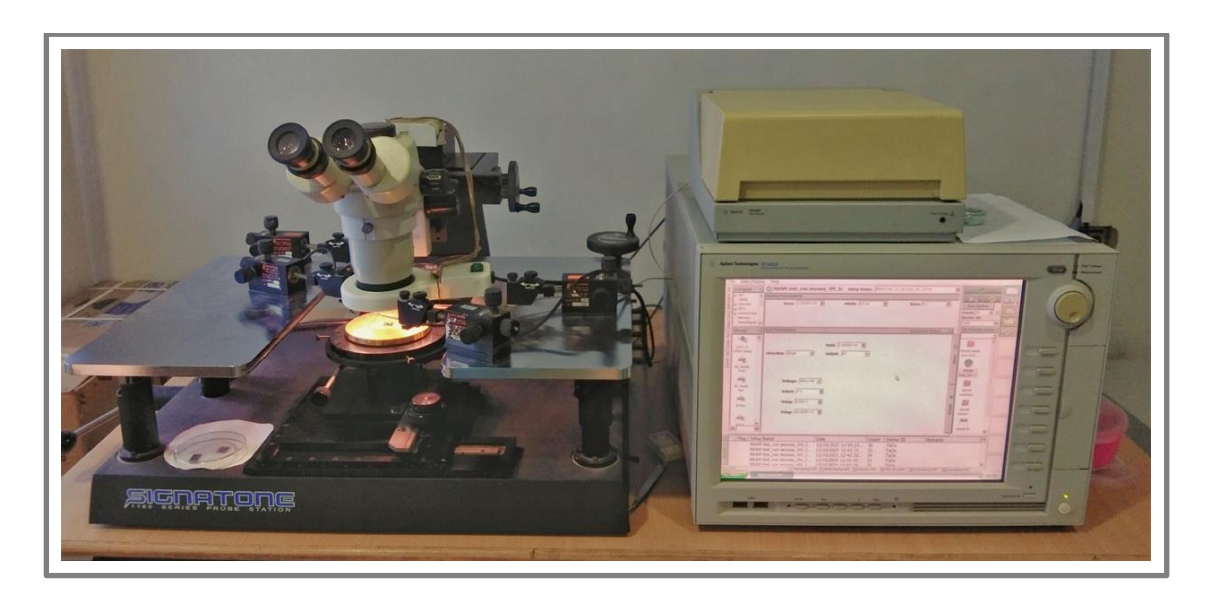


Fig. 2.22: Agilent technologies (B1500A) semiconductor device analyzer with attached Signatone probe station - P1160 at CFN, UoH [29].

In the present thesis, electrical characterizations such as I-V in voltage range from -5 V to 5 V and C-V in voltage range from -5 V to 5 V at 1 MHz frequency have been performed on HfO<sub>2</sub> thin film, HfO<sub>2</sub>/GaO<sub>x</sub> bi-layer and HfO<sub>2</sub>/Au-NPs/HfO<sub>2</sub> based MOS structures by using an Agilent technologies (B1500A) semiconductor device analyzer with attached Signatone probe station - P1160 at CFN, UoH.

### 2.5. Conclusions

The details of the experimental methods, experimental facilities, fabrication and characterization techniques that are used to complete the investigations of the present thesis work are discussed. Complete experimental details used in various experiments are specified in the relevant chapters.

# 2.6. References

- [1] N. Selvakumar, Barshilia, C. Harish, *Solar Energy Materials and Solar Cells* **2012**, 98, 1-23.
- [2] M. Ohring, Materials Science of Thin Films (2nd ed.), Academic Press. 2001, 215.
- [3] J. George, "Preparation of thin films", Marcel Dekker, Inc., New York, 1992, 13–19.
- [4] D. M. Mattox, "Handbook of Physical Vapor Deposition (PVD) Processing", Cambridge University Press, 2014.
- [5] K. S. S. Harsha, "Principles of Physical Vapor Deposition of Thin Films", Elsevier, Great Britain 2006, 400.
- [6] R. D. Mathis Company Evaporation Sources Catalog, by R. D. Mathis Company, 1-12, 1992.
- [7] Gamma source 1200cc, http://www.britatom.gov.in/htmldocs/products06c.html.
- [8] http://www.iuac.res.in/accel/paras.
- [9] http://www.iuac.res.in/accel/pell/index.html.
- [10] E. Rutherford, *Philosophical Magazine Series* 6 **1911**, 21, 669–688.
- [11] S. Rubin, T. O. Passell, E. Bailey, *Analytical Chemistry* **1957**, 29, 736.
- [12] http://www.iuac.res.in/accel/paras/index.html.
- [13] "Intro to Field Emission", Field Emission / Ion Microscopy Laboratory, Purdue University, Dept. of Physics. Archived from the original **2007**.
- [14] https://fas.dsi.a-star.edu.sg/equipments/auger.aspx.
- [15] Rudenberg, Reinhold, "Configuration for the enlarged imaging of objects by electron beams", Patent DE906737, **1931**.
- [16] "A Brief History of the Microscopy Society of America". microscopy.org.
- [17] "https://acronyms.thefreedictionary.com/JCPDS"

- [18] A. W. Grove, "Rontgen's Ghosts: Photography, X-Rays, and the Victorian Imagination". *Literature and Medicine* **1997**, 16 (2), 141–173.
- [19] W. H. Bragg, W. L. Bragg, "The Reflexion of X-rays by Crystals". Proc. R. Soc. Lond. A 1913, 88, 428–38.
- [20] http://prism.mit.edu/xray/oldsite/Bruker.
- [21] P. Scherrer, Göttinger Nachrichten Gesell 1918, 2, 98.
- [22] https://www.nano.pitt.edu/sites/default/files/D8.
- [23] https://acronyms.thefreedictionary.com/JCPDS.
- [24] Stephen M. Cohen, "Modular Spectro fluorometer-the Fluorolog-3".
- [25] Misra, Prabhakar, Dubinskii, Mark, *Ultraviolet Spectroscopy and UV Lasers. New York: Marcel Dekker.* **2002**, ISBN 0-8247-0668-4.
- [26] Banerjee, Somaditya, "C. V. Raman and Colonial Physics: Acoustics and the Quantum". *Physics in Perspective*, **2014**, 16 (2), 146–178.
- [27] O. Stenzel, "The Physics of thin film Optical Spectra: Introduction", Springer, Germany. 1996.
- [28] http://www.jascoinc.com/spectroscopy.
- [29] http://www.keysight.com/en/pd-582565-pn-B1500A/semiconductor-device-analyzer-?cc=IN&lc=eng.

# Effects of Thermal Annealing and Gamma Irradiation on the structural and electrical properties of HfO<sub>2</sub> thin films deposited on GaAs

The main aim of the study presented in this chapter is optimization of film thickness deposited under various deposition times to synthesize reproducible HfO<sub>2</sub> films with good quality using RF magnetron sputtering deposition technique. Thin films of HfO<sub>2</sub> were synthesized on Semi-Insulating GaAs substrates and the role of deposition time on the HfO<sub>2</sub> films have been studied. Further, thin films of HfO<sub>2</sub> synthesized using optimized growth parameters were exposed to thermal annealing and gamma irradiation. Effects of post deposition thermal annealing and gamma irradiation on the structural changes and subsequent effects on the electrical properties of HfO<sub>2</sub> films have been discussed (part of this work is published in AIP Conference Proceedings 2019, 2115, 030021).

### 3.1. Introduction

A thin film is a monolayer or several layers of the target material with the film thickness ranging from fractions of a nanometer to several micrometers [1]. Thin films of various materials such as metals, semiconductors, insulators etc. have tremendous advantages when compared to their bulk properties and have been extensively used in the applications of optoelectronic, micro/nanoelectronic devices and solar cells [2-4]. Thin films of different materials have been chosen depending on their applications. In modern Integrated Chip (IC) fabrication technology, the rapid advancement of deposition techniques has resulted in substantial progress in improving the thin films with best quality [5]. These superior quality thin films have found diverse applications in modern micro/nano-electronic device technologies. The surface morphology, interface properties, size and structure of the films deposited by various deposition techniques play an important role on the device quality [6]. Hence, it is important to study the physical mechanisms involved at the time of thin film deposition like the interaction with charged particles, surface morphology of the target material, chemical reactions, adherence between the target material and substrate etc. [7]. In addition to these physical mechanisms, the deposition conditions at the time of PVD process like distance between target and substrate, deposition pressure, substrate temperature, gas flow rate, deposition power and target material density etc. have also been used to tune the thin film properties [8]. The functionality of the micro/nano-electronic devices in modern IC technology developed from these superior quality thin films are explicitly useful owing to structural, optical properties as well as electrical properties of these thin films, particularly in modern Complementary Metal Oxide Semiconductor (CMOS) devices [9, 10]. However, advancement of thin film deposition techniques have shown a significant improvement in modern CMOS technology. Increasing the number of MOS devices on an IC became mandatory as the size is being scaled down to a few nanometers to improve the device performance [11]. Principally, most of the target materials can be grown as thin films by applying different thin film deposition techniques. There are two well-known methods namely Physical and Chemical deposition methods, that have been used to grow different materials depending on their nucleation and transport properties. Physical deposition techniques include Sputtering and evaporation etc. Chemical deposition techniques include Sol-gel, Plating and Chemical Vapor Deposition (CVD) etc. In the physical deposition method, the target material is in the form of solid. During this deposition, the target material evaporates into atomic spices when an appropriate external power

is applied. These atomic species which are ejected from the target material move towards the substrate and get deposited on it by the nucleation process. By increasing the time of deposition, thickness of the deposited film can be increased and a continuous uniform film of desired thickness can be grown on the substrate. Among many physical deposition methods, Pulsed Laser Deposition (PLD) technique [12, 13], electron beam (e-beam) evaporation technique [14] and RF magnetron sputtering technique [15] have been used widely for growing thin films of metals and insulators. On the other hand, Direct Current (DC) sputtering technique and Thermal evaporation technique [16] have been used in growing thin films of metals.

RF and DC magnetron sputtering methods have been used widely in depositing high-quality uniform thin films of insulators and metals respectively for laboratory applications. In this technique, an external power using RF or DC power source is applied to the target material in a low pressure and in inert gas (Ar) atmosphere to generate plasma. These generated Ar ions then collide very strongly with the target material and the atoms ejected from the target material. These ejected atoms of target material travel towards the substrate and get deposited on it. In magnetron sputtering, the strong magnetic field is used to confine the plasma and electrons which results in ionizations within the relevant area of the target sample. In recent years, RF Magnetron sputtering technique has been used widely to grow high-k dielectric Hafnium oxide (HfO<sub>2</sub>) thin films, because it offers high quality uniform films, good control over the deposition and reduced cost when compared to other physical deposition techniques.

In CMOS technology, typical SiO<sub>2</sub> gate oxide has been replaced by HfO<sub>2</sub> (dielectric constant 18-25 and band gap 5.8 eV) as the gate oxide in some advanced CMOS transistors by Intel in 2007 [17]. It is important to note that, in Silicon CMOS technology, use of Si as the standard semiconductor was encouraged because it has outstanding interface properties with the dielectric SiO<sub>2</sub> [18]. However, SiO<sub>2</sub> has already been replaced by Hafnium oxide (HfO<sub>2</sub>) in the current technology [17, 19]. For further device scaling, it is presently followed by an attempt to replace the Si with superior high mobility semiconductors [20]. Among them, III-V and III-VI compound semiconductors, such as GaAs, GaN, InAs, GaSb, InAlAs and Ga<sub>2</sub>O<sub>3</sub> can achieve the proposed MOS devices with high-performance characteristics [21, 22]. Among these compound semiconductors GaAs attracted more attention in recent years due to its higher electron mobility

as the electron mobility of GaAs is around six times greater than that of Si, which makes it an attractive substrate for the future high-speed applications in CMOS devices [23].

HfO<sub>2</sub> is a fascinating material for a wide range of applications due to its exceptional material properties such as high density, high dielectric constant (k), wide band gap and comparatively good thermal stability [24]. It has been used in various categories of applications like a high-k gate dielectric in some advanced transistors for memory applications [25] and optical coatings [26] etc. Thermal Annealing (TA) and Rapid Thermal Annealing (RTA) are capable of crystallizing HfO<sub>2</sub> thin films [27-29]. HfO<sub>2</sub> is mainly known to exist in three crystallographic phases at ambient pressure depending on the annealing temperatures. It exists in monoclinic phase (m-HfO<sub>2</sub>) in the temperature range of room temperature (RT) to 1700<sup>o</sup> C, transforms to tetragonal (t-HfO<sub>2</sub>) at higher temperatures greater than 1700° C and at very high temperatures greater than 2600° C, it becomes cubic (c-HfO<sub>2</sub>) [30]. The phase change of HfO<sub>2</sub> from amorphous phase to monoclinic phase can lead to change in dielectric constant from 25 to 18 and band gap from 5.8 eV to 6.13 eV [31, 32]. Therefore, the structural changes in HfO<sub>2</sub> like formation of grains and crystallization can intensely affect its electrical properties and other material properties. Kopani et al. [33] reported that the growth rate of crystalline HfO<sub>2</sub> nuclei increases as the temperature of thermal annealing increases. Hence, the structural changes in RF Magnetron sputtered HfO<sub>2</sub> thin films such as grain growth, phase transformation due to post deposition annealing and consequent effects on the electrical characteristics may be useful for more exploration.

In recent years, enormous development has taken place in the fabrication of HfO<sub>2</sub> high-k dielectric based MOS devices [34]. Existing data of HfO<sub>2</sub> based device applications in the radiation harsh environments is still insufficient. Therefore, the challenges like, reliability and durability are being currently being actively considered for the advanced HfO<sub>2</sub> based MOS device technology [35]. Particularly, the electrical performance of the device in radiation harsh environments is essential for space, nuclear power plant and radiation based medicine applications. In previous research reports, A. Y. Kang et al. [36] stated that mostly electrons are confined in the HfO<sub>2</sub> based MOS devices when they are subjected to irradiation. C. Z. Zhao et al. [37], while F. B. Ergin et al. [38] have described that both electrons and holes are trapped due to gamma irradiation. J. M. Rafi et al. [39] and Y. F. Mu et al. [40, 41] reported that trapping effects due to both positive and negative charges can be detected in the gate injection conditions. X. Liu et al. [42] and S. Maurya [43]

observed positive trapped charges in the HfO<sub>2</sub> based MOS devices and arbitrary passivation of interface trapped charges due to radiation. On the other hand, deposition parameters and deposition techniques also play a significant role in the device performance due to radiation induced effects. J. T. Ryan et al. [44], and C. Liang et al. [45] explained the effects of deposition conditions on radiation induced trapping charges in HfO<sub>2</sub>. G. Lucovsky et al. [46] demonstrated the existence of various charge trapping processes in high-k dielectrics because of change in microstructures. In most of the research, HfO<sub>2</sub> thin films synthesized by using ALD technique have been reported and it is feasible that the HfO<sub>2</sub> thin films synthesized using other deposition techniques such as RF magnetron sputtering, may be helpful because thin film properties like structure, uniformity, density of initial trapped charges etc. may vary for different deposition processes.

Gamma irradiation is known to cause ionization in materials through generation of Compton scattered electrons and production of Electron-Hole Pairs (EHPs) which results in mobilization or creation of traps/defects. The generation of energetic electrons or ionization and production of EHPs depend on the amount of energy deposited to the target material due to gamma irradiation [47, 48]. The pre-existing defects/traps in the high-k dielectrics confine these moveable charges which can affect the electrical characteristics due to trapped charges [49]. Furthermore, gamma radiation can produce oxygen vacancies in the high-k dielectric gate oxides. Therefore, irradiation induced ionization/defect-creation is expected to affect the electrical characteristics of HfO<sub>2</sub> high-k dielectric based MOS devices.

In this chapter, we have used different deposition conditions to optimize the growth parameters to synthesize good quality HfO<sub>2</sub> thin films on GaAs substrates by RF magnetron sputtering technique. Effects of growth parameters and thermal annealing on the structural and electrical properties of HfO<sub>2</sub> thin films have been discussed. Further, the optimization conditions and effects of gamma irradiation on the electrical characteristics of HfO<sub>2</sub>/GaAs based MOS structures have also been discussed.

# 3.2. Experimental Details

**3.2.1. Synthesis of HfO<sub>2</sub> thin films:** To optimize the growth parameters, HfO<sub>2</sub> thin films of various thickness under different deposition conditions were deposited on Semi-Insulating (undoped) GaAs (100) substrates by using RF magnetron sputtering (13.6 MHz) method. Before the

deposition, substrates were cut into pieces of 1 cm x 1 cm each and cleaned using an ultrasonication process by dipping in acetone followed by isopropanol and deionized water for 5 min each. Then, these were dried with nitrogen gas and immediately loaded into the chamber. The optimized distance of 125 mm between HfO<sub>2</sub> target and GaAs substrates was maintained and RF power of 60 W was applied to the HfO<sub>2</sub> target during the deposition. These parameters were chosen based on our earlier experiments on Si substrates [50]. When the pressure inside the chamber reached to 4 x 10<sup>-6</sup> mbar, 30 SCCM of argon gas was released and the deposition pressure of 2 x 10<sup>-2</sup> mbar was recorded. Commercially purchased 99.99% pure HfO<sub>2</sub> target of two inch diameter was used. HfO<sub>2</sub> films of various thickness were synthesized on GaAs by varying deposition time. HfO<sub>2</sub> thin films were synthesized using 10, 15, 20 and 30 min of deposition time.

- **3.2.2. Sample Characterization:** The role of deposition time on HfO<sub>2</sub> films was studied by employing different characterization techniques. As-grown films at different deposition times were scanned by using the Field emission scanning electron microscope (FESEM) to observe the film structure and morphology (model: Carl ZEISS, FEG, ultra-55). FESEM Energy Dispersive X-ray Spectroscopy analysis (EDX) measurements were carried-out to study the elemental composition. Grazing incident x-ray diffraction (GIXRD) measurements were performed with an incidence angle of  $0.5^{\circ}$  to study the phase of HfO<sub>2</sub> thin films (model: Bruker D8 Advance diffractometer with Cu K $\alpha$ ,  $\lambda = 1.54$  Å). The X-Ray Reflectivity (XRR) measurements were performed using Bruker D8 Advance diffractometer with Cu K $\alpha$ ,  $\lambda = 1.54$  Å. Using Rutherford Backscattering Spectroscopy (RBS) measurements, thickness of the films and elemental compositions have been investigated using He<sup>2+</sup> ions (2 MeV, scattering angle 165°) at IUAC, New Delhi. Further, the thickness of as-grown films were measured by performing cross sectional FESEM measurements and thickness profile measurements using Ambios XP 200 Profilometer.
- **3.2.3. Thermal Annealing:** One set of samples containing HfO<sub>2</sub> thin films synthesized using the optimized deposition time of 30 min were annealed in the temperature range of 200  $^{0}$ C to 600  $^{0}$ C for 1 hour in N<sub>2</sub> atmosphere. After placing the sample inside the tubular furnace, the rate of increase in the temperature was maintained to be 4  $^{0}$ C/min for all samples.
- **3.2.4. Gamma irradiation:** Another set of samples containing HfO<sub>2</sub> thin films synthesized using the optimized deposition time of 30 min were subjected to <sup>60</sup>Co gamma (1.25 MeV) irradiation at a constant radiation dose rate of 4.6 KGy/hr by using a Gamma chamber-1200 at IUAC, New

Delhi. By varying the sample exposure time to the gamma rays, the gamma irradiation doses of 2 KGy, 4 KGy, 8 KGy, 16 KGy, 32 KGy, 48 KGy and 64 KGy were achieved.

**3.2.5. Fabrication and electrical characterization of MOS structures:** HfO<sub>2</sub> thin films synthesized at various deposition conditions, thermally annealed and gamma irradiated samples were used to fabricate Au/HfO<sub>2</sub>/GaAs based MOS structures by depositing top and bottom contacts to perform electrical measurements. Metal contacts of Au were deposited (~ 100 nm thick and 1 mm in diameter using a shadow mask) as top electrode (TE). Adhesive and conductive Ag paste along with Al foil was used as a bottom electrode (BE). The TE/HfO<sub>2</sub> and Si/BE interfaces are expected to behave in the same manner for both the devices with or without Au NPs inside HfO<sub>2</sub>. Hence the differences in leakage currents and storage capacity are attributed to the annealing and irradiation effects. Electrical characterizations such as Leakage current - Voltage (I-V) and Capacitance - Voltage (C-V) were performed using an Agilent technologies (B1500A) semiconductor device analyzer to evaluate the effects of deposition time, thermal annealing and gamma irradiation on the electrical characteristics of these MOS structures.

### 3.3. Results and discussions

**3.3.1. Effects of growth parameters:** The role of deposition time on HfO<sub>2</sub> films was studied by employing different characterization techniques. The thickness of HfO<sub>2</sub> films were estimated by Profilometer and cross X-FESEM measurements. The cross sectional FESEM images are shown in Fig. 3.1. The estimated thickness of HfO<sub>2</sub> films using cross sectional FESEM measurements of films grown at deposition time of 10, 15, 20 and 30 min are found to be 11 nm, 17 nm, 22 nm and 37 nm respectively. The data obtained from Profilometer measurements are shown in Fig. 3.2. The estimated thickness of HfO<sub>2</sub> films grown at deposition time of 10, 15, 20 and 30 min are found to be 13 nm, 16 nm, 21 nm and 35 nm respectively using these measurements. These values are given in table 3.1. The uniformity is found increasing with deposition time. Uniform HfO<sub>2</sub> thin films of thickness around 35 nm have been synthesized at the deposition time of 30 min.

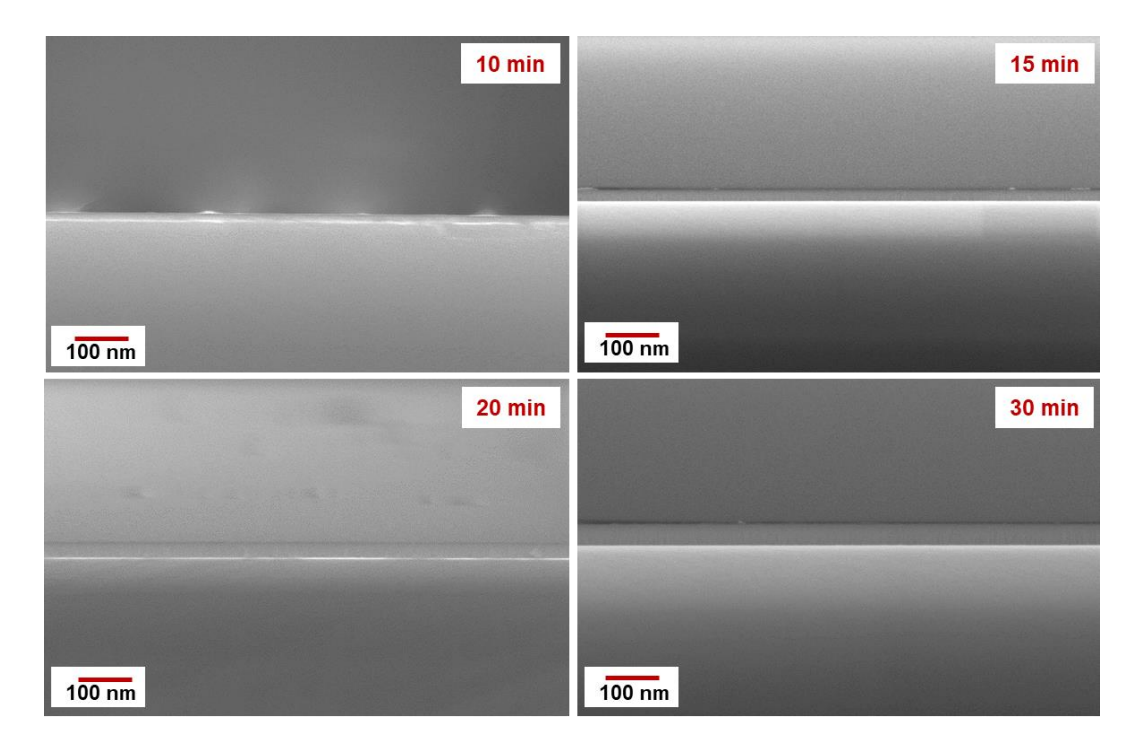


Fig. 3.1: Cross sectional FESEM images of HfO<sub>2</sub> thin films grown on GaAs substrates at deposition time of 10, 15, 20 and 30 min.

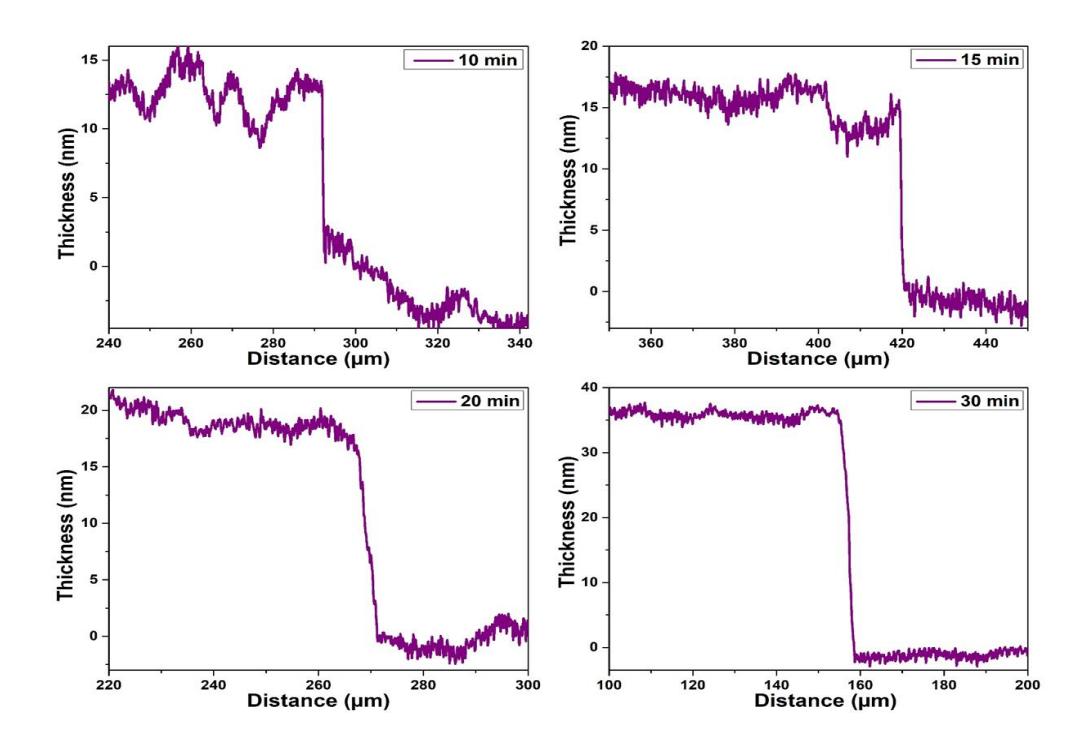


Fig. 3.2: Estimation of HfO<sub>2</sub> film thickness using Profilometer measurements.

Furthermore, the thickness and elemental compositions of the HfO<sub>2</sub> films have also been estimated by performing RBS measurements. The RBS spectra with SIMNRA simulations as a function of deposition time are shown in Fig. 3.3. The values of Calibration offset and Energy per channel were obtained from a standard calibration sample (Au/glass). The values of Calibration offset and Energy per channel as 73.65 keV and 0.98 keV/ch respectively were used for SIMNRA simulation. The thickness of HfO<sub>2</sub> thin films grown for deposition times of 10 min, 15 min, 20 min and 30 min were estimated using the simulation and found to be 11 nm, 18 nm, 22 nm and 38 nm respectively. To estimate HfO<sub>2</sub> film thickness and stoichiometry from the fitting curve using SIMNRA simulation, bulk density corresponding to HfO<sub>2</sub> as 9.68 g/cm<sup>3</sup> has been considered.

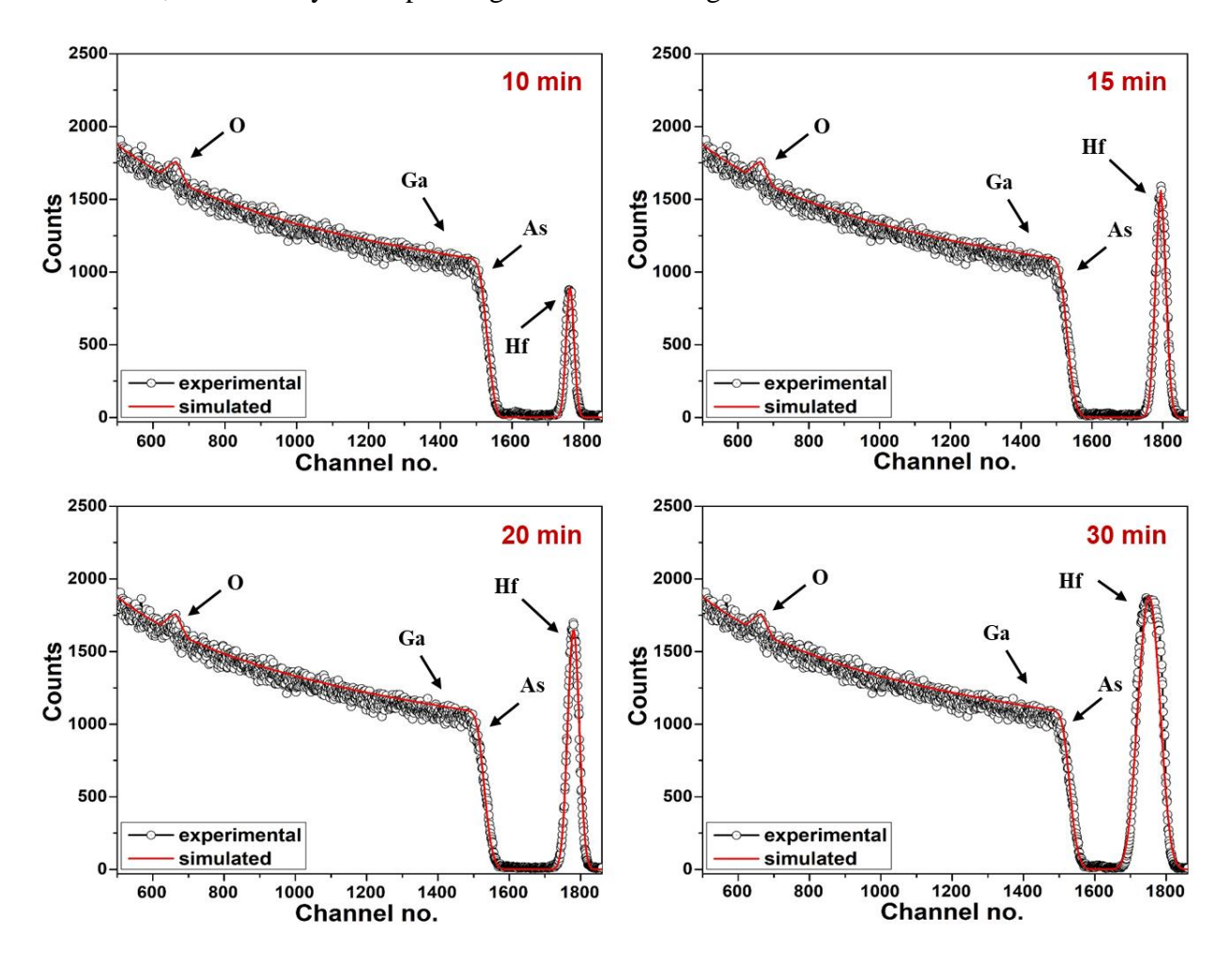


Fig. 3.3: RBS spectra of HfO<sub>2</sub> thin films deposited on GaAs with SIMNRA simulation.

The estimated thickness and stoichiometry of HfO<sub>2</sub> films using cross sectional FESEM, Profilometer and RBS measurements are summarized and presented in Table 3.1.

| Deposition<br>Time | Film thickness (nm) |                        |              | Stoichiometry of the            |
|--------------------|---------------------|------------------------|--------------|---------------------------------|
|                    | RBS                 | FESEM<br>Cross-section | Profilometer | film from RBS analysis (%) Hf:O |
| 10 min             | 11                  | 11                     | 13           | 22:78                           |
| 15 min             | 18                  | 17                     | 16           | 26:74                           |
| 20 min             | 22                  | 22                     | 21           | 29:71                           |
| 30 min             | 38                  | 37                     | 35           | 36:64                           |

Table 3.1: The estimated thickness of HfO<sub>2</sub> films obtained using RBS, cross sectional FESEM and Profilometer measurements.

The role of deposition time on the structure and morphology of HfO<sub>2</sub> film surfaces were studied using the FESEM measurements. The FESEM images of HfO<sub>2</sub> thin films deposited on GaAs substrates as a function of deposition time are shown in Fig. 3.4.

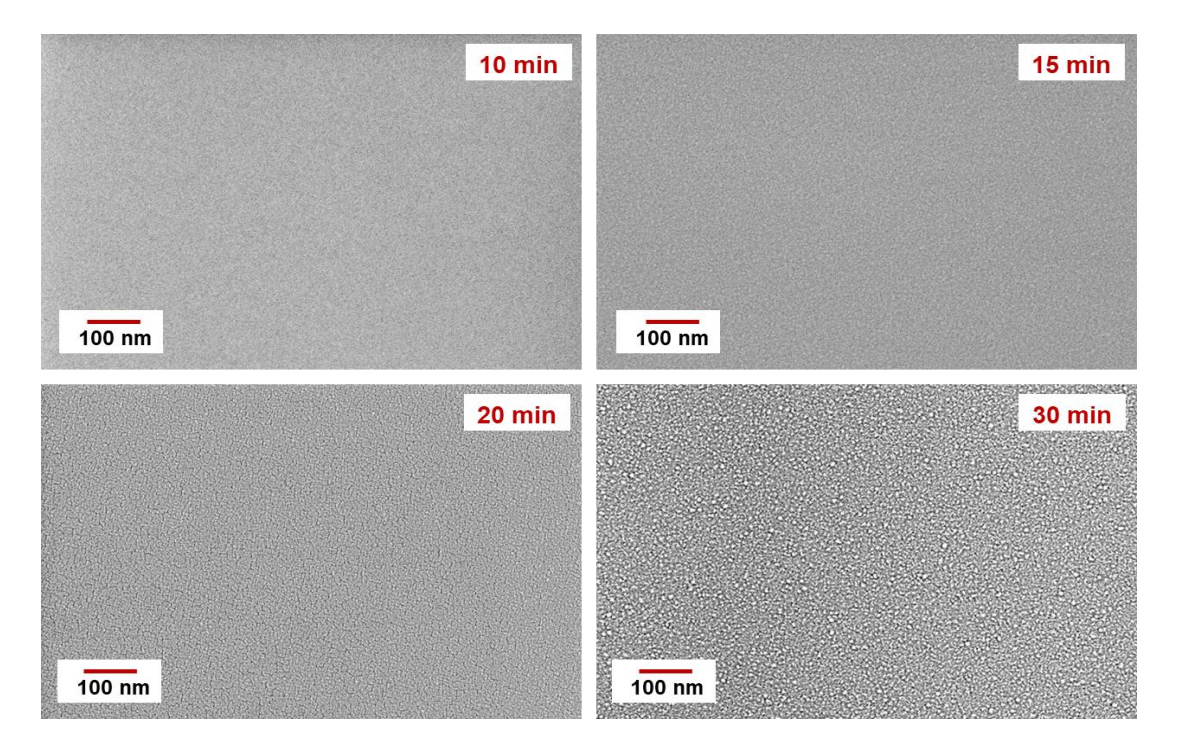


Fig. 3.4: FESEM images of HfO<sub>2</sub> thin films deposited on GaAs substrates as a function of deposition time.

HfO<sub>2</sub> thin films grown for deposition times of 10 min and 15 min have smooth surfaces with no distinguishable formation of HfO<sub>2</sub> grains. Evolution of very small grains has been observed for the sample grown for deposition time of 20 min. For the sample grown for deposition time of 30 min, formation of evenly distributed grains with distinguishable but uniform size has been observed. HfO<sub>2</sub> thin films grown for deposition time of 30 min shows good uniformity, good stoichiometry and formation of uniform grains.

GIXRD measurements were performed on all the samples and the diffraction patterns of HfO<sub>2</sub> thin films as a function of deposition time are shown in Fig. 3.5. GIXRD patterns of HfO<sub>2</sub> thin films grown at various deposition times indicate dominance of the amorphous phase of HfO<sub>2</sub>. Therefore, all the HfO<sub>2</sub> thin films grown using RF sputtering at room temperature are predominantly amorphous in nature, independent of the deposition time though there are significant changes in their morphology.

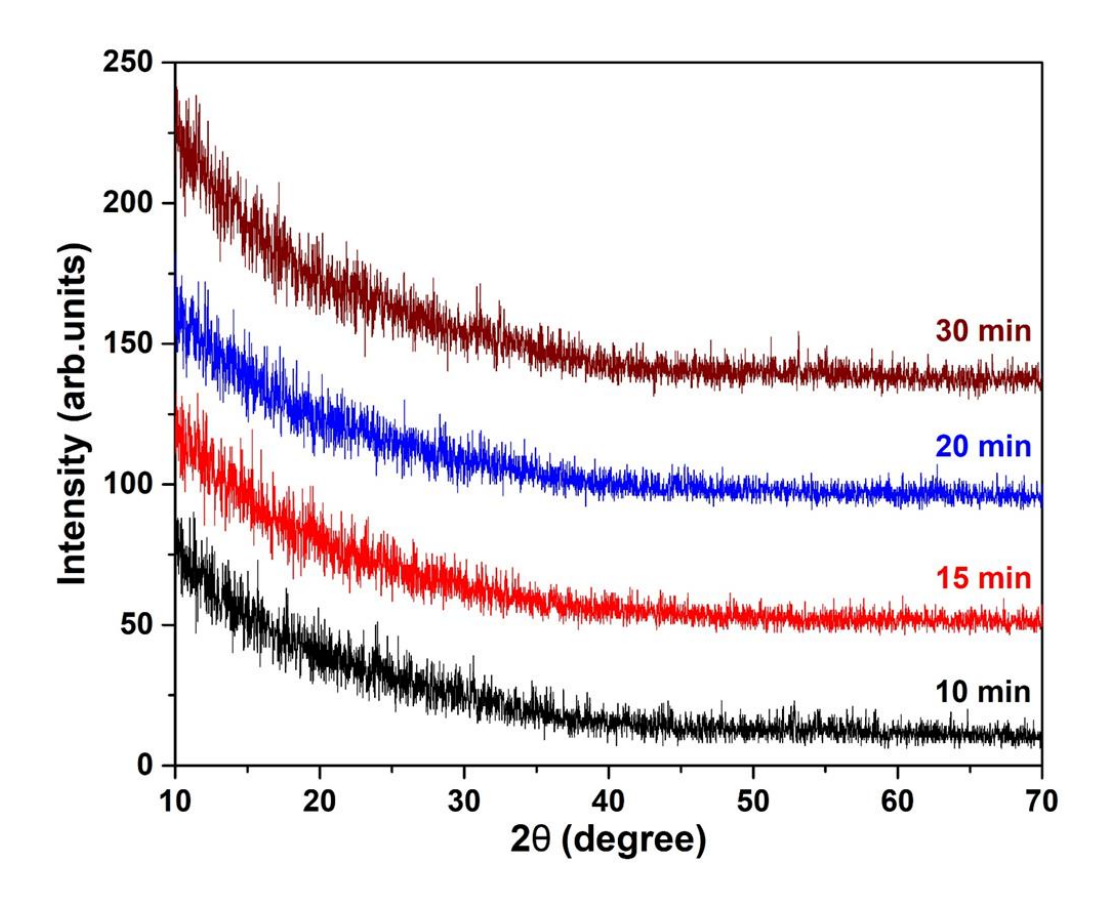


Fig. 3.5: GIXRD patterns of HfO<sub>2</sub> thin films deposited on GaAs substrates as a function of deposition time.

As mentioned earlier,  $Au/HfO_2/GaAs/Ag$  MOS structures were fabricated by depositing top and bottom electrodes. The role of deposition time on the leakage current density through the  $HfO_2$  thin films grown at various deposition times were studied by performing leakage current - voltage (I-V) measurements as shown in Fig. 3.6(a). From the I-V characteristics, leakage current is found to decrease with increasing deposition time which is reasonable as the thickness of  $HfO_2$  thin films increases with the deposition time. As shown in Fig. 3.6(b), the current density at applied voltage of -1 V of sample grown for 10 min of deposition time is around 2.3 x  $10^{-5}$  A/cm<sup>2</sup>, which is decreased to 5.2 x  $10^{-6}$  A/cm<sup>2</sup> for the sample grown for 15 min of deposition time. At the same applied voltage, the leakage current density has been decreased to 1.7 x  $10^{-6}$  A/cm<sup>2</sup> for the sample grown for 20 min of deposition time. Further increasing the deposition time to 30 min, the leakage current density decreases to  $8.0 \times 10^{-7}$  A/cm<sup>2</sup>. However, the increase in thickness is about 3 times (~ 11 nm to ~ 35 nm) but the leakage current density is decreases by almost three orders of magnitude for the sample grown for 30 min of deposition time when compared to that of sample grown for 10 min of deposition time. This confirms the formation of reasonably good stoichiometric films with less number of defects when the film is deposited for 30 min.

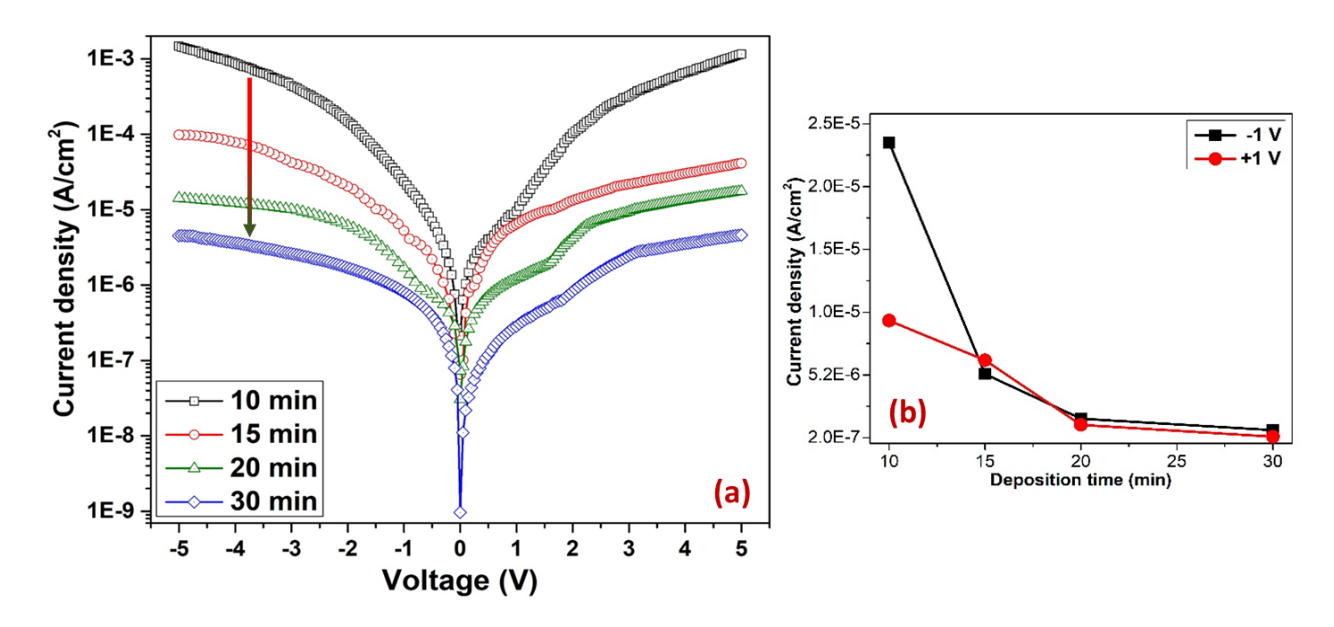


Fig. 3.6: (a) I-V characteristics of Au/HfO<sub>2</sub>/GaAs based MOS structures and (b) current density at applied voltage of  $\pm 1$  V as a function of HfO<sub>2</sub> film deposition time.

From this study, HfO<sub>2</sub> thin films grown for different deposition times, it is noticed that the film thickness and uniformity of the film increases with increasing deposition time. Good stoichiometry and formation of HfO<sub>2</sub> grains with distinguishable size have been observed for the film grown for 30 min of deposition time. Leakage current is found to decrease with increasing deposition time. Hence, the optimized growth parameters such as deposition time of 30 min, RF power of 60W, Ar gas flow of 30 SCCM and substrate to target distance of 125 mm have been maintained to deposit HfO<sub>2</sub> thin films for further studies like thermal annealing, gamma irradiation and SHI irradiation.

**3.3.2. Effects of thermal annealing:** A set of HfO<sub>2</sub> thin films grown under the optimized growth parameters (deposition time of 30 min, RF power of 60W, Ar gas flow of 30 SCCM and substrate to target distance of 125 mm) were thermally annealed in the temperature range of 200 °C to 600 °C for 1 hour each in N<sub>2</sub> atmosphere. Effects of thermal annealing on the structural and electrical characteristics of HfO<sub>2</sub> thin films have been studied by using different characterizations.

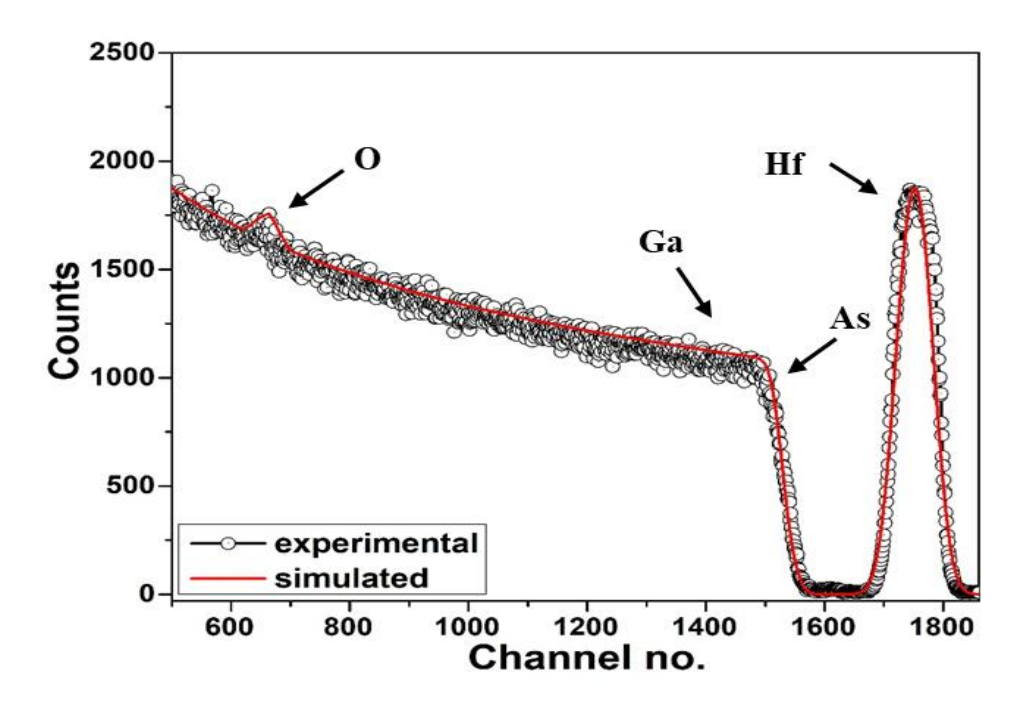


Fig. 3.7: RBS spectrum of pristine HfO<sub>2</sub> thin film with SIMNRA simulation.

The thickness estimation and elemental composition of as-grown HfO<sub>2</sub> films have been estimated by performing RBS and FESEM – EDX measurements. The RBS spectrum of pristine HfO<sub>2</sub> film with SIMNRA simulation is shown in Fig. 3.7. The values of Calibration offset and Energy per channel were obtained from a standard calibration sample (Au/glass). These values of Calibration

offset and Energy per channel namely 73.65 keV and 0.98 keV/ch respectively were used for SIMNRA simulation. The SIMNRA simulation studies show the estimated thickness to be around 38 nm with elemental composition around 36% of Hf and 64% of O.

The EDX spectrum of pristine HfO<sub>2</sub> thin film shown in Fig. 3.8. EDX analysis shows the elemental composition of the film is around 39% of Hf and 61% of O which is consistent with the RBS analysis.

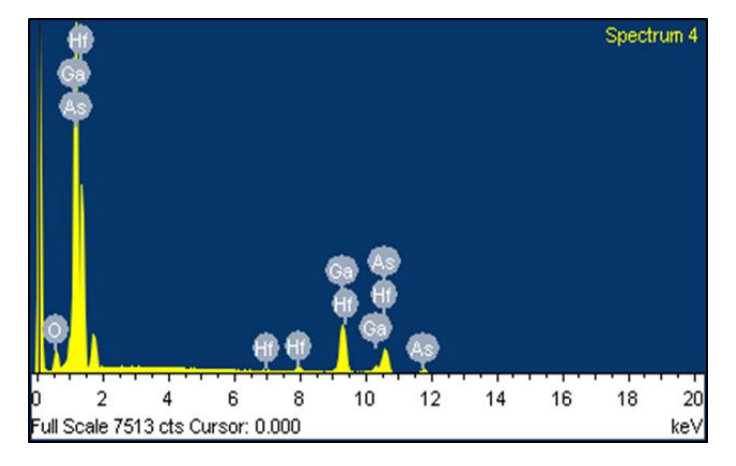


Fig. 3.8: EDX spectrum of pristine HfO<sub>2</sub> thin film grown on GaAs.

The XRR pattern of pristine HfO<sub>2</sub> thin film is shown in Fig. 3.9. The thickness of HfO<sub>2</sub> film is found to be around 35 nm from XRR analysis.

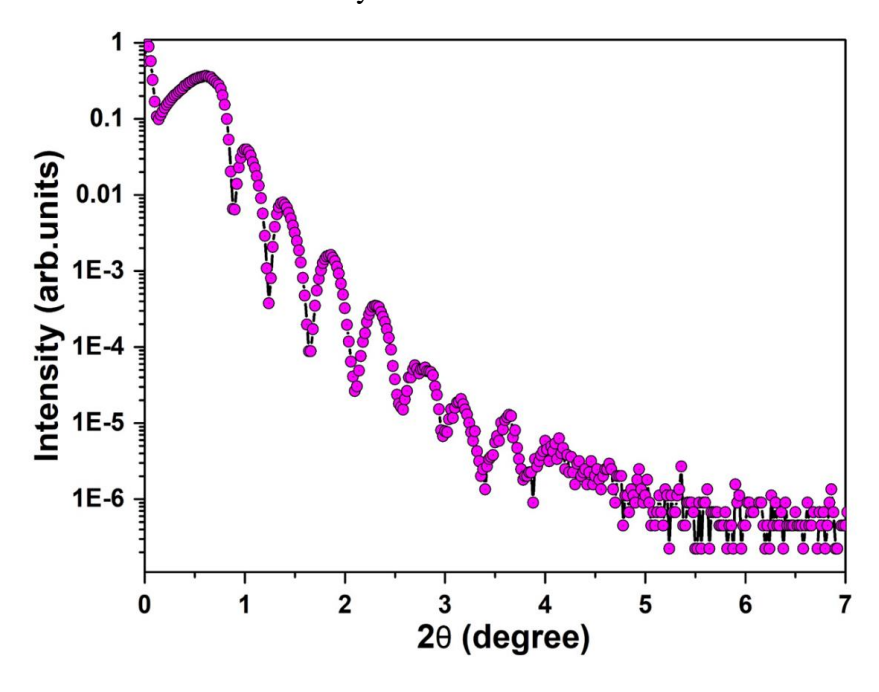


Fig. 3.9: XRR pattern of pristine HfO<sub>2</sub> thin film grown on GaAs.

The effects of thermal annealing on the morphology of HfO<sub>2</sub> thin film surfaces were examined by performing FESEM measurements. The FESEM images of pristine and thermal annealed HfO<sub>2</sub> thin film surfaces are shown in Fig. 3.10.

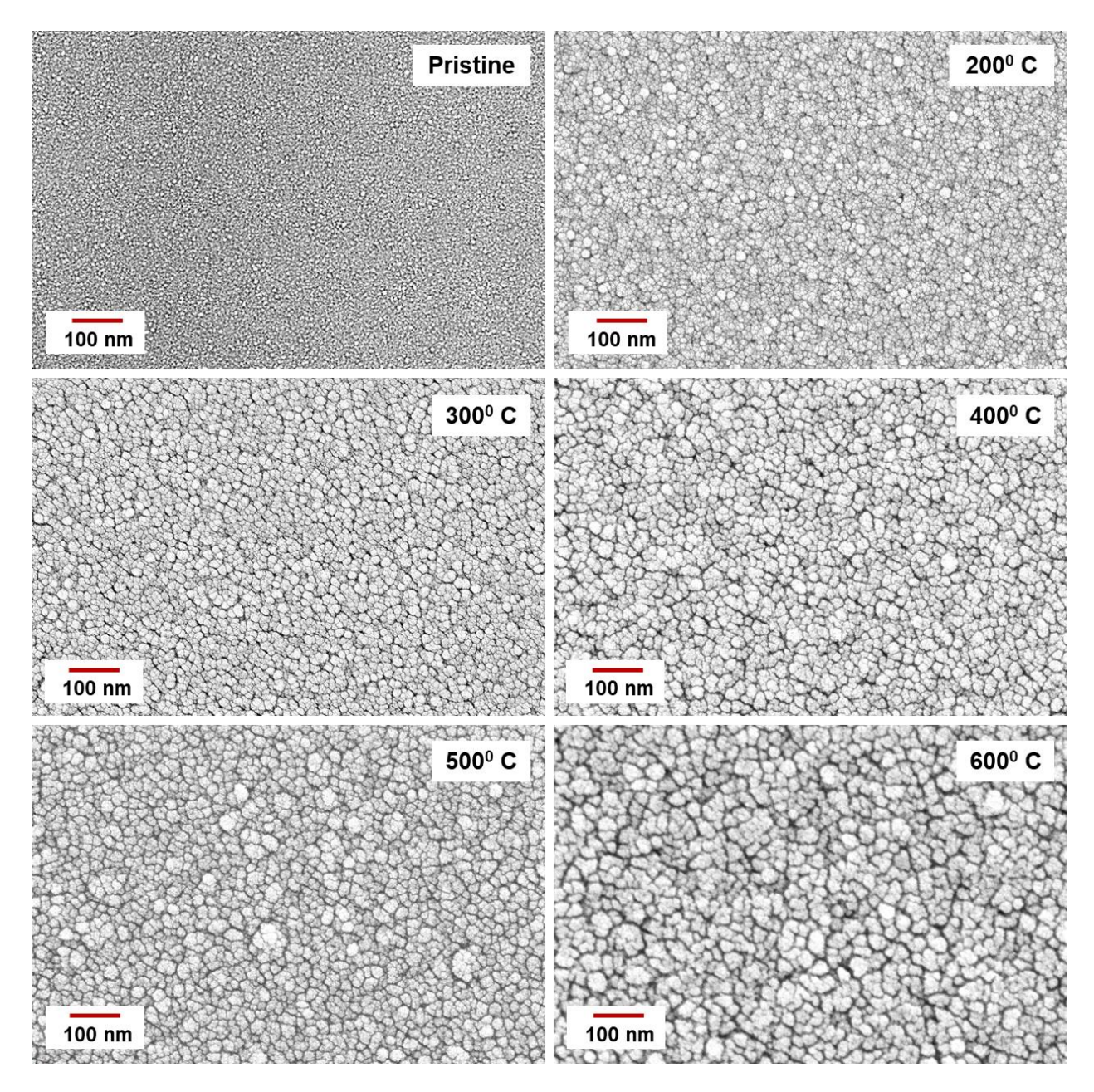


Fig. 3.10: FESEM images of pristine and thermal annealed HfO<sub>2</sub> thin film surfaces.

From these images, it is observed that the pristine HfO<sub>2</sub> film possesses a smooth surface with uniformly distributed grains. After thermal annealing, variation in surface structure of HfO<sub>2</sub> thin films and a monotonic increase in the grain size have also been observed which may be attributed

to the possible agglomeration of grains due to thermal annealing. Formation of new grains with increased size and grain boundaries have been observed as a result of thermal annealing. It is observed that the growth rate of crystalline HfO<sub>2</sub> nuclei is found to increase as the temperature of thermal annealing increases. These results are consistent with the previous reports in the relevant literature [33].

GIXRD measurements were performed on pristine and thermally annealed samples to study the effects of thermal annealing on the phase transformation of HfO<sub>2</sub> thin films. The diffraction patterns of as-grown and annealed HfO<sub>2</sub> thin films are shown in Fig. 3.11.

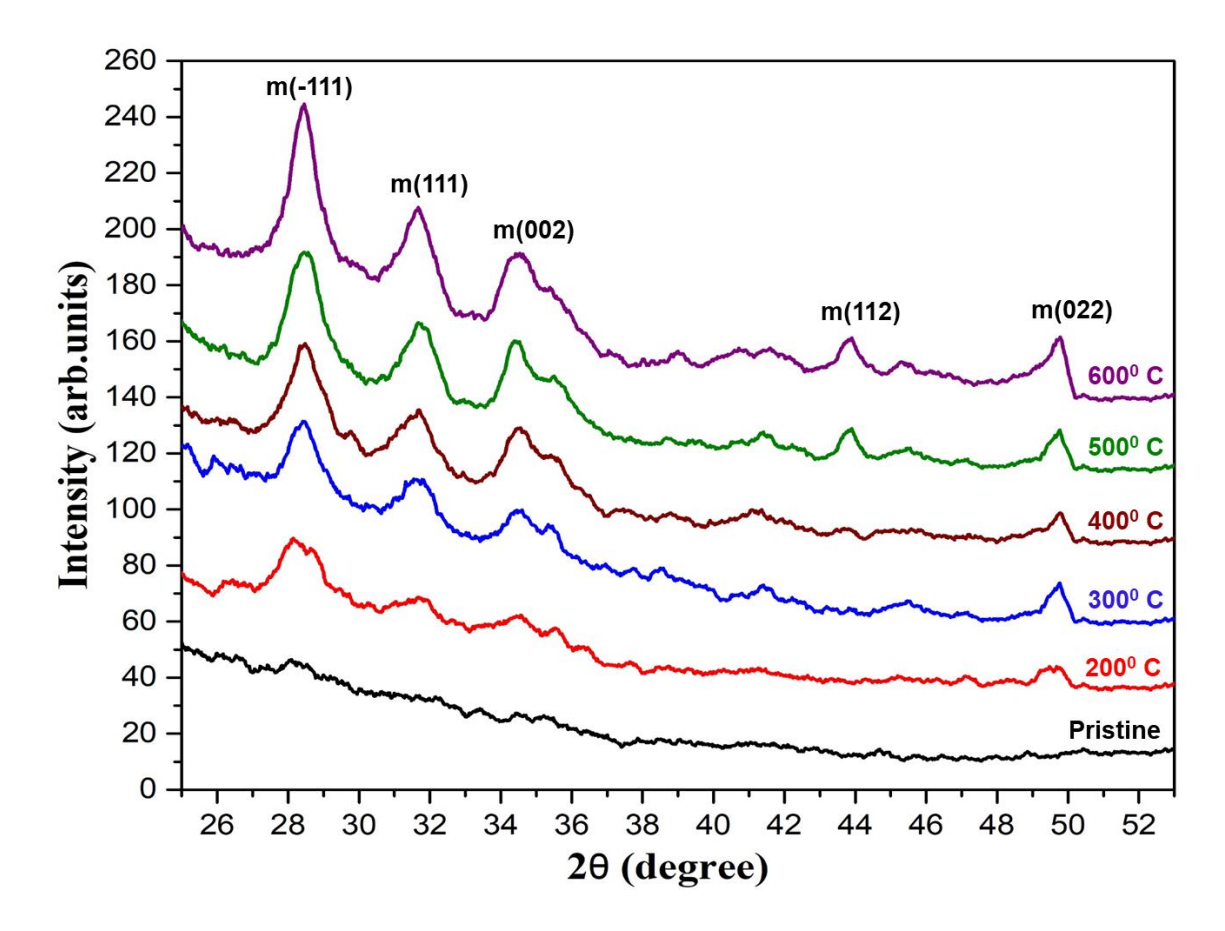


Fig. 3.11: GIXRD patterns of as-grown and thermal annealed HfO<sub>2</sub> thin films.

Pristine films exhibit amorphous nature while the thermally annealed films consist of nano-crystallites. From GIXRD patterns, the introduction of monoclinic phase of  $HfO_2$  has been observed. At the annealing temperature of  $300^{\circ}$  C, evolution of crystalline peaks corresponding to the m(-111), m(111) and m(022) crystal (m: monoclinic) planes have been observed. Upon increasing the annealing temperature to  $600^{\circ}$  C, apart from increase in the intensity of these peaks,

new crystalline peaks corresponding to m(002) and m(112) planes have also been observed. It is confirmed that these crystal planes correspond to the monoclinic phase of HfO<sub>2</sub> using standard JCPDS file (PDF#06-0318). Thus, introduction of crystalline phase of HfO<sub>2</sub> has been observed when pristine amorphous films were subjected to thermal annealing up to the temperature range of 600° C. Further to confirm the phase transformation of HfO<sub>2</sub> thin films due to thermal annealing, pristine and annealed films were characterized by performing micro Raman measurements and the data is shown in Fig. 3.12.

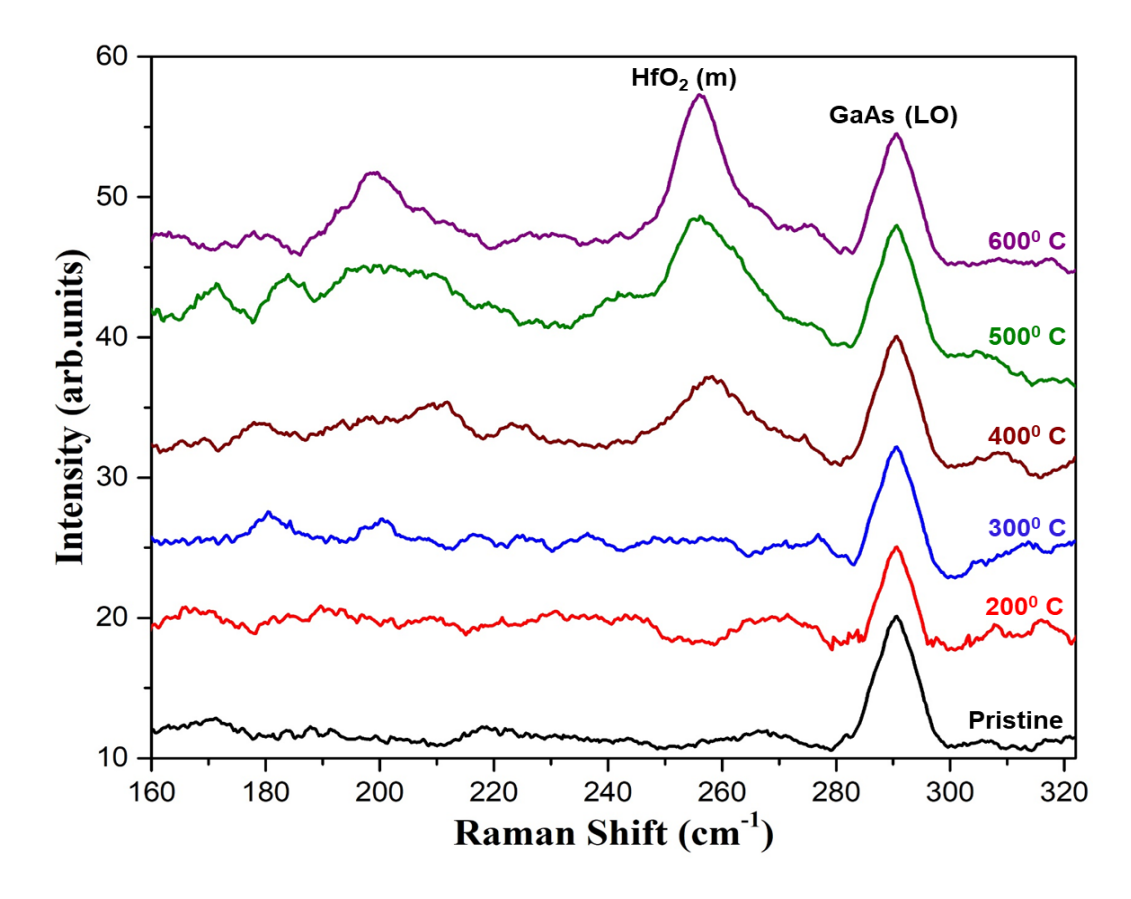


Fig. 3.12: Micro Raman spectra of pristine and thermal annealed HfO<sub>2</sub> thin films.

From Raman spectra, pristine film consists of only one peak corresponding to LO mode of GaAs substrate. With increasing annealing temperature, evaluation of a new peak at Raman shift of 256 cm<sup>-1</sup> has been observed. This observed Raman peak at 256 cm<sup>-1</sup> corresponds to the monoclinic phase of HfO<sub>2</sub> [51]. Here, the results obtained from GIXRD and Raman measurements, within the experimental error bars, are consistent with each other. Therefore, it is confirmed from these measurements that crystallization of HfO<sub>2</sub> has taken place when pristine amorphous films were subjected to thermal annealing. This observation is consistent with the literature as the introduction

of monoclinic phase is expected at elevated temperatures in HfO<sub>2</sub> [30, 52]. The observed structural changes in HfO<sub>2</sub>, like formation of grains and crystallization can significantly affect the electrical properties of MOS structures.

The impact of thermal annealing on the leakage current density (through the pristine and thermally annealed HfO<sub>2</sub> thin films) is studied by leakage current vs voltage (I-V) measurements and the data is shown in Fig. 3.13(a). The observed structural modifications due to thermal annealing can subsequently cause changes in I-V characteristics of MOS structures. It is observed that the leakage current density of the MOS structure decreases with increasing the annealing temperature up to  $300^{\circ}$  C. This decrease in the leakage current may be attributed to annealing of pre-existing defects in the pristine MOS structures. Further increasing the temperature above  $300^{\circ}$  C, significant increase in the leakage current has been observed up to the annealing temperature of  $600^{\circ}$  C.

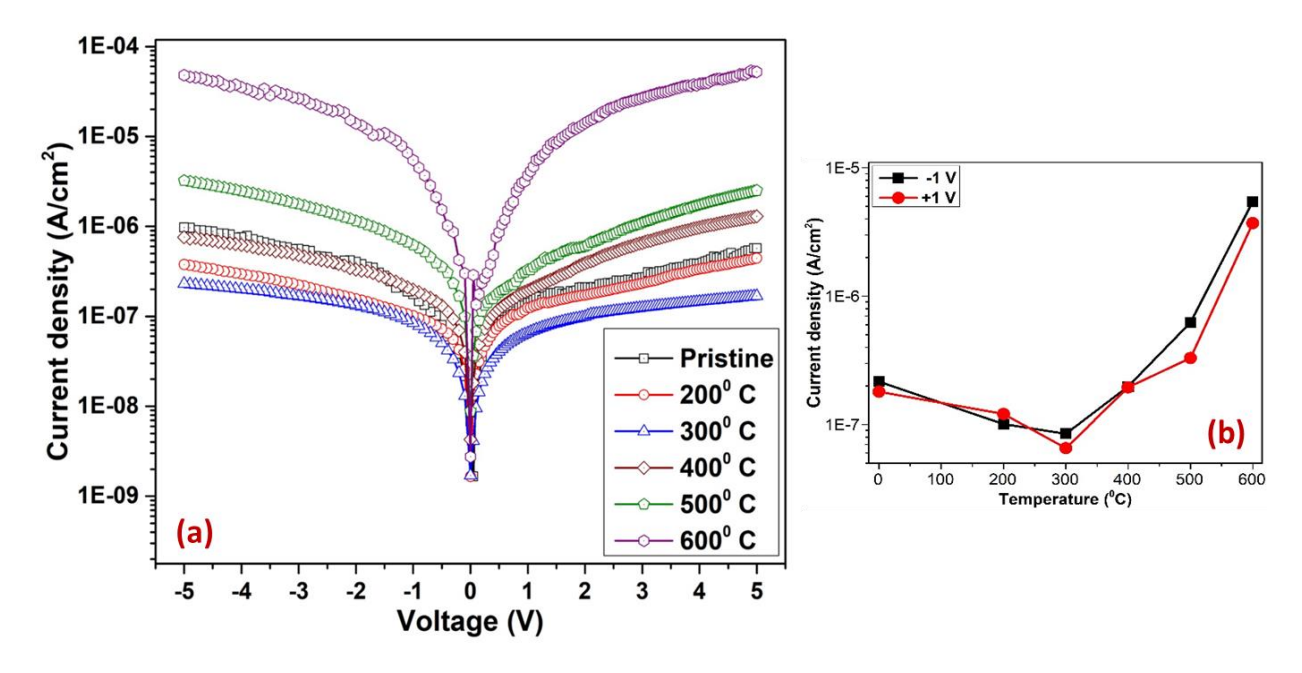


Fig. 3.13: (a) I-V characteristics of Au/HfO<sub>2</sub>/GaAs based MOS structures and (b) current density at applied voltage of  $\pm 1$  V as a function of thermal annealing temperature.

As shown in Fig. 3.13(b), the current density at applied voltage of -1 V decreases from  $2.2 \times 10^{-7}$  A/cm<sup>2</sup> to  $1.0 \times 10^{-7}$  A/cm<sup>2</sup> when the pristine sample is annealed to  $200^{0}$  C. At the same applied voltage, the leakage current density has been decreased to  $8.5 \times 10^{-8}$  A/cm<sup>2</sup> for the annealing temperature of  $300^{0}$  C. Further increasing the annealing temperature to  $400^{0}$  C and  $500^{0}$  C, the leakage current density increases to  $2.0 \times 10^{-7}$  A/cm<sup>2</sup> and  $6.2 \times 10^{-7}$  A/cm<sup>2</sup> respectively. Upon

increasing the annealing temperature to  $600^{0}$  C, it further increases to  $5.4 \times 10^{-6}$  A/cm<sup>2</sup>. This increase in the leakage current may be attributed to the observed structural changes such as crystallization and grain agglomeration in HfO<sub>2</sub> thin films due to thermal annealing. Particularly, change in dielectric constant of HfO<sub>2</sub> due to phase transformation from amorphous to monoclinic [31, 32].

**3.3.2. Effects of Gamma irradiation:** Another set of HfO<sub>2</sub> thin films grown under the optimized growth parameters (deposition time of 30 min, RF power of 60 W, Ar gas flow of 30 SCCM and substrate to target distance of 125 mm) were exposed to gamma irradiation with different doses (2 KGy - 64 KGy). The effects of gamma irradiation on the electrical characteristics of Au/HfO<sub>2</sub>/GaAs based MOS structures are studied by performing I-V measurements as shown in Fig. 3.14(a). From I-V characteristics, it is observed that the leakage current density rises systematically with increasing gamma dose.

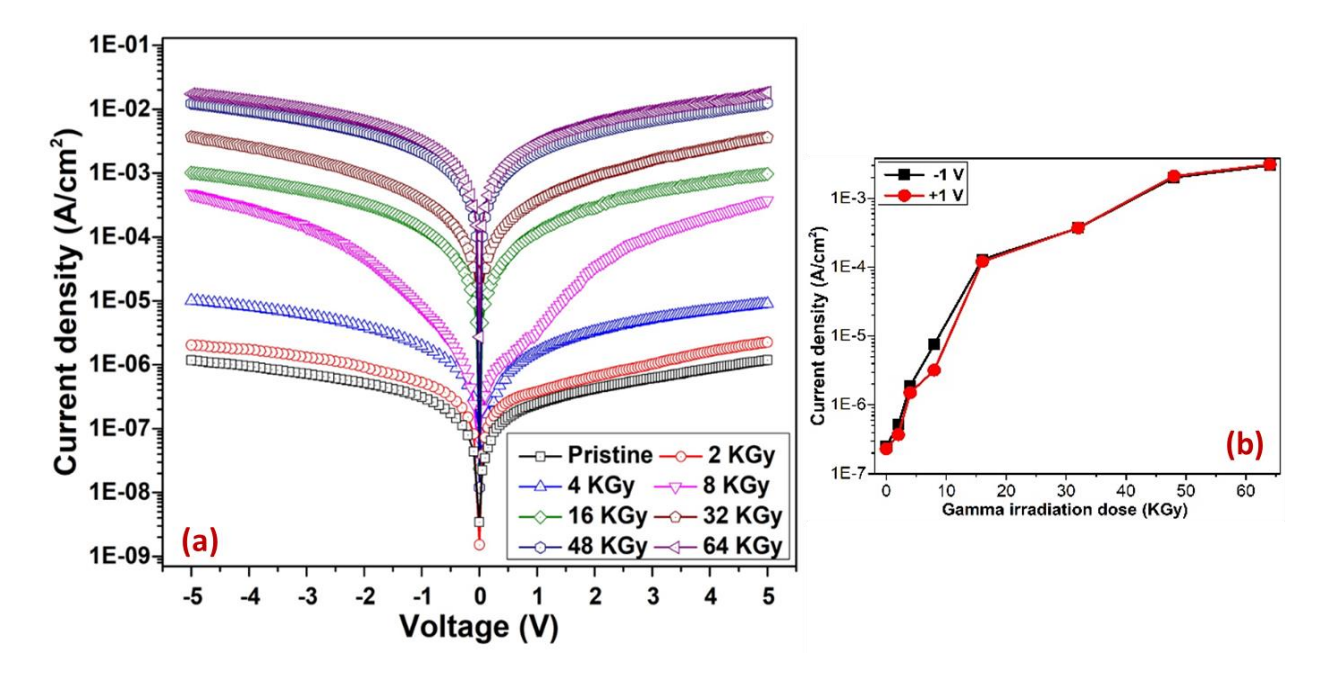


Fig. 3.14: (a) I-V characteristics of Au/HfO<sub>2</sub>/GaAs based MOS structures and (b) current density at applied voltage of  $\pm 1$  V.

As shown in Fig. 3.14(b), the current density at applied voltage of -1 V increases from 2.5 x 10<sup>-7</sup> A/cm<sup>2</sup> to 5.2 x 10<sup>-7</sup> A/cm<sup>2</sup> when the pristine sample is irradiated to a dose of 2 KGy. At the same applied voltage, the leakage current density has been increased to 1.9 x 10<sup>-6</sup> A/cm<sup>2</sup> for the irradiation dose 4 KGy. Further increasing the dose to 8 KGy and 16 KGy, the leakage current

density increases to 7.6 x  $10^{-6}$  A/cm<sup>2</sup> and 1.3 x  $10^{-4}$  A/cm<sup>2</sup> respectively. Upon increasing the dose to 32 KGy, it increases to 3.7 x  $10^{-4}$  A/cm<sup>2</sup>. The leakage current density further increases to 2.2 x  $10^{-3}$  A/cm<sup>2</sup> and 3.1 x  $10^{-3}$  A/cm<sup>2</sup> for the irradiation doses 48 KGy and 64 KGy respectively.

This increase in leakage current with respect to irradiation dose shows the existence of several types of defects in oxide films. This is due to the increase of interface traps and oxide trapped charge densities. Pre-existing defects in the film have the capability to trap the moveable electron-hole pairs produced through the irradiation process prior to the recombination. The possibility of recombination of electron-hole pairs would be high in the absence of any defects during the gamma irradiation. On the other hand, the existence of defects are expected when these type of devices are used in radiation harsh environments like those encountered in space and nuclear power plants. Therefore, this study is essential to realize these radiation damage evolution mechanisms and radiation tolerance of such devices when they are operated in radiation harsh environments.

### 3.4. Conclusions

Thin films of HfO<sub>2</sub> were synthesized on Semi-Insulating GaAs substrates using RF magnetron sputtering deposition technique. The role of deposition time on HfO<sub>2</sub> films were studied by employing different characterization techniques. It is observed that the film thickness and uniformity of the film increases with increasing deposition time. All the HfO<sub>2</sub> thin films grown at room temperature by varying deposition time are amorphous in nature. Good stoichiometry and formation of HfO<sub>2</sub> grains with distinguishable size have been observed for the film grown for 30 min of deposition time leakage current is found to decrease with increasing deposition time which is reasonable and attributed to the increasing of thickness and possible improvement in the film quality. After thermal annealing, variation in surface structure of HfO<sub>2</sub> thin films and a systematic increase in the grain size have also been observed which may be attributed to the possible agglomeration of grains. Introduction of crystalline phase of monoclinic HfO<sub>2</sub> has been observed when pristine amorphous films were subjected to thermal annealing up to the temperature range of 600° C. The leakage current density of the MOS structure decreases with increase in the annealing temperature up to 300° C which may be accredited to the possible annealing of defects that are pre-existing in the pristine MOS structures. Further increase in the temperature above 300<sup>0</sup> C led to a significant increase in the leakage current which may be attributed to the observed

structural changes of HfO<sub>2</sub> thin films such as crystallization and grain agglomeration. An orderly increase in current density as a function of gamma dose indicates the pre-existence of defects followed by production of additional defects in the pristine and irradiated MOS structures. This study is essential to realize and understand the electrical performance and radiation tolerance of such devices when they are operated in high temperature and radiation harsh environments.

## 3.5. References

- [1] G. Korotchenkov, "Thin metal films". *Handbook of Gas Sensor Materials. Integrated Analytical Systems. Springer.* **2013**, 153-166.
- [2] Van der Kooi, C.J.; Elzenga, J.T.M.; Dijksterhuis, J.; Stavenga, D.G, *Journal of the Royal Society Interface*. **2016**, 14, 0933.
- [3] M. Birkholz, K.-E. Ehwald. D. Wolansky, I. Costina, C. Baristyran-Kaynak, M. Fröhlich, H. Beyer, A. Kapp, F. Lisdat, *Surf. Coat. Technol.* **2010**, 204, 2055-2059.
- [4] MacLeod, H. Angus, Thin-Film Optical Filters (4th ed.). *Taylor Francis*. **2010**, ISBN 978-1-4200-7302-7.
- [5] R. K. Nahar, Vikram Singh, Aparna Sharma, J. Mat. Sci.: Mat. In Ele. 2007, 18, 615.
- [6] M. C. Busch, A. Slaoui, P. Siffert, E. Dooryhee, M. Toulemonde, J. Appl. Phys. 1992, 71 2596.
- [7] T. P. Ma, Y. Nishioka, E. F. da Silva, "The Physics and Chemistry of SiO<sub>2</sub> and the Si-SiO<sub>2</sub> Interface", (ed. by) C. R. Helms, B. E. Deal, Plenum, New York **1988**.
- [8] Vikram Singh, N. Shashank, Dinesh Kumar, R. K. Nahar, *Rad. Eff. Def. Solids.* **2012**, 3, 204.
- [9] T. Yunogami, T. Mizutani, J. Appl. Phys. 1993, 73, 8184.
- [10] F. Belgin Ergin, Rasit Turan, Sergiu T. Shishiyanu, Ercan Yilmaz, *Nucl. Inst. and Meth. in Phys. Res. B* **2010**, 268, 1482.
- [11] A. Y. Kang, P. M. Lenahan, J. F. Conley Jr., *IEEE Trans. On Nuclear Science* **2002**, 49, 2636.

- [12] He, Zhenping; Kretzschmar, Ilona, *Langmuir* **2012**, 28, 9915-9919.
- [13] I. Adesida, A. Mahajan, E. Andideh, M. Asif Khan, D. T. Olsen, and J. N. Kuznia, *Appl. Phys. Lett.* **1993**, 63, 2777.
- [14] K. Ishii, Journal of Vacuum Science and Technology A 1989, 7, 256-258.
- [15] E. Fortunato, P. Barquinha, R. Martins, *Advanced Materials* **2012**, 24, 2945-2986.
- [16] N. Selvakumar, Barshilia, C. Harish, *Solar Energy Materials and Solar Cells* **2012**, 98, 1-23.
- [17] "Intel's Fundamental Advance in Transistor Design Extends Moore's Law, Computing Performance", Intel News Release, 2007, <a href="https://www.intel.com/pressroom/archive/releases/2007/20071111comp.htm">https://www.intel.com/pressroom/archive/releases/2007/20071111comp.htm</a>.
- [18] K. K. Hung, Y. C. Cheng, J. Appl. Phys. 1987, 62, 4204.
- [19] J. Robertson, Eur. Phys. J. Appl. Phys. **2004**, 28, 265-29.
- [20] M. Higashiwaki, H. Murakami, Y. Kumagai, A. Kuramata, *Jpn. J. Appl. Phys.* **2016**, Part 1 55, 1202A1.
- [21] Y. C. Wang, M. Hong, J. M. Kuo, J. P. Mannaerts, J. Kwo, H. S. Tsai, J. J. Krajewski, Y. K. Chen, A. Y. Cho, *IEEE Electron Device Lett.* **1999**, 20, 9, 457-459.
- R. B. Brown, B. Bernhardt, M. La Macchia, J. Abrokwah, P. N. Parakh, T. D. Basso, S. M. Gold, S. Stetson, C. R. Gauthier, D. Foster, B. Crawforth, T. K. McQuire, K. Sakallah, R. J. Lomax, T. N. Mudge, *IEEE Trans. Very Large Scale Integr. Syst.* 1998, 6, 1, 47-51.
- [23] T. Mimura, K. Odani, N. Yokoyama, Y. Nakayama, M. Fukuta, *IEEE Trans. Electron Devices* **1978**, 25, 6, 573-579.
- [24] Maciej Gutowski, John E. Jaffe, Chun-Li Liu, Matt Stoker, Rama I. Hegde, Raghaw S. Rai, Philip J. Tobin, *Applied Physics Letters* **2002**, 80, 1897.
- [25] R. Stoklas, D. Gregusova, S. Hasenohrl, E. Brytavskyi, M. Tajna, K. Frohlich, S. Hascik,J. K. Mgregor et al *Appl Surf Sci.* 2018, 461, 255-259.
- [26] Y. Wei, Q. Xu, Z. Wang, Z. Liu, F. Pan, Q. Zhang, J. Wang et al J Alloys Compd. 2018, 735, 1422-1426.

- [27] M. Y. Ho, H. Gong, G. D. Wilk, B. W. Busch, M. L. Green, P. M. Voyles, *J Appl Phys.*2003, 93(3), 1477-1481.
- [28] J. Shim, J. A. Rivera, R. Bashir, *Nanoscale* **2013**, 5, 10887-10893.
- [29] Miyata N, Appl Phys Lett. **2018**, 113(25), 251601.
- [30] C. Zhao, G. Roebben, M. Heyns, O. Van Der Biest, *Key Engineering Materials Vols.* **2002**, 206-213, 1285-1288
- [31] M. Vargas, N. R. Murphy, C. V. Ramana, *Opt Mater (Amst)* **2014**, 37, 621-628.
- [32] Y. Wang, F. Zahid, J. Wang, H. Guo, *Phys Rev B* **2012**, 85, 224110.
- [33] M. Kopani, M. Milula, E. Pincik, H. Kobayashi, M. Takahashi et al *Appl Surf Sci* **2018**, 301, 24-27.
- [34] Halid Mulaosmanovic, Evelyn T Breyer, Stefan Dünkel, Sven Beyer, Thomas Mikolajick, Stefan Slesazeck, *Nanotechnology* **2021**, 32, 502002.
- [35] Yong-Bin Kim, *Trans. Electr. Electron. Mater.* **2010**, 11(3) 93.
- [36] A. Y. Kang, P. M. Lenahan, J. F. Conley, *IEEE T Nucl Sci* **2002**, 49, 2636-2642.
- [37] C, Z. Zhao, S. Taylor, M. Werner, P. R. Chalker, R. J. Potter, J. M. Gaskell, A. C. Jones, *J Vac Sci Technol B* 2009, 27, 411-415.
- [38] F. B. Ergin, R. Turan, S. T. Shishiyanu, E. Yilmaz, *Nucl Instrum Meth B* **2010**, 268, 1482-1485.
- [39] J. M. Rafi, M. B. Gonzalez, K. Takakura, I. Tsunoda, M. Yoneoka, O. Beldarrain, M. Zabala, *Solid State Electron* **2013**, 89, 198-206.
- [40] Y. F. Mu, C. Z. Zhao, Y. F. Qi, S. Lam, C. Zhao, Q. F. Lu, Y. T. Cai, I. Z. Mitrovic,
   S. Taylor, P. R. Chalker, *Nucl Instrum Meth B* 2016, 372, 14-28.
- [41] Y. F. Mu, C. Z. Zhao, Q. F. Lu, C. Zhao, Y. F. Qi, S. Lam, I. Z. Mitrovic, S. Taylor,P. R. Chalker, *IEEE T Nucl Sci* 2017, 64, 673-682.

- [42] X. Liu, Y. Q. Lei, Y. H. Cheng, 2016 Joint IEEE International Symposium on the Applications of Ferroelectrics, European Conference on Application of Polar Dielectrics and Piezoelectric Force Microscopy Workshop 2016.
- [43] S. Maurya, *J Mater Sci-Mater El.* **2016**, 27, 12796-12802.
- [44] J. T. Ryan, P. A. Lenahan, A. Y. Kang, J. F. Conley, G. Bersuker, P. Lysaght, *IEEE T Nucl Sci.* **2005**, 52, 2272-2275.
- [45] C. Liang, Y. Su, E. X. Zhang, K. Ni, M. L. Alles, R. D. Schrimpf, D. M. Fleetwood, S. J. Koester, *IEEE T Nucl Sci.* **2017**, 64, 170-175.
- [46] G. Lucovsky, D. M. Fleetwood, S. Lee, H. Seo, R. D. Schrimpf, J. A. Felix, J. Luning, L.
  B. Fleming, M. Ulrich, D. E. Aspnes, *IEEE T Nucl Sci.* 2006, 53, 3644-3648.
- [47] N. Manikanthababu, N. Arun, M. Dhanunjaya, S.V.S. Nageswara Rao, A. P. Pathak, *Rad. Eff. and Def. in Sol.* **2016**, 171, 77-86.
- [48] Holt, Joshua, Cady, Nathaniel, Yang-Scharlotta, Jean, *IEEE*, *IIRW Final Report* **2015**, 978-1-4673-8.
- [49] M. Laya Krishnan, V. V. Ravi Kanth Kumar, Journal of Luminescence 2020, 217, 116745.
- [50] M. Dhanunjaya, N. Manikanthababu, A. P. Pathak, S. V. S. Nageswara Rao, *AIP Conference Proceedings* **2016**, 1731, 080071.
- [51] A. Y. Kang, P. M. Lenahan, J. F. Conley, Jr. IEEE Trans. Nucl. Sci. 2002, 49(6), 2636-2642.
- [52] Debaleen Biswas, Manavendra Narayan Singh, Anil Kumar Sinha, Satyaranjan Bhattacharyya, Supratic Chakraborty, *J. Vac. Sci. Technol. B* **2016**, 34, 022201.

# Effects of Swift Heavy Ion (SHI) irradiation on the structural and electrical properties of HfO<sub>2</sub> thin-films deposited on GaAs

This chapter provides a brief report on the SHI irradiation induced effects on grain agglomeration and introduction of crystalline phases in otherwise amorphous HfO2 thin films deposited on GaAs substrates. These modifications in the films due to Swift Heavy Ion (SHI) irradiation were observed by performing Field Emission Scanning Electron Microscope (FESEM), Rutherford Backscattering Spectroscopy (RBS) technique, Photoluminescence (PL), X-Ray Reflectivity (XRR) and Grazing Incident X-Ray Diffraction (GIXRD) measurements. An orderly increase in the size of spherical grains and increase in the roughness of the films have been noticed. As-grown HfO2 thin films exhibit amorphous nature. Ion irradiation has introduced monoclinic and tetragonal phases in otherwise amorphous thin films of HfO2. Further, Au/HfO2/GaAs based MOS structures have been fabricated to study the effects of SHI irradiation on the electrical properties of these devices. The leakage current conduction through the gate oxide has been studied using the Poole-Frenkel and Fowler-Nordheim tunneling mechanisms by examining the leakage current—voltage characteristics.

### 4.1. Introduction

As discussed in previous chapters, microelectronics has undergone enormous development with an increasing performance of integrated circuits. Particularly in modern CMOS technology, the down-scaling of transistor size leads to an exponential increase in the number of transistors on a chip to follow the law predicted in 1960's by the Intel co-founder Gorden E. Moore [1, 2]. In standard Silicon CMOS technology, if the thickness of a typical SiO<sub>2</sub> gate oxide layer decreases below the tunneling limit, leakage current increases enormously, which leads to heat generation and more power consumption [3, 4]. For every 0.2 nm reduction of SiO<sub>2</sub> layer thickness, the tunneling current increases by around one order of magnitude [5]. To avoid the leakage current due to tunneling, thicker gate oxide layers are mandatory. As the oxide layer becomes thicker, the electrical characteristics of a transistor have to be maintained by introducing new gate oxide materials which have advanced dielectric constant (k) as it is directly proportional to the capacitance density (C/A), whereas capacitance density is inversely proportional to the dielectric layer thickness. SiO<sub>2</sub> has been replaced by HfO<sub>2</sub> (dielectric constant 18-25 and band gap 5.8 eV) as the gate oxide in some advanced CMOS transistors by Intel in 2007 [6]. It is important to note that, in Silicon CMOS technology, use of Si as the standard semiconductor was encouraged because it has outstanding interface properties with the dielectric SiO<sub>2</sub> [7]. However, in the microelectronics community, standard gate oxide SiO<sub>2</sub> has been replaced by HfO<sub>2</sub>. For further device scaling, it is presently followed by an attempt to replace the Si with superior high mobility semiconductors. Among them, III-V and III-VI compound semiconductors, such as GaAs, GaN, InAs, GaSb, InAlAs and Ga<sub>2</sub>O<sub>3</sub> can achieve the proposed MOS devices with high-performance characteristics [8, 9]. Among these compound semiconductors, GaAs attracted maximum attention in recent years due to its higher electron mobility. The electron mobility of GaAs is around six times greater than that of Si, which makes it an attractive substrate for the future high-speed applications in CMOS devices [10].

It is well known that Swift Heavy Ion (SHI) irradiation can be used for the synthesis and characterization and modification of materials in the nanometer region due to its spatial selectivity [11-13]. This technique is more useful because of good control of irradiation fluence and energy of incident ions. At lower energies (< 0.5 MeV/u), nuclear energy loss (energy transfers to atomic nuclei) dominates, which leads to shift of target atoms via elastic scattering. For higher (> 0.5

MeV/u) energies, the electronic energy loss dominates, which leads to local ionization that can cause track formation [14] and damage production [15] in the target material. The ion tracks with nanometer diameters formed due to SHI irradiation have been used in a wide range of nanoscience applications [16, 17]. In the process of SHI irradiation, when an ion passes through the target material, it deposits a very huge amount of energy to the target atoms in the form of electronic and nuclear energy losses, which results in inter-diffusion/inter-mixing at the interface [18, 19]. Phase transformation and diffusion of the target material due to heavy ion irradiation on different materials has been studied extensively in the last few years [20-22]. Ion beam irradiation studies revealed the existence of both electron and hole traps in HfO<sub>2</sub> thin films, whereas in SiO<sub>2</sub> only electron traps were seen [23, 24]. Previous reports suggest that, SHI induced phase transformation of HfO<sub>2</sub> depends on the primary phase [25, 26]. Amorphous HfO<sub>2</sub> films were transformed into monoclinic, whereas initially monoclinic HfO<sub>2</sub> films were transformed into tetragonal phase after irradiation [27, 28]. Furthermore, the performance of HfO<sub>2</sub>/Si based MOS capacitors can be improved by SHI irradiation via reduction in the tunneling current up-to the critical fluence (i.e. track overlap fluence) and above this critical fluence the leakage current density increases resulting in failure of the device [29-31]. The energy deposited in the target material via electronic and nuclear energy losses due to SHI irradiation results in Crystallization, grain agglomeration and intermixing at the interface of target materials. Therefore, it is significant to realize and understand the SHI irradiation effects on the surface morphology, crystallization and ion induced defect creation in HfO<sub>2</sub> films. These HfO<sub>2</sub>/GaAs based MOS structures are expected to be used in many devices in space and medical applications such as radiological treatment equipment and physics experiments associated with high energy such as nuclear power plants. Therefore the SHI irradiation response studies of these MOS structures on their electrical characteristics will be worthwhile.

In this chapter, HfO<sub>2</sub> thin films (~ 30 nm) synthesized on GaAs were irradiated by 120 MeV Ag ions. SHI irradiation induced effects on grain agglomeration and introduction of crystalline phases in otherwise amorphous HfO<sub>2</sub> thin films will be discussed. Further, Au/HfO<sub>2</sub>/GaAs based MOS structures have been fabricated to study the effects of SHI irradiation on the electrical properties of these devices. The leakage current conduction through the gate oxide has been studied using the Poole-Frenkel and Fowler-Nordheim tunneling mechanisms by examining the leakage current–voltage characteristics.

# 4.2. Experimental Methods

**4.2.1. Synthesis of HfO<sub>2</sub> thin films:** HfO<sub>2</sub> thin films of 30 nm thickness were deposited on Semi-Insulating (un-doped) GaAs (100) substrates by using RF magnetron sputtering (13.6 MHz) method. Before the deposition, GaAs substrates were cut into pieces of 1 cm x 1 cm each and cleaned using an ultra-sonication process by dipping in acetone followed by isopropanol and deionized water for 5 min each. Then, these were dried with nitrogen gas and immediately loaded into the chamber. The optimized distance of 125 mm between HfO<sub>2</sub> target and GaAs substrates was maintained and RF power of 60 W was applied to the HfO<sub>2</sub> target during the deposition. When the pressure inside the chamber reached to 2.48 x 10<sup>-6</sup> mbar, 30 SCCM of argon gas was released and the deposition pressure of 2.14 x 10<sup>-2</sup> mbar was recorded.

**4.2.2. SHI irradiation:** These samples of structure HfO<sub>2</sub>/GaAs were then subjected to SHI irradiation with 120 MeV Ag ions using a Pelletron accelerator (15 UD tandem) at Inter University Accelerator Centre (IUAC), New Delhi, India. The projected range, S<sub>e</sub> - electronic energy loss and S<sub>n</sub> - nuclear energy loss of 120 MeV Ag ions in HfO<sub>2</sub> (density 9.68 g/cm<sup>3</sup>) film were estimated as 8.5 μm, 24.9 keV/nm and 0.14 keV/nm correspondingly. A standard and familiar SRIM software was used for estimation of these parameters [32]. To avoid the local heating and to achieve uniform irradiation, a continuous and low ion beam current of 0.5 particle nano-Ampere (pnA) was used and scanned over the sample area of 1 cm x 1 cm. The time of irradiation required to achieve the fluence has been calculated by using the following equation 4.1.

$$Time (sec) = \frac{Flunce \left(\frac{ions}{cm^2}\right) X Area (cm^2)}{6.25 X 10^{12} X Beam current (pnA)}$$
(4.1)

By varying the pre calculated time of irradiation, the ion fluence ranging from  $1 \times 10^{12}$  ions/cm<sup>2</sup> to  $1 \times 10^{14}$  ions/cm<sup>2</sup> was achieved and the details are given in Table 4.1.

| Sample Name | Irradiation<br>Fluence  | Energy<br>of Ion | Average stopping power in HfO <sub>2</sub> film (~ 30 nm) |             |
|-------------|-------------------------|------------------|---|-------------|
|             | (ions/cm <sup>2</sup> ) | (MeV)            | $\mathbf{S}_{\mathbf{e}}$                                 | Sn          |
| HGP         | Pristine                |                  |   |             |
| HG1E12      | 1 x 10 <sup>12</sup>    |                  |   |             |
| HG5E12      | $5 \times 10^{12}$      | 120 MeV          | 24.9 keV/nm   | 0.14 keV/nm |
| HG1E13      | 1 x 10 <sup>13</sup>    | Ag               |   |             |
| HG5E13      | 5 x 10 <sup>13</sup>    |                  |   |             |
| HG1E14      | 1 x 10 <sup>14</sup>    |                  |   |             |

Table 4.1: Sample Name, energy of ion used in irradiation and SRIM Calculation details.

**4.2.3. Sample Characterization:** The effects of irradiation on these films were studied by employing different characterization techniques to study the impact of SHI irradiation. Rutherford backscattering spectroscopy (RBS) measurements (using 2 MeV He<sup>2+</sup> ions at 165° of scattering angle at IUAC, New Delhi, India) have been performed on these samples to estimate the thickness and elemental composition of different layers. Diffusion/inter-mixing of layers at the interfaces has also been studied using RBS spectra. The acquired RBS spectra were simulated using SIMNRA-7.01 software. Furthermore, the thickness of the as-grown sample was estimated by cross-sectional Field Emission Scanning Electron Microscope (FESEM) and Ambios XP 200 Profilometer. Surface morphology and evolved grains after irradiation were studied by the measurements of a FESEM (using Carl ZEISS, FEG, ultra-55 at the University of Hyderabad). Grazing incident x-ray diffraction (GIXRD) measurements were performed on as-grown and irradiated HfO<sub>2</sub> films using Bruker D8 Advance diffractometer with Cu K $\alpha$ ,  $\lambda$  = 1.54 Å. The X-Ray Reflectivity (XRR) measurements were performed to study the film roughness. Defect dynamics of pristine and irradiated HfO<sub>2</sub> thin films were studied by performing Photoluminescence (PL) measurements (model: Fluorolog with Xenon lamp of 450 W and resolution of 0.3 nm).

**4.2.4. Fabrication and characterization of MOS structures:** Au/HfO<sub>2</sub>/GaAs based MOS structures were fabricated by depositing top and bottom contacts to perform electrical measurements. Metal contacts of Au were deposited (~ 100 nm thick and 1 mm in diameter using a shadow mask) as top electrode (TE). Adhesive and conductive Ag paste along with Al foil was used as a bottom electrode (BE). These two interfaces, TE/HfO<sub>2</sub> (metal/oxide) and GaAs/BE (semiconductor/metal) are expected to behave in the same manner for all the devices. The schematics of 120 MeV ion irradiation and fabrication of Au/HfO<sub>2</sub>/GaAs based MOS structures are shown in Fig. 4.1. Electrical characterizations such as Leakage current – Voltage (I-V) in voltage range from -5 V to 5 V were performed to evaluate the effects of SHI irradiation on the electrical characteristics of these MOS structures. These electrical measurements were performed using an Agilent technologies-B1500A semiconductor device analyzer at Centre for Nanotechnology (CFN), University of Hyderabad.

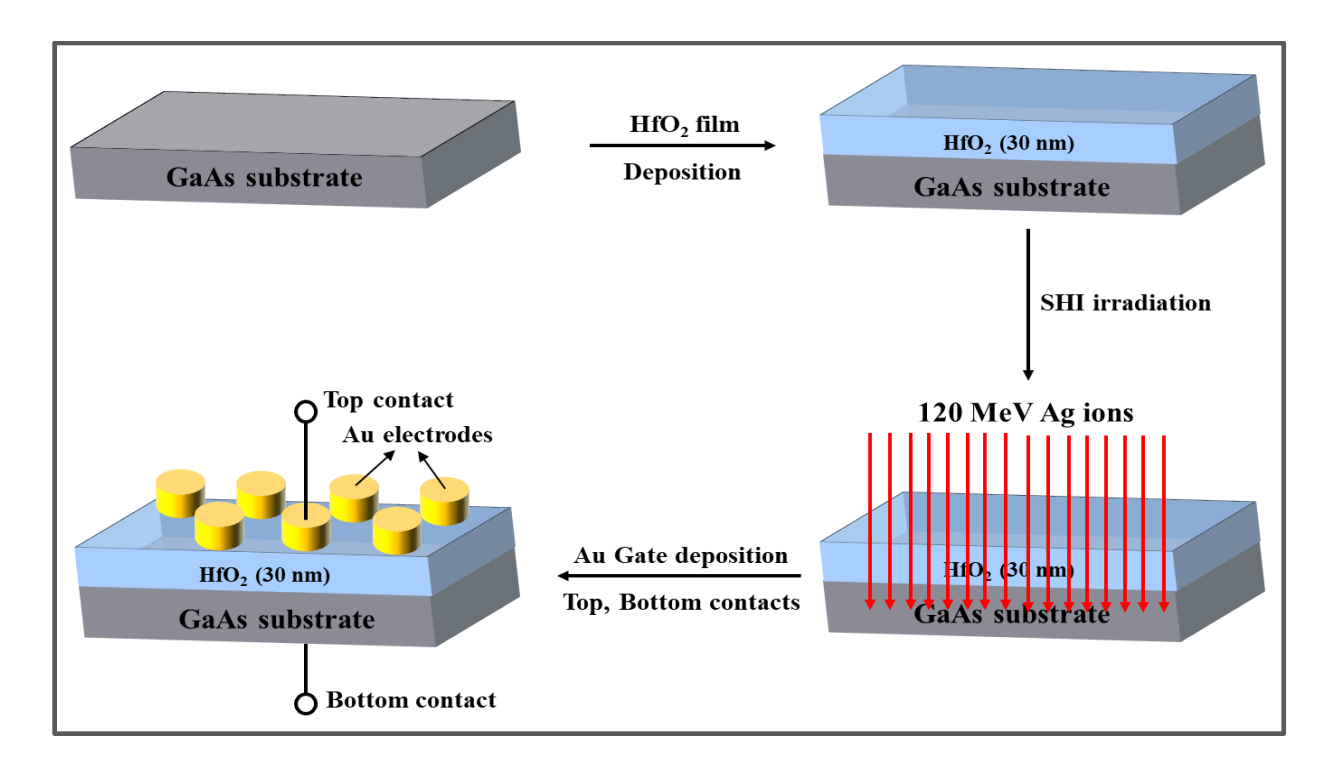


Fig. 4.1: Schematic representation of SHI irradiation and fabrication of MOS structures.

### 4.3. Results and discussions

**4.3.1.** Characterization of thickness and stoichiometry of pristine thin films: The Pristine and SHI-irradiated HfO<sub>2</sub> thin films deposited by the RF magnetron sputtering technique were examined by different characterization methods to study the impact of SHI irradiation. Primarily, the thickness of as-grown HfO<sub>2</sub> film was estimated by cross sectional FESEM and Profilometer measurements as shown in Fig. 4.2(a-b). The estimated thickness of as-grown HfO<sub>2</sub> film using cross sectional FESEM and Profilometer measurements were found to be as 32 nm and 35 nm respectively.

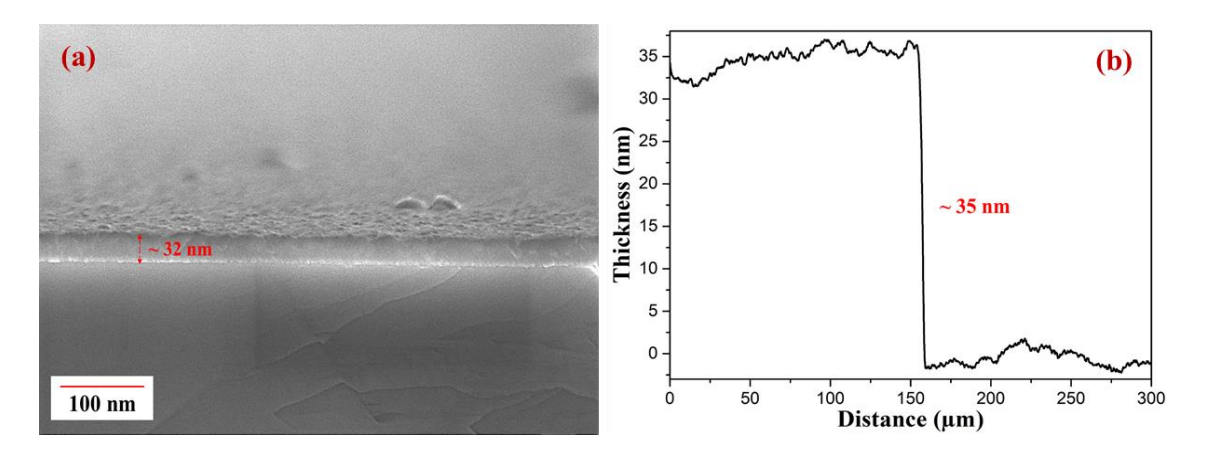


Fig. 4.2: Estimation of as-grown HfO<sub>2</sub> film thickness using (a) cross sectional FESEM and (b) Profilometer measurements.

Further, the film thickness and elemental compositions of the as deposited HfO<sub>2</sub> film have been estimated by performing RBS measurements. The RBS spectrum with SIMNRA simulation is shown in Fig. 4.3.

The values of Calibration offset and Energy per channel were obtained from a standard calibration of sample (Au/glass). The values of Calibration offset and Energy per channel as 73.63 keV and 0.989 keV/ch respectively were used for SIMNRA simulation. The thickness of HfO<sub>2</sub> thin film was estimated using the simulation and found to be around 42 nm with the stoichiometry of around 36% Hf and 64% O. To estimate HfO<sub>2</sub> film thickness and stoichiometry from the fitting curve using SIMNRA simulation, bulk density corresponding to HfO<sub>2</sub> as 9.68 g/cm<sup>3</sup> has been considered.

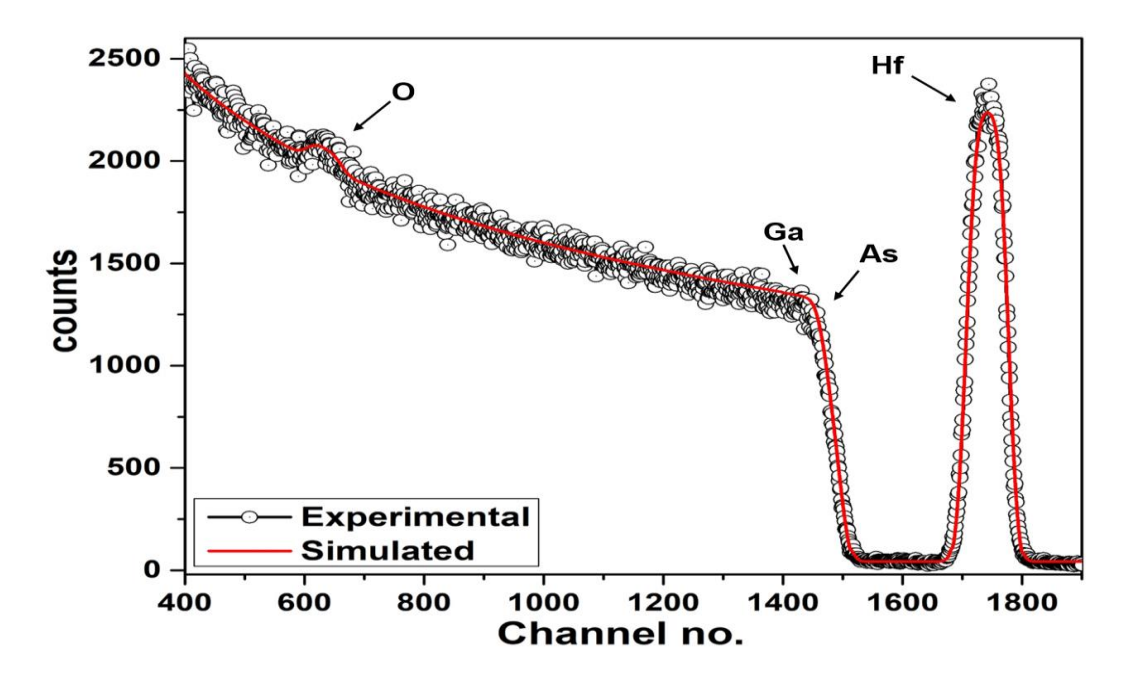


Fig. 4.3: RBS spectrum of as-grown HfO<sub>2</sub> thin film deposited on GaAs with SIMNRA simulation.

# 4.3.2. Impact of SHI irradiation

The motivation of the present work is to elucidate the electronic energy loss effects due to SHI irradiation on the grain structure and crystallization of the target material and consequent effects on the electrical properties of HfO<sub>2</sub> thin films. In HfO<sub>2</sub>, the critical value of S<sub>e</sub> for development of ion tracks is around 20 keV/nm [27]. Here, we have used 120 MeV Ag ion beam such that the electronic energy loss (24.9 keV/nm) dominates nuclear energy loss (0.14 keV/nm) in HfO<sub>2</sub> and 0.5 pnA ion beam current to maintain uniform energy deposition throughout the film with minimal local heating effects.

a) Surface structure and Grain agglomeration: The structure, morphology of HfO<sub>2</sub> film surfaces and SHI induced grain agglomeration were studied using the FESEM measurements. The FESEM images of the pristine and SHI-irradiated HfO<sub>2</sub> thin films synthesized on GaAs are shown in Fig. 4.4(a-f). As-deposited HfO<sub>2</sub> thin film consists of a smooth surface with uniform HfO<sub>2</sub> grains. From FESEM images, it is observed that with increasing radiation fluence, the structure and size of the HfO<sub>2</sub> grains have been modified. As-deposited HfO<sub>2</sub> film consists of a smooth surface with uniformly small grains. As the SHI irradiation fluence increases, the small grains start growing, which leads to the development of new grain boundaries with increasing grain size. Thus, the irradiated films consist of uniform spherical grains with increased size. This increase in the

size of grains with increasing ion irradiation may be attributed to the possible agglomeration of grains within the affected area.

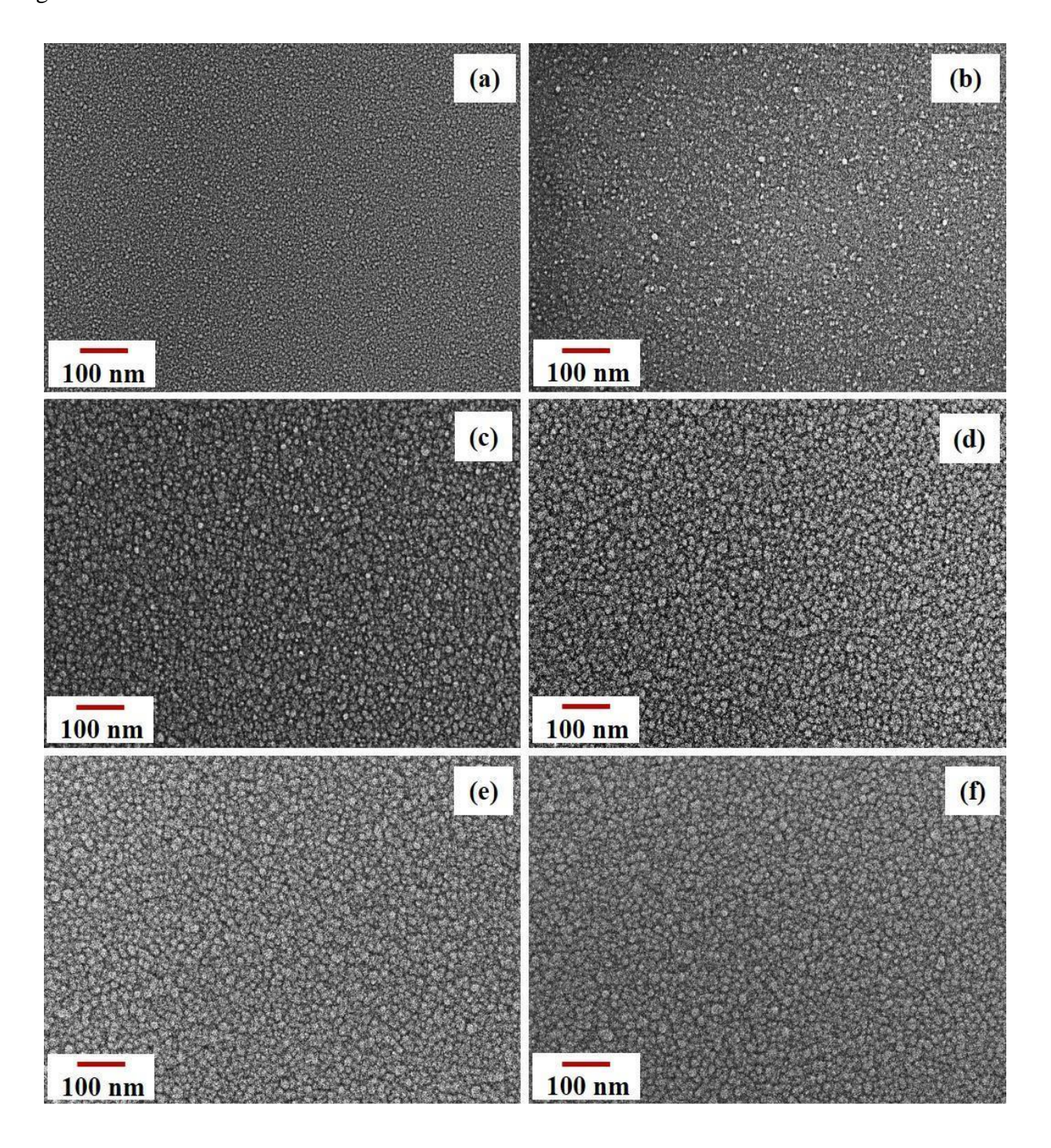


Fig. 4.4: FESEM images of as-grown and SHI-irradiated  $HfO_2$  thin films as a function of fluence. (a) Pristine, (b)  $1x10^{12}$  ions/cm<sup>2</sup>, (c)  $5x10^{12}$  ions/cm<sup>2</sup>,

(d)  $1x10^{13}$  ions/cm<sup>2</sup>, (e)  $5x10^{13}$  ions/cm<sup>2</sup> and (f)  $1x10^{14}$  ions/cm<sup>2</sup>.

The diameters of the as-grown and the modified grains due to irradiation were calculated and the average diameter as a function of irradiation dose were estimated by Gauss fittings. The graphical representation with Gauss fit is presented in Fig. 4.5(a-f).

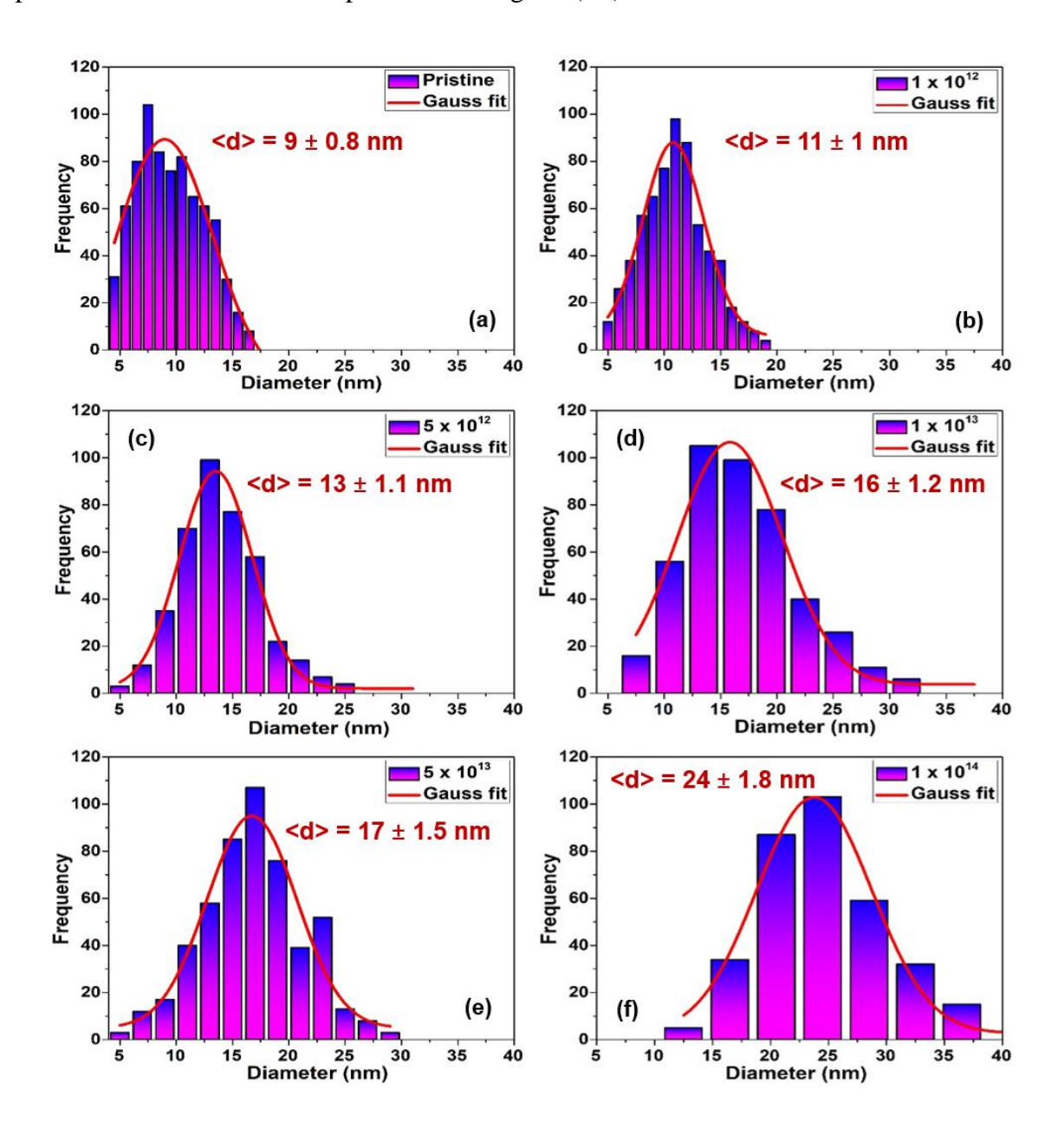


Fig. 4.5: Size distribution of HfO<sub>2</sub> grains as a function of ion irradiation fluence (a) Pristine, (b)  $1x10^{12}$  ions/cm<sup>2</sup>, (c)  $5x10^{12}$  ions/cm<sup>2</sup>, (d)  $1x10^{13}$  ions/cm<sup>2</sup>, (e)  $5x10^{13}$  ions/cm<sup>2</sup> and (f)  $1x10^{14}$  ions/cm<sup>2</sup>.

As-deposited HfO<sub>2</sub> thin films have the grains of average diameter 9 nm. At the irradiation fluence of  $1 \times 10^{12}$  ions/cm<sup>2</sup>, the grains started growing and the average diameter increased to 11 nm. Upon increasing the ion irradiation fluence to  $5 \times 10^{12}$ ,  $1 \times 10^{13}$  and  $5 \times 10^{13}$  ions/cm<sup>2</sup>, the grains further grew in size and the average diameters increased to 13 nm, 16 nm and 17 nm. At the topmost fluence of  $1 \times 10^{14}$  ions/cm<sup>2</sup>, the grains further increase in size and the average diameter increases to 24 nm. This increase in the size of grains with increasing ion irradiation may be attributed to the possible agglomeration of grains within the affected area due to ion induced diffusion. Therefore due to the SHI irradiation, the grains were agglomerated and their average diameters have been increased from 9 nm to 24 nm. Thus, due to SHI irradiation, the average grain size increases to almost 2.5 times, when compared to that of pristine film.

b) SHI irradiation induced phase transformations: The energy deposited through electronic energy loss by SHI leads to the structural phase transformation in HfO<sub>2</sub> thin films. GIXRD measurements were performed on all these samples and the diffraction patterns of as-deposited and irradiated HfO<sub>2</sub> thin films are shown in Fig. 4.6. As-grown HfO<sub>2</sub> thin films exhibit amorphous nature whereas the irradiated films consist of nano-crystallites which confirm the introduction of crystalline phases. Up to the fluence of 5 x 10<sup>12</sup> ions/cm<sup>2</sup>, the film remains in an amorphous phase. At the radiation fluence of 1 x 10<sup>13</sup> ions/cm<sup>2</sup>, evolution of peaks corresponding to the (110), (-111), (111), (200) and (102) crystal planes have been observed. Upon increasing the fluence to 5 x 10<sup>13</sup> ions/cm<sup>2</sup>, a new peak corresponding to the (002) plane, in addition to the above mentioned planes, has been observed. It is confirmed that the newly introduced planes correspond to the monoclinic HfO<sub>2</sub> using typical JCPDS file (PDF#06-0318). At the maximum fluence of 1 x 10<sup>14</sup> ions/cm<sup>2</sup>, in addition to above mentioned planes, new crystal plane (011) corresponding to monoclinic HfO<sub>2</sub> and crystal planes (110), (101) corresponding to tetragonal phase of HfO<sub>2</sub> confirmed by standard JCPDS file (PDF#00-008-0342) have been observed. In HfO<sub>2</sub>, the critical value of Set for introduction of monoclinic phases in otherwise amorphous HfO2 thin films is around 20 keV/nm [27]. In the present study, the electronic energy loss (24.9 keV/nm) of 120 MeV Ag ion is greater than Set. Hence, SHI induced evolution of crystalline phases such as monoclinic phase at lower irradiation fluence and tetragonal phase at higher irradiation fluence may be possible by subjecting the amorphous HfO<sub>2</sub> thin films to 120 MeV Ag ion irradiation. In previous reports, amorphous HfO<sub>2</sub> films synthesized on Si and quartz were subjected to 100 MeV Ag ion irradiation. Monoclinic phase was introduced below the fluence of 5 x 10<sup>13</sup> ions/cm<sup>2</sup>, whereas the tetragonal phase was introduced in initially monoclinic  $HfO_2$  films after the irradiation fluence of 1 x  $10^{14}$  ions/cm<sup>2</sup> [27, 28]. In the present study, it is observed that, starting with the amorphous phase, introduction of monoclinic phase up to the irradiation fluence of 5 x  $10^{13}$  ions/cm<sup>2</sup> takes place. Then at the highest irradiation fluence of 1 x  $10^{14}$  ions/cm<sup>2</sup>, in addition to the monoclinic phase, evolution of the tetragonal phase of  $HfO_2$  (mixed phase) has also been observed. These results are consistent with the previous reports on the SHI induced phase transformations in  $HfO_2$  [25-28] and yet both the monoclinic and tetragonal phases are observed in films that are subjected to high fluence. Further, this study also examines the electrical properties of the films that were subjected to high fluence.

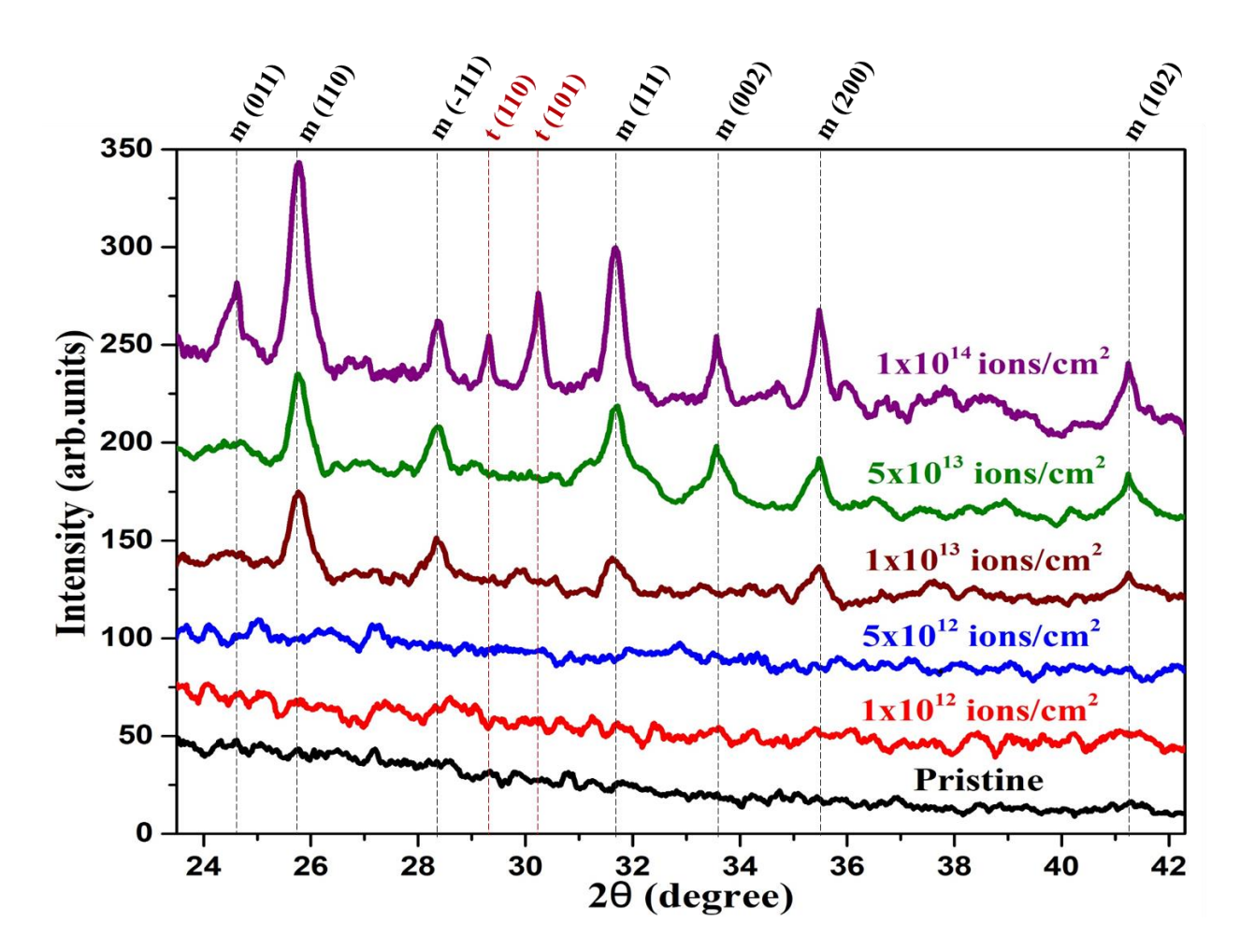


Fig. 4.6: GIXRD patterns of as-grown and SHI irradiated HfO<sub>2</sub> thin films as a function of irradiation fluence (dashed lines direct the peak positions of the crystal planes corresponds to monoclinic (m) and tetragonal (t) phases of HfO<sub>2</sub>).

HfO<sub>2</sub> is mainly known to exist in three crystallographic phases at ambient pressure depending on the temperature. It exists in monoclinic phase (m-HfO<sub>2</sub>) in the temperature range of room temperature (RT) to 1700<sup>o</sup> C, transforms to tetragonal (t-HfO<sub>2</sub>) at higher temperatures greater than 1700° C and at very high temperatures greater than 2600° C, it becomes cubic (c-HfO<sub>2</sub>). Zhao and Vanderbilt [33] predicted  $k \sim 18$  for m-HfO<sub>2</sub>,  $k \sim 70$  for t-HfO<sub>2</sub> and  $k \sim 29$  for c-HfO<sub>2</sub> using density functional theory calculations. The bandgap of the t-HfO<sub>2</sub> is also found to be larger (6.11 eV) than that of m-HfO<sub>2</sub> (5.78 eV) [34]. Furthermore, the t-HfO<sub>2</sub> is denser and has a higher Knoop hardness [35]. Pavel Ondracka et al. [36] reported that the density of HfO<sub>2</sub> changes when it undergoes phase transformations. The density of HfO<sub>2</sub> increases when it transforms from amorphous to crystalline phases i.e. monoclinic, tetragonal and cubic. C. E. Curtis et al. [37] reported that, when HfO<sub>2</sub> transforms from monoclinic to tetragonal phase, the density of tetragonal HfO<sub>2</sub> increases by 3.4% over that of monoclinic HfO<sub>2</sub>. Therefore, the t-HfO<sub>2</sub> is expected to be better over the thermodynamically stable m-HfO<sub>2</sub> in many applications, including electronic devices, wherever HfO<sub>2</sub> is used. The transformations of tetragonal and cubic phases cannot be retained at RT even with the use of ultrafast quenching, due to their lower free surface energies [38]. At RT, HfO<sub>2</sub> in monoclinic phase is considered as utmost stable. In some reports, it is suggested that the stabilization of t-HfO<sub>2</sub> and c-HfO<sub>2</sub> phases can also be achieved by doping with various materials like Si, Y, Eu and Fe [39-41]. On the other hand, doping can affect the essential properties of pure HfO<sub>2</sub> such as binding energy, bond length and most importantly dielectric properties. Thus, it is very important to develop a new facile method such as ion beam irradiation to obtain t-HfO2 and c-HfO<sub>2</sub> at low temperatures without affecting its essential properties.

c) SHI irradiation induced defect dynamics: Ion beam irradiation technique is known to crystallize the high-k dielectric material in the nm region by raising its temperature up to melting point. The defects (O-vacancies) that are created through the irradiation, generate strain fields in the target material and this generated strain field is responsible for the phase transformations in high-k dielectrics [42]. PL measurements were performed to study the defect (O-vacancies) dynamics in HfO<sub>2</sub> thin films (as-deposited and ion irradiated) and the spectra are shown in Fig. 4.7 (a-f) and the assignment of defects related to various types of O-vacancies are shown in Table 4.2. The excitation energy of 3.5 eV was used such that the excitation energy is much lower than the bandgap of HfO<sub>2</sub>. Therefore, the detected PL within the range of excitation energy is mainly due to the transition from defect/mid-bandgap states.

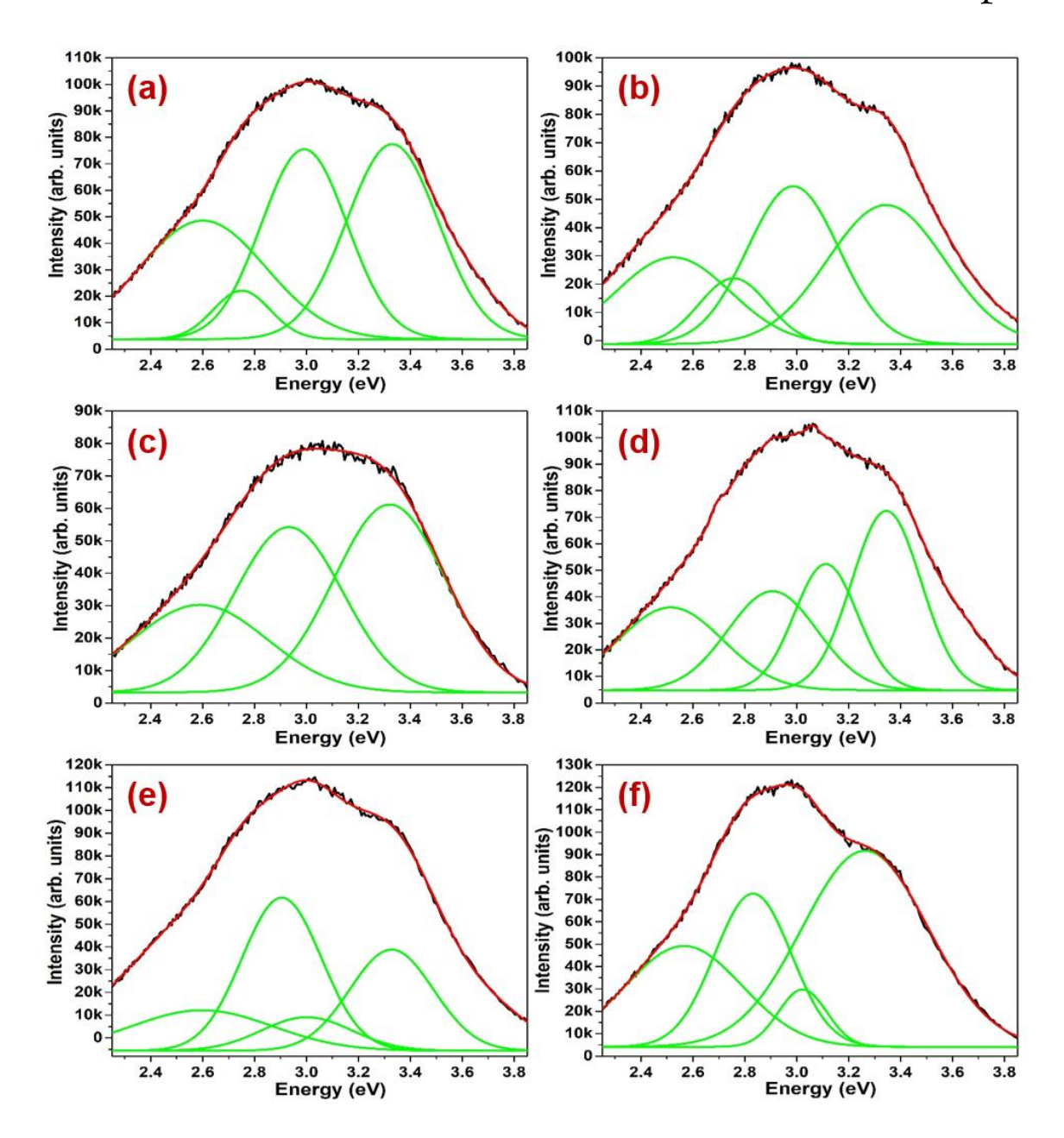


Fig. 4.7: PL spectra of pristine and SHI irradiated HfO<sub>2</sub> thin films synthesized on GaAs

(a) Pristine, (b) 1x10<sup>12</sup> ions/cm<sup>2</sup>, (c) 5x10<sup>12</sup> ions/cm<sup>2</sup>,

(d) 1x10<sup>13</sup> ions/cm<sup>2</sup>, (e) 5x10<sup>13</sup> ions/cm<sup>2</sup> and (f) 1x10<sup>14</sup> ions/cm<sup>2</sup>.

The PL spectra of as-grown film has shown a broad peak which is de-convoluted as a combination of multiple peaks corresponding to 2.5 eV, 2.7 eV, 2.9 eV and 3.3 eV using peak fitting. The observed PL peaks are attributed to the defect states related to O-vacancies in HfO<sub>2</sub> thin films [27, 28, 43, 44]. Wen et al. [43] stated that the PL peak positions at 2.7 and 2.9 eV correspond to the

positively charged O-vacancy states known as Vo<sup>2+</sup> and Vo<sup>+</sup> respectively. The de-convoluted PL peak around 3.3 eV corresponds to Vo [44].

| Irradiation dose                        | PL peak positions | Defect assignment  | Intensity (%) |
|---|-------------------|--------------------|---------------|
| Pristine                                | 2.5 eV            | -                  | 27%           |
|   | 2.7 eV            | $\mathrm{Vo}^{2+}$ | 6%            |
|   | 2.9 eV            | $\mathrm{Vo}^+$    | 32%           |
|   | 3.3 eV            | Vo                 | 35%           |
| 1x10 <sup>12</sup> ions/cm <sup>2</sup> | 2.5 eV            | -                  | 22%           |
|   | 2.7 eV            | $Vo^{2+}$          | 9%            |
|   | 2.9 eV            | $Vo^+$             | 33%           |
|   | 3.3 eV            | Vo                 | 36%           |
| 5x10 <sup>12</sup> ions/cm <sup>2</sup> | 2.5 eV            | -                  | 23%           |
|   | 2.9 eV            | $\mathrm{Vo}^+$    | 36%           |
|   | 3.3 eV            | Vo                 | 41%           |
| 1x10 <sup>13</sup> ions/cm <sup>2</sup> | 2.5 eV            | -                  | 23%           |
|   | 2.9 eV            | $\mathrm{Vo}^+$    | 24%           |
|   | 3.1 eV            | -                  | 22%           |
|   | 3.3 eV            | Vo                 | 31%           |
| 5x10 <sup>13</sup> ions/cm <sup>2</sup> | 2.5 eV            | -                  | 20%           |
|   | 2.9 eV            | $Vo^+$             | 41%           |
|   | 3.0 eV            | -                  | 10%           |
|   | 3.3 eV            | Vo                 | 29%           |
| 1x10 <sup>14</sup> ions/cm <sup>2</sup> | 2.5 eV            | -                  | 24%           |
|   | 2.9 eV            | $Vo^+$             | 23%           |
|   | 3.0 eV            | -                  | 5%            |
|   | 3.3 eV            | Vo                 | 48%           |

Table 4.2: PL peak positions and defect assignment related to O-vacancies.

After SHI irradiation, the PL peak at 2.7 eV corresponding to O-vacancy (Vo<sup>2+</sup>) has been suppressed completely. At the irradiation fluence  $5x10^{12}$  ions/cm<sup>2</sup>, a minimum number of O-vacancies with low intensity have been observed in the PL spectra which may be attributed to the SHI induced annealing of defects at lower irradiation dose. With further increase of the irradiation fluence to  $1x10^{13}$  ions/cm<sup>2</sup>, evolution of new PL peak around 3.1 eV with increased intensity has been observed which is shifted to lower energy (~ 3.0 eV) at higher fluences. This newly evolved defect peak around 3.1 eV may be associated with the charged oxygen defect state [45]. These results are consistent with the previous reports on HfO<sub>2</sub> films [27, 28, 46]. The variation in the

defect configuration related to O-vacancies and slight shift in the peak positions due to SHI irradiation indicate the generation of strain within the film which is responsible for the observed SHI induced evolution of crystalline phases in HfO<sub>2</sub> thin films. However, in present study, the c-HfO<sub>2</sub> phase has not been observed as the transformation from tetragonal phase to cubic phase is not sensitive to SHI induced strain [47].

d) SHI irradiation induced mixing and surface roughness: As mentioned earlier, in the current generation of Metal Oxide Semiconductor Field Effect Transistor (MOSFET) based devices, HfO<sub>2</sub> has already occupied the space of SiO<sub>2</sub> [7]. Therefore, it is significant to elucidate the strength of HfO<sub>2</sub> interface with different superior semiconductors. It is recognized that SiO<sub>2</sub> is highly susceptible over the Si to irradiation induced track formation. This encouraged us to understand the effects of SHI on HfO<sub>2</sub>/GaAs interface even though the SHI induced inter-mixing is observed in Si/HfO<sub>2</sub>, HfO<sub>2</sub>/GaO<sub>x</sub>/Si, HfO<sub>2</sub>/SiON/Si and HfO<sub>2</sub>/SiO<sub>2</sub>/Si interfaces [29, 30, 31, 48]. SHI irradiation can result in diffusion of elements and inter-mixing of layers across the interfaces [49, 50]. RBS spectra of pristine and SHI-irradiated samples with different fluence are shown in Fig. 4.8. Surprisingly, no significant changes in the RBS spectra were observed, within the experimental limits, in the irradiated films over pristine films.

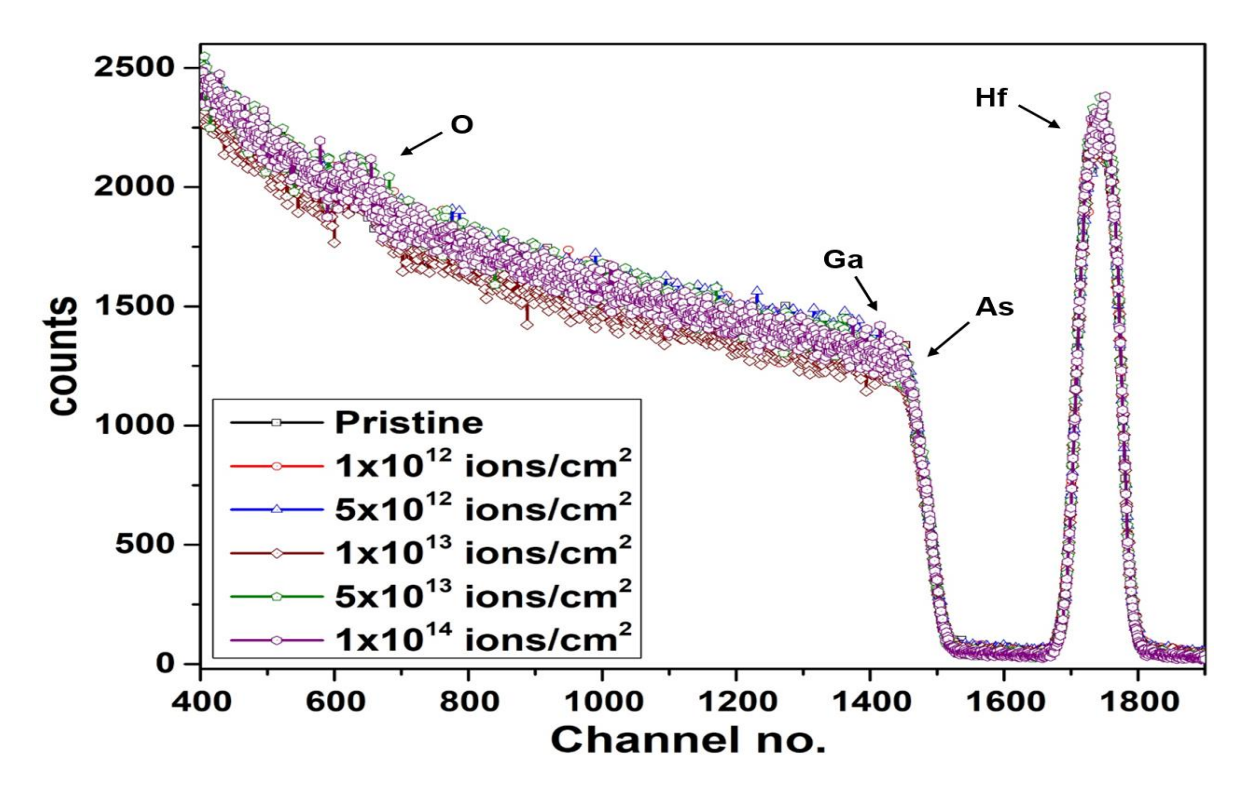


Fig. 4.8: RBS spectra of pristine and SHI-irradiated HfO<sub>2</sub> thin films as a function of fluence.

XRR measurements were performed to evaluate the SHI irradiation effects on the surface roughness of the film and XRR patterns of pristine and SHI-irradiated samples with different fluence are shown in Fig. 4.9. The appearance of clear interference fringes confirm the presence of bi-layer with a sharp interface. Decrease in the number of fringes with increasing irradiation fluence has been noticed in the XRR patterns due to the probable increase in the surface roughness of films. At the highest fluence, no fringes are observed, maybe due to the domination of film and interface roughness.

This observation can be understood based on the fact that if the electronic energy loss go beyond the threshold value, track overlap occurs. This mechanism is well known for the ion track formation, which can be attributed to local melting followed by quenching of target material within the affected area [51, 52].

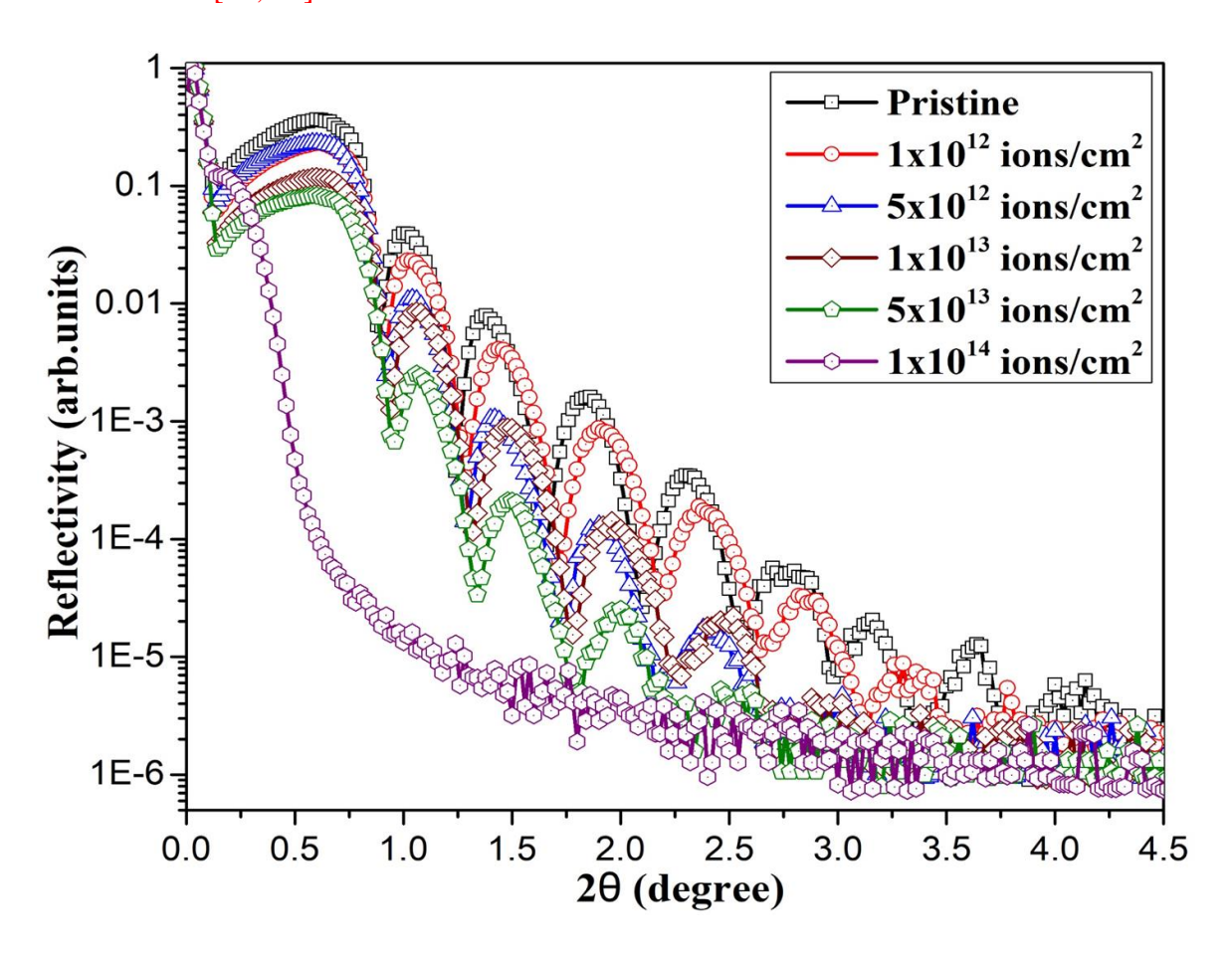


Fig. 4.9: XRR patterns of pristine and SHI irradiated HfO<sub>2</sub> thin films as a function of fluence.

e) Electrical characteristics: Au/HfO<sub>2</sub>/GaAs MOS structures were fabricated by creating top and bottom electrodes on pristine and SHI irradiated samples. The leakage current density through the gate oxide of pristine and irradiated films were studied by performing I-V measurements on the corresponding MOS structures as shown in Fig. 4.10(a). As shown in Fig. 4.10(b), the current density at applied voltage of 1 V decreases from 2.8 x 10<sup>-7</sup> A/cm<sup>2</sup> to 1.3 x 10<sup>-7</sup> A/cm<sup>2</sup> when the pristine sample is irradiated to a fluence of 1 x 10<sup>12</sup> ions/cm<sup>2</sup>. At the same applied voltage, the leakage current density has been decreased to 3.4 x 10<sup>-8</sup> A/cm<sup>2</sup> for the irradiation fluence of 5 x 10<sup>12</sup> ions/cm<sup>2</sup>. Further increasing the irradiation fluence to 1 x 10<sup>13</sup> ions/cm<sup>2</sup> and 5 x 10<sup>13</sup> ions/cm<sup>2</sup>, the leakage current density increases to 9.0 x 10<sup>-7</sup> A/cm<sup>2</sup> and 5.0 x 10<sup>-6</sup> A/cm<sup>2</sup> respectively. Upon increasing the irradiation fluence to 1 x 10<sup>14</sup> ions/cm<sup>2</sup>, it further increases to 1.5 x 10<sup>-5</sup> A/cm<sup>2</sup>.

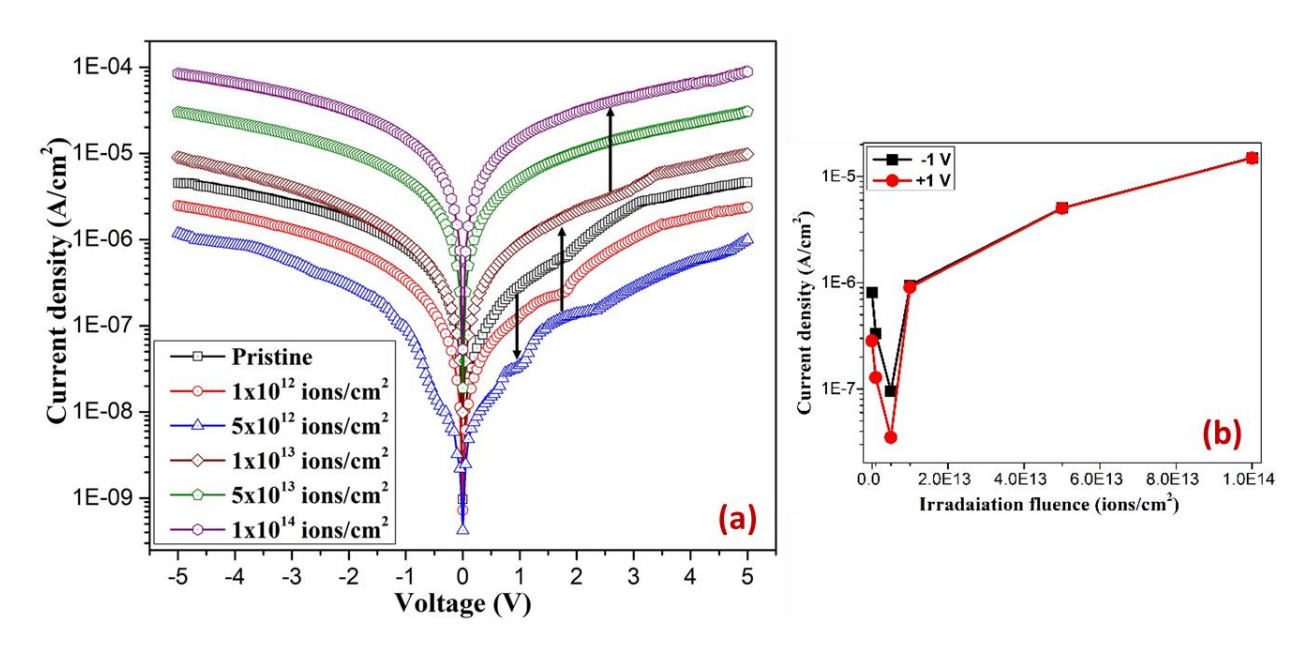


Fig. 4.10: (a) I-V characteristics of Au/HfO<sub>2</sub>/GaAs based MOS structures and (b) current density at applied voltage of  $\pm 1~V$ 

(direction of arrows shows decreasing/increasing of leakage current density).

As discussed, the ion induced structural modifications consequently cause changes in I-V curves. It is well-known that the electronic excitations produced due to SHI irradiation at lower fluences can results annealing of defects in the film [53]. It is observed that the leakage current density of MOS structure decreases for the irradiation fluences  $1 \times 10^{12}$  and  $5 \times 10^{12}$  ions/cm<sup>2</sup>. Here it is vital to note that decrease in the leakage current density means improvement in the device electrical characteristics. In this study the critical ion fluence of  $5 \times 10^{12}$  ions/cm<sup>2</sup> has been found to improve

the electrical performance of the device. An increase in the fluence above this critical value of irradiation fluence, can cause more damage creation in the film due to track overlap and formation of inter-diffusion/inter-mixing layers at the interface, leading to increase in the leakage current density which can worsen the device performance. This study indicates that the electrical characteristics of HfO<sub>2</sub>-GaAs based MOS devices can be improved by tuning the SHI irradiation fluence. Therefore the SHI irradiation response studies of these MOS structures on their electrical characteristics will be worthwhile as these MOS structures are expected to be used in many devices in radiation environments.

The charge carriers that tunnel through the gate oxide are responsible for this leakage current and can be elucidated by examining several conduction mechanisms such as Direct Tunneling (DT), Poole-Frenkel (PF) tunneling and Fowler-Nordheim (FN) tunneling [54-56]. The DT mechanism is applicable to thin-films of thickness less than ~ 6 nm [57]. However, the HfO<sub>2</sub> film thickness in this study is around 30 nm, therefore DT is not expected to be significant. Measured I-V curves with PF and FN tunneling fittings are shown in Fig. 4.11(a-b). In the figure solid lines indicate the theoretical fittings. The following equations 4.2 and 4.3 are used to fit the I-V curves with PF and FN tunneling mechanisms respectively [55, 58].

$$J_{PF} = EF_{ox}exp\left[-\frac{q\Phi - \beta\sqrt{F_{ox}}}{\xi KT}\right]$$
 (4.2)

$$J_{FN} = \frac{q^3}{16\pi^2\hbar\Phi_b} F_{ox}^2 \exp \exp \left[ -\frac{4\sqrt{2m_{ox}^*}\Phi_b^{\frac{3}{2}}}{\hbar q} \frac{1}{F_{ox}} \right]$$
(4.3)

In these equations,  $F_{ox}$  is the electric field through the dielectric layer  $HfO_2$  and  $\xi$  (value in between 1 and 2 which is constant) is the factor obtained by acceptor compensation. Other well-known constants are like Boltzmann's constant (K), Charge of electron (q), Temperature (T) and reduced Planck constant (h). Here,  $\Phi_b$  is the barrier height among the conduction bands at  $HfO_2/Si$  interface and  $m_{ox}^*$  is the effective mass of electrons in the dielectric layer  $HfO_2$ .

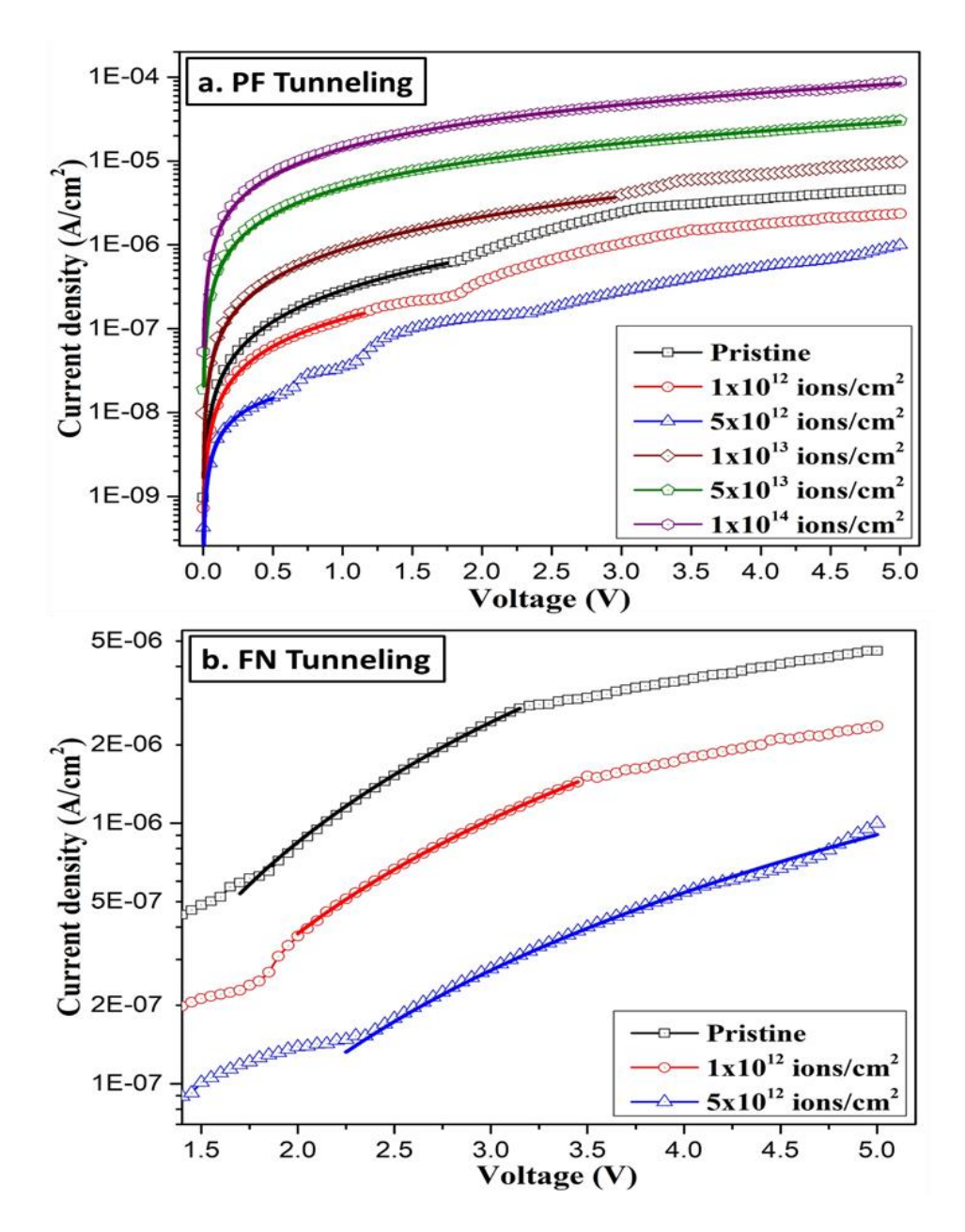


Fig. 4.11: Measured I-V curves characterized by theoretical (a) PF tunneling and (b) FN tunneling mechanisms (solid lines indicate the theoretical fittings).

The PF tunneling mechanism mostly deals with the defects or traps within the film. The I-V characteristics of pristine MOS structure follows PF tunneling up to 1.75 V, which indicates the existence of defects/traps in the as-grown sample and thereafter FN tunneling has been observed. The barrier of the gate oxide will become triangular with increase in the applied voltage and the electron can tunnel through it. This is observed at the higher voltages and governed by the FN tunneling mechanism. The PF tunneling decreases with the increasing SHI irradiation up to the

critical fluence of 5 x 10<sup>12</sup> ions/cm<sup>2</sup>, and domination of FN tunneling has been observed. This further confirms the decrease in defects/traps due to ion induced defect annealing leading to decrease in the leakage current density up to the critical fluence. Above the critical fluence, MOS structures favor PF tunneling mechanism, which is attributed to increase of traps due to SHI induced defect creation in the film because of ion induced defect creation. The corresponding traps in the band-gap can lead to the observed increase in the leakage current density that can worsen the device performance.

However, defects annealing dominates below the critical fluence, whereas defect creation dominates above the critical fluence. Hence, SHI induced defect annealing results in decrease (improvement) in the tunneling current and SHI induced defect creation results in an increase (worsen) in the tunneling current of HfO<sub>2</sub>/GaAs based MOS devices. This can be understood as two competing processes such as SHI irradiation induced defect annealing at lower irradiation fluences and defect/trap creation at higher irradiation fluences. The defect annealing is due to the inelastic collisions, which leads to excitation/ionization of atoms followed by relaxation, while defect creation is also due to inelastic collisions that lead to track formation at higher fluence [59]. Inelastic collisions can leave damage beyond a critical fluence which is above track overlap fluence. This damage including grain agglomeration and introduction of crystalline phases in HfO<sub>2</sub> may be explained by the well-known thermal spike model [25-27, 60].

In our earlier reports, SHI induced modifications of HfO<sub>2</sub> thin films are explained by using thermal spike model [27, 28]. In this model, two coupled differential equations given below are used to estimate the evolution of electronic and lattice temperatures.

$$C_e \frac{\partial T_e}{\partial t} = \frac{1}{r} \frac{\partial}{\partial r} \left[ r K_e \frac{\partial T_e}{\partial r} \right] - g (T_e - T_\alpha) + A(r, t) \tag{4.4}$$

$$C_a \frac{\partial T_a}{\partial t} = \frac{1}{r} \frac{\partial}{\partial r} \left[ r K_a \frac{\partial T_a}{\partial r} \right] \mp g (T_e - T_\alpha)$$
 (4.5)

In these equations,  $C_e$  and  $C_a$  are the electronic and atomic specific heats respectively.  $K_e$ ,  $K_a$  are the thermal conductivities.  $T_e$  and  $T_a$  are temperatures of the electronic and atomic systems. r and g are the radial distance g electron phonon coupling parameter respectively.

The outcomes of thermal spike model calculations for high-k dielectric HfO<sub>2</sub> performed by M. Dhanunjaya et al. are shown in Fig. 4.12.

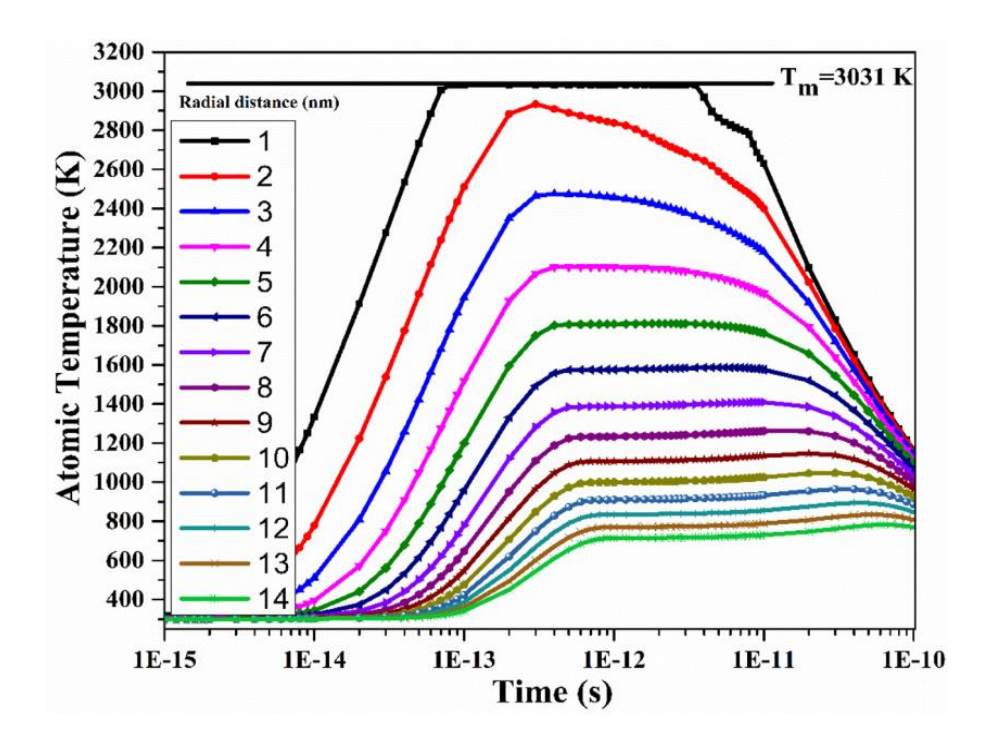


Fig. 4.12: Results of thermal spike calculations for HfO<sub>2</sub> [27].

The electronic energy loss ( $\sim$  24.9 keV/nm) deposited through 120 MeV Ag ion irradiation can increase the material up to its melting range within timescales of picosecond within the effective region. This extremely fast rise in the temperature up to the phase transition temperature results phase transformations. The observed SHI irradiation induced crystallization (evolution of monoclinic and tetragonal phases) indicates this rise in the temperature at the highest fluence  $(1x10^{14} \text{ ions/cm}^2)$  is equivalent to the tetragonal phase transition temperature of HfO<sub>2</sub>. The estimated track radius using thermal spike calculations is around 5-7 nm. These results are consistent with our earlier studies. This study confirm the SHI irradiation induced transient thermal spike within the effective region.

# 4.4. Conclusions

Using RF magnetron sputtering deposition method, uniform thin films of  $HfO_2$  (30 nm) have been synthesized on 1 x 1 cm<sup>2</sup> sized GaAs substrates. The thickness of pristine film has been estimated by cross-sectional FESEM and Profilometer measurements. RBS measurements have been

performed on as-grown samples and simulated the spectra with SIMNRA to estimate the thickness and elemental composition. These pristine samples were subjected to irradaiation using 120 MeV Ag ions for several irradiation fluences. SHI irradiation induced effects on grain agglomeration and introduction of crystalline phases in otherwise amorphous HfO<sub>2</sub> thin films were studied by employing different characterization techniques. From FESEM measurements, it has been observed that the pristine HfO<sub>2</sub> thin film consists of a smooth surface with uniform grains. A systematic growth in the size of grains from 9 nm to 24 nm and surface roughness with increasing irradiation fluence have been observed. This increase in the size of grains with increasing ion irradiation fluence might be attributed to possible agglomeration of grains within affected region. Pristine film shows amorphous phase, then with increasing fluences, the introduction of monoclinic phase and at the highest fluence evolution of tetragonal phase within HfO<sub>2</sub> films have been noticed as a result of ion induced crystallization. High-k dielectric and high mobility semiconductor based MOS structures (Au/HfO<sub>2</sub>/GaAs) were fabricated and ion irradiation effects on the electrical characteristics (I-V) of these structures, have been studied. It is observed that the leakage current density of MOS structure decreases with increase in the irradiation fluence up to a critical fluence (5 x 10<sup>12</sup> ions/cm<sup>2</sup>) and upon increasing the fluence above the critical fluence, leads to increase in the leakage current density. Further, the I-V characteristics have been investigated using PF and FN tunneling mechanisms to estimate the involvement from several processes to the leakage current due to tunneling with respect to applied voltage. The tunneling examinations shown the pre-existence of several type of defects in the as-deposited samples. The effect of PF tunneling was found to be decreasing up to the critical fluence (5 x 10<sup>12</sup> ions/cm<sup>2</sup>) which confirms the decrease in the density of defects/traps due to ion induced defect annealing. However, above the critical fluence, PF tunneling mechanism dominates which is attributed to increase of traps/defects which results to rise in the tunneling current. Hence, SHI induced defect annealing results in decrease (improvement) in the tunneling current and SHI induced defect creation results in an increase (worsen) in the tunneling current of HfO<sub>2</sub>/GaAs based MOS devices. Thus, ion induced annealing of defects at lower fluences is almost established now by our studies in HfO2 based MOS structures that are fabricated in different conditions.

# 4.5. References

- [1] A. Allan, D. Edenfeld, W. H. Joyner, A. B. Kahng, M. Rodgers, Y. Zorian, "2001 technology roadmap for semiconductors in Computer" 2002, 35, 1, 42-53.
- [2] G. D. Wilk, R.M Wallace, J.M Anthony, J. Appl. Phys. 2001, 89, 5243.
- [3] E. Y. Wu, E. J. Nowak, A. Vayshenker, W. L. Lai, D. L. Harmon, *IBM J. Res. and Dev.* **2002**, 46, 2/3.
- [4] M. L Green, E. P Gusev, R. Degraeve, E. L Garfunkel, J. Appl. Phys. 2001, 90, 2057.
- [5] D. A. Muller, T. Sorsch, S. Moccio, F. H. Baumann, K. Evans-Lutterodt, G. Timp, *Nature* **1999**, 399, 758–761.
- [6] "Intel's Fundamental Advance in Transistor Design Extends Moore's Law, Computing Performance", Intel News Release, **2007**, <a href="https://www.intel.com/pressroom/archive/releases/2007/20071111comp.htm">https://www.intel.com/pressroom/archive/releases/2007/20071111comp.htm</a>.
- [7] J. Robertson, Eur. Phys. J. Appl. Phys. **2004**, 28, 265-29.
- [8] Y. C. Wang, M. Hong, J. M. Kuo, J. P. Mannaerts, J. Kwo, H. S. Tsai, J. J. Krajewski, Y. K. Chen, A. Y. Cho, *IEEE Electron Device Lett.* 1999, 20, 9, 457-459.
- R. B. Brown, B. Bernhardt, M. La Macchia, J. Abrokwah, P. N. Parakh, T. D. Basso, S.
   M. Gold, S. Stetson, C. R. Gauthier, D. Foster, B. Crawforth, T. K. McQuire, K. Sakallah,
   R. J. Lomax, T. N. Mudge, *IEEE Trans. Very Large Scale Integr. Syst.* 1998, 6, 1, 47-51.
- [10] T. Mimura, K. Odani, N. Yokoyama, Y. Nakayama, M. Fukuta, *IEEE Trans. Electron Devices* **1978**, 25, 6, 573-579.
- [11] Y. K. Mishra, A. Kumar, D. K. Avasthi, J. Polym. Mater. 2008, 25, 303.
- [12] D. K. Avasthi, Y. K. Mishra, F. Singh, J. P. Stoquert, Nucl. Instr. and Meth. in Phys. Res. B 2010, 268 (19), 3027.
- [13] D. K. Avasthi, Def. Sci. J. 2009, 59, 401.
- [14] J. Zhang, M. Lang, R. C. Ewing, R. Devanathan, W. J. Weber, M. Toulemonde, *J. Mater. Res.* **2010**, 25, 1344-51.

- [15] M. Toulemonde, W. J. Weber, G. Li, V. Shutthanandan, P. Kluth, T. Yang, Y. Wang, Y. Zhang, *Phys. Rev. B* **2011**, 83, 054106.
- [16] R. Hellborg, H. Whitlow, Y. Zhang, "*Ion beams in nanoscience and technology*". Berlin Heidelberg: Springer-Verlag. **2009**, 369-87.
- [17] R, Neumann, Nucl. Instrum. Methods Phys. Res. B 2013, 3, 14, 4-10.
- [18] K. Xiong, J. Robertson, M. Gibson, S. J. Clark, Appl. Phys. Lett. 2005, 87, 183505.
- [19] J. Kim, K. Yong, J. Electrochem. Soc. **2005**, 152(4), F45.
- [20] Shyama Rath, D. Kabiraj, D. K. Avasthi, A. Tripathi, K. P. Jain, Manoj Kumar, H. S. Mavi,A. K. Shukla, *Nucl. Instr. and Meth. in Phys. Res. B* 2007, 263, 419-423.
- [21] B. Schuster, M. Lang, R. Klein, C. Trautmann, R. Neumann, A. Benyagoub, *Nucl. Instr. and Meth. in Phys. Res. B* **2009**, 267, 964-968.
- [22] A. Benyagoub, A. Audren, J. Appl. Phys. **2009**, 106, 083516.
- [23] M. R. Shaneyfelt, D. M. Fleetwood, J. R. Schwank, K. L. Hugh, *IEEE Trans. Electron. Dev.* 1991, 38(6), 1187-1194.
- [24] N. Manikanthababu, N. Arun, M. Dhanunjaya, V. Saikiran, S.V.S. Nageswara Rao, A.P. Pathak, *Rad. Eff. Def. Sol.* **2015**, 170(3), 207-217.
- [25] A. Benyagoub, *Phys. Rev. B* **2005**, 72(9), 21–24.
- [26] M. Dhanunjaya, K. Vinod Kumar, N. Manikanthababu, S.V.S. Nageswara Rao, A.P. Pathak, *Nucl. Instr. and Meth. in Phys. Res. B* **2019**, 446, 37-42.
- [27] M. Dhanunjaya, S. A. Khan, A. P. Pathak, D. K. Avasthi, S. V. S. Nageswara Rao, *J. Phys. D: Appl. Phys.* 2017, 50, 505301.
- [28] M. Dhanunjaya, D. K. Avasthi, A. P. Pathak, S. A. Khan, S. V. S. Nageswara Rao, *Applied Physics A* **2018**, 124:587.
- [29] N. Manikanthababu, T. K. Chan, S. Vajandar, V. Saikiran, A. P. Pathak, T. Osipowicz, S.V.S. Nageswara Rao, *Appl. Phys. A* 2017, 123:303.
- [30] N. Manikanthababu, S. Vajandar, N. Arun, A.P. Pathak, K. Asokan, T. Osipowicz, T. Basu, S.V.S. Nageswara Rao, Appl. Phys. Lett. 2018, 112, 131601.

- [31] N. Manikanthababu, V. Saikiran, T. Basu, K. Prajna, S. Vajandar, A.P. Pathak, B.K. Panigrahi, T. Osipowicz, S.V.S. Nageswara Rao, *Thin Solid Films* **2019**, 682, 156-162.
- [32] J. F. Ziegler, "SRIM-2003". Nucl. Instr. Meth. B. 2004, 219-220: 1027.
- [33] X. Zhao, D. Vanderbilt, *Phys. Rev. B* **2002**, 65, 233106.
- [34] H. Jiang, R. I. Gomez-Abal, P. Rinke, M. Scheffler, *Phys. Rev. B: Condens. Matter Mater. Phys.* **2010**, 81, 1-9.
- [35] R. R. Manory, T. Mori, I. Shimizu, S. Miyake, G. Kimmel, J. Vac. Sci. Technol. A 2002, 20, 549.
- [36] Pavel Ondracka, David Holec, David Necas, Lenka Zajickova, J. Phys. D: Appl. Phys. 2016, 49, 395301.
- [37] C. E. Curtis, L. M. Doney, J. R. Johnson, J. Amer. Ceram. Soc. 1954, 37, 458-465.
- [38] Girija S. Chaubey, Yuan Yao, Julien P. A. Makongo, Pranati Sahoo, Dinesh Misra, Pierre F. P. Poudeu, John B. Wiley, *RSC Adv.* **2012**, 2, 9207-9213.
- [39] M. Villanueva-Ibanez, C. Le Luyer, O. Marty, J. Mugnier, *Optical Materials* **2003**, 24, 51.
- [40] C. Y. Chain, L. C. Damonte, S. Ferrari, E. Munoz, C. Rodr'ıguez Torres, A. F. Pasquevich, *J. of Alloys and Compounds* **2010**, 495, 527.
- [41] T. S. N. Sales, F. H. M. Cavalcante, B. Bosch-Santos, L. F. D. Pereira, G. A. Cabrera-Pasca, R. S. Freitas, R. N. Saxena, A. W. Carbonari, *AIP Advances* **2017**, 7, 056315.
- [42] P. Balasaritha, S. Amirthapandian, P. Magudapathy, R.M. Sarguna, S. K. Srivastava, B. K. Panigrahi, *Journal of Nuclear Materials* **2018**, 508, 385-394.
- [43] R. T. Wen, L. S. Wang, H. Z. Guo, Y. Chen, G. H. Yue, D. L.Peng, T. Hihara, K. Sumiyama, *Mater. Chem. Phys.* **2011**, 130, 823-826.
- [44] T.V. Perevalov, V. Sh. Aliev, V.A. Gritsenko, A.A. Saraev, V.V. Kaichev, *Microelectron*. *Eng.* **2013**, 109, 21-23.
- [45] T.V. Perevalov, D.V. Gulyaev, V.S. Aliev, K.S. Zhuravlev, V.A. Gritsenko, A.P. Yelisseyev, *J. Appl. Phys.* **2014**, 116, 244109.

- [46] N. Arun, L. D. Varma Sangani, K. Vinod Kumar, A. Mangababu, M. Ghanashyam Krishna, A. P. Pathak, S. V. S. Nageswara Rao, *Journal of Materials Science: Materials in Electronics* 2021, 32, 2973-2986.
- [47] A.A. Boulbitch, P. Toledano, *Phys. Rev. Lett.* **1998**, 81, 838-841.
- [48] K. Vinod Kumar, N. Arun, A. Mangababu, Sunil Ojha, S. V. S. Nageswara Rao, A. P. Pathak, *Rad. Eff. Def. Sol.* **2020**, 175, 1-2, 150-159.
- [49] G. Agarwal, P. Sharma, I. P. Jain, Appl. Surf. Sci. 2006, 253, 1165-1169.
- [50] N. Bansal, S. Kumar, S. A. Khan, R. S. Chauhan, *Radiat. Eff. Def. Solids* 2016, 171, 290-296.
- [51] M. Toulemonde, S. Bouffard, F. Studer, *Nucl. Instrum. Methods Phys. Res. B* **1994**, 91, 108.
- [52] M. Toulemonde, Ch. Dufour, A. Meftah, E. Paumier, *Nucl. Instrum.Methods Phys. Res. B* **2000**, 166-167, 903.
- [53] G. K. Mehta, *Nucl. Instrum. Meth. A* **1996**, 382, 335-342.
- [54] K. Y. Cheong, J. H. Moon, H. J. Kim, W. Bahng, Nam-Kyun Kim, J. Appl. Phys. 2008, 103, 084113.
- [55] J. C. Ranuarez, M. J. Deen, Chih-Hung Chen, *Microele. Reliab.* **2006**, 46(12), 1939-1956.
- [56] M. Lenzlinger, E. H. Snow, J. Appl. Phys. 1969, 40, 278-283.
- [57] Khairurrijal, W. Mizubayashi, S. Miyazaki, M. Hirose, J. Appl. Phys. 2000, 87, 3000.
- [58] A. Paskaleva, A. J. Bauer, M. Lemberger, S. Zucher, J. Appl. Phys. 2004, 95, 5583.
- [59] D. K. Avasthi and G. K. Mehta, "Swift Heavy Ions for Materials Engineering and Nanostructuring", Springer Series in Materials Science **2011**, 1.
- [60] A. Benyagoub, Eur. Phys. J. B 2003, 34, 395-398.

# Effects of Swift Heavy Ion (SHI) and Gamma irradiation on the structural and electrical properties of HfO<sub>2</sub>/GaO<sub>x</sub> thin films

This chapter provides a brief report on the SHI irradiation induced effects on  $HfO_2/GaO_x$  bilayered films synthesized on p-type Silicon (100) substrates. As-grown films contain highly strained inhomogeneous large grains. The average grain size decreases with increasing fluence which is attributed to SHI induced grain fragmentation. Ion-induced inter-diffusion/inter-mixing of Hf and Ga elements has been observed which leads to the development of inter-mixing of layers at the interfaces. Further,  $HfO_2/GaO_x/Si$  based Metal Oxide Semiconductor (MOS) capacitors have been fabricated and the effects of SHI irradiation and Gamma irradiation on the electrical properties of these devices have been discussed in detail (part of this work is published in Rad. Eff. Deff. In Sol. 2020, 175 (1-2), 150-159).

### 5.1. Introduction

As discussed in previous chapters, in the current generation of Metal Oxide Semiconductor Field Effect Transistor (MOSFET) based devices, HfO<sub>2</sub> has already occupied the space of SiO<sub>2</sub> as the gate dielectric introduced in 2007 by Intel [1]. For the next generation high-power electronic devices, there is a great demand for high-performance power semiconductor based devices [2-5]. However, this requirement cannot be accomplished by Si-based standard electronics devices. Alternate semiconductors which have an energy bandgap more than 3 eV (wide bandgap) with advanced break-down fields than that of Si, are attractive candidates for the next generation highpower electronic devices [6-9]. Hence, the current interest is to replace the Si with alternate high mobility and wide bandgap semiconductors for power electronic device applications [5]. Among the many superior semiconductor materials, III-V group and III-VI group compound semiconductors such as GaAs, GaN, GaSb, InAs and Ga<sub>2</sub>O<sub>3</sub> etc. are capable to attain the future high speed devices with good electrical characteristics [10]. In recent times, Gallium Oxide (Ga<sub>2</sub>O<sub>3</sub>) in monoclinic phase (β-phase) has engrossed substantial attention due to its ultra-wide band gap of 4.8 eV (at room temperature) and can be used in advanced power electronic devices which can be operated at high temperatures with high speed [11-13]. Furthermore, the theoretical critical electric field of Ga<sub>2</sub>O<sub>3</sub> is 8 MV/cm which is very high and well developed melt growth methods at low cost are already there to fabricate single crystal Ga<sub>2</sub>O<sub>3</sub> substrates with large size [14]. These unique material properties explore the potential of Ga<sub>2</sub>O<sub>3</sub> wide bandgap semiconductors for the next generation high-power electronic devices. In the past few years, β-Ga<sub>2</sub>O<sub>3</sub> based electronic devices such as Schottky barrier diodes and UV-photodetectors have been fabricated productively together with MOSFETs and MESFETs for high-power electronic device applications [15-19]. Higashiwaki et al. pioneered Ga<sub>2</sub>O<sub>3</sub> based MESFETs using single-crystal β-Ga<sub>2</sub>O<sub>3</sub> [20]. Tadjer et al. [21] developed a MOS based transistor on β-Ga<sub>2</sub>O<sub>3</sub> substrates using HfO<sub>2</sub> gate oxide. Respectable interface properties of high-k gate dielectrics like HfO<sub>2</sub> with Ga<sub>2</sub>O<sub>3</sub> are essential for fabricating high competence MOS devices to enhance the electrical characteristics and to condense off-state leakage currents. Hence the interface studies between HfO<sub>2</sub> and Ga<sub>2</sub>O<sub>3</sub> and electrical studies of HfO<sub>2</sub>/Ga<sub>2</sub>O<sub>3</sub> based high-k/wide band-gap MOS devices are necessary to develop high speed and low power consumption in future MOS devices.

Swift Heavy Ion (SHI) irradiation is a promising tool used in material synthesis, material characterization and modification of target materials [22-24]. In recent years, ion induced grain agglomeration, grain fragmentation, phase transformations, inter-diffusion/inter mixing [25, 26] and subsequent effects on the electrical performance of MOS devices have been reported [27-33]. The energy deposited in the target material via electronic and nuclear energy losses due to SHI irradiation results in grain fragmentation and inter-diffusion/intermixing at the interface of target materials [34, 35]. Therefore, it is significant to realize the SHI irradiation effects on surface morphology, intermixing, ion induced defect creation and subsequent effects on the electrical characteristics of MOS capacitors. Gamma irradiation is another technique to produce defects. It can produce defects all over the target material with a lesser amount of density compared to SHI irradiation. It can cause ionization in the sample which results in the production of electron-hole pairs. The defects and interface traps which are already present in the as-grown sample confine these moveable charges. The production of electron-hole pairs and defect creation can be increased by increasing the gamma irradiation dose. These defects may lead to effects in the electrical characteristics of MOS capacitors [36]. Hence the effects induced by gamma irradiation on electrical performance can be governed by the pre-existing defects in the as-grown film before gamma irradiation. In addition, gamma irradiation can create oxygen vacancies as well as interface traps in the sample [37-39], which also affect the electrical properties of MOS capacitors. The study may give valuable information to understand the electrical performance (I-V and C-V) of MOS capacitors by subjecting them to gamma irradiation to use these devices securely in radiation environments. These MOS structures are expected to be used in many devices in space and medical applications such as radiological treatment equipments and physics experiments associated with high energy such as nuclear power plants. Therefore the radiation (SHI and Gamma) response studies of these MOS capacitors on their electrical characteristics will be worthwhile.

# 5.2. Experimental details

**5.2.1. Synthesis of thin films:** Thin films of  $GaO_x$  and  $GaO_x/HfO_2$  bi-layers were synthesized on Si using RF magnetron sputtering technique. Boron-doped p-type Silicon (100) wafers with a resistivity of 1-10  $\Omega$  cm were cut into pieces (1 x 1 cm<sup>2</sup>) each and ultrasonically cleaned in acetone, isopropanol and deionized water (DIW) for 5 min each. Then, these pieces were dried using nitrogen gas and immediately loaded on the sample holder inside the chamber at a distance of 12.5

cm from the sputtering target. Then the chamber was evacuated up to the pressure of 2.64 x 10<sup>-6</sup> mbar and then Ar and N<sub>2</sub> gases of 15 SCCM and 10 SCCM (in 3:2 ratio) respectively were released inside the chamber. Initially GaO<sub>x</sub> thin films of ~ 30 nm were synthesized on Si by applying an optimized RF power of 40 W. These GaO<sub>x</sub>/Si structures were examined using various characterization techniques to estimate the thickness and stoichiometry of the as-grown films. Throughout the deposition, the sample holder was rotated with 10 rpm speed to attain the uniform growth of films at room temperature and the deposition pressure of  $2.2 \times 10^{-2}$  mbar was maintained. Using the same deposition conditions, another set of GaO<sub>x</sub> films of ~ 150 nm thickness were deposited on Si substrates. Once the deposition of GaO<sub>x</sub> film was completed, then again the chamber was evacuated up to the pressure of 2.6 x 10<sup>-6</sup> mbar without breaking the vacuum, and 30 SCCM of Ar gas was released. An optimized RF power of 60 W was used to synthesize HfO<sub>2</sub> films of ~ 30 nm thickness on top of as-grown GaO<sub>x</sub> films. To synthesize GaO<sub>x</sub> and HfO<sub>2</sub> films GaN and HfO<sub>2</sub> sputter targets were used respectively. Hasina F. Hug et al. [40] had previously reported that it is possible to grow GaO<sub>x</sub> films when GaN targets were sputtered. The existence of O and the nonexistence of N in our RF sputtered films was confirmed by various characterization methods.

**5.2.2. SHI irradiation:** One set of as-deposited HfO<sub>2</sub>/GaO<sub>x</sub>/Si structured samples were subjected to SHI irradiation by Ag ions of energy 120 MeV using a Pelletron accelerator (15 UD tandem) at IUAC, New Delhi, India. The projected range,  $S_e$  - electronic energy loss and  $S_n$  - nuclear energy loss of 120 MeV Ag ions in HfO<sub>2</sub> (density 9.68 g/cm<sup>3</sup>) film were estimated as 8.5  $\mu$ m, 24.9 keV/nm and 0.14 keV/nm correspondingly. A standard and familiar SRIM software was used for estimation of these parameters [41]. To avoid the sample heating effects and to achieve uniform irradiation all over the surface of the target material, a continuous ion beam of a low and constant current of 0.5 particle nano-Ampere (pnA) was used and the beam was scanned over the thin films of area 1 x 1 cm<sup>2</sup>. The time of irradiation required to achieve the fluence has been calculated by using the following equation 5.1 (As discussed in previous chapters). By varying the pre calculated time of irradiation, the ion fluence ranging from 1 x  $10^{12}$  ions/cm<sup>2</sup> to 1 x  $10^{14}$  ions/cm<sup>2</sup> was achieved.

$$Time (sec) = \frac{Flunce \left(\frac{ions}{cm^2}\right) X Area (cm^2)}{6.25 X 10^{12} X Beam current (pnA)}$$
(5.1)

- **5.2.3. Gamma irradiation:** Another set of as-grown HfO<sub>2</sub>/GaO<sub>x</sub>/Si structured samples were exposed to Gamma irradiation by <sup>60</sup>Co gamma rays of energy 1.25 MeV using the Gamma source 1200cc at IUAC, New Delhi, India. For all the samples the dose rate of 4.64 kGy/h was maintained. A number of radiation doses were achieved by subjecting the samples to gamma source for different time durations. The samples were irradiated at various doses 4 kGy, 8 kGy, 16 kGy, 32 kGy, 48 kGy and 64 kGy.
- **5.2.4. Sample Characterization:** The as-grown GaO<sub>x</sub> thin films deposited on Si substrates were examined using Field Emission Scanning Electron Microscope - Energy Dispersive X-ray Spectroscopy analysis (FESEM-EDX), Grazing incident x-ray diffraction (GIXRD) and High Resolution Rutherford Backscattering Spectrometry (HRBS)/Channeling experiments were carried-out to estimate the thickness, crystal structure and stoichiometry of the films. GIXRD measurements were performed using Bruker D8 Advance diffractometer with Cu K $\alpha$ ,  $\lambda = 1.54$  Å at University of Hyderabad. The HRBS/Channeling measurements were performed using 500 keV He<sup>+</sup> ions at 65° of scattering angle at the Centre for Ion Beam Applications, National University of Singapore, Singapore. Further, as-deposited and irradiated HfO<sub>2</sub>/GaO<sub>x</sub> films with various ion fluences were characterized by different techniques to observe the effects of SHI irradiation. RBS measurements have been performed at IUAC, New Delhi, India using 2 MeV He<sup>2+</sup> ions at 165° of scattering angle. RBS results were used to evaluate the thickness and elemental composition of different layers as a function of irradiation fluence. SHI induced inter-diffusion/inter-mixing of layers has also been studied in detail using RBS measurements. The acquired RBS spectra of different samples as a function of irradiation fluence were simulated by SIMNRA-7.01 software [42]. The thickness of HfO<sub>2</sub> and GaO<sub>x</sub> layers and corresponding elemental composition of each layer have been estimated in detail by the simulation. Further, the thickness of the as grown sample was measured and confirmed by performing cross sectional FESEM measurements and thickness profile measurements using Ambios XP 200 Profilometer. Surface morphology of HfO<sub>2</sub>/GaO<sub>x</sub> bilayer films and SHI induced grain agglomeration/fragmentation were studied by FESEM measurements using Carl ZEISS, FEG, ultra-55 at University of Hyderabad.

**5.2.5. Fabrication and electrical characterization of MOS capacitors:** Au/HfO<sub>2</sub>/GaO<sub>x</sub>/Si structured MOS capacitors were fabricated using as-grown, SHI irradiated and Gamma irradiated samples by depositing top and bottom contacts to perform electrical measurements. As top contact, metal electrodes of 100 nm thick Au dots with 1 mm in diameter were synthesized using a shadow mask on top of HfO<sub>2</sub> film surfaces. As bottom contact, Epoxy resin and conductive Ag paste on Al foil was used underneath the Si substrates. These two interfaces, TE/HfO<sub>2</sub> (metal/oxide) and Si/BE (semiconductor/metal) are expected to behave in the same manner for all the devices. The schematics of SHI/Gamma irradiation and the fabrication of Au/HfO<sub>2</sub>/GaO<sub>x</sub>/Si based MOS structures are shown in Fig. 5.1. Electrical characterizations such as Leakage current – Voltage (I-V) and Capacitance- Voltage (C-V) in voltage range from -5 V to 5 V were performed to evaluate the effects of SHI irradiation on the electrical characteristics of these MOS structures. These electrical measurements were performed using an Agilent technologies-B1500A semiconductor device analyzer at Centre for Nanotechnology (CFN), University of Hyderabad.

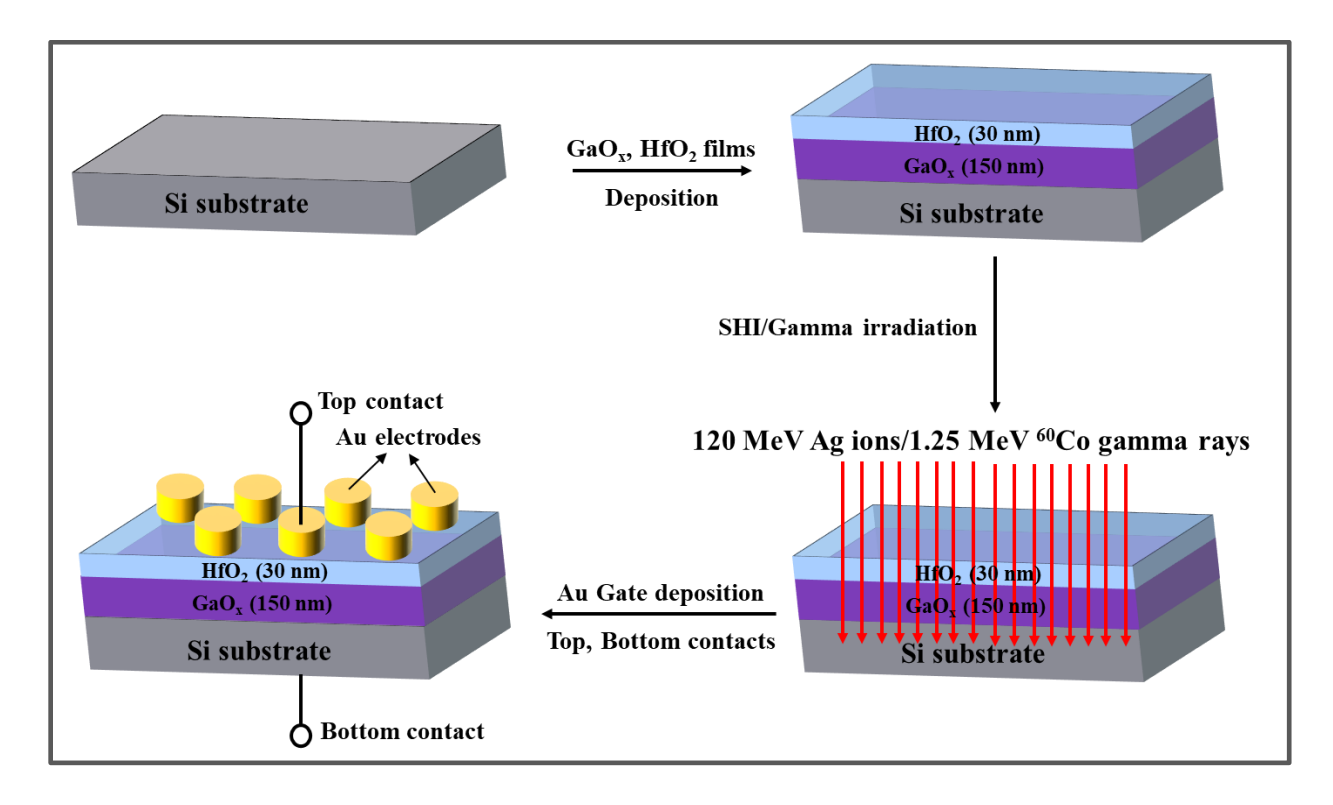


Fig. 5.1: Schematic representation of SHI/Gamma irradiation and fabrication of MOS structures.

# 5.3. Results and discussions

# **5.3.1.** Characterization of thickness and stoichiometry of pristine thin films:

### A. Characterization of GaO<sub>x</sub> thin films:

The elemental composition and thickness of as-deposited GaO<sub>x</sub> films were evaluated by using FESEM-EDX and HRBS measurements. The EDX spectrum and elemental composition of as-deposited GaO<sub>x</sub> thin film are shown in Fig. 5.2 and Table 5.1 respectively. EDX analysis shows presence of Ga and O elements with atomic percentages around 17% and 25% respectively on Si substrate.

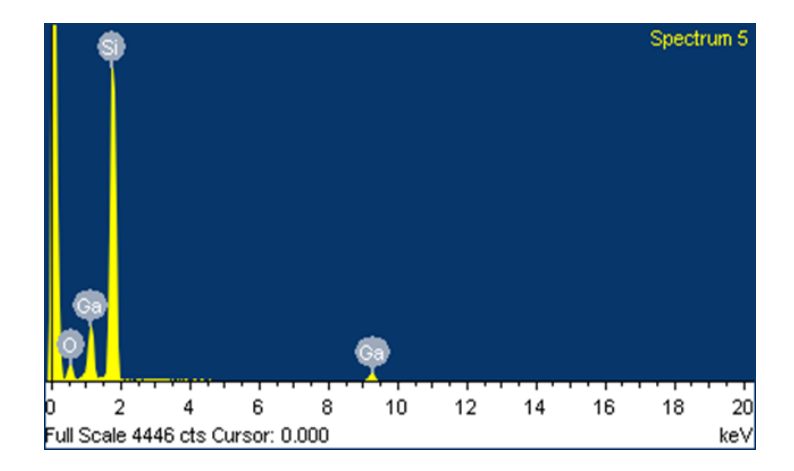


Fig. 5.2: EDX spectrum of as-deposited GaO<sub>x</sub> thin film.

| Element | Weight% | Atomic% |
|---------|---------|---------|
| 0       | 20.38   | 24.97   |
| Si      | 62.72   | 57.57   |
| Ga      | 16.90   | 17.46   |

Table 5.1: Elemental composition of as-deposited GaO<sub>x</sub> thin film.

The HRBS (random and channeled) measurements were carried-out for as-deposited  $GaO_x$  thin films. The random, SIMNRA simulated and channeled spectra of the as-deposited  $GaO_x$  thin film are shown in Fig. 5.3. From simulation, the stoichiometry of the film is estimated to be around 42% of Ga and 58% of O. The estimated thickness of  $GaO_x$  film was around 32 nm. The GIXRD pattern of as-deposited  $GaO_x$  thin film (see Fig. 5.4) shows an amorphous phase.

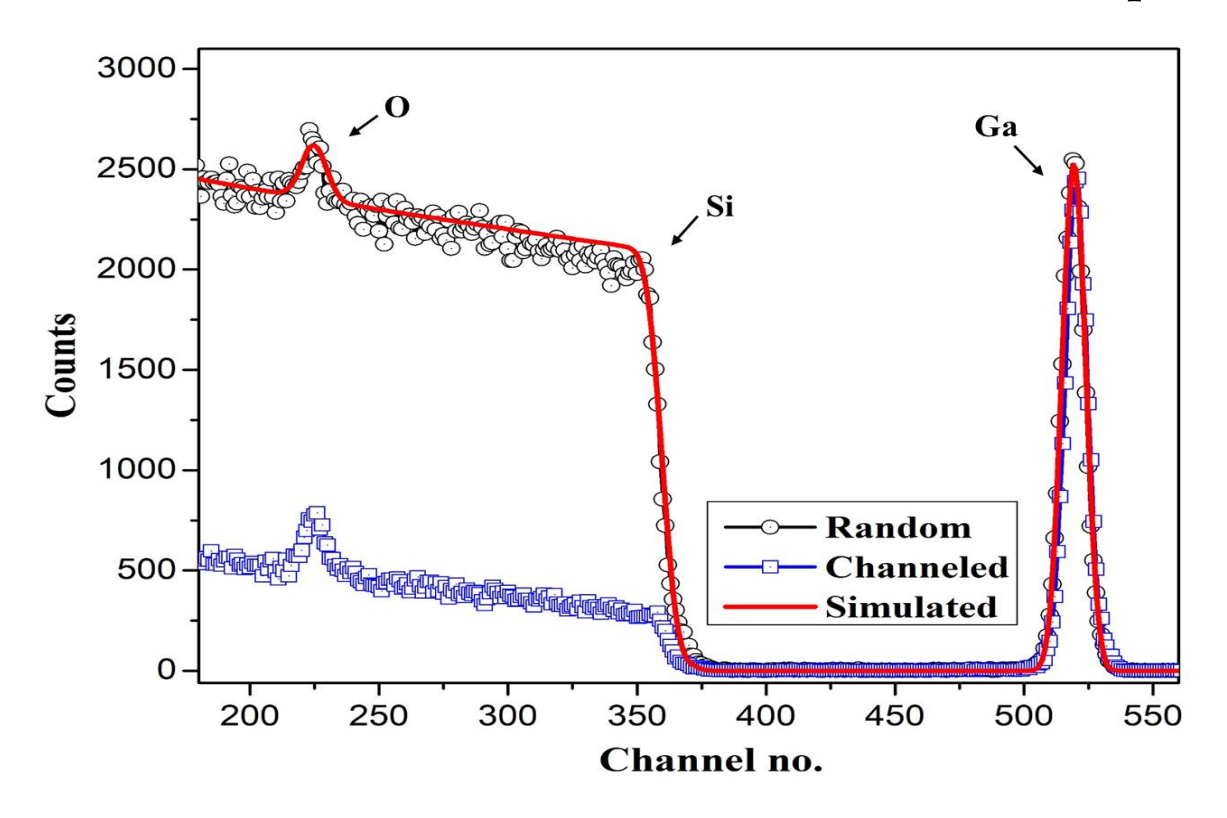


Fig. 5.3: HRBS (random and channeled) spectra of as-deposited  $GaO_x$  thin film with SIMNRA simulation.

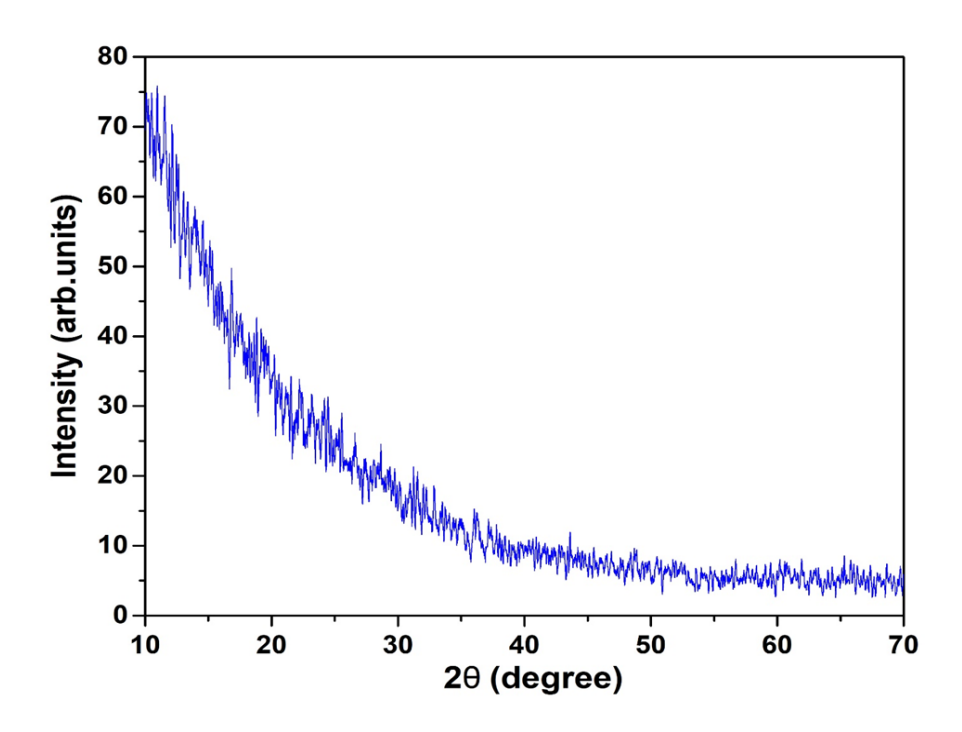


Fig. 5.4: GIXRD pattern of as-deposited GaO<sub>x</sub> thin film.

### B. Characterization of HfO<sub>2</sub>/GaO<sub>x</sub> bi-layer thin films:

The pristine and SHI irradiated HfO<sub>2</sub>/GaO<sub>x</sub> bi-layer thin films grown by RF magnetron sputtering system were studied by different characterization techniques to investigate the impact of SHI irradiation on structural and electrical properties of the films. The thicknesses of as-grown HfO<sub>2</sub> and GaO<sub>x</sub> films were estimated by cross sectional FESEM measurements as shown in Fig. 5.5(a). The estimated thicknesses of as-grown HfO<sub>2</sub> and GaO<sub>x</sub> films were found to be as 35 nm and 160 nm respectively and the total film thickness was estimated as 195 nm. Further, the bi-layer film (HfO<sub>2</sub>/GaO<sub>x</sub>) thickness was confirmed by thickness measurements performed using Profilometer as shown in Fig. 5.5(b) and found as around 192 nm. The EDX spectrum and elemental composition of as-deposited HfO<sub>2</sub>/GaO<sub>x</sub> bi-layer thin film are shown in Fig. 5.6 and Table 5.2 respectively. EDX analysis shows presence of Hf, Ga and O elements with atomic percentages around 8%, 15% and 30% respectively on Si substrate.

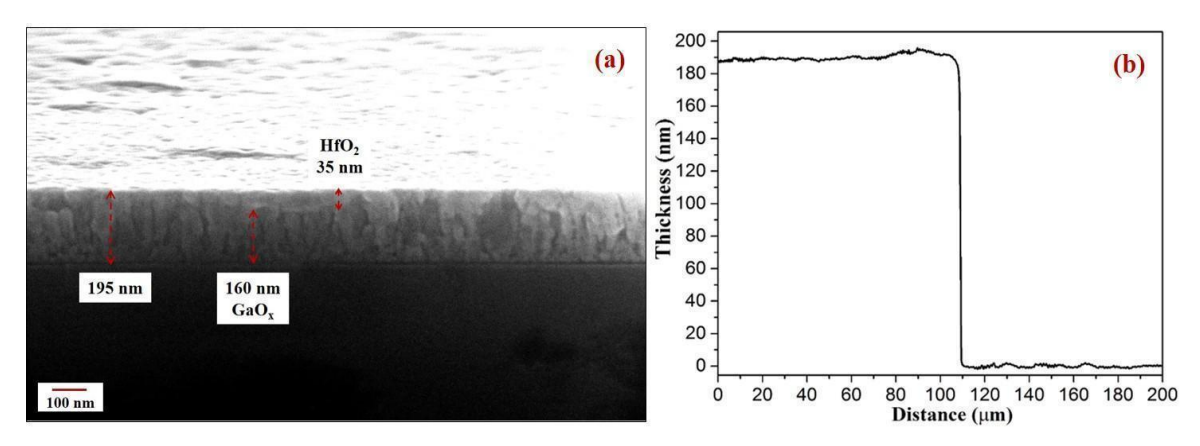


Fig. 5.5: Estimation of as-grown HfO<sub>2</sub>/GaO<sub>x</sub> bi-layer film thickness using (a) cross sectional FESEM measurements and (b) Profilometer measurements (total film thickness).

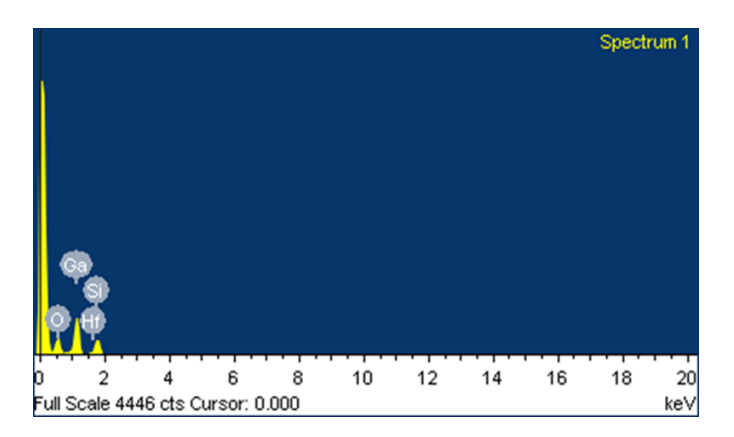


Fig. 5.6: EDX spectrum of as-deposited HfO<sub>2</sub>/GaO<sub>x</sub> bi-layer thin film.

| Element | Weight% | Atomic% |
|---------|---------|---------|
| 0       | 20.87   | 30.00   |
| Si      | 56.11   | 46.78   |
| Ga      | 13.03   | 15.22   |
| Hf      | 10.00   | 8.00    |

Table 5.2: Elemental composition of as-deposited HfO<sub>2</sub>/GaO<sub>x</sub> bi-layer thin film.

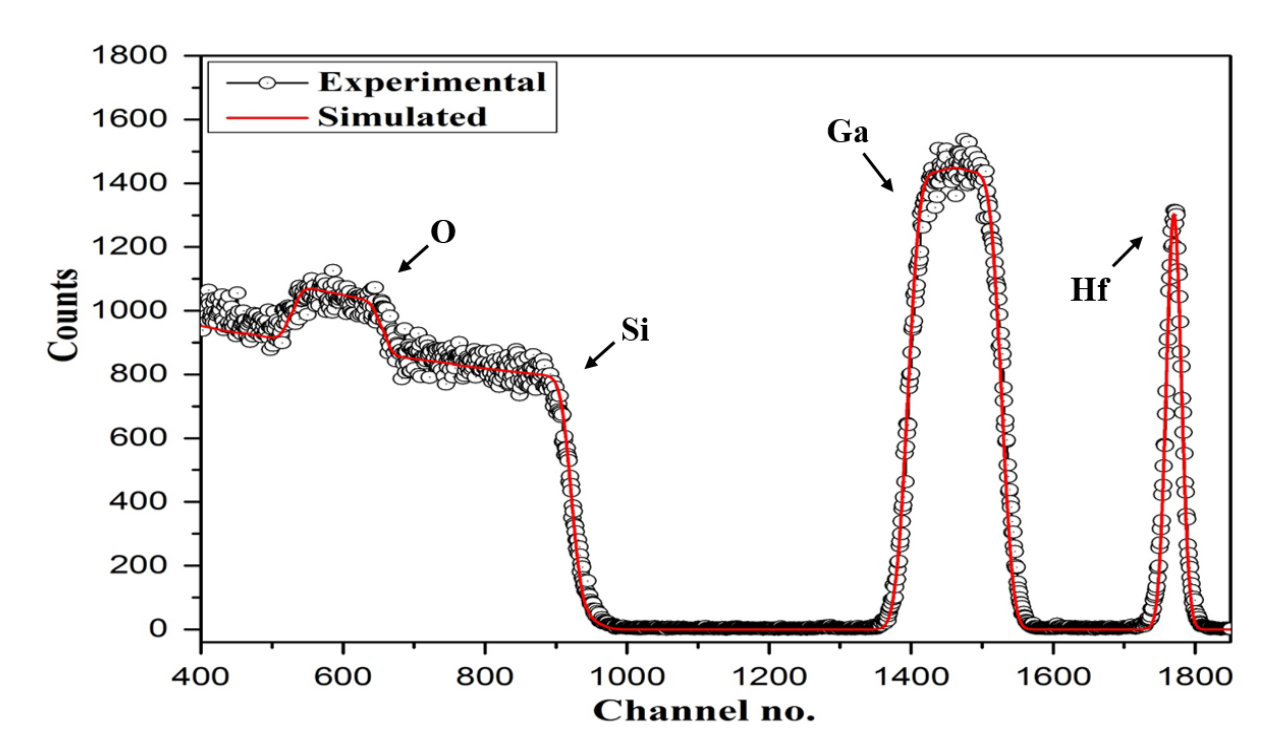


Fig. 5.7: RBS spectrum of as-grown HfO<sub>2</sub>/GaO<sub>x</sub> bi-layer thin film deposited on Si with SIMNRA simulation.

RBS measurements were performed on as-grown  $HfO_2/GaO_x$  bi-layer thin films and simulated using SIMNRA as shown in Fig. 5.7. The values of Calibration offset and Energy per channel were obtained from a standard calibration sample ( $Au/SiO_2$ ). The obtained values of Calibration offset and Energy per channel were 73.63 keV and 0.989 keV/ch respectively, which were used in simulation of measured RBS spectrum. The stoichiometry of the film estimated from the SIMNRA simulation fitting corresponds to  $HfO_2$  and  $Ga_2O_3$ . The thicknesses of individual layers of  $HfO_2$  and  $GaO_x$  were also estimated from the fitted SIMNRA curve and found as ~ 34 nm and ~ 162 nm respectively. To estimate the thickness and stoichiometry of the film from the fitting curve, bulk

densities corresponding to HfO<sub>2</sub> and Ga<sub>2</sub>O<sub>3</sub> as 9.68 g/cm<sup>3</sup> and 6.44 g/cm<sup>3</sup> respectively have been considered [43-46].

### 5.3.2. Effects of SHI irradiation

a) Surface structure and Grain fragmentation: The structure, morphology of surface of the films and SHI induced grain fragmentation were studied using the FESEM measurements. The FESEM images of the as grown and SHI irradiated HfO<sub>2</sub>/GaO<sub>x</sub> bi-layer films deposited on Si substrates as a function of ion irradiation fluence are shown in Fig. 5.8 (a-f). As-deposited HfO<sub>2</sub>/GaO<sub>x</sub> film surface contains large sized non-uniform grains which are irregularly oriented. Moreover, each large grain is an arrangement of smaller grains. Generally, this type of surface morphology is lightly packed, less dense and has a very poor bond among the grains [47]. From FESEM images, it is observed that with increasing radiation fluence, the structure and size of the grains have been modified. The diameters of the as-grown and the modified spherical grains due to irradiation were calculated and the average diameter as a function of irradiation dose were estimated by Gauss fittings. The graphical representation with Gauss fit is presented in Fig. 5.9 and statistical analysis of estimated mean diameter of spherical grains has been summarized in Table 5.3.

As grown films show inhomogeneous grains with an average diameter of 34.5 nm. For irradiated film at the fluence of  $1x10^{12}$  ions/cm<sup>2</sup>, the large grains start disrupting without any observable changes in structure while the size of the grains are reduced to 31 nm. Upon further increase of the irradiation fluence to  $5x10^{12}$  ions/cm<sup>2</sup>, the grains became more disrupted and new grains started forming within the large grains with a reduced grains size of 28.6 nm. At the irradiation fluence of  $1x10^{13}$  ions/cm<sup>2</sup>, the formation of new grains further increased within the original large grains and the average diameter of the spherical grains further reduced to 25.9 nm. Upon further increasing the irradiation fluence to  $5x10^{13}$  ions/cm<sup>2</sup>, the original large grains were totally demolished and the formation of new individual grains with uniform spherical structure started with further reduced average spherical diameter of 16.1 nm. At the highest irradiation fluence of  $1x10^{14}$  ions/cm<sup>2</sup>, the film surface is smoothened and the formation of identical spherical grains with further reduced average grain size of 13.8 nm has been observed. Thus, the mean diameter of grains is decreased from 34.5 nm to 13.8 nm with increasing the SHI irradiation fluence demonstrating an important manifestation of SHI irradiation, known as ion beam smoothening.

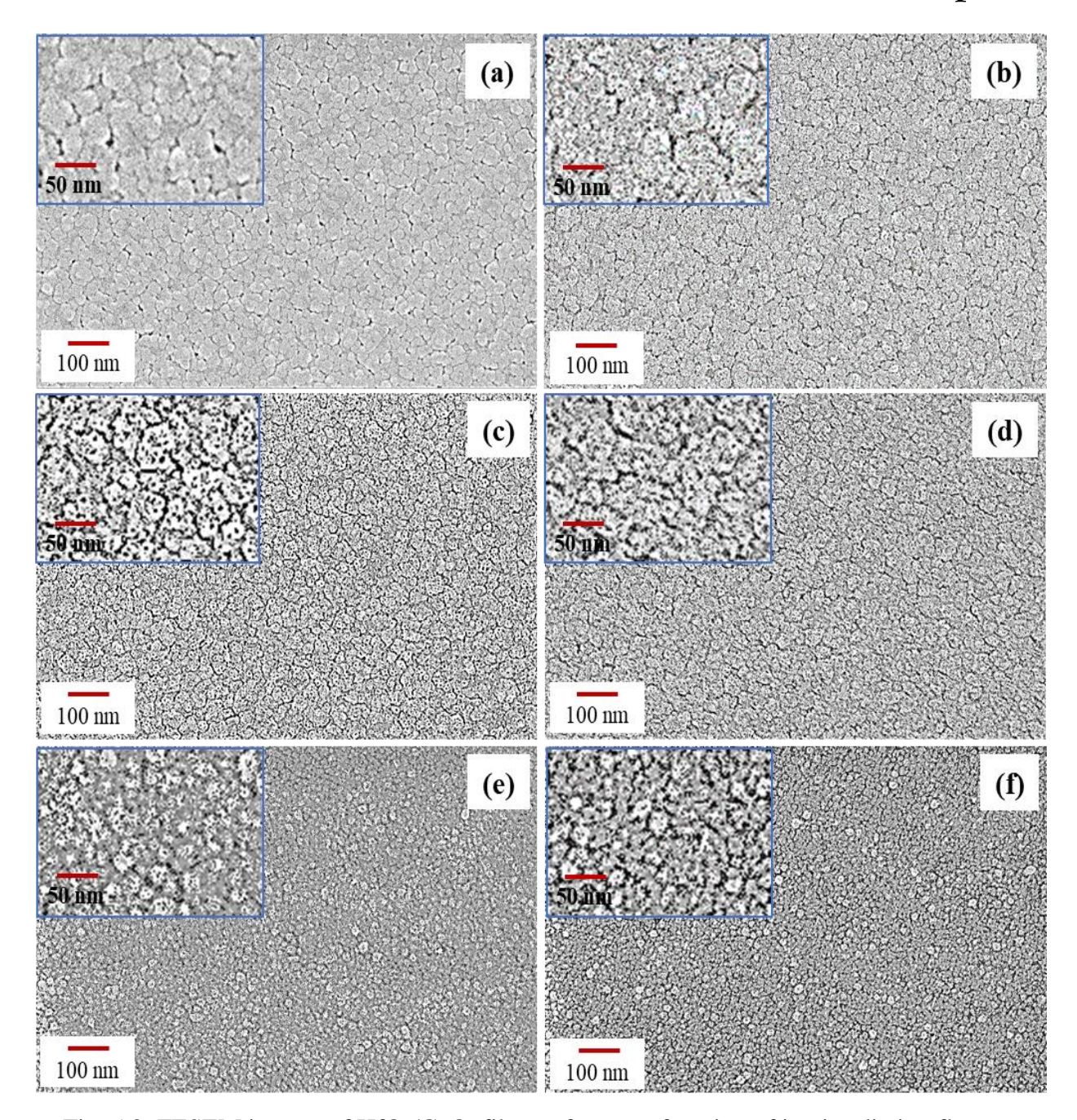


Fig. 5.8: FESEM images of  $HfO_2/GaO_x$  film surface as a function of ion irradiation fluence (a) Pristine, (b)  $1x10^{12}$  ions/cm<sup>2</sup>, (c)  $5x10^{12}$  ions/cm<sup>2</sup> (d)  $1x10^{13}$  ions/cm<sup>2</sup>, (e)  $5x10^{13}$  ions/cm<sup>2</sup> and (f)  $1x10^{14}$  ions/cm<sup>2</sup> (inset: zoomed image shows grains within the grains)

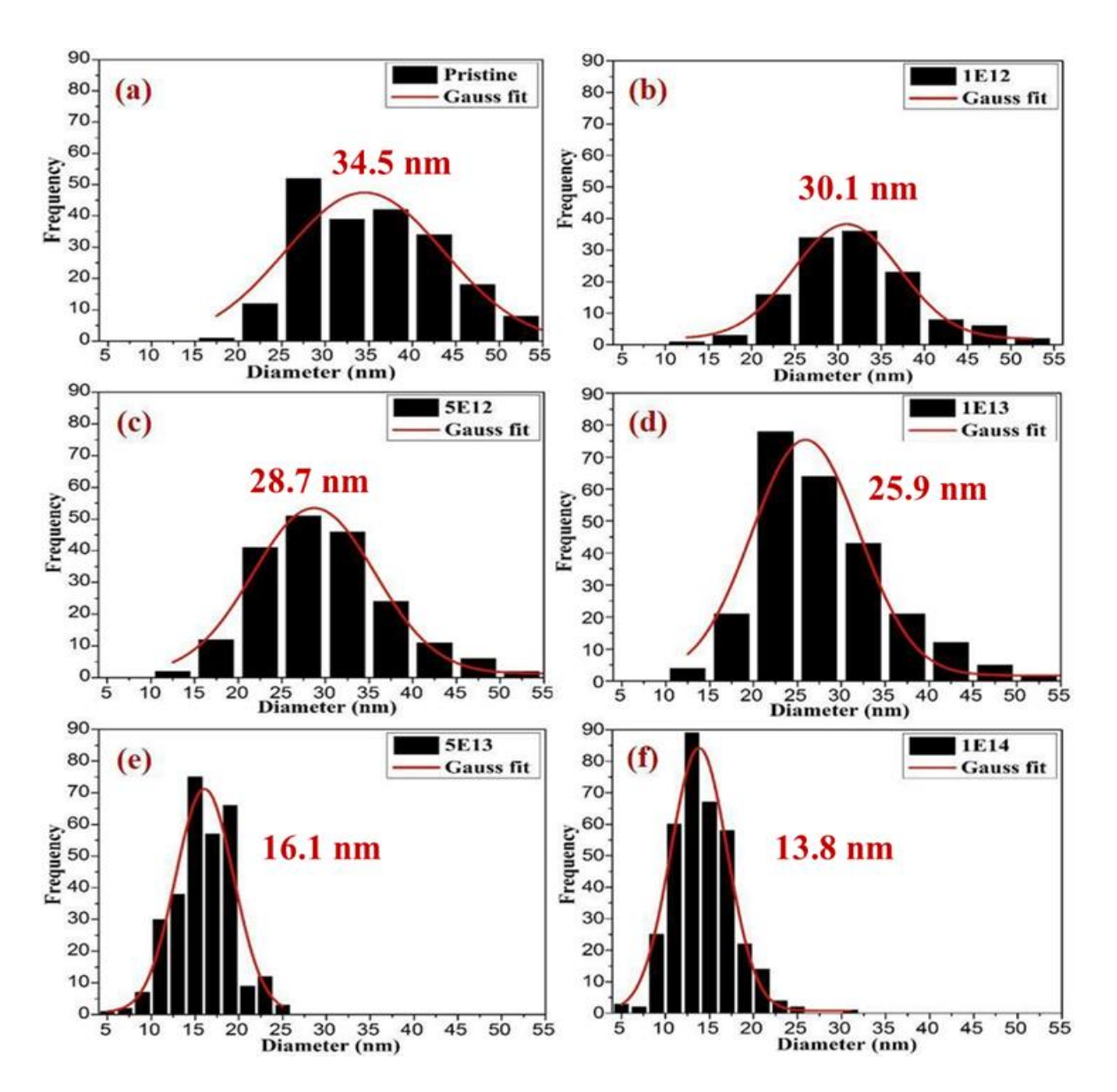


Fig. 5.9: Size distribution of as-grown and SHI irradiated  $HfO_2/GaO_x$  grains as a function of ion irradiation fluence

 $\label{eq:constraint} \mbox{(a) - Pristine, (b)} - 1x10^{12} \mbox{ ions/cm}^2, \mbox{ (c)} - 5x10^{12} \mbox{ ions/cm}^2 \mbox{ } \\ \mbox{(d)} - 1x10^{13} \mbox{ ions/cm}^2, \mbox{ (e)} - 5x10^{13} \mbox{ ions/cm}^2 \mbox{ and (f)} - 1x10^{14} \mbox{ ions/cm}^2.$ 

| Sample ID | Irradiation dose<br>(ions/cm²) | Avg. diameter of spherical grains (nm) | Standard deviation (nm) |
|-----------|--------------------------------|--|-------------------------|
| Pristine  | 0                              | 34.5                                   | 9.1                     |
| 1E12      | 1 x 10 <sup>12</sup>           | 30.1                                   | 7.0                     |
| 5E12      | 5 x 10 <sup>12</sup>           | 28.7                                   | 6.1                     |
| 1E13      | 1 x 10 <sup>13</sup>           | 25.9                                   | 5.4                     |
| 5E13      | 5 x 10 <sup>13</sup>           | 16.1                                   | 3.3                     |
| 1E14      | 1 x 10 <sup>14</sup>           | 13.8                                   | 3.1                     |

Table 5.3: Average diameters of as-grown and SHI irradiated spherical HfO<sub>2</sub>/GaO<sub>x</sub> grains as a function of irradiation fluence.

The change in grain size and surface morphology of the film after SHI irradiation can be explained in terms of SHI induced grain fragmentation within the grains of the film. In literature, SHI induced grain fragmentation in fluoride thin films has been reported [48, 49]. This type of surface morphology of large grains for as-grown films corresponds to very high strained grains. The highly strained grain structures are expected to be relaxed to become stress-free during the irradiation process leading to the grain fragmentation. Therefore the electronic energy loss due to SHI irradiation plays the main role in observed changes in film surface morphology, grain fragmentation and formation of new individual homogeneous spherical grains.

GIXRD measurements were performed on HfO<sub>2</sub>/GaO<sub>x</sub> bi-layer thin films and the diffraction patterns are shown in Fig. 5.10. All the HfO<sub>2</sub>/GaO<sub>x</sub> bi-layer thin films exhibit amorphous nature. However, no significant changes in the phase of HfO<sub>2</sub>/GaO<sub>x</sub> bi-layer thin films were observed in the irradiated films over as-grown films, even-though there are significant changes in their morphology.

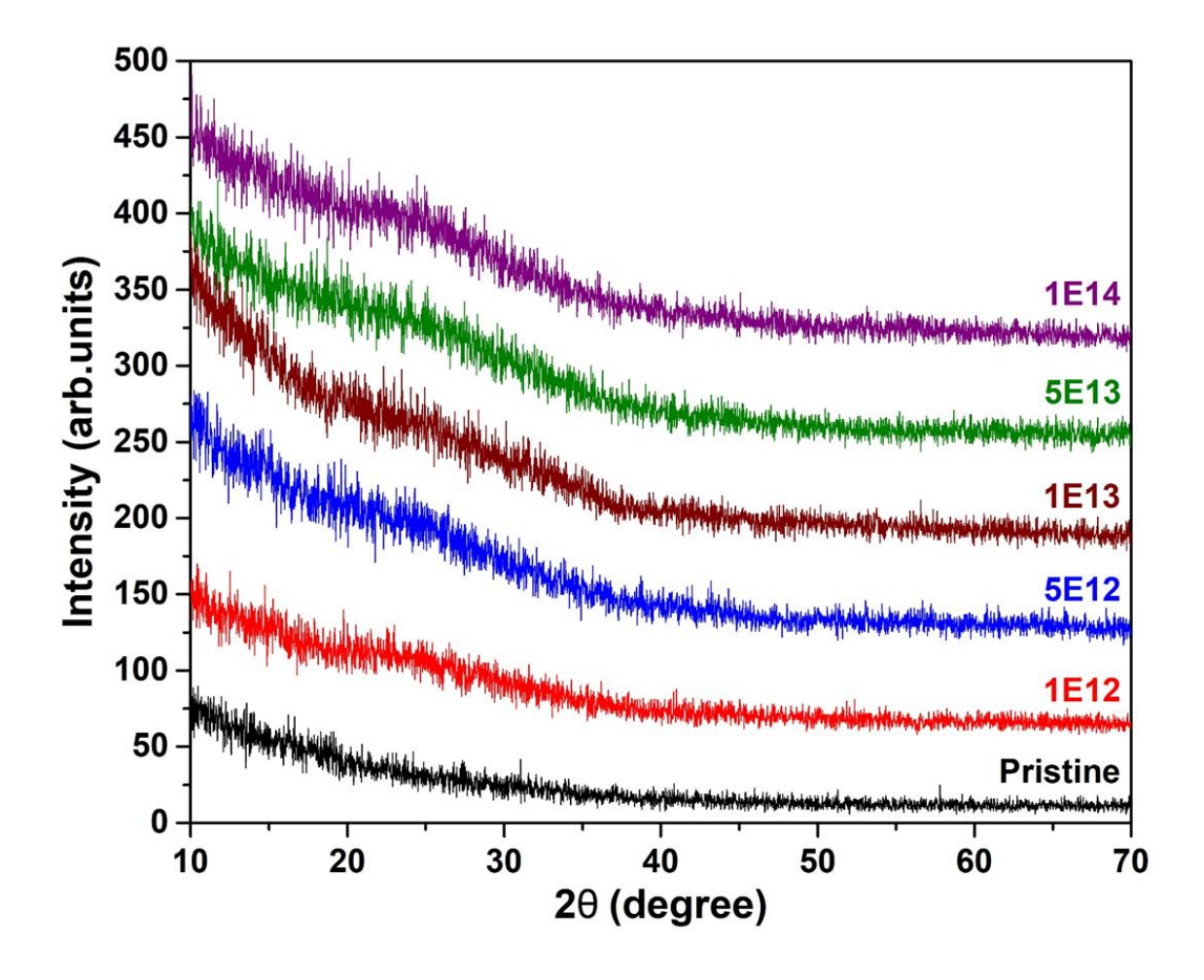


Fig. 5.10: GIXRD patterns of HfO<sub>2</sub>/GaO<sub>x</sub> bi-layer thin films.

As mentioned earlier, in some advanced CMOS transistors, standard gate oxide SiO<sub>2</sub> has been replaced by HfO<sub>2</sub> [1]. Therefore, it is significant to elucidate the strength of HfO<sub>2</sub> interface with different superior semiconductors. It is recognized that SiO<sub>2</sub> is highly susceptible over the Si to irradiation induced track formation. This encouraged us to understand the effects of SHI on HfO<sub>2</sub>/GaAs interface even though the SHI induced inter-mixing is observed in Si/HfO<sub>2</sub>, HfO<sub>2</sub>/GaO<sub>x</sub>/Si, HfO<sub>2</sub>/SiON/Si and HfO<sub>2</sub>/SiO<sub>2</sub>/Si interfaces [27, 32]. SHI irradiation can cause inter-diffusion of elements and can lead to the formation of inter-mixing of layers across the interfaces [50-52]. Hafnium, Oxygen and Gallium atoms are expected to diffuse across the HfO<sub>2</sub>/GaO<sub>x</sub> and HfO<sub>2</sub>/Si interfaces under SHI irradiation.

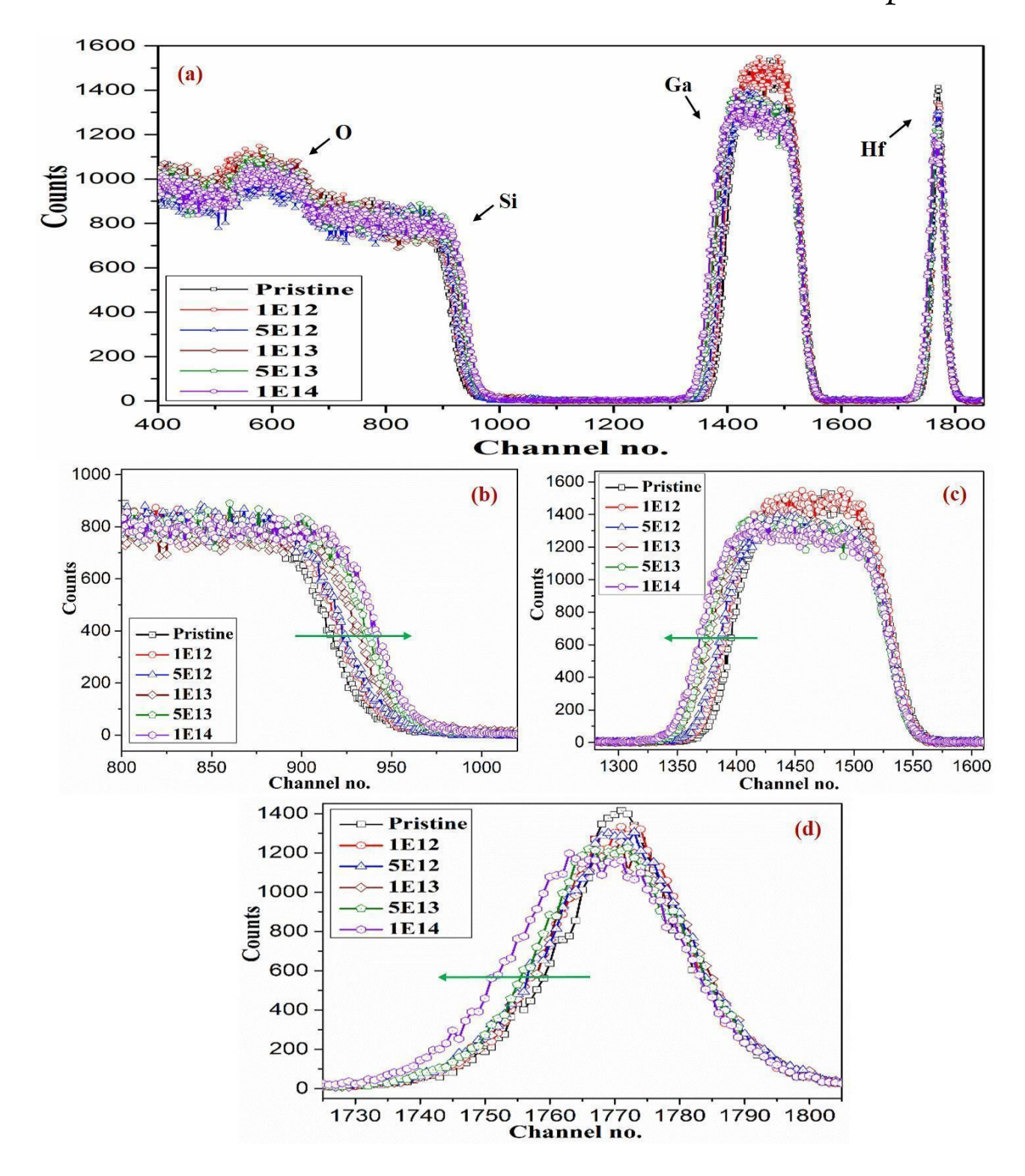


Fig. 5.11(a) - RBS spectra of as-grown and irradiated samples as a function of irradiation fluence. (b), (c), (d) - zoomed spectra corresponding to the surface edges of Si, Ga and Hf respectively.

Measured RBS spectra of as-grown and SHI irradiated samples as a function of irradiation fluence are shown in Fig. 5.11(a). Particularly, the zoomed spectra corresponding to the surface edges of Si, Ga and Hf are shown in Fig. 5.11(b), Fig. 5.11(c) and Fig 5.11(d) respectively. From these zoomed spectra of Si, Hf and Ga, it is observed that Hf and Ga diffuse in the direction of arrow i.e. towards the substrate, whereas Si diffuses in the opposite direction. This can lead to the development of intermixed layers at the interfaces. On the other hand, an inter-mixing of layer in between HfO<sub>2</sub> and Si is necessary for HfO<sub>2</sub> based MOS devices as HfO<sub>2</sub> itself is not thermally stable on Si. Therefore, it is significant to understand the irradiation effects on "Si/GaO<sub>x</sub>/HfO<sub>2</sub>" interfaces. Current study offers valuable information for studying the effects of SHI irradiation on such "Si/GaO<sub>x</sub>/HfO<sub>2</sub>" interfaces.

b) Electrical characteristics: MOS capacitors were fabricated by making top and bottom electrodes on as-grown and SHI irradiated samples. The current conduction mechanisms of these MOS capacitors were studied by performing I-V measurements while the High frequency (1 MHz) C-V measurements were performed to understand the memory performance as a function of irradiation fluence and the data is shown in Fig. 5.12(a) and Fig. 5.13(a). From I-V characteristics, the value of leakage current density at -1 V is seen to decrease from 1.4 x 10<sup>-9</sup> A/cm<sup>2</sup> to 6.8 x 10<sup>-1</sup>  $^{10}$  A/cm<sup>2</sup> for the irradiation fluence of  $1x10^{12}$  ions/cm<sup>2</sup> when compared to that of as-grown MOS structure as shown in Fig. 5.12(b). For the irradiation fluence of 5x10<sup>12</sup> ions/cm<sup>2</sup>, the leakage current density is found around 1.5 x 10<sup>-9</sup> A/cm<sup>2</sup>, which is attributed to the annealing of defects in the as-grown film through the electronic ionization/excitation produced due to SHI irradiation. Upon increasing the fluence to  $1 \times 10^{13}$  ions/cm<sup>2</sup>, an increase in the leakage current density to 2.1 x 10<sup>-9</sup> A/cm<sup>2</sup> has been observed. This leakage current density is almost equal to that of the as-grown MOS structure. Further increase in the irradiation fluences to 5x10<sup>13</sup> ions/cm<sup>2</sup> and 1x10<sup>14</sup> ions/cm<sup>2</sup> lead to a systematic rise in the tunneling current to 1.0 x 10<sup>-8</sup> A/cm<sup>2</sup> and 1.3 x 10<sup>-8</sup> A/cm<sup>2</sup> respectively. This can be attributed to SHI induced defect creation upon a certain fluence and interdiffusion/intermixing effects. Thus, the tunneling current decreases up to a certain irradiation fluence and increases above this critical fluence. This increase in leakage current density can lead to local heating effects and may further deteriorate the device performance. The existence of critical fluence suggests that a low dose treatment can improve the device performance and suggests a limit on the highest fluence that a device can withstand during various processing steps and or in their real time operation.

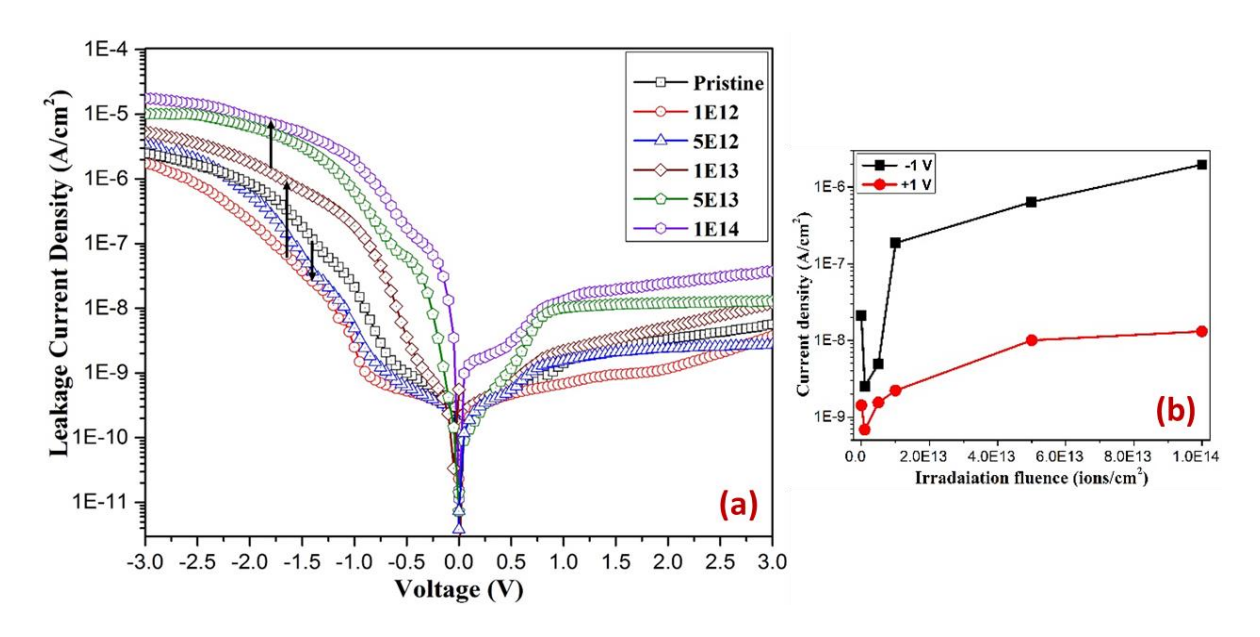


Fig. 5.12: (a) I-V characteristics of MOS capacitors and (b) current density at applied voltage of  $\pm 1$  V as a function of SHI irradiation fluence.

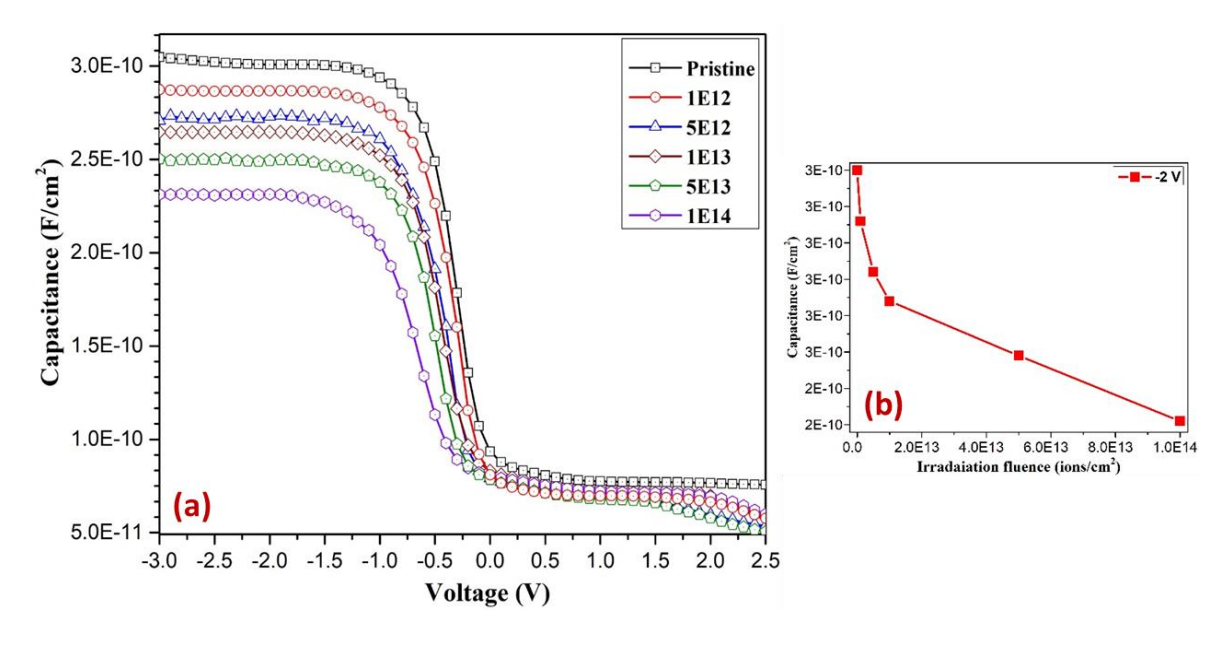


Fig. 5.13: (a) C-V characteristics of MOS capacitors and (b) accumulation capacitance at applied voltage of -2 V as a function of SHI irradiation fluence.

As discussed above, when an Ion interacts with a solid, at lower fluences, annealing of defects takes place due to inelastic collisions of ions with the target atoms i.e. electron energy loss which results in ionization and excitation of target atoms. It is observed that, up to the critical fluence  $(5x10^{12} \text{ ions/cm}^2)$  SHI induced defect annealing dominates and after this critical fluence, SHI

induced defect formation and possible development of intermixing layer dominates. Hence, for the fluences above this critical fluence, an orderly increase in the leakage current density has been observed. This phenomenon of SHI induced defects annealing, defect creation and inter-diffusion/in-intermixing effects are consistent with our earlier studies on SHI irradiation effects on HfO<sub>2</sub>/SiO<sub>2</sub>/Si and HfO<sub>2</sub>/Si interfaces [27, 32, 53].

From the C-V characteristics, an orderly decrease in the capacitance in the accumulation region with an increase of radiation fluence has been observed as shown in Fig. 5.13(b). It can be attributed to the inter-diffusion or formation of inter-mixing layer at the interface which leads to a change in thickness and dielectric constant of the oxide layer. As the irradiation fluence increases, a shift in flat band voltage and mid gap voltage towards the negative voltage have also been observed. This direction of flat band voltage shift indicates the polarity of SHI irradiation induced trapped charges on the oxide layer. Negative voltage shows an increase in the number of positive trapped charges. During the process, electrons can be swept out due to their higher mobility when compared to holes. Hence, the produced holes are trapped in the oxide layer which are responsible for a negative shift in the flat band voltage Thus, SHI irradiation results an orderly decrease in the capacitance in the accumulation region and an increase in the number of positive trapped charges due to SHI induced mixed layer and defect creation respectively. Hence, this study gives valuable information when such MOS structures based devices are to be used in harsh radiation environments, expected to be encountered in space, medical applications and experiments associated with high energy such as nuclear power plants.

#### 5.3.3. Effects of Gamma irradiation

Gamma irradiation is another technique to study the influence of defects on the performance of electronic devices. Gamma irradiation can produce defects all over the target material with a lesser amount of density compared to SHI irradiation. A set of as-grown samples were subjected to irradiation at numerous doses 4 kGy, 8 kGy, 16 kGy, 32 kGy, 48 kGy and 64 kGy at a constant irradiation dose rate of 4.64 kGy/h.

**Electrical characteristics:** MOS capacitors were fabricated by making top and bottom electrodes on as-grown and gamma irradiated samples. The current conduction mechanisms of these MOS capacitors were studied by performing I-V measurements while the High frequency (1 MHz) C-V measurements were performed to understand the memory performance as shown in Fig. 5.14 (a)

and Fig. 5.15(a). An orderly increase in the tunneling current has been observed with increasing of gamma dose.

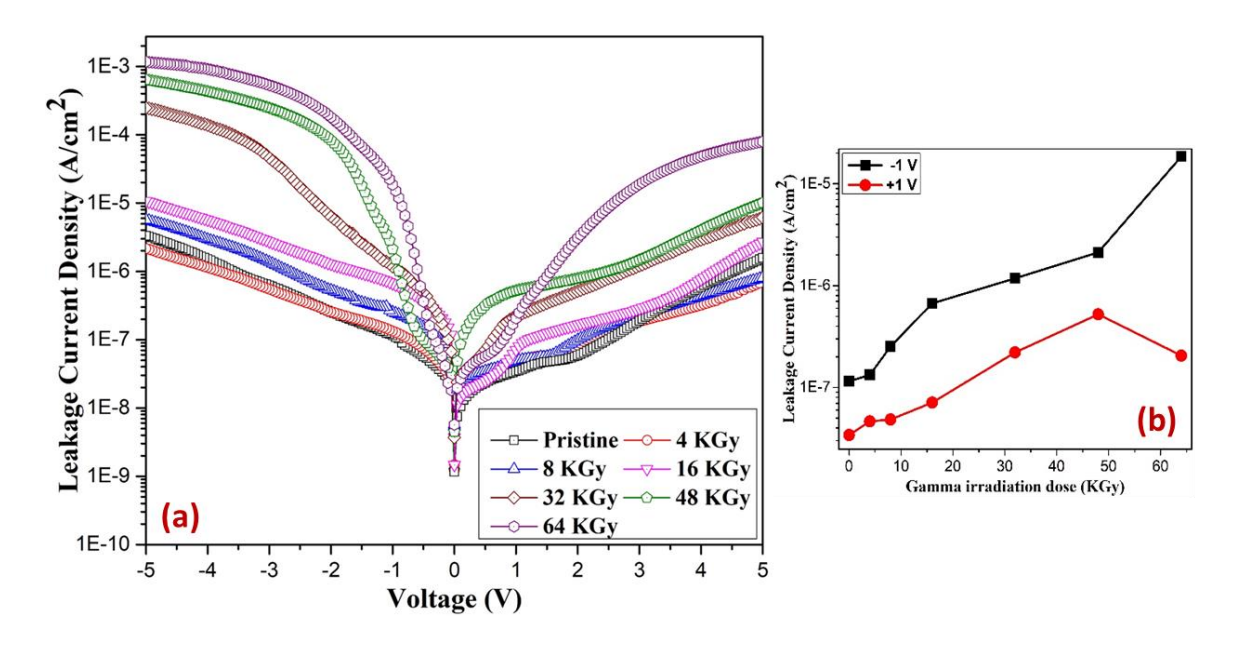


Fig. (a) 5.14: I-V measurements of MOS capacitors and (b) current density at applied voltage of ±1 V as a function of gamma irradiation dose.

From I-V characteristics, it is observed that the leakage current density rises systematically with increasing gamma dose. As shown in Fig. 5.14(b), the value of leakage current density at -1 V increases from 1.2 x 10<sup>-7</sup> A/cm² to 1.4 x 10<sup>-7</sup> A/cm² when the as-grown sample is irradiated with a dose of 4 KGy. At the same applied voltage, the leakage current density is found to increase to 2.5 x 10<sup>-7</sup> A/cm² for the irradiation dose of 8 KGy. With further increase in the dose to 16 KGy, the leakage current density increases to 6.6 x 10<sup>-7</sup> A/cm². Upon increasing the dose to 32 KGy, the current density increases to 1.2 x 10<sup>-6</sup> A/cm². At this dose, the leakage current density got increased by an order of magnitude when compared to that of an as-grown sample. The leakage current density further increases to 2.2 x 10<sup>-6</sup> A/cm² and 1.8 x 10<sup>-5</sup> A/cm² for the irradiation doses of 48 KGy and 64 KGy respectively. Almost two orders of magnitudes increase in the tunneling current for these doses is observed as compared to that of an as-grown sample. This increase in leakage current with respect to irradiation dose shows the existence of several types of defects in oxide films. This is due to the increase of interface traps and oxide trapped charge densities. On the other hand, the existence of defects are expected when these type of devices are used in radiation harsh environments.

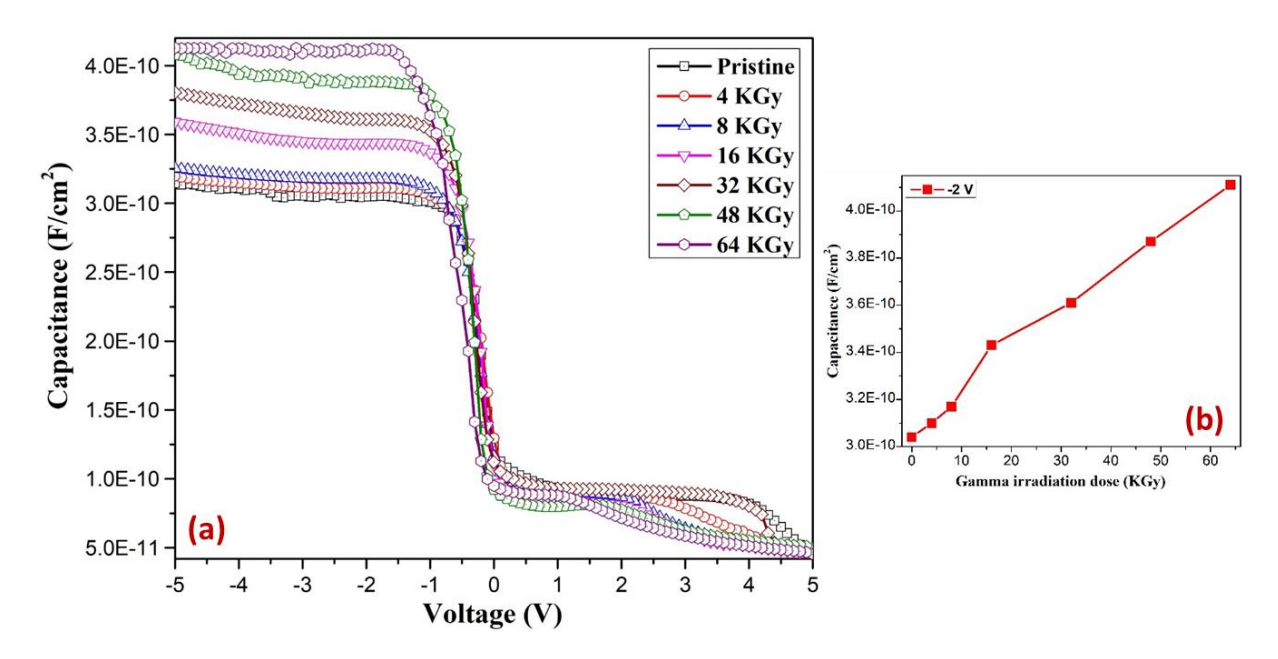


Fig. 5.15: (a) C-V measurements of MOS capacitors and (b) accumulation capacitance at applied voltage of -2 V as a function of gamma irradiation dose.

From the C-V characteristics, a systematic increase in the accumulation capacitance as a function of irradiation fluence has been observed as shown in Fig. 5.15(b). As the gamma irradiation dose increases, production of electron-hole pairs is expected to increase and these moveable charges may get trapped by the defects that are present in the as-grown samples which results in higher accumulation capacitance. The presence of trapped charges can increase the capacitance density [54]. Therefore, the pre-existing defects in the as-grown film mostly contribute to the increase in the accumulation capacitance. In addition to the increase in the accumulation capacitance, slight shift in the flat-band voltage towards negative voltage has been observed for higher gamma irradiation doses. As mentioned above, this direction of flat band voltage shift indicates the polarity of gamma irradiation induced trapped charges. Negative voltage shows an increase in the number of positive trapped charges. This study suggests that the presence of defects and the initial structure of the samples may encourage the subsequent development of defects induced by gamma irradiation. Pre-existing defects in the film have the capability to trap the moveable electron-hole pairs produced through the irradiation process prior to the recombination. The possibility of recombination of electron-hole pairs would be high in the absence of any defects during the gamma irradiation. On the other hand, the existence of defects are expected when these type of devices are used in radiation harsh environments like those encountered in space and nuclear power plants.

Therefore, this study is essential to realize these radiation damage evolution mechanisms and radiation tolerance of such devices when they are operated in radiation harsh environments.

#### **5.4. Conclusions**

Using RF magnetron sputtering deposition method, bi-layered thin films of GaO<sub>x</sub> (150 nm)/HfO<sub>2</sub> (30 nm) have been synthesized on 1 x 1 cm<sup>2</sup> sized Si substrates. The thickness of each layers have been estimated by cross-sectional FESEM and Profilometer measurements. RBS measurement has been performed on an as-grown sample and simulated the spectra with SIMNRA to estimate the thickness and elemental composition. One set of as-deposited HfO<sub>2</sub>/GaO<sub>x</sub>/Si structured samples were subjected to SHI irradiation by Ag ions of energy 120 MeV for various irradiation fluences and the structural and electrical properties of as-grown and SHI irradiated samples have been studied by employing different characterization techniques. From FESEM measurements, it has been observed that as-grown films contain highly strained, inhomogeneous and non-uniform large grains with average grain size of 34.5 nm which are arbitrarily oriented. SHI irradiated films show development of new grains with decreased average size. At highest irradiation fluence, formation of homogeneous spherical uniform grains with average size of 13.8 nm have been observed. This decrease in the grain size is attributed to SHI induced grain fragmentation. The highly strained grain structures are expected to be relaxed to become stress-free during the irradiation process to induce grain fragmentation. After SHI irradiation, SHI induced inter-diffusion of atoms and formation of intermixing layers at the interfaces have been observed. HfO<sub>2</sub>/GaO<sub>x</sub> based MOS capacitors have been fabricated by depositing top and bottom electrodes on as-grown and SHI irradiated samples to study the SHI irradiation induced effects on the electrical characteristics of these MOS capacitors. At lower irradiation fluences, due to SHI induced annealing of defects, a decrease in the leakage current density has been observed up to the fluence of 5x10<sup>12</sup> ions/cm<sup>2</sup>. Further increase in the irradiation fluences to above the critical fluence results an orderly increase in the leakage current density. This increase in the leakage current density can be attributed to SHI induced defect creation up to a certain fluence and inter-diffusion/intermixing effects. Thus, the tunneling current decreases up to a certain irradiation fluence. Then upon increasing the fluence beyond that fluence, results in increase of leakage current density that leads to increase in local heating effects. Hence the device performance may further worsen during its operation. From the C-V characteristics, a systematic increase in the accumulation capacitance as a function of

that can modify the effective thickness of the oxide. In addition to the decrease in the accumulation capacitance, shift in flat band voltage and mid gap voltage towards the negative voltage has also been observed which is attributed to increase in number of positive trapped charges as a function of irradiation fluence. Another set of as-grown samples were subjected to gamma irradiation. From I-V measurements we notice a systematic increase in the leakage current density with gamma irradiation dose increase, which is attributed to the pre-existence of defects in the as-grown samples and increased defects and trapped charges due to gamma irradiation. From the C-V characteristics, a systematic increase in the accumulation capacitance and a slight shift in the flatband voltage towards negative voltage as a function of irradiation fluence is noticed which may be accredited to the probable increase in number of positive trapped charges. Therefore, this irradiation induced study gives valuable information when such devices are to be used in harsh radiation environments as these MOS structures are expected to be used in many devices in space, medical applications and experiments associated with high energy such as nuclear power plants.

# 5.5. References

- [1] "Intel's Fundamental Advance in Transistor Design Extends Moore's Law, Computing Performance", Intel News Release, 2007,

  <a href="https://www.intel.com/pressroom/archive/releases/2007/20071111comp.htm">https://www.intel.com/pressroom/archive/releases/2007/20071111comp.htm</a>.
- [2] S. J. Pearton, R. Deist, F. Ren, L. Liu, A. Y. Polyakov, J. Kim, *J. Vac. Sci. Technol. A* **2013**, 31, 050801.
- [3] M. Higashiwaki, K. Sasaki, A. Kuramata, T. Masui, S. Yamakoshi, *Phys. status Solidi* **2014**, 211, 21.
- [4] S. Rafique, L. Han, M. J. Tadjer, J. A. Freitas, N. A. Mahadik, H. Zhao, *Appl. Phys. Lett.* 2016, 108, 182105.
- [5] M. Higashiwaki, H. Murakami, Y. Kumagai, A. Kuramata, *Jpn. J. Appl. Phys.* **2016**, Part 1 55, 1202A1.
- [6] M. Higashiwaki, G. H. Jessen, *Appl. Phys. Lett.* **2018**, 112.

- [7] J. Millan, P. Godignon, X. Perpina, A. Perez-Tomas, J. Rebollo, *IEEE Trans. Power Electron.* **2014**, 29, 2155.
- [8] M. A. Mastro, A. Kuramata, J. Calkins, J. Kim, F. Ren, S. J. Pearton, *ECS J. Solid State Sci. Technol.* **2017**, 6, P356.
- [9] Y. H. Zhang, Z. X. Mei, H. L. Liang, X. L. Du, Chin. Phys. B 2017, 26.
- [10] Heike Riel, Lars-Erik Wernersson, Minghwei Hong, Jesus A. del Alamo, "Materials Research Society Bulletin" **2014**, 39, 668-677.
- [11] S. Pearton, J. Yang, P. H. Cary IV, F. Ren, J. Kim, M. J. Tadjer, M. A. Mastro, *Appl. Phys. Rev.* **2018**, 5, 011301.
- [12] M. A. Mastro, A. Kuramata, J. Calkins, J. Kim, F. Ren, S. Pearton, *ECS J. Solid State Sci. Technol.* **2017**, 6, P356–P359.
- [13] M. Higashiwaki, K. Sasaki, H. Murakami, Y. Kumagai, A. Koukitu, A. Kuramata, T. Masui, S. Yamakoshi, *Semicond. Sci. Technol.* 2016, 31, 034001.
- [14] M. Higashiwaki, K. Sasaki, A. Kuramata, T. Masui, S. Yamakoshi, *Appl. Phys. Lett.* **2012**, 100, 013504.
- [15] Hang Dong, Shibing Long, Haiding Sun, Xiaolong Zhao, Qiming He, Yuan Qin, Guangzhong Jian, Xuanze Zhou, Yangtong Yu, Wei Guo, Wenhao Xiong, Weibing Hao, Ying Zhang, Huiwen Xue, Xueqiang Xiang, Zhaoan Yu, Hangbing Lv, QiLiu, Ming Liu, *IEEE Electron Device Letters* **2019**, 40, 9.
- [16] Kohei Sasaki, Quang Tu Thieu, Daiki Wakimoto, Yuki Koishikawa, Akito Kuramata, Shigenobu Yamakoshi, *Applied Physics Express* **2017**, 10, 124201.
- [17] M. H. Wong, K. Sasaki, A. Kuramata, S. Yamakoshi, M. Higashiwaki, *IEEE Electron Device Lett.* **2016**, 37, 212.
- [18] Hang Dong, Wenxiang Mu, Yuan Hu, Qiming He, Bo Fu, Huiwen Xue, Yuan Qin, Guangzhong Jian, Ying Zhang, Shibing Long, Zhitai Jia, Hangbing Lv, Qi Liu, Xutang Tao and Ming Liu, *AIP Advances* **2018**, 8, 065215.
- [19] A. J. Green, K. D. Chabak, M. Baldini, N. Moser, R. Gilbert, R. C. Fitch, G. Wagner, Z. Galazka, J. McCandless, A. Crespo, K. Leedy, G. H. Jessen, *IEEE Electron Device Lett*.

- **2017,** 38, 790.
- [20] M. Higashiwaki, K. Sasaki, T. Kamimura, M. Hoi Wong, D. Krishnamurthy, A. Kuramata,
   T. Masui, S. Yamakoshi, *Appl. Phys. Lett.* 2013, 103, 123511.
- [21] M. J. Tadjer, N. A. Mahadik, V. D. Wheeler, E. R. Glaser, L. Ruppalt, A. D. Koehler, K. D. Hobart, C. R. Eddy, F. J. Kub, *ECS J. Solid State Sci. Technol.* **2016**, 5, P468–P470.
- [22] D. K. Avasthi, Y.K. Mishra, F. Singh, J.P Stoquert. Nucl. Inst. Meth. Phys. Res. B 2010, 268(19), 3027.
- [23] Y. K. Mishra, A. Kumar, D.K. Avasthi, J. Polym. Mat. 2008, 25(3), 303.
- [24] D. K. Avasthi, Def. Sci. J. 2009, 59, 401.
- [25] M. Dhanunjaya, D. K. Avasthi, A. P. Pathak, S. A. Khan, S. V. S. Nageswara Rao, *Appl. Phys. A* 2018, 124:587.
- [26] M. Dhanunjaya, S A Khan, A P Pathak, D K Avasthi, S V S Nageswara Rao, J. Phys. D: Appl. Phys. 2017, 50, 505301.
- [27] N. Manikanthababu, T. K. Chan, S. Vajandar, V. Saikiran, A. P. Pathak, T. Osipowicz, S.V.S. Nageswara Rao, *Appl. Phys. A* **2017**, 123:303.
- [28] B. C. Hendrix, A. S. Borovik, C. Xu, J.F. Roeder, T. H. Baum, M. J. Bevan, M. R. Visokay, J. J. Chambers, A. L. Rotondaro, H. Bu, L. Colombo, *Appl. Phys. Lett.* 2002, 80, 2362.
- [29] S. K. Srivastava, R. Kumar, D. Kabiraj, R.S. Patel, A. K. Majumdar, A. Gupta, D. K. Avasthi, *Nucl. Instr. Meth. Phys. Res. B* **2006**, 243, 304.
- [30] H. Amekura, S. Mohapatra, U. B. Singh, S.A. Khan, P. K. Kulriya, N. Ishikawa, N. Okubo,D. K. Avasthi, *Nanotechnology* 2014, 25,435301.
- [31] N. Manikanthababu, M. Dhanunjaya, S.V.S. Nageswara Rao, A.P. Pathak, *Nucl. Inst. Meth. Phys. Res. B* **2016**, 379, 230.
- [32] N. Manikanthababu, S. Vajandar, N. Arun, A. P. Pathak, K. Asokan, T. Osipowicz, T. Basu, and S. V. S. Nageswara Rao, *Appl. Phys. Lett.* **2018**, 112, 131601.
- [33] M. Dhanunjaya, K. Vinod Kumar, N. Manikanthababu, S.V.S. Nageswara Rao, A.P. Pathak, *Nucl. Instr. Methods Phys. Res. B* **2019**, 446, 37–42.

- [34] G. Szenes, *Phys. Rev. B* **1995**, 51, 8026.
- [35] G.S. Virdi, B.C. Pathak, D.K. Avasthi, D. Kanjilal, *Nucl. Instr. Methods Phys. Res. B* **2002**, 187, 189–200.
- [36] P. C. McIntyre, ECS Transactions **2007**, 11, 235–249.
- [37] N. Manikanthababu, N. Arun, M. Dhanunjaya, S. V. S. Nageswara Rao, *Radiat. Eff. Defects Solids* **2016**, 171, 77–86.
- [38] S. J. Maurya, *Mater. Sci. Mater. Electron.* **2016**, 27, 12796–12802.
- [39] F. Yuan, Z. Zhang, J. C. Wang, L. Pan, J. Xu, C. S. Lai, *Nanoscale Res. Lett.* **2014**, 9, 1–6.
- [40] Hasina F. Huq, Rocio Y. Garza, Roman Garcia-Perez, *Journal of Modern Physics* **2016**, 7, 2028-2037.
- [41] J. F. Ziegler, "SRIM-2003". Nucl. Instr. Meth. B. **2004**, 219-220: 1027.
- [42] M. Mayer, *SIMNRA User's Guide*, Report IPP 9/113, **1997** (MaxPlanck-Institut fur Plasmaphysik, Garching, Germany).
- [43] H. Bender, T. Conard, O. Richard, B. Brijs, J. Pétry, W. Vandervorst, C. Defranoux, P. Boher, N. Rochat, C. Wyon, P. Mack, J. Wolstenholme, R. Vitchev, L. Houssiau, J. J. Pireaux, A. Bergmaier, G. Dollinger, *Proceedings of the Electrochemical Society* 2003, 2003–03, 223-232.
- [44] D. Triyoso, R. Liu, D. Roan, M. Ramon, N. V. Edwards, R. Gregory, D. Werho, J. Kulik, G. Tam, E. Irwin, X-D. Wang, L. B. La, C. Hobbs, R. Garcia, J. Baker, B. E. White, Jr., P. Tobin, J. Electrochem. Soc. 2004, 151, F220.
- [45] http://www.tamura-ss.co.jp/en/release/20131122/pdf/150210.pdf
- [46] E. G. Villora, S. Arjoca, K. Shimamura, D. Inomata, K. Aoki, *Proc. of SPIE* **2014**, 8987, 89871U.
- [47] Xinyi Dai, Aijun Zhou, Lidong Feng, Ying Wang, Jin Xu, Jingze Li, *Thin Solid Films* **2014**, 567, 64–71.
- [48] Manvendra Kumar, Ratnesh K. Pandey, Parasmani Rajput, S. A. Khan, Fouran Singh, D. K. Avasthi, Avinash C. Pandey, *J. Alloy and Comp.* 2017, 695, 83-90.

- [49] M. Toulemonde, A. Benyagoub, C. Trautmann, N. Khalfaoui, M. Boccanfuso, C. Dufour, F. Gourbilleau, J. J. Grob, J. P. Stoquert, J. M. Costantini, F. Haas, E. Jacquet, K. O. Voss, and A. Meftah, *Phy. Rev. Lett.* 2012, 85, 054112.
- [50] Garima Agarwal, Pratibha Sharma, I.P. Jain, Applied Surface Science 2006, 253, 1165-69.
- [51] Nisha Bansal, Sarvesh Kumar, Saif Ahmad Khan, R.S. Chauhan, *Radiation Effects and Defects In Solids* **2016**, 171, 290–296.
- [52] Vantari Siva, Abdelhak chettah, Biswarup Satpati, S. Ojha, D. Kanjilal, Pratap K. Sahoo, *RSC Advances* **2016**, 6, 58950–58956.
- [53] N. Manikanthababu, V. Saikiran, T. Basu, K. Prajna, S. Vajandar, A.P. Pathak, B.K. Panigrahi, T. Osipowicz, S.V.S. Nageswara Rao, *Thin Solid Films* **2019**, 682, 156–162.
- [54] N. Manikanthababu, N. Arun, M. Dhanunjaya, S.V.S. Nageswara Rao, A. P. Pathak, *Radiation Effects and Defects in Solids* **2016**, 171:1-2, 77-86.

# Effects of Laser Annealing on the structural and electrical properties of HfO<sub>2</sub> and Au/HfO<sub>2</sub> thin films deposited on Si

The main aim of this chapter is to report on fabrication of high-density arrays of gold nanoparticles on the surface of HfO2 thin films without altering the phase of HfO2 using an athermal laser annealing technique. HfO2 (~ 30 nm) thin films synthesized on Si substrates by ebeam evaporation technique were exposed to Laser Annealing. Structural and electrical properties of pristine and laser annealed HfO2 thin films have been studied as a function of the number of laser pulses incident on the sample. It is observed that pristine and laser annealed films are predominantly amorphous in nature, though there are observable changes in their morphology. Further, Au ( $\sim 5$  nm) and amorphous  $HfO_2$  ( $\sim 10$  nm) films deposited on Si by thermal evaporation and e-beam evaporation methods respectively were subjected to Laser Annealing to produce an array of Au nanoparticles. Here, it is necessary to note that the usual thermal annealing methods would modify the phase of the HfO2. The structural modifications and optical properties of asgrown and laser annealed gold nanoparticles have been elucidated by performing FESEM, GIXRD and UV-Vis absorption measurements. The leakage current conduction through the gate oxide with and without embedded Au nanoparticles has been studied by several tunneling mechanisms by investigating the Leakage current – Voltage (I-V) characteristics. Memory performance of MOS structures with and without embedded Au nanoparticles has been studied by Capacitance – Voltage (C-V) measurements. Applications of these high-density Au nanoparticles in the fabrication of SERS substrates for molecular detection and floating gate type memory devices have been discussed in detail (part of this work is published in J Mater Sci: Mater Electron. 2022, 32:2973-2986).

#### 6.1. Introduction

In previous chapters, the effects of electronic excitation induced by Gamma irradiation and SHI irradiation on the structural changes and subsequent effects on the electrical characteristics of HfO<sub>2</sub> thin films deposited on high mobility and wide band gap semiconductors have been studied. In this chapter, the effects of electronic excitation induced by laser annealing/irradiation on HfO<sub>2</sub> thin films will be discussed. In recent years, the effects of electronic excitation by laser annealing/irradiation on various properties has attracted significant attention [1, 2]. Laser irradiation/annealing induced defect creation in oxides, crystallization and inter-diffusion/intermixing by using ultrafast lasers have been reported [3-5]. Rittman et al. [6] reported the phase transition in ZrO<sub>2</sub> from monoclinic to tetragonal phase by employing ultrafast laser irradiation and the results are consistent with the phase transformations due to SHI irradiation [7].

As discussed in previous chapters, the standard gate oxide SiO<sub>2</sub> has been replaced by HfO<sub>2</sub> in some advanced CMOS transistors [8]. Further, to increase the storage capacity and to improve the retention characteristics of floating gate-based flash memory devices, incorporation of metal or semiconductor nanoparticles (NPs) in-between the two high-k dielectric gate oxide layers has been proposed [9-12]. In flash memory devices, an electrically floating metal gate is there within the gate oxide [13]. In 1967, a polysilicon-based floating gate-based flash memory was invented by D. Kahng and S. M. Sze [14]. This will certainly increase the dielectric loss and leakage current as compared to that of an oxide without an embedded floating metal gate. However, this gate is essential for getting the memory feature. In current flash memory devices, a metal floating gate within the gate oxide and a common gate on the top of the gate oxide are there [13]. When a high V<sub>GS</sub> is applied such that a huge Avalanche current flows during the set operation. This will induce a charge on the embedded floating gate. Now, ideally, this charge on the floating gate cannot escape even if the V<sub>GS</sub> is removed. This charge will turn the device ON and hence the device is non-volatile. This charge can be removed only by applying reverse voltage or by subjecting it to UV for erasing the memory. Hence an embedded floating metal gate is required for fabricating these memory devices. Now this continuous floating gate is being replaced by "isolated metal NPs" [15]. The dielectric loss will be less for the device with isolated metal NPs based floating gate memory devices than that of a device with continuous floating metal gate [16]. The floating gatebased memory devices with embedded metal NPs have the benefits of extensive range of workfunctions, unconventional efficiency and low operating voltages as compared to the memory devices with embedded semiconductor NPs [17]. When an array of isolated NPs is used as a floating gate, then each isolated particle will store the charge. Some particles will hold the total charge even if they lose their charge over some unwanted leakage paths. Hence, such a memory device will have superior retention characteristics as compared to that of the devices which use a continuous metal layer as an embedded floating gate [16].

To increase the storage capacity and to improve the retention properties of these floating gate-based memory devices, integration of large work-function metal NPs like Silver (Ag), Gold (Au) and Platinum (Pt) in-between the two oxide layers have been reported [18]. Among these NPs with large work-functions, Au NPs gained more attention because they are easily produced, possess greater density of states and large work function (5.1 eV), which produces deep potential well that avoids retention loss of the devices and improves carrier confinement [19, 20]. One more significant use of these isolated metal NPs is in the fabrication of substrates for SERS spectroscopy based molecular detection. Large work-function isolated metal NPs such as Au and Ag, have significance in SERS studies for molecular detection because they can favor plasmonic resonance [21, 22]. The SERS studies for molecular detection essentially deal with the improvement in the electromagnetic field due to the confined surface plasmon resonance. This improvement in the electromagnetic field is directly related to the size, shape, uniformity and density of metal NPs [23, 24].

For producing an array of high density Au NPs, several thin film deposition techniques such as RF/DC Sputtering, electron beam (e-beam) evaporation, Chemical Vapor Deposition (CVD) and Atomic Layer deposition (ALD) have been used [25-28]. To achieve the uniform spherical NPs, post deposition Thermal Annealing (TA), Rapid Thermal Annealing (RTA) and Ion beam irradiation methods have been used [29, 30]. Floating gate type memory devices with high density metal NPs have large charge storage capacity. On the other hand, floating gate type memory devices with good uniform metal NPs are helpful in enhancing the reproducibility of device properties [31]. TA and RTA procedures have been widely used to produce Au NPs in-between two HfO<sub>2</sub> thin-film layers [32, 33]. However, the usual TA and Ion beam irradiation procedures are known to crystallize the tunneling oxide layer which result in an increase in the leakage currents due to tunneling and can deteriorate the device properties, particularly, for modern alternate high-

k dielectric oxides like HfO<sub>2</sub> [34-36]. Now, the main challenge is to produce an array of high-density metal NPs without affecting the phase of the underneath tunneling oxide layer. Non-thermal methods such as Laser Annealing (LA) offer alternate techniques to anneal layers of interest without altering the phase of the substrates and/or the surrounding medium.

In 2016, Nikolaos Kalfagiannis et al. [37] suggested this method of Modifying NP Arrays by Laser Induced Self Assembly (MONA-LISA) to yield the pre-determined patterns of metal nanostructures. In 2018, L. Kastanis et al. [38] used the LA method to achieve uniformly spaced Au nanocrystals (NCs) and developed n-Si/SiO<sub>2</sub>/Au-NCs/Y<sub>2</sub>O<sub>3</sub>/Au structured floating gate type memory devices. LA is a technique capable of producing Au NPs because it offers a high degree of control over the formation of NPs and it has a benefit of defect minimization in the underneath tunneling oxide layer [39]. Furthermore, the LA method can be used in producing uniformly high-density metal NPs in-between the gate oxide layers without modifying the phase of high-k dielectric oxides.

In this chapter, the structural and electrical properties of pristine and laser annealed HfO<sub>2</sub> thin films have been studied as a function of the number of laser pulses incident on the sample. Further, this non-thermal LA technique has been used to synthesize an array of high density Au NPs on the surface of amorphous HfO<sub>2</sub> thin-films without modifying the phase of HfO<sub>2</sub>. Structural and optical properties of these Au NPs have been studied. The leakage current conduction through the gate oxide with and without embedded Au NPs has been studied by several tunneling mechanisms by investigating the I-V characteristics. Memory performance of MOS structures with and without embedded Au nanoparticles has been studied by C-V measurements. These Au NPs can be used as SERS substrates for molecular detection and embedded Au NPs in HfO<sub>2</sub> matrix can enhance the storage capacity of the floating gate type memory devices.

# **6.2. Experimental details**

**6.2.1. Synthesis of thin films:** The main objectives of this chapter are 1) to study the effects of LA on the structural changes and subsequent effects on the electrical characteristics of HfO<sub>2</sub> thin-films, 2) to fabricate a high density array of Au NPs on the surface of HfO<sub>2</sub> by LA method without affecting the phase of HfO<sub>2</sub>. For this purpose, we have deposited HfO<sub>2</sub> thin-films of  $\sim 30$  nm and  $\sim 10$  nm on Boron doped p-type (1-10  $\Omega$ cm) Silicon (100) and Quartz substrates using electron

beam (e-beam) evaporation system. Prior to the deposition, Si and Quartz substrates were cut into the pieces of size 1 cm x 1 cm each and cleaned using ultra-sonication in acetone followed by isopropanol and deionized water each for 5 min. Then, these substrates were dried with nitrogen gas and instantly loaded into the chamber. We used commercially available pellets of  $HfO_2$  (purity 99%) as a target material for e-beam evaporation to deposit  $HfO_2$  thin-films on these substrates. After loading the substrates, the deposition chamber was evacuated to  $1.4 \times 10^{-6}$  mbar pressure. 10 standard cubic centimeters per minute (SCCM) of  $O_2$  gas was pumped into the chamber throughout the deposition of  $HfO_2$  thin-films. On the surfaces of these as-grown ~ 10 nm  $HfO_2$  thin-films, a thin non-continuous layer of Au (~ 5 nm) was deposited using thermal evaporation method in the same deposition chamber without disturbing the vacuum.

**6.2.2. Laser Annealing:** These HfO<sub>2</sub> thin-films of ~ 30 nm and Au (~ 5 nm)/HfO<sub>2</sub> (~ 10 nm) bilayered samples were subjected to LA by using a Kr F excimer laser system having the wavelength of 248 nm (Coherent-Complex Pro 102 F available in-house) at the repetition rate of 10 Hz. The laser fluence (300 m J cm<sup>-2</sup>) and laser spot size (1 x 1 cm<sup>2</sup>) were maintained constant throughout the LA process for all the samples. HfO<sub>2</sub> thin-films of ~ 30 nm thickness were subjected to LA by varying the number of laser pulses from 100 to 2000. Further, an array of uniform and high density spherical Au NPs have been synthesized by changing the number of laser pulses incident on the sample. An array of high density spherical Au NPs have been produced by varying the number of laser pulses from 100 to 500.

**6.2.3. Sample Characterization**: As-grown and laser annealed HfO<sub>2</sub> and Au/HfO<sub>2</sub> bi-layer thin films deposited on Si and Quartz substrates as a function of number of laser pulses, were characterized by different techniques to study the effects of LA. FESEM measurements were performed on as-grown and laser annealed HfO<sub>2</sub> and Au-NPs/HfO<sub>2</sub> films deposited on Si to estimate the size, surface morphology and uniformity using Carl ZEISS, FEG, ultra-55 microscope available in-house. FESEM - Energy Dispersive X-ray Spectroscopy analysis (EDX) measurements were performed to study the elemental composition. Ultra Violet - Visible (UV-Vis) absorption measurements (in the range of 200 nm – 1100 nm) of as-grown and laser annealed Au-NPs/HfO<sub>2</sub> films deposited on quartz substrates as a function of number of laser pulses were performed using UV-visible-NIR spectrometer. Grazing incident x-ray diffraction (GIXRD) measurements were performed on as-grown and laser annealed HfO<sub>2</sub> and Au-NPs/HfO<sub>2</sub> films

deposited on Si to study the phase changes using Bruker D8 Advance diffractometer with Cu K $\alpha$ ,  $\lambda = 1.54$  Å. Surface Enhanced Raman Spectroscopy (SERS) measurements were performed by drop-casting Rhodamine 6G (R6G) dye on the surface of as-grown and laser annealed Au-NPs/HfO<sub>2</sub> films deposited on Si. A laser of 632 nm excitation wavelength (LabRAM HR Evolution-HORIBA Scientific confocal Raman microscope with 100X magnification available inhouse) has been used for SERS measurements.

**6.2.4. Fabrication and electrical characterization of MOS capacitors:** On top of these uniform spherical Au NPs produced on HfO<sub>2</sub>/Si using LA at 500 laser pulses, one more layer of HfO<sub>2</sub>  $\sim 20$ nm was synthesized by same e-beam evaporation technique under the same deposition conditions used for depositing tunneling oxide layer of HfO<sub>2</sub>. This new layer of HfO<sub>2</sub> of thickness ~ 20 nm is considered as a blocking layer. As top electrode (TE), metal electrodes of 100 nm thick Au dots with 1 mm in diameter were synthesized using a shadow mask on top of the blocking layer of HfO<sub>2</sub> and as-grown and laser annealed HfO<sub>2</sub> (~ 30 nm) thin-films. As bottom electrode (BE), Epoxy resin and conductive Ag paste on Al foil was used underneath the Si substrates. To compare the influence of laser annealed Au NPs embedded in HfO<sub>2</sub> matrix on the electrical characteristics, a MOS capacitor without embedded Au NPs in the oxide layer (pristine HfO<sub>2</sub> ~ 30 nm) was also fabricated. These two interfaces TE/HfO2 (metal/oxide) and Si/BE (semiconductor/metal) are expected to behave in the same manner for both the devices with and without Au NPs in the HfO<sub>2</sub> layer. Therefore, the changes in the electrical characteristics (leakage currents and Capacitance hysteresis) of these MOS capacitors are attributed to the presence or absence of Au NPs in the oxide layer. The schematics of laser annealing and final structures of MOS capacitors without Au NPs (Au/HfO<sub>2</sub>/Si) and with Au NPs (Au/HfO<sub>2</sub>/Au-NPs/HfO<sub>2</sub>/Si) are shown in Fig. 6.1 and Fig. 6.2 respectively. Electrical characterizations such as Leakage current – Voltage (I-V) in voltage range from -5 V to 5 V and Capacitance – Voltage (C-V) in the same voltage range at 1 MHz frequency were performed on both the devices with and without Au NPs in the HfO<sub>2</sub> layer by using an Agilent technologies (B1500A) semiconductor device analyzer at in-house Centre for Nanotechnology (CFN).

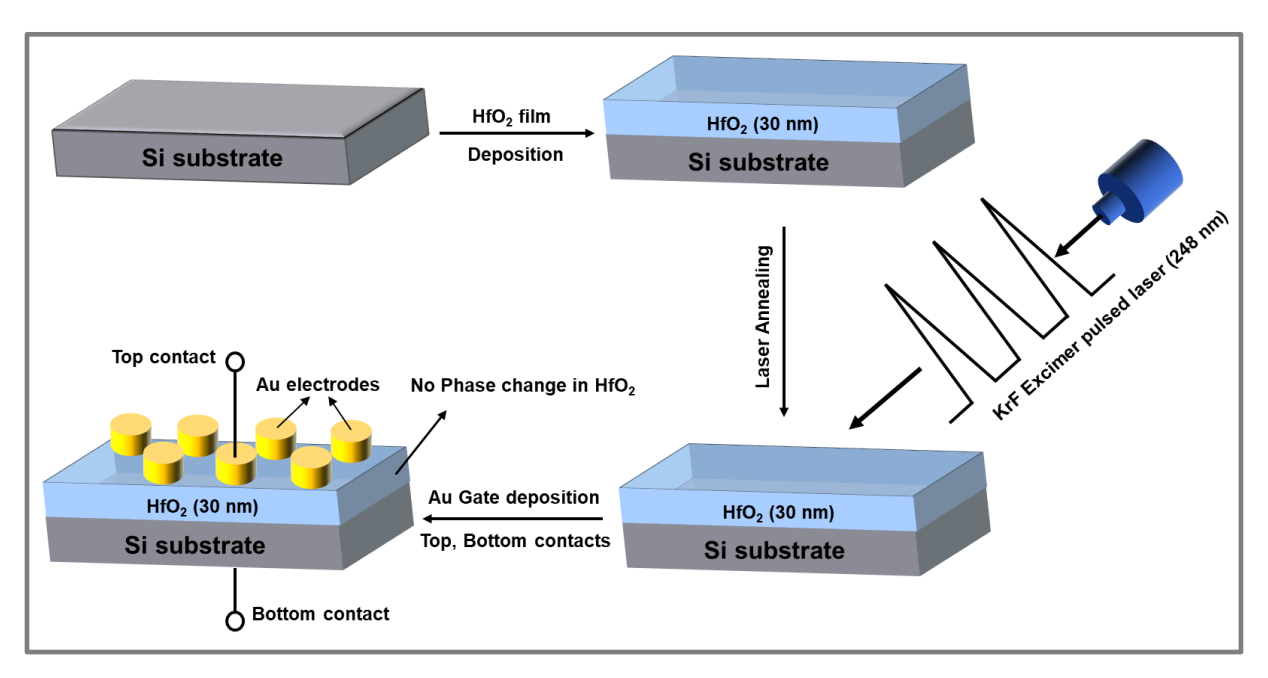


Fig. 6.1: Schematic representation of laser annealing and fabrication of HfO<sub>2</sub> based MOS capacitor without Au NPs.

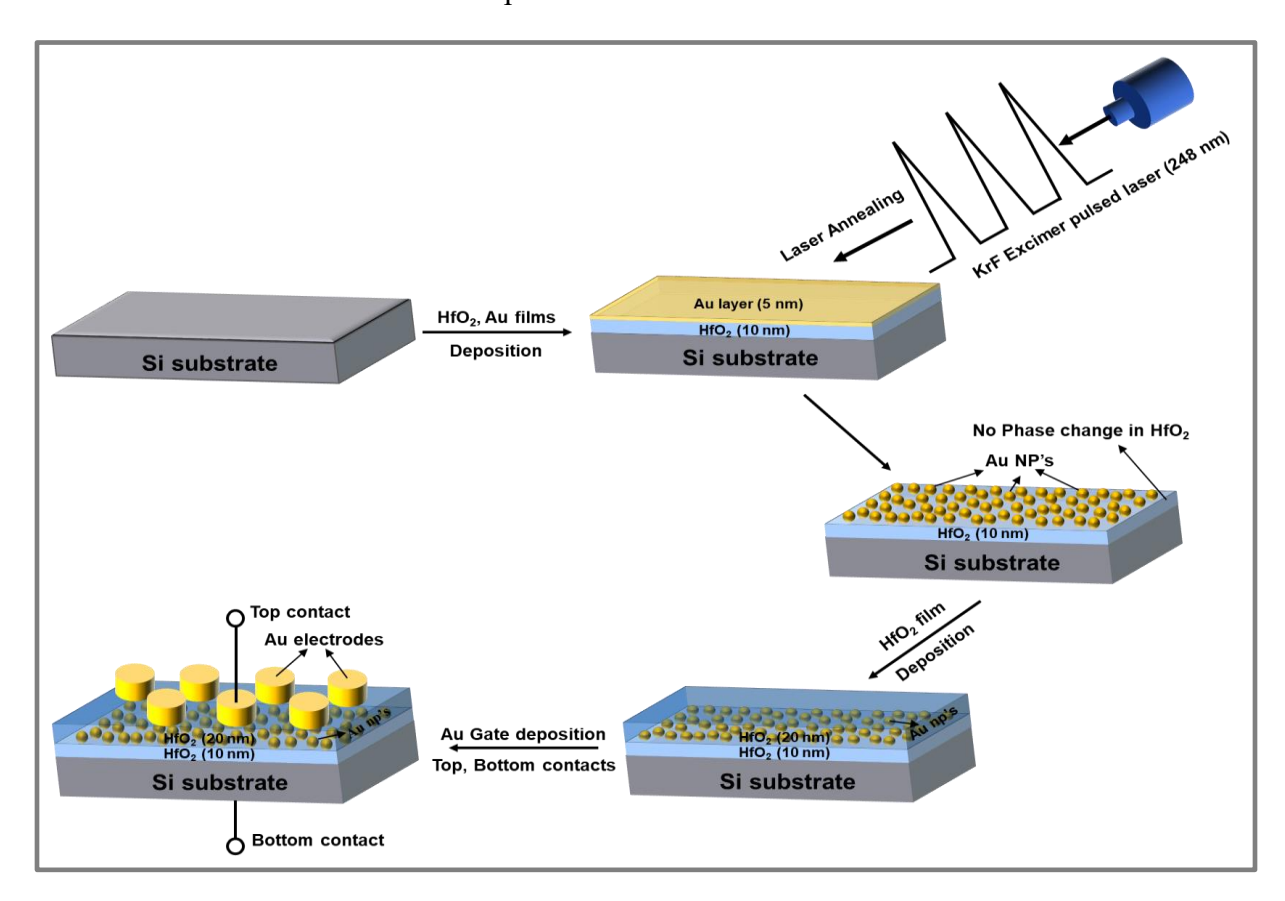


Fig. 6.2: Schematic representation of fabrication of Au NPs embedded HfO<sub>2</sub> dielectric based MOS capacitor.

# 6.3. Results and discussions

# A. Effects of laser annealing on the structural and electrical properties of HfO2 thin films:

 $HfO_2$  thin films of ~ 30 nm thickness were subjected to LA by varying the number of laser pulses from 100 to 2000. The structural modifications and electrical characteristics of pristine and laser annealed  $HfO_2$  thin films have been studied by employing various characterization techniques.

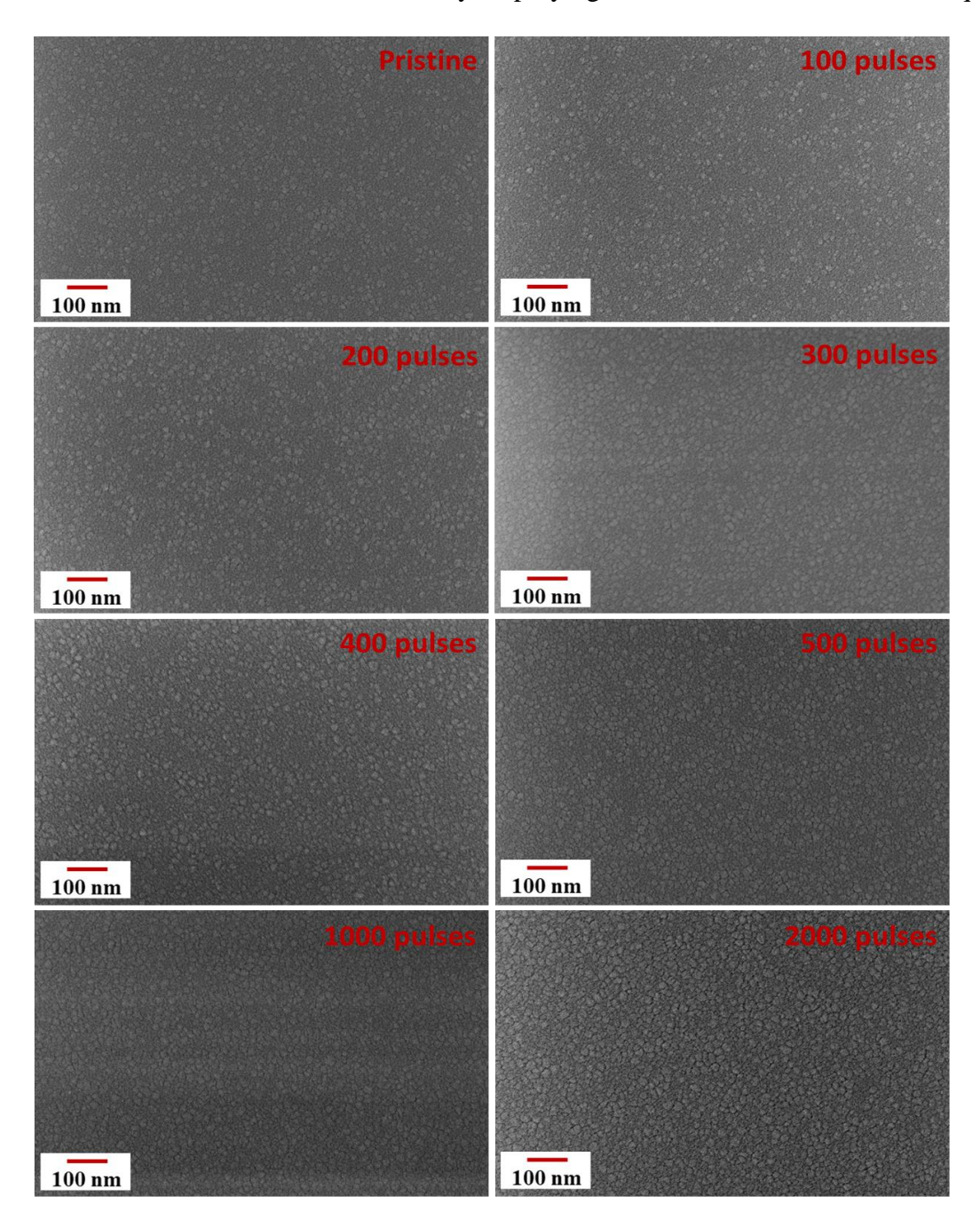


Fig. 6.3: The FESEM images of as-grown and laser annealed HfO<sub>2</sub> thin films.

The structure and morphology of the surface of HfO<sub>2</sub> thin films were studied by performing FESEM measurements. The FESEM images of as-grown and laser annealed HfO<sub>2</sub> thin films are shown in Fig. 6.3.

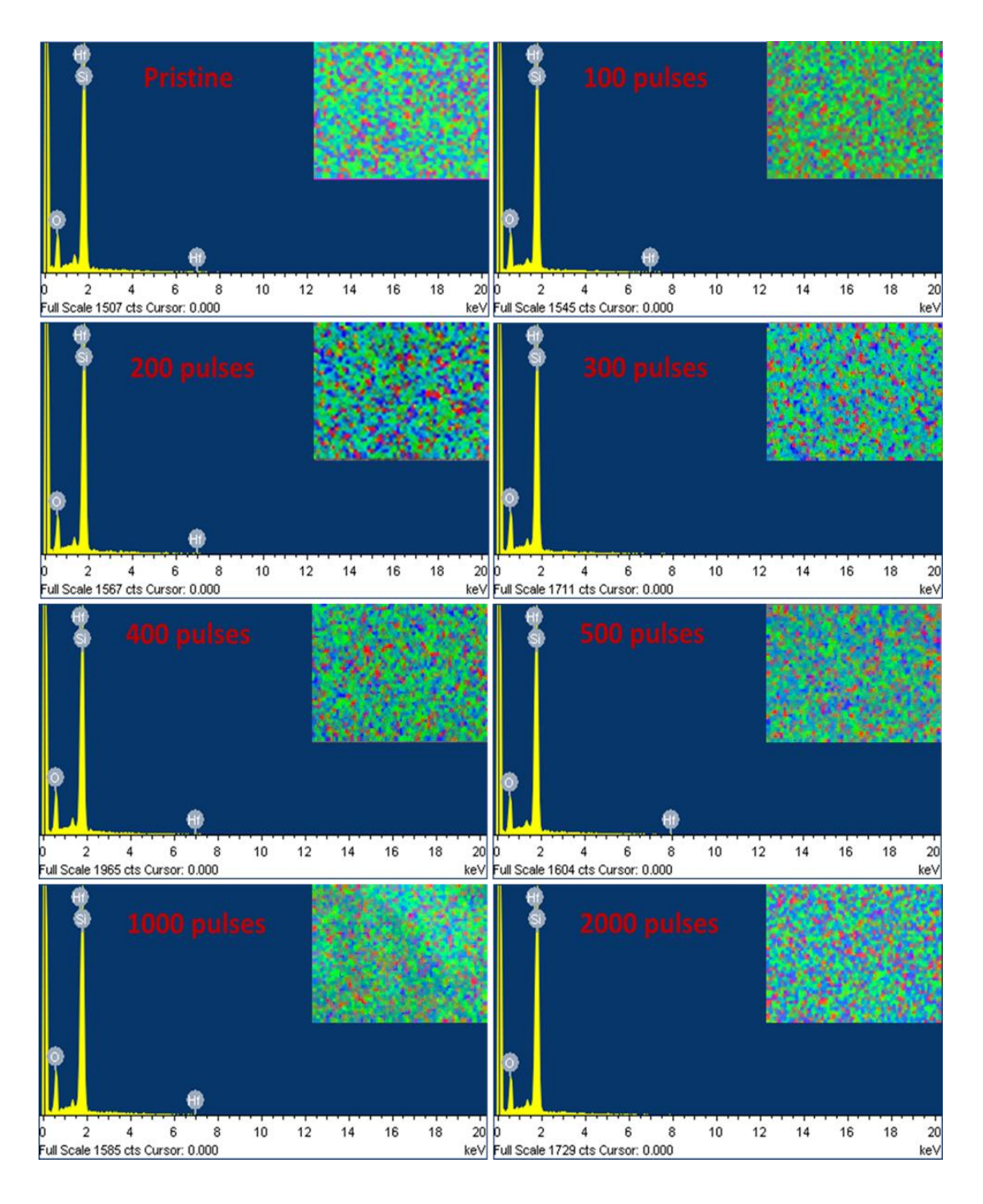


Fig. 6.4: The EDX spectra of pristine and laser annealed HfO<sub>2</sub> thin films (inset: color mapping of elemental compositions; Si - Green, Hf - Blue, O - Red).

From FESEM images, changes in the surface structure, morphology and size of the grains have been observed with increasing number of laser pulses. As-deposited HfO<sub>2</sub> film consists of a smooth surface with uniformly small grains. As the number of laser pulses increases, the small grains start growing, which leads to the formation of new grain boundaries with increasing grain size as a function of the number of laser pulses. Thus, the laser annealed HfO<sub>2</sub> films consist of uniform grains with increase in size and surface density. This increase in the grain size with increasing number of laser pulses may be attributed to a possible agglomeration of grains under electronic excitation. Similar effects were earlier observed in ion-irradiated samples [34].

The elemental compositions of the pristine and laser annealed HfO<sub>2</sub> thin films were elucidated by FESEM-EDX analysis. The EDX spectra and elemental compositions of pristine and laser annealed HfO<sub>2</sub> thin films are shown in Fig. 6.4. EDX analysis suggests that the stoichiometry of the pristine and laser annealed HfO<sub>2</sub> thin films are almost the same. This conforms the fact that the film is intact even after 2000 laser pulses.

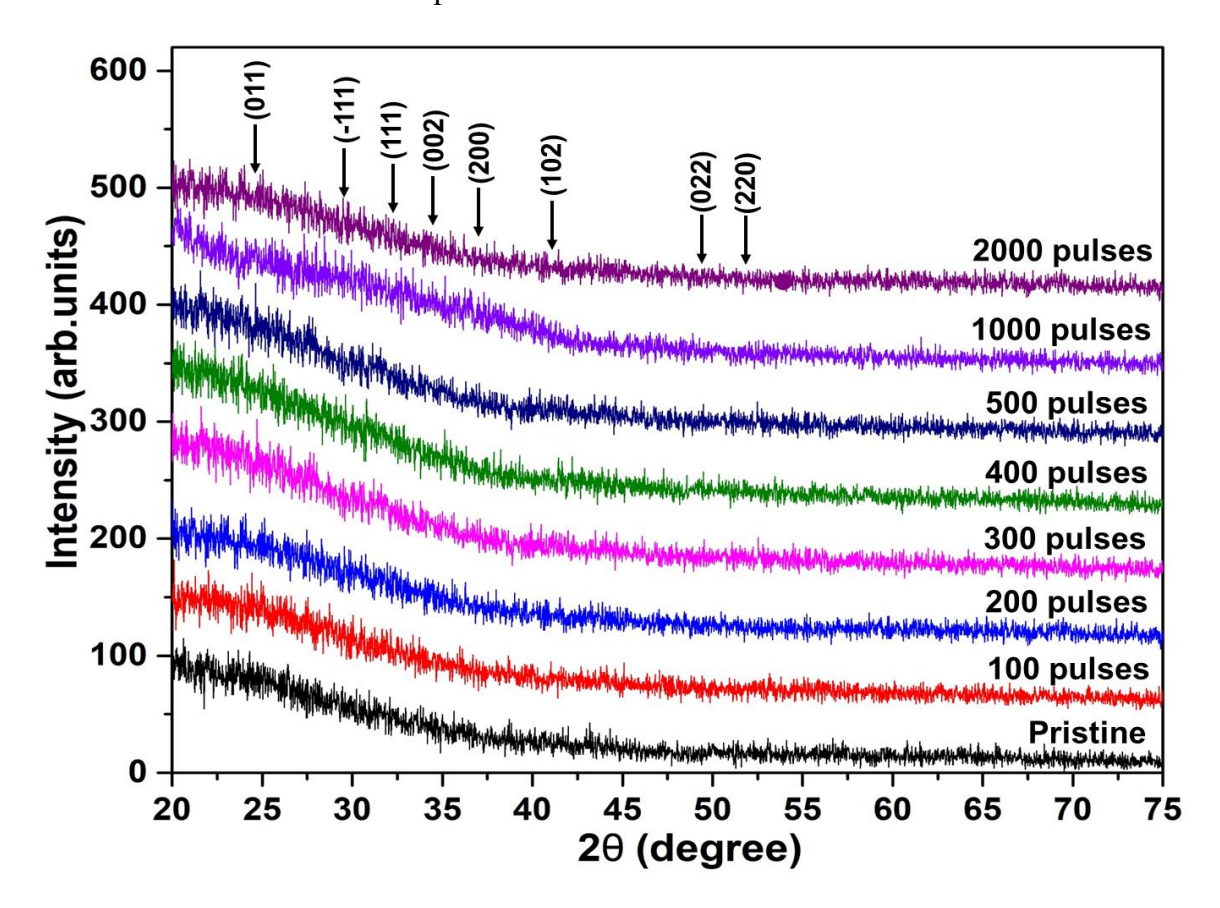


Fig. 6.5: GIXRD patterns of pristine and laser annealed HfO<sub>2</sub> thin films. (Arrows show the expected crystal planes corresponding to the monoclinic HfO<sub>2</sub>)

GIXRD measurements were performed on the pristine and laser annealed HfO<sub>2</sub> thin films to study the effects of LA on the crystalline phases in HfO<sub>2</sub> films. GIXRD patterns of as-grown and laser annealed HfO<sub>2</sub> thin films are shown in Fig. 6.5 as a function of the number of laser pulses. The GIXRD pattern of pristine HfO<sub>2</sub> thin film indicates dominance of the amorphous phase of HfO<sub>2</sub>. The GIXRD patterns of laser annealed HfO<sub>2</sub> thin films did not show the evolution of any crystalline phases in HfO<sub>2</sub> thin films up to 2000 laser pulses. Therefore, the pristine and laser annealed HfO<sub>2</sub> thin films are predominantly amorphous in nature, though there are observable changes in their morphology.

PL measurements were performed to study the defect (O-vacancies) dynamics in as-grown and laser annealed HfO<sub>2</sub> thin films and the spectra are shown in Fig. 6.6. The assignment of defects related to various types of O-vacancies are shown in Table 6.1. The excitation energy of 3.5 eV was used such that the excitation energy is much lower than the bandgap of HfO<sub>2</sub>. Therefore, the detected PL within the range of excitation energy is mainly due to the transition from defect/mid-bandgap states.

The PL spectra of as-grown film shows a broad peak which is de-convoluted as a combination of multiple peaks corresponding to 401 nm (~ 3.1 eV), 432 nm (~ 2.9 eV) and 478 nm (~ 2.6 eV) using peak fitting. Some of the observed PL peaks are attributed to the defect states related to known O-vacancies in HfO<sub>2</sub> thin films [34, 40, 41]. It is observed that, with increasing number of laser pulses the intensity of the PL spectra decreases with a slight shift in the peak positions which may be attributed to the annealing of defects due to laser annealing. The PL spectra of HfO<sub>2</sub> film annealed with 2000 laser pulses show evolution of new peak around 467 nm (~ 2.7 eV). Wen et al. [40] stated that the PL peak positions at 2.7 and 2.9 eV correspond to the positively charged O-vacancy states known as Vo<sup>2+</sup> and Vo<sup>+</sup> respectively.

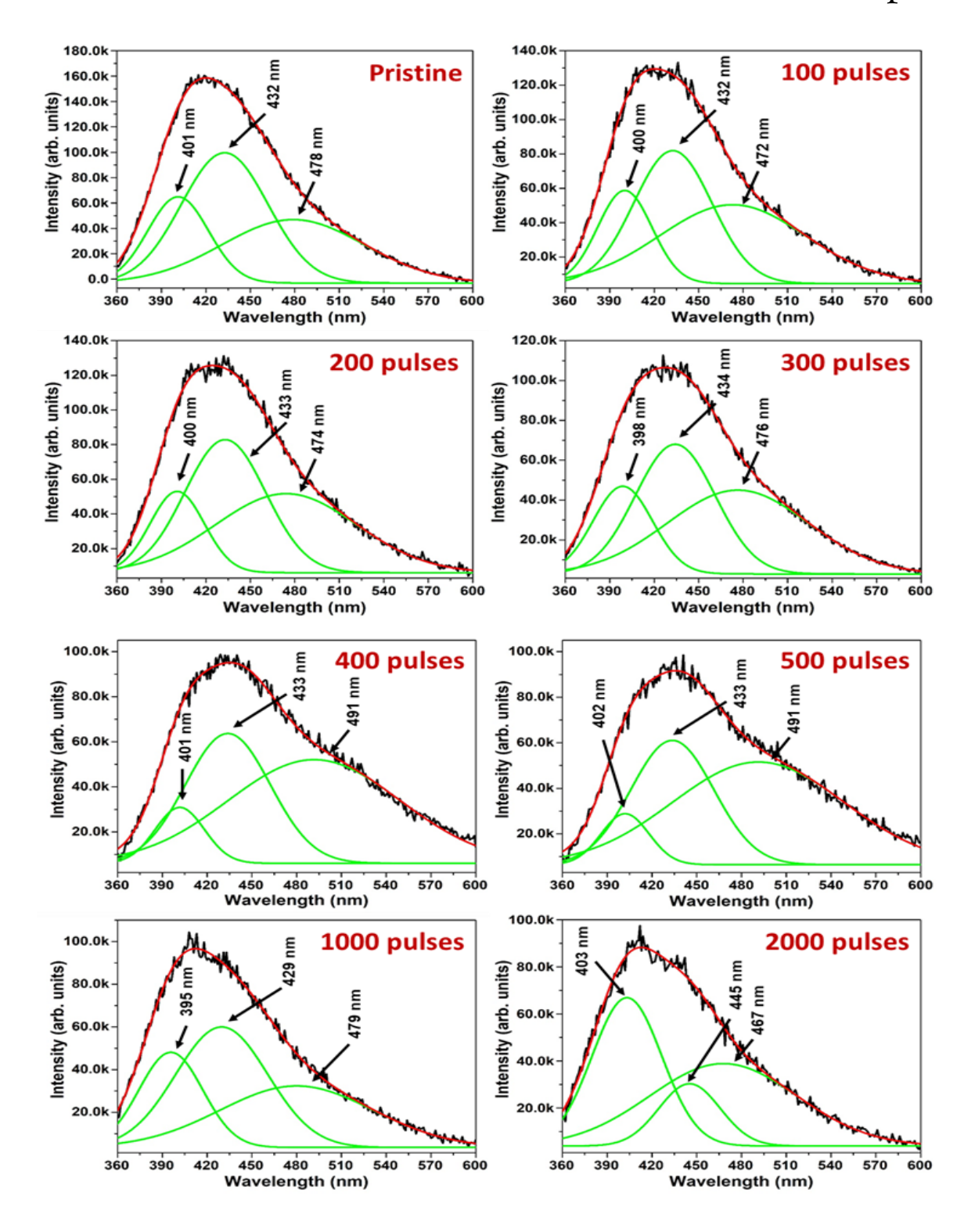


Fig. 6.6: PL spectra of pristine and laser annealed HfO<sub>2</sub> thin films.

| Number of laser pulses | PL peak positions (nm) | Defect assignment |
|------------------------|------------------------|-------------------|
| Pristine               | 401 (3.1 eV)           | -                 |
|                        | 432 (2.9 eV)           | $Vo^+$            |
|                        | 478 (2.6 eV)           | -                 |
| 100 pulses             | 400 (3.1 eV)           | -                 |
|                        | 432 (2.9 eV)           | $Vo^+$            |
|                        | 472 (2.6 eV)           | -                 |
| 200 pulses             | 400 (3.1 eV)           | -                 |
|                        | 433 (2.9 eV)           | $Vo^+$            |
|                        | 474 (2.6 eV)           | -                 |
| 300 pulses             | 398 (3.1 eV)           | -                 |
|                        | 434 (2.9 eV)           | $\mathrm{Vo}^+$   |
|                        | 476 (2.6 eV)           | -                 |
| 400 pulses             | 401 (3.1 eV)           | -                 |
|                        | 433 (2.9 eV)           | ${ m Vo}^+$       |
|                        | 491 (2.5 eV)           | -                 |
| 500 pulses             | 402 (3.1 eV)           | -                 |
|                        | 433 (2.9 eV)           | $Vo^+$            |
|                        | 491 (2.5 eV)           | -                 |
| 1000 pulses            | 395 (3.1 eV)           | -                 |
|                        | 429 (2.9 eV)           | $Vo^+$            |
|                        | 479 (2.6 eV)           | -                 |
| 2000 pulses            | 403 (3.1 eV)           | -                 |
| _                      | 445 (2.9 eV)           | $\mathrm{Vo}^+$   |
|                        | 467 (2.7 eV)           | $Vo^{2+}$         |

Table 6.1: PL peak positions and defect assignment related to O-vacancies.

Further, to study the effects of laser annealing on the electrical properties, Au/HfO<sub>2</sub>/Si MOS capacitors were fabricated by depositing top and bottom electrodes. The current conduction and capacitance of the MOS capacitors were studied by performing I-V and C-V measurements on the corresponding MOS capacitors as shown in Fig. 6.7 and Fig. 6.8 respectively.

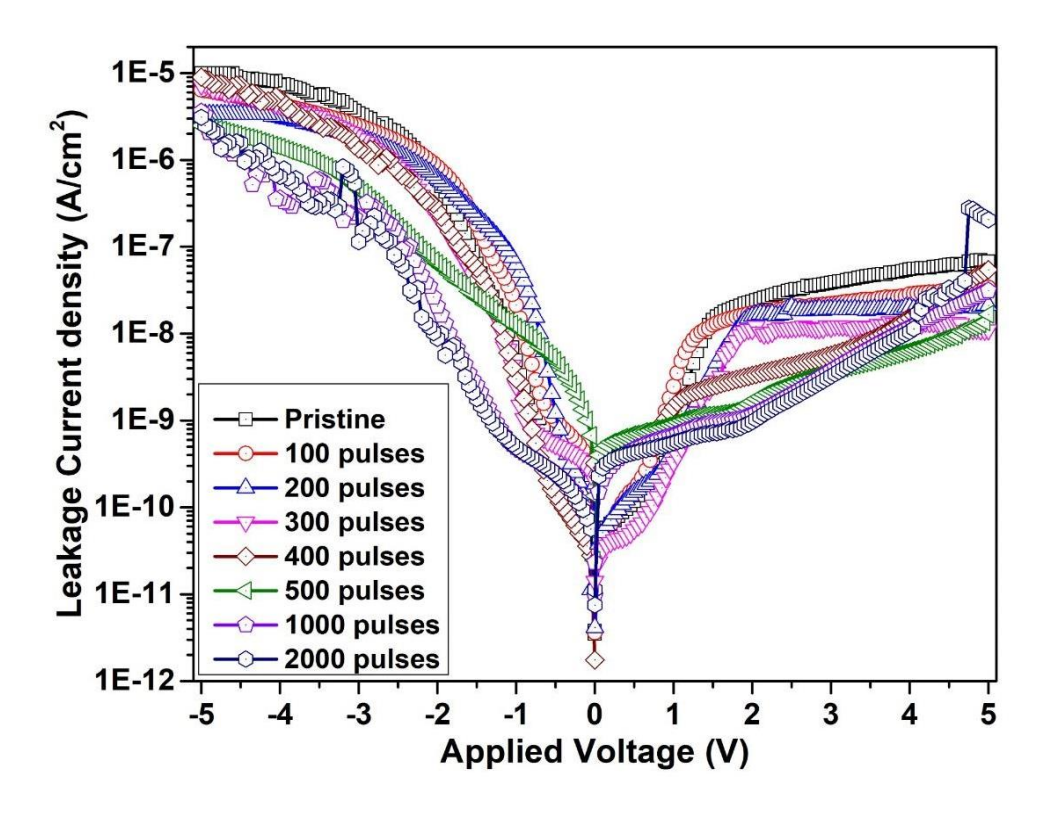


Fig. 6.7: I-V characteristics of pristine and laser annealed HfO<sub>2</sub> based MOS capacitors.

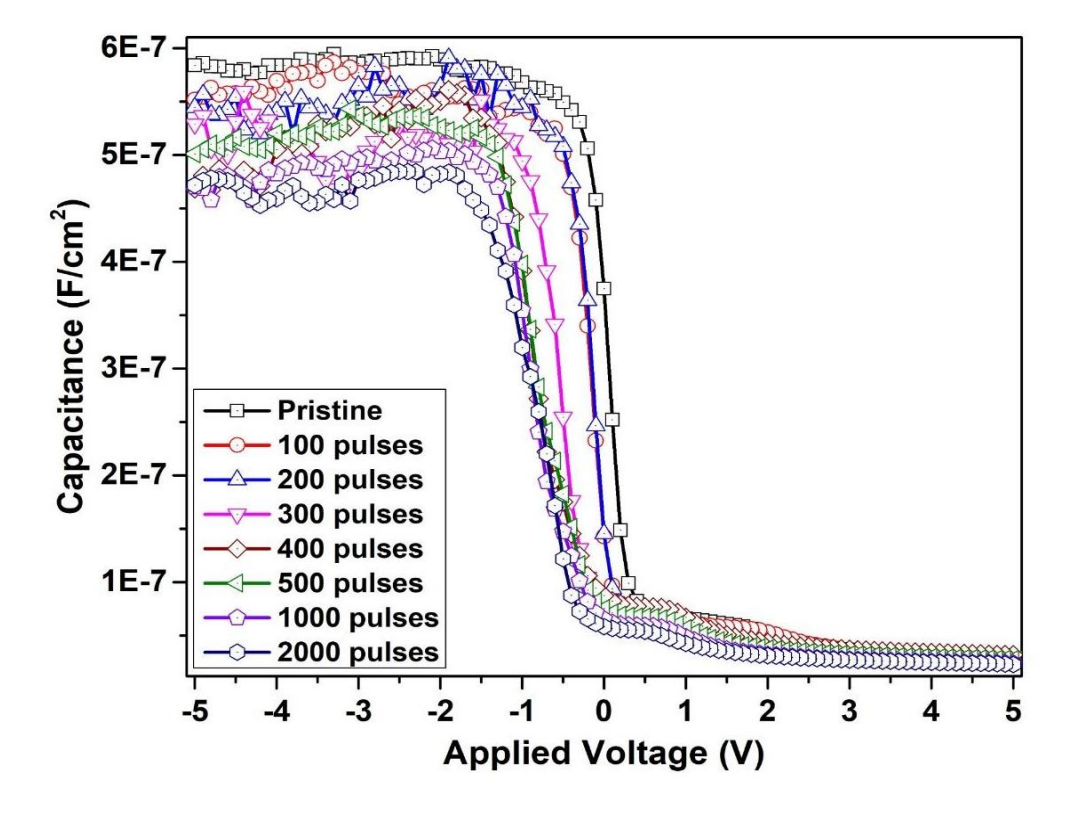


Fig. 6.8: C-V characteristics of pristine and laser annealed HfO<sub>2</sub> based MOS capacitors.

From I-V characteristics, a slight decrease in the leakage current density has been observed with increasing number of laser pulses which may be attributed to the observed defect annealing due to laser annealing. From C-V characteristics, a slight shift in the flat band voltage towards negative voltage with decrease in the accumulation capacitance has been observed with increasing number of laser pulses. This may be attributed to the structural modification of HfO<sub>2</sub> thin films and observed variations in the defect states due to laser annealing.

Effects of laser annealing on the structural changes and subsequent effects on the electrical characteristics of HfO<sub>2</sub> thin films have been studied. The main result of this study is that, as-grown HfO<sub>2</sub> thin films are in amorphous phase and they remain the same (predominantly amorphous in nature) before and after laser annealing though there are observable changes in their morphology. It is reported that the usual thermal annealing and Ion beam irradiation processes are known to crystallize the modern alternate high-k dielectric oxides like HfO<sub>2</sub>, which results in an increase in the leakage currents due to tunneling and can deteriorate the device properties [34-36]. Hence, the alternate techniques like laser annealing can improve the HfO<sub>2</sub> based MOS device characteristics by minimizing defects in the HfO<sub>2</sub> films. Therefore, this technique can be further used to produce metal nanoparticles on the surface/inside of HfO<sub>2</sub> thin films without modifying the phase of HfO<sub>2</sub> for floating gate type memory device applications.

#### B. Effects of laser annealing on Au/HfO<sub>2</sub> bi-layer thin films:

As-grown Au/HfO<sub>2</sub> bi-layer thin film was characterized by FESEM-EDX analysis to study the elemental composition in the film. EDX spectrum and elemental composition of as-grown film are shown in Fig. 6.9 and Table 6.2 respectively. EDX analysis shows the presence of Au, Hf and O elements with atomic percentages around 5%, 16% and 34% respectively on Si substrate.

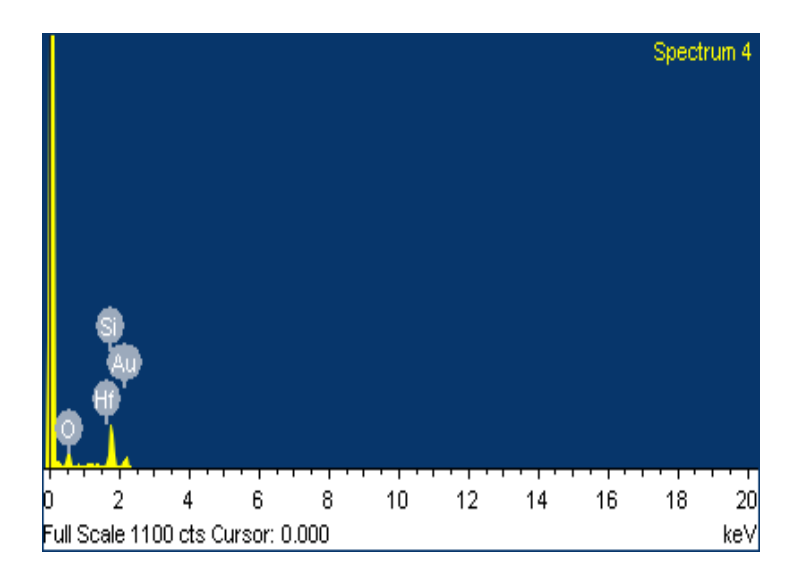


Fig. 6.9: EDX spectrum of as-grown Au/HfO<sub>2</sub> bi-layer.

| Element | Weight% | Atomic% |
|---------|---------|---------|
| ок      | 15.47   | 33.92   |
| Si K    | 35.24   | 45.00   |
| Hf M    | 34.33   | 16.10   |
| Au M    | 14.96   | 4.98    |

Table 6.2: Elemental composition of as-grown Au/HfO<sub>2</sub> bi-layer.

These bi-layered thin films were subjected to LA by varying the number of laser pulses incident on the sample from 100 to 500. The structural, optical and electrical properties of as-grown and laser annealed samples were studied by different characterization techniques.

**6.3.1. Morphology and Optical properties of Au NPs:** The structural and optical properties of pristine and laser annealed Au NPs as a function of number of laser pulses were studied by FESEM and UV-Vis absorption measurements respectively to observe the impact of LA. The structure, morphology and size of Au NPs on the surface of HfO<sub>2</sub> thin films were studied by performing FESEM measurements. The FESEM images of as-grown and laser annealed Au NPs are shown in Fig. 6.10 (a-f).

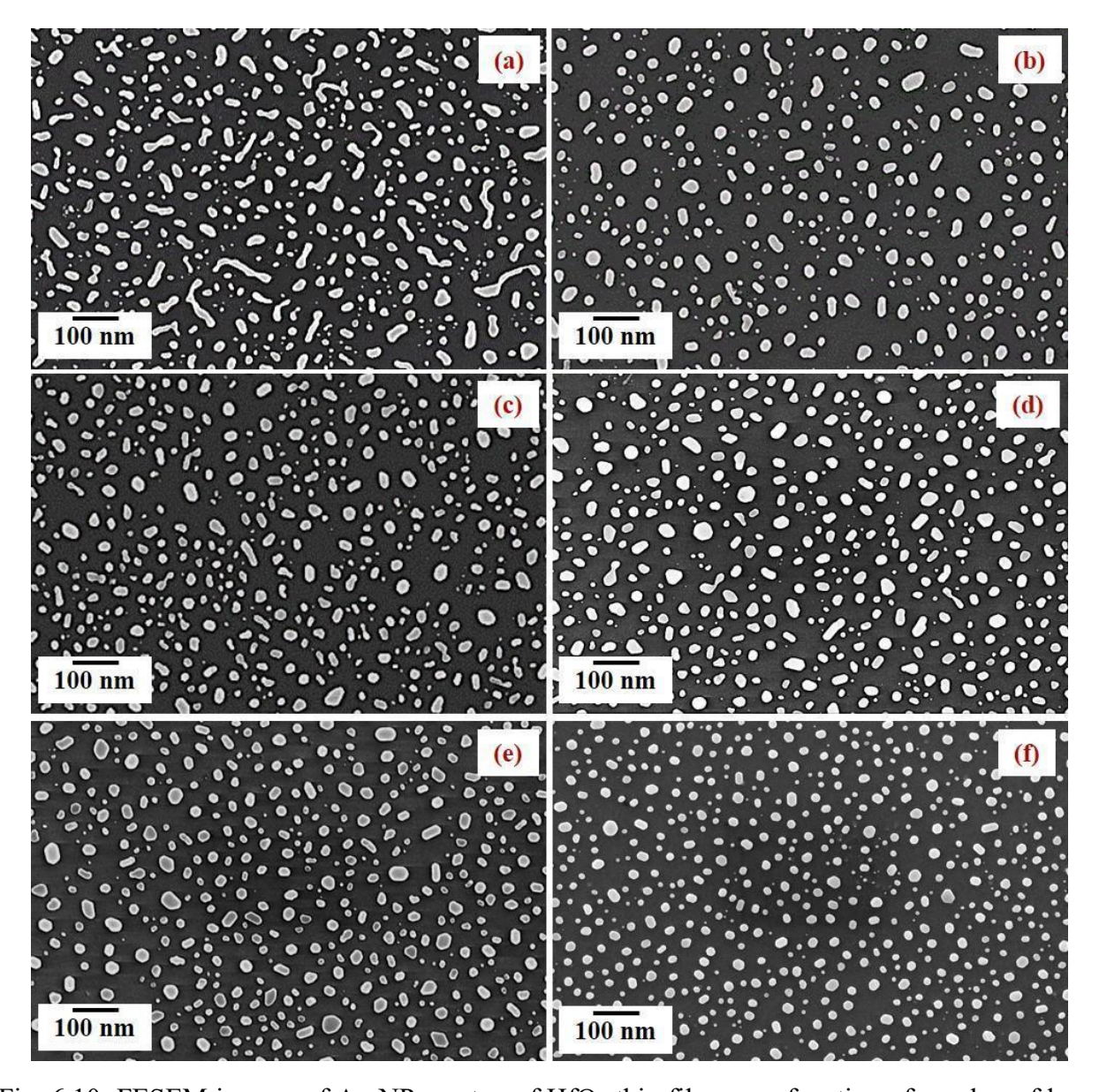


Fig. 6.10: FESEM images of Au NPs on top of HfO<sub>2</sub> thin films as a function of number of laser pulses (a) Pristine, (b) 100 pulses, (c) 200 pulses, (d) 300 pulses, (e) 400 pulses and (f) 500 pulses.

During the LA process the energy of the laser pulse was maintained as 300 m J cm<sup>-2</sup> for all the samples and the number of laser pulses varied from 100 to 500. The FESEM images confirm the formation of spherical Au NPs due to LA on the surface of HfO2. As expected, the as-deposited sample consists of an incomplete Au layer with the formation of islands. These islands of the Au layer are not uniform in size and randomly oriented. It is well known that an array of Au NPs are created when such an incomplete layer is exposed to heat treatment [31, 34]. On the other hand, heat treatments are known to crystallize the tunneling oxide layer HfO<sub>2</sub> which results in an increase in the leakage current density due to tunneling and can deteriorate the device properties [36-38]. Here the main objective is to realize a high-density array of Au NPs by LA without affecting the phase of the underneath high-k dielectric oxide layer HfO<sub>2</sub>. From FESEM images it is clearly observed that the density of spherical Au NPs increases with increase in the number of laser pulses. Furthermore, the Au NPs attain uniform spherical shape. A high-density array of spherically shaped uniform Au NPs has been produced on the surfaces of HfO<sub>2</sub> thin films when an incomplete Au layer has been subjected to LA. The laser annealed samples show that the average size of the Au NPs reduces with increase in the number of laser pulses and an array of high density spherical Au NPs has been produced by LA at 500 laser pulses.

The size distribution of as-grown and laser annealed Au NPs on the surfaces of HfO<sub>2</sub> thin films has been studied in detail by estimating the average diameter, standard deviation in size distribution and surface density of Au NPs using ImageJ software. Here the Au NPs in spherical shape are only considered for estimating the average size. The data obtained from ImageJ software is plotted as a histogram and the mean diameter of as-grown and laser annealed Au NPs has been estimated by Gaussian fittings. The statistical analysis of the size of as-grown and laser annealed spherical Au NPs as a function of number of laser pulses is tabulated in Table 6.3 and the histograms with Gaussian fitting are presented in Fig. 6.11. The estimated mean diameter of spherical Au NPs in an as-grown incomplete Au layer is around 21.9 nm and the surface density of Au NPs is around  $3.75 \times 10^{10}$  NPs.cm<sup>-2</sup>. When this as-grown Au layer is subjected to LA at 100 laser pulses, the mean diameter of spherical Au NPs increases to around 23.7 nm and the surface density of Au NPs also increases to around  $3.93 \times 10^{10}$  NPs.cm<sup>-2</sup>. At 200 laser pulses, the mean diameter of spherical Au NPs decreases to around 19.6 nm and the surface density of Au NPs further increases to around  $6.12 \times 10^{10}$  NPs.cm<sup>-2</sup>.

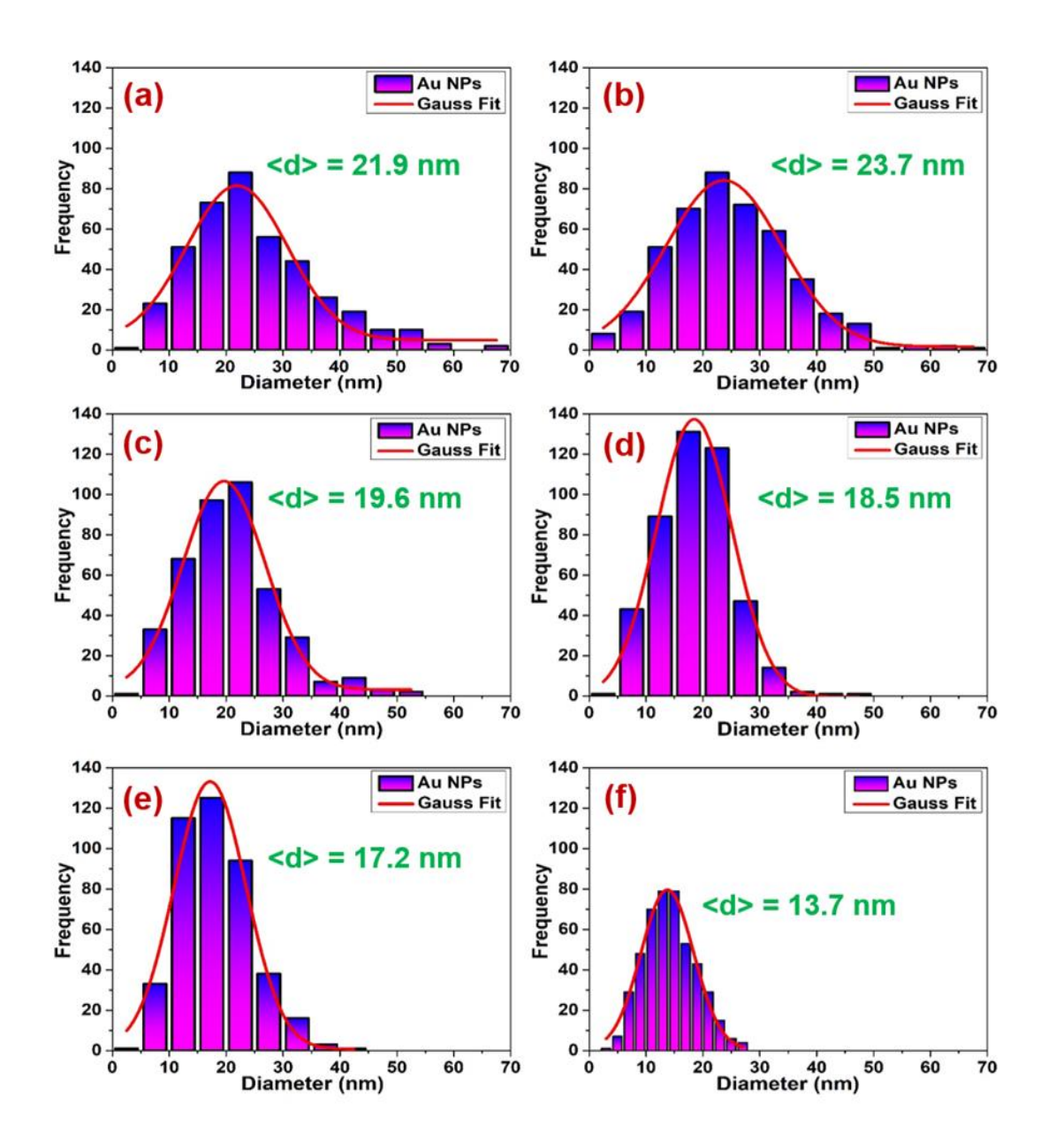


Fig. 6. 11: Size distribution of spherical Au NPs on the surface of HfO<sub>2</sub> thin films as a function of number of laser pulses

(a) Pristine, (b) 100 pulses, (c) 200 pulses, (d) 300 pulses, (e) 400 pulses, and (f) 500 pulses.

With further increase in the number of laser pulses to 300, the mean diameter of spherical Au NPs further decreases to around 18.5 nm and the surface density of Au NPs further increases to around 9.00 x 10<sup>10</sup> NPs.cm<sup>-2</sup>. Upon increasing the number of laser pulses to 400, the mean diameter of spherical Au NPs further decreases to around 17.2 nm and the surface density of Au NPs further

increases to around 1.23 x 10<sup>11</sup> NPs.cm<sup>-2</sup>. At the highest number of laser pulses of 500, the mean diameter of spherical Au NPs further decreases to around 13.7 nm and the surface density of Au NPs further increases to around 1.64 x 10<sup>11</sup> NPs.cm<sup>-2</sup>. This decrease in the size and standard deviation in size distribution of Au NPs indicates the increase in the uniformity of Au NPs. The surface density of spherical Au NPs increases from 3.75 x 10<sup>10</sup> NPs.cm<sup>-2</sup> to 1.64 x 10<sup>11</sup> NPs.cm<sup>-2</sup> due to LA with increase in the number of laser pulses to 500. Therefore, an array of high density Au NPs with good uniformity in shape has been synthesized on the surface of HfO<sub>2</sub> thin films using the LA method.

| Number of laser<br>pulses | Avg. diameter of<br>Au NPs (nm) | Standard deviation in<br>the size distribution of<br>Au NPs (nm) | Surface density of<br>Au NPs (no. of<br>NPs.cm <sup>-2</sup> ) |
|---------------------------|---------------------------------|--|--|
| 0                         | 21.9                            | 8.8  | 3.75 x 10 <sup>10</sup>  |
| 100                       | 23.7                            | 10.1   | 3.93 x 10 <sup>10</sup>  |
| 200                       | 19.6                            | 7.2  | 6.12 x 10 <sup>10</sup>  |
| 300                       | 18.5                            | 6.6  | 9.00 x 10 <sup>10</sup>  |
| 400                       | 17.2                            | 6.3  | 1.23 x 10 <sup>11</sup>  |
| 500                       | 13.7                            | 4.6  | 1.64 x 10 <sup>11</sup>  |

Table 6.3: Statistical analysis of size of Au NPs as a function of number of laser pulses.

The optical properties of Au NPs on the surface of HfO<sub>2</sub> have been studied by performing UV-Vis absorption measurements. Absorption spectra of as-grown and laser annealed Au NPs are shown in Fig. 6.12. From the UV-Vis absorption measurements, it is observed that with increase in the number of laser pulses, the wavelength for maximum absorbance ( $\lambda_{max}$ ) shifts towards shorter wavelengths. In addition to the shift in the position of  $\lambda_{max}$ , narrowing of the absorption spectra has also been observed. This can be explained as follows: the smaller sized spherical Au NPs predominantly absorb light and show the  $\lambda_{max}$  at  $\sim 520$  nm, whereas spherical Au NPs of larger diameter exhibit increase in scattering and show  $\lambda_{max}$  shift towards longer wavelengths (red-shift) with peak broadening. As the average size of spherical Au NPs decreases, the  $\lambda_{max}$  decreases which is in good agreement with the previous reports that the wavelength with maximum absorbance

shifts towards the longer wavelengths (red-shift) as the average size of Au NPs becomes larger [42,43]. This further confirms that the average size of the Au NPs decreases due to LA as a function of the number of laser pulses and an array of high density Au NPs with good uniformity in shape have been synthesized at 500 laser pulses.

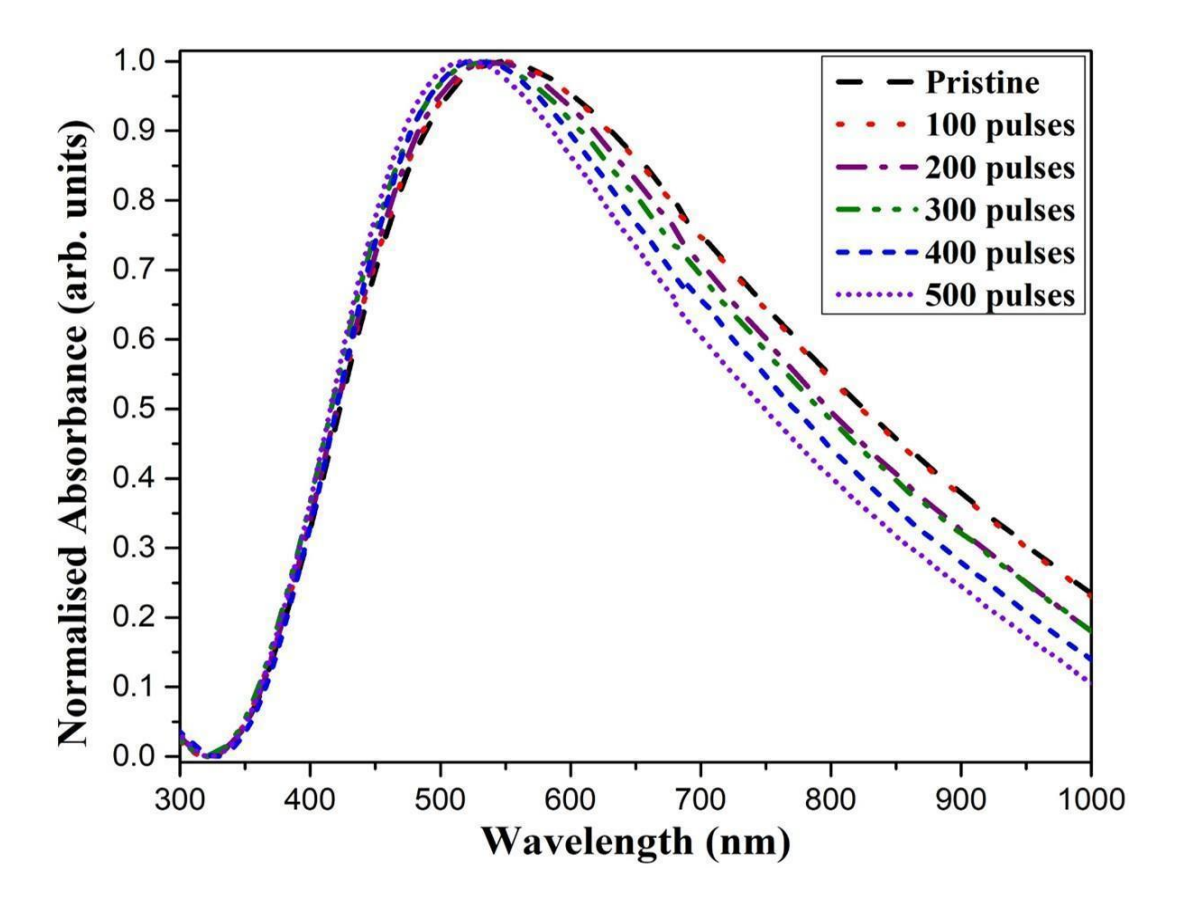


Fig. 6.12: UV-visible Absorbance spectra of Au NPs as a function of the number of laser pulses.

**6.3.2. Crystal structure of Au/HfO<sub>2</sub> bi-layers:** GIXRD measurements were performed on pristine and laser annealed Au/HfO<sub>2</sub> bi-layers to study the effects of LA on the crystalline structure of the films. GIXRD patterns of as-grown and laser annealed Au NPs on the surface of HfO<sub>2</sub> thin films are shown in Fig. 6.13. The GIXRD pattern consists of the peaks corresponding to the crystalline phases of Au and do not show the evolution of any crystalline phases in HfO<sub>2</sub> thin films before and after LA up to 500 number of laser pulses.

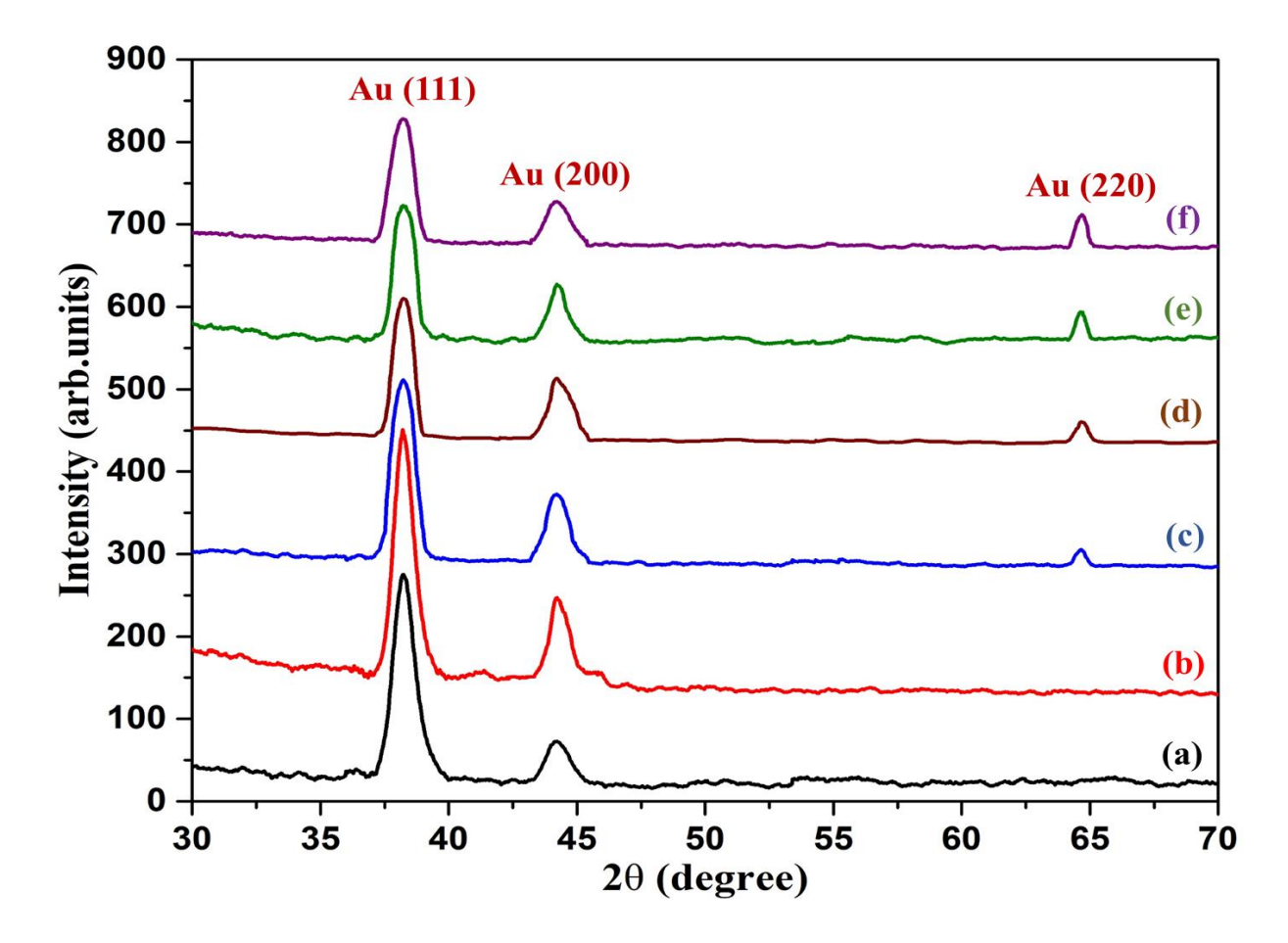


Fig. 6.13: GIXRD patterns of pristine and laser annealed Au/HfO<sub>2</sub> bi-layers
(a) Pristine, (b) 100 pulses, (c) 200 pulses, (d) 300 pulses, (e) 400 pulses and (f) 500 pulses.

From GIXRD measurements, it has been observed that as deposited Au NPs on the surface of HfO<sub>2</sub> thin films exhibit crystalline phases of Au correspond to (111), (200) crystalline planes and no crystalline peak corresponds to any crystal planes of HfO<sub>2</sub>, confirming the amorphous nature of HfO<sub>2</sub> thin films. As the LA increases up to 300 laser pulses, in addition to the above crystal planes of Au, evolution of new crystal planes (220) of Au has been observed and HfO<sub>2</sub> remains in an amorphous phase. Upon increasing the number of laser pulses to the maximum count of 500, only crystal planes corresponding to Au have been observed and the spectra still did not show evolution of any crystalline phases in HfO<sub>2</sub> thin films. Thus, the phase of HfO<sub>2</sub> thin films remains in amorphous nature and un-affected due to LA up to 500 number of laser pulses. Therefore, from GIXRD measurements, it is confirmed that an array of high density spherical Au NPs have been synthesized on the surface of HfO<sub>2</sub> thin films using LA technique without affecting the phase of HfO<sub>2</sub>.

**6.3.3. SERS studies of R6G dye on Au NPs:** The SERS technique is very sensitive to the surface which is responsible for enhancement in Raman scattering of molecules on metal NPs such as Au, Ag and Cu [44, 45]. The enhancement takes place when the confined surface plasmon gets excited by the incident light and enhances the electromagnetic field of the metal NPs which is responsible for the enhancement in Raman scattering up to  $10^5 - 10^7$  [44, 45]. This enhancement in Raman scattering depends on the size, shape, uniformity and homogeneity of metal NPs [23, 24].

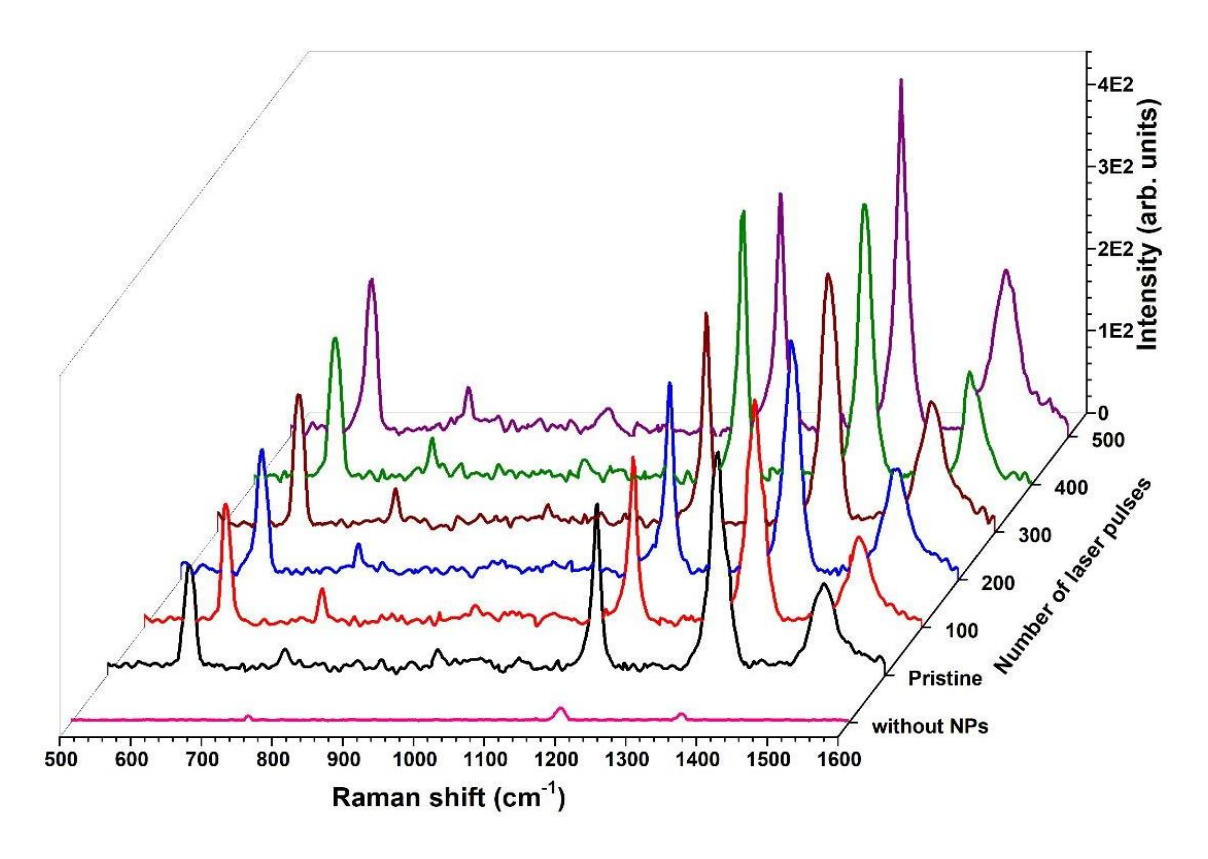


Fig. 6.14: Raman spectra of Rhodamine 6G (R6G) with and without Au NPs as a function of the number of laser pulses.

For the past few years, SERS method used for molecular detection and in other applications has been investigated because it offers easy sample preparation with considerable enhancement in Raman scattering. It is a non-destructive technique, more sensitivity and less detection limit [46-52]. In recent years, metal NPs of Ag and Au have been extensively used in SERS studies owing to their exclusive physical properties which depend on the shape, density and size of the metal NPs [53, 54]. In current studies, Au NPs have attracted interest due to its biocompatibility. Au NPs

have been used in the application of Bio-technological systems because they exhibit an excitation near to the IR region [55].

SERS measurements of R6G dye (drop-casted solution of 20 µl R6G of 10 nM concentration) were performed on top of as-grown and laser annealed Au NPs. The SERS spectra of R6G dye without Au NPs (R6G/HfO<sub>2</sub>/Si) and with Au NPs (R6G/Au-NPs/HfO<sub>2</sub>/Si) as a function of number of laser pulses are shown in Fig. 6.14. From SERS measurements, considerable enhancement in the Raman scattering of R6G molecules has been observed in presence of high density spherical Au NPs. A systematic increase in the intensities of SERS peaks corresponding to R6G dye has been observed as the number of laser pulses increases which is attributed to the increase in the density of Au NPs on the surface. These Au NPs act as hot-spots which are responsible for enhancement in SERS, as a function of the number of laser pulses. For signifying the role of SERS substrates for molecular detection, Raman Enhancement Factor (EF) has been calculated from the Raman scattering spectra using the following Eq. 6.1 [56].

Raman Enhancement Factor (EF) = 
$$\frac{I_{SERS}N_{RS}}{I_{RS}N_{SERS}}$$
 (6.1)

Where  $I_{SERS}$  and  $I_{RS}$  are the maximum intensities corresponding to Raman scattering of R6G molecules which are adsorbed on the surface of SERS substrates (R6G/Au-NPs/HfO<sub>2</sub>/Si) and non-SERS substrates (R6G/HfO<sub>2</sub>/Si) respectively. Here R6G dye on the surface of HfO<sub>2</sub> i.e. without Au NPs is considered as non-SERS substrates (R6G/HfO<sub>2</sub>/Si).  $N_{SERS}$  and  $N_{RS}$  are the number of R6G molecules on Au NPs (SERS substrates) and HfO<sub>2</sub> (non-SERS substrates) with the values, 10 nM and 10 mM respectively. The value of Raman Enhancement Factor (EF) as  $2.6 \times 10^7$  has been estimated for the as-grown SERS substrate corresponding to the Raman scattering peak at  $\sim 1364 \text{ cm}^{-1}$ . The estimated EF with respect to surface density of laser annealed Au NPs as a function of the number of laser pulses is shown in Fig. 6.15. An order of magnitude increase in the estimated EF has been observed as the surface density of Au NPs increases as a function of the number of laser pulses. For the SERS substrate, which is laser annealed at 100 laser pulses, the value of EF is found as  $2.7 \times 10^7$  and  $2.8 \times 10^7$  for the samples annealed at 100 and 200 laser pulses respectively. Further increasing the number of laser pulses to 300 and 400, the EF increases to  $3.1 \times 10^7$  and  $3.4 \times 10^7$  respectively. For the highest number of laser pulses 500, further increase in EF of  $4.3 \times 10^7$  has been observed.

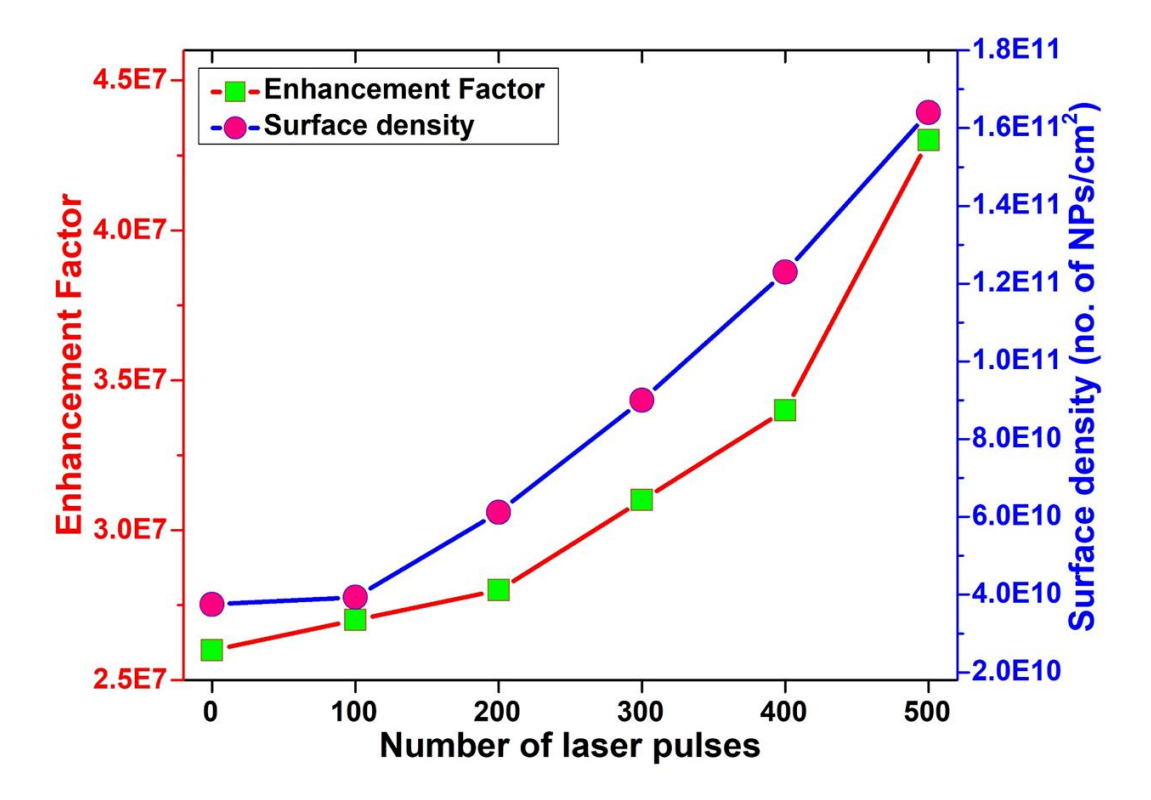


Fig. 6.15: Enhancement Factor and surface density of Au NPs as a function of number of laser pulses.

This enhancement in Raman scattering not only confirms the formation of an array of high density spherical Au NPs but also presents itself as a substitute non-thermal technique to synthesize SERS substrates. Hence, a non-thermal technique like LA is considered to be useful in preparation of SERS substrates with considerable enhancement in Raman scattering for molecular detection. Hereafter, the samples containing an array of high density Au NPs with good uniformity which are annealed with 500 laser pulses (referred to as "with Au NPs") are used for further application such as Au NPs embedded HfO<sub>2</sub> based MOS capacitors.

**6.3.4. Electrical characteristics of MOS capacitors:** An array of high density spherical Au NPs produced on the surface of HfO<sub>2</sub> thin films using LA of 500 laser pulses is used to fabricate MOS capacitors to study the electrical characteristics (referred to as "with Au NPs"). For comparing the role of an array of high density Au NPs embedded in HfO<sub>2</sub> matrix in device electrical performance, a MOS capacitor without Au NPs in the HfO<sub>2</sub> layer of similar thickness (~ 30 nm) is also fabricated (referred to as "without Au NPs") under the same deposition conditions.

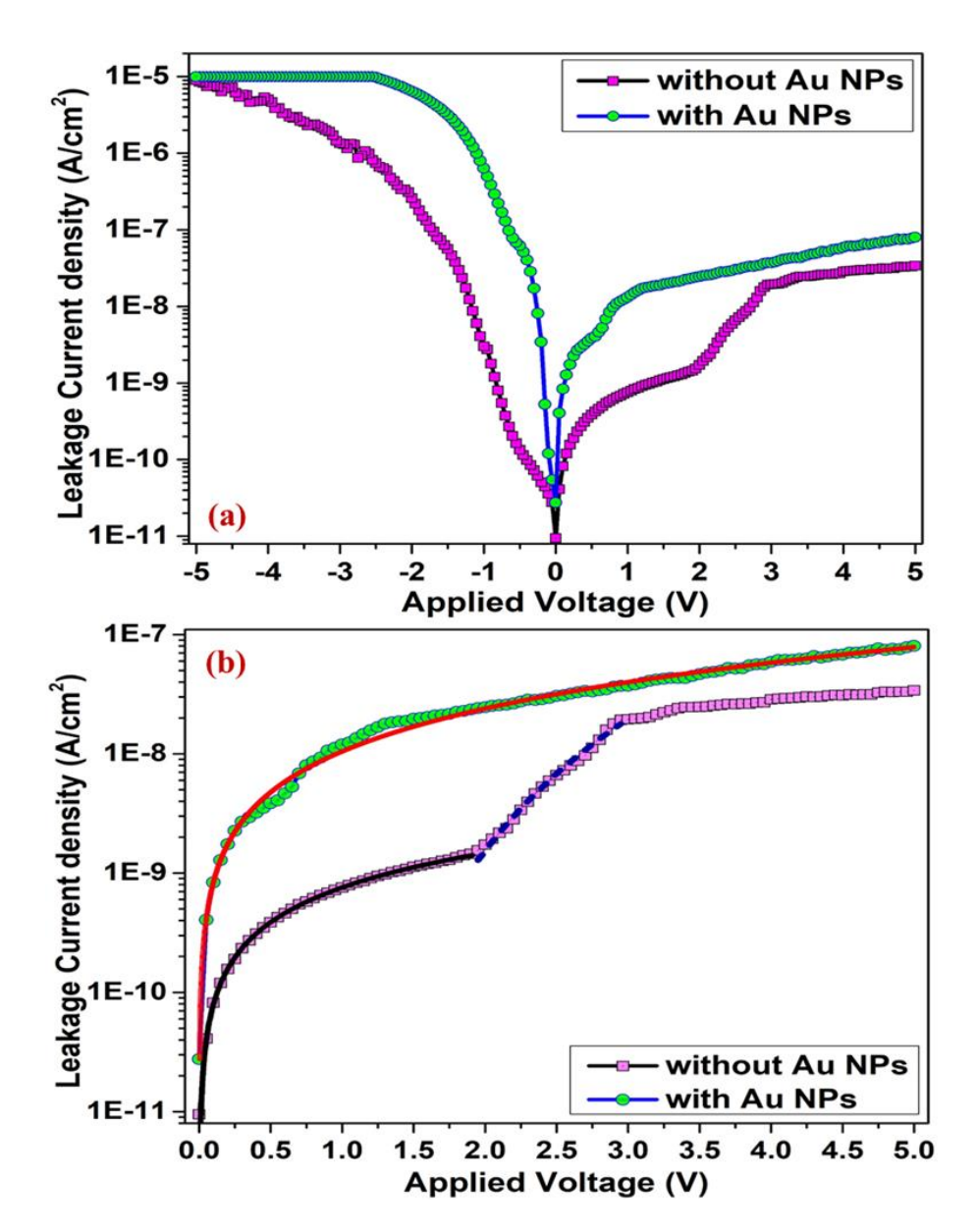


Fig. 6.16(a): I-V characteristics of HfO<sub>2</sub> based MOS structures with and without Au NPs.
(b): Leakage current characterized by PF and FN tunneling mechanisms (solid lines indicate PF tunneling and dashed line indicates FN tunneling).

The leakage current conduction mechanisms of these MOS capacitors through the gate oxide HfO<sub>2</sub> in the presence and absence of embedded Au NPs were studied by performing I-V measurements (-5 V to 5 V) shown in Fig. 6.16(a). As expected, the leakage current density is high in both forward and reverse bias applied voltages for the MOS capacitors with embedded Au NPs in HfO<sub>2</sub> dielectric media when compared to that of MOS capacitors with pure HfO<sub>2</sub> layer i.e. without embedded Au NPs. When voltage is applied through the gate, the electrons that tunnel through the

HfO<sub>2</sub> dielectric layer are responsible for this increase in the leakage current density. This leakage current density as a function of applied voltage can be elucidated by examining the I-V curves with several well-established theoretical conduction mechanisms such as Direct Tunneling (DT), Poole-Frenkel (PF) tunneling and Fowler-Nordheim (FN) tunneling [57-59]. The leakage current due to DT is responsible when the electrons directly tunnel through the dielectric layer and is relevant to the gate oxides with thickness of less than 4 nm [60]. Hence, in the present study the leakage current due to DT is not expected to be significant as the gate oxide HfO<sub>2</sub> thickness is ~ 30 nm for both the devices. The data obtained by performing I-V measurements are used to fit with theoretical PF and FN tunneling models as shown in Fig. 6.16(b). In the Fig. 6.16(b) solid lines indicate PF tunneling and dashed line indicate FN tunneling mechanisms. The experimental I-V characteristics of both the devices have been examined using the theoretical tunneling models to evaluate the contribution from various processes to the leakage current due to tunneling as a function of applied voltage. For fitting the experimental I-V data with theoretical PF and FN tunneling models, the following equations 6.2 and 6.3 have been used respectively [58, 61].

$$J_{PF} = EF_{ox}exp\left[-\frac{q\Phi - \beta\sqrt{F_{ox}}}{\xi KT}\right]$$
 (6.2)

$$J_{FN} = \frac{q^3}{16\pi^2\hbar\Phi_b} F_{ox}^2 \exp \exp \left[ -\frac{4}{3} \frac{\sqrt{2m_{ox}^*}\Phi_b^{\frac{3}{2}}}{\hbar q} \frac{1}{F_{ox}} \right]$$
 (6.3)

In these equations,  $F_{ox}$  is the electric field through the dielectric layer  $HfO_2$  and  $\xi$  (value in between 1 and 2 which is constant) is the factor obtained by acceptor compensation. Other well-known constants are like Boltzmann's constant (K), Charge of electron (q), Temperature (T) and reduced Planck constant (h). Here,  $\Phi_b$  is the barrier height among the conduction bands at  $HfO_2/Si$  interface and  $m_{ox}^*$  is the effective mass of electrons in the dielectric layer  $HfO_2$ .

From the examination of I-V characteristics using theoretical PF and FN tunneling models, it is found that, for the MOS capacitors with pure HfO<sub>2</sub> i.e. without embedded Au NPs in the HfO<sub>2</sub> dielectric layer, the leakage current due to PF tunneling is prominent at lower applied voltages i.e. from 0 V to 1.9 V. Upon increasing the applied voltage further i.e. greater than 2 V, the leakage current due to FN tunneling dominates from 2.0 V to 2.95 V. An exponential increase in the leakage current density as a function of applied voltage (2.0 V - 2.95 V) due to FN tunneling has

been observed. The leakage current due to FN tunneling takes place, when the applied voltage is effectively high, the barrier of dielectric oxide becomes triangular in shape and at the edge of the triangle the barrier becomes thinner than the original barrier. At this high applied voltage, the electrons can tunnel easily through this thinner triangular barrier and leakage current increases exponentially. Thus, for the MOS capacitors without embedded Au NPs in the HfO2 dielectric layer, the leakage current due to PF tunneling is prominent at lower applied voltages (< 2 V) and the leakage current due to FN tunneling dominates for higher voltages (2.0 V - 2.95 V). The I-V characteristics and leakage current conduction due to various tunneling mechanisms in HfO<sub>2</sub> based MOS devices are consistent with our previous studies [35]. For the MOS capacitors with embedded Au NPs in the HfO<sub>2</sub> dielectric media, the leakage current due to PF tunneling alone has been observed when the applied voltage varied from 0 V to 5 V. The leakage current in dielectric oxides due to PF tunneling is mainly attributed to the presence of defects in the dielectric layers. These defects in the dielectric layers act as charge trapping centers and confine the charges. In MOS capacitors with embedded Au NPs in the HfO<sub>2</sub> dielectric media, the leakage current due to PF tunneling may be attributed to the charge trapping favored by the embedded Au NPs within the dielectric oxide HfO<sub>2</sub>. Therefore, the array of high density isolated Au NPs produced by LA acts as charge trapping centers in the gate dielectric oxide HfO<sub>2</sub>. These charge trapping centers are capable of limiting the channel current flow by capture or emission of electrons. Here, when the forward bias voltage is applied through the electrodes, the electrons which are tunneling through the gate dielectric oxide HfO<sub>2</sub>, are trapped by the Au NPs within the gate dielectric oxide HfO<sub>2</sub>. Thus, the leakage current density is more for the MOS capacitors with embedded Au NPs when compared to that of MOS capacitors without embedded Au NPs. This phenomenon of leakage current due to tunneling as a function of applied voltage is governed by the PF tunneling mechanism.

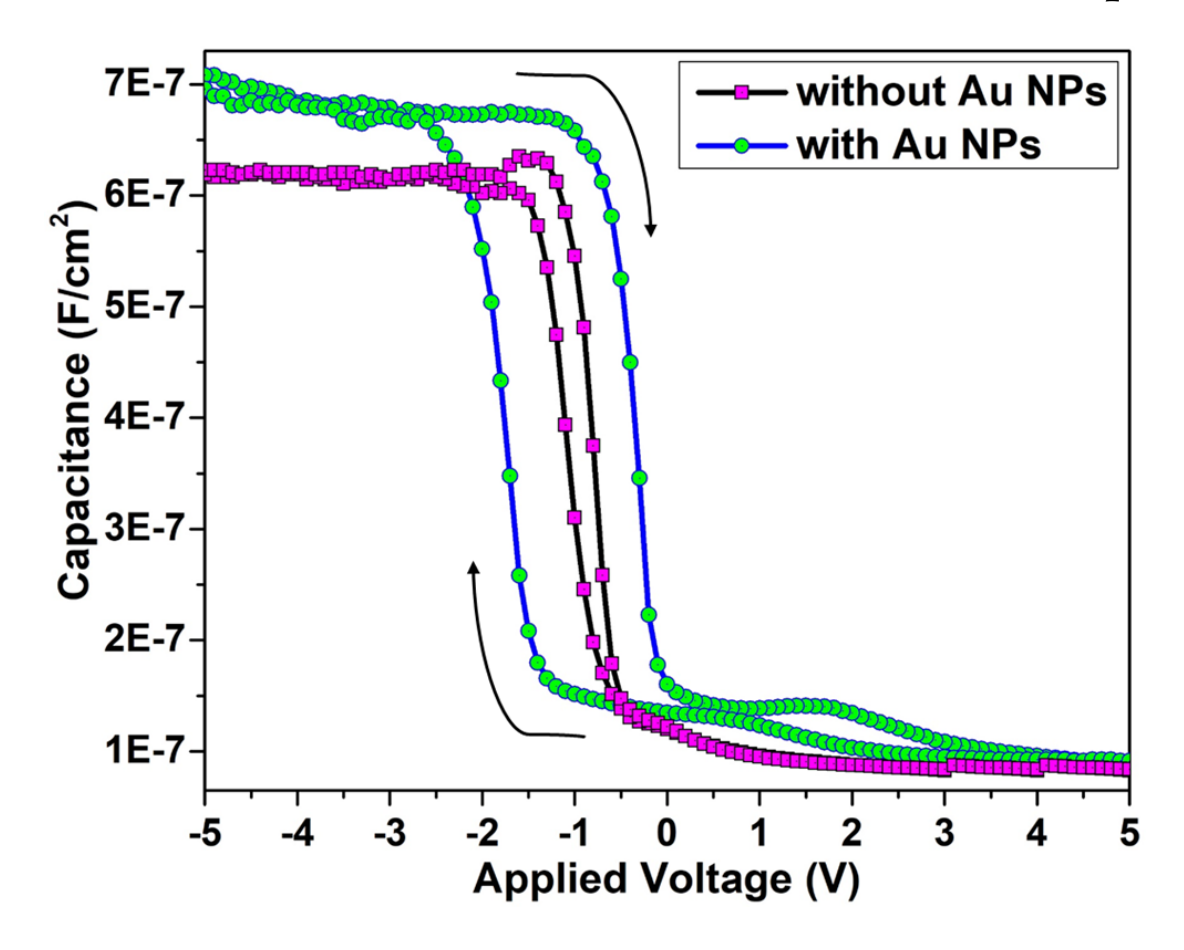


Fig. 6.17: C-V characteristics of HfO<sub>2</sub> based MOS capacitors with and without Au NPs.

High frequency (1 MHz) C-V measurements were performed on MOS capacitors with embedded Au NPs in HfO<sub>2</sub> dielectric media and MOS capacitors with pure HfO<sub>2</sub> layer i.e. without embedded Au NPs shown in Figure 6.17. The C-V hysteresis measurements were used to study the memory performance of both the MOS capacitors i.e. with and without embedded Au NPs. For MOS capacitors with embedded Au NPs in HfO<sub>2</sub> dielectric media, an increase in the accumulation capacitance and broadening in the C-V hysteresis loop has been observed when compared to that of MOS capacitors with pure HfO<sub>2</sub> layer i.e. without embedded Au NPs. As discussed above, the array of high density isolated Au NPs produced by LA acts as charge trapping centers in the gate dielectric oxide HfO<sub>2</sub>. These isolated Au NPs store the charge. Hence, the storage capacity has been increased by introducing an array of high density isolated Au NPs in HfO<sub>2</sub> dielectric media. This phenomenon can be explained as follows: when a negative bias voltage is applied, the holes which tunnel from the substrate are trapped by the array of Au NPs, whereas for a voltage applied in forward bias, the electrons tunneling from the substrate are stored in the array of Au NPs. The

C-V curve of the MOS capacitor without embedded Au NPs in HfO<sub>2</sub> dielectric exhibits a narrower hysteresis loop, which indicates that the as-deposited HfO<sub>2</sub> layer consists of low density of defects/charge trapping centers within the film. The C-V hysteresis loop of the MOS capacitor with embedded Au NPs in HfO<sub>2</sub> dielectric shows a large memory window, which indicates the improved storage capacity of the MOS capacitor due to embedded Au NPs when compared to that of MOS capacitor without embedded Au NPs within the HfO<sub>2</sub> dielectric oxide layer. Thus, the storage capacity of the device has been improved due to the introduction of high density spherical Au NPs in-between the oxide layers. Hence, the electrical characteristics suggest that an array of high density spherical Au NPs created in the HfO<sub>2</sub> gate dielectric media using non-thermal LA technique may be safely used in the microelectronic compatible floating gate memory device applications.

### 6.4. Conclusions

In this chapter, the effects of LA on the structural and electrical properties of HfO<sub>2</sub>, Au/HfO<sub>2</sub> bilayer thin films have been studied. As-grown HfO<sub>2</sub> thin films are in amorphous phase and the crystal structure of HfO<sub>2</sub> thin films remain the same (predominantly amorphous in nature) before and after laser annealing though there are observable changes in their morphology. The main result of this chapter is the use of a non-thermal LA technique in synthesizing an array of high density Au NPs on the surface of HfO<sub>2</sub> thin films without altering the phase of the underlying oxide layer (HfO<sub>2</sub>). These high density Au NPs, which are embedded in HfO<sub>2</sub> dielectric media, can be used as charge trapping centers in HfO<sub>2</sub>/Au-NPs/HfO<sub>2</sub>/Si based floating gate type MOS capacitors. An array of high density Au NPs has been produced on the surface of HfO<sub>2</sub> thin films by subjecting the incomplete Au layer to LA as a function of the number of laser pulses. From FESEM images, it is clearly observed that the density of spherical Au NPs increases with increase in the number of laser pulses. The laser annealed samples show that the average size of the Au NPs reduces with increase in the number of laser pulses and an array of high density spherical Au NPs has been produced on the surface of HfO<sub>2</sub> thin films by LA at 500 number of laser pulses. The average size of spherical Au NPs in as-deposited sample is 21.9 nm, which decreases to 13.7 nm at 500 laser pulses. While the surface density of spherical Au NPs increases from 3.75 x 10<sup>10</sup> NPs.cm<sup>-2</sup> to 1.64 x 10<sup>11</sup> NPs.cm<sup>-2</sup> with increase in the number of laser pulses to 500. From the UV-Vis absorption measurements, it is observed that with increase in the number of laser pulses,  $\lambda_{max}$  shifts in the

direction of shorter wavelengths accompanied by narrowing of the absorption spectra. This further confirms that the average size of the Au NPs decrease with increase in number of laser pulses. Thus, an array of high density Au NPs with good uniformity in shape has been synthesized at 500 laser pulses. The GIXRD spectra consists of the peaks corresponding to the crystalline phases of Au and did not show the evolution of any crystalline phases in HfO<sub>2</sub> thin films before and after LA. Therefore, an array of high density spherical Au NPs has been produced on the surface of HfO<sub>2</sub> thin films using LA technique without affecting the phase of HfO<sub>2</sub>. From SERS measurements, considerable enhancement in the Raman scattering of R6G molecules has been observed in presence of high density spherical Au NPs. The improvement in EF ( $\sim 10^7$ ) has been observed due to laser annealed Au NPs. Therefore, a non-thermal technique like LA can be considered useful in preparation of SERS substrates with considerable enhancement in Raman scattering for molecular detection. The leakage current conduction mechanisms of these MOS capacitors through the gate oxide HfO<sub>2</sub> in the presence and absence of embedded Au NPs were studied using PF and FN tunneling mechanisms by examining the I-V characteristics. For the MOS capacitors without embedded Au NPs in the HfO<sub>2</sub> dielectric layer, the leakage current due to PF tunneling is prominent at lower applied voltages and the leakage current due to FN tunneling dominates for higher applied voltages. Whereas for the MOS capacitors with embedded Au NPs in the HfO<sub>2</sub> dielectric media, the leakage current due to PF tunneling alone has been observed which is attributed to the charge trapping by the embedded Au NPs. The C-V hysteresis loop of the MOS capacitor with embedded Au NPs in HfO2 dielectric shows a large memory window, which indicates the improved storage capacity of the MOS capacitor due to embedded Au NPs when compared to that of MOS capacitor without embedded Au NPs within the HfO2 dielectric oxide layer. These SERS studies and electrical characteristics suggest that an array of high density spherical Au NPs may be created in the HfO2 gate dielectric media using non-thermal LA technique, which is useful in preparation of SERS substrates for molecular detection and in fabricating microelectronic compatible floating gate memory devices.

### **6.5.** References

- [1] Ayman M. Mostafa, *Journal of Molecular Structure* **2021**, 1226, 129407.
- [2] Aswin Asaithambi, Roland Kozubek, M. Günther, Prinz, Francesco Reale, Erik Pollmann, Marcel Ney, Cecilia Mattevi, Marika Schleberger, Axel Lorke, *Phys. Status Solidi RRL* **2021**, 15, 2000466.
- [3] E. Majkova, S. Luby, M. Jergel, Y. Chushkin, E. D'Anna, A. Luches, M. Martino, P. Mengucci, G. Majni, Y. Kuwasawa, S. Okayasu, *Applied Surface Science* 2003, 208-209, 394-398.
- [4] P. Darmawan, P. S. Lee, Y. Setiawan, J. Ma, T. Osipowicz, *Appl. Phys. Lett.* **2007**, 91, 092903.
- [5] M. Jergel, A. Anopchenko, E. Majkova, M. Spasova, S. Luby, V. Holy, M. Brunel, A. Luches, M. Martino, *Thin Solid Films* **2000**, 373, 216-221.
- [6] D. R. Rittman, C. L.Tracy, A. B.Cusick, M. J.Abere, B. Torralva, R. C. Ewing, S. M. Yalisove, *Appl. Phys. Lett.* 2015, 106, 171914-171918.
- [7] B. Schuster, F. Fujara, B. Merk, R. Neumann, T. Seidl, C. Trautmann, Nucl. *Instruments Methods B* **2012**, 277, 45 52.
- [8] "Intel's Fundamental Advance in Transistor Design Extends Moore's Law, Computing Performance", Intel News Release, 2007, https://www.intel.com/pressroom/archive/releases/2007/20071111comp.htm.
- [9] Sandip Tiwari, Farhan Rana, Hussein Hanafi, Allan Hartstein, Emmanuel F. Crabbe, Kevin Chan, *Appl. Phys. Lett.* **1996**, 68, 1377.
- [10] Weihua Guan, Shibing Long, Ming Liu, Zhigang Li, Yuan Hu, Qi Liu, *J. Phys. D: Appl. Phys.* **2007**, 40, 2754.
- [11] T. Jiang, Z. Shao, H. Fang, W. Wang, Q. Zhang, D. Wu, X. Zhang, J. Jie, ACS Appl. Mater. Interfaces 2019, 11, 27, 24367-24376.
- [12] M. Olmedo, C. Wang, K. Ryu, H. Zhou, J. Ren, N. Zhan, C. Zhou, J. Liu, ACS Nano 2011, 5, 10, 7972-7977.

- [13] S. M. Sze, "Physics of semiconductor devices", New York: Wiley 1981.
- [14] D. Kahng, S. M. Sze, *Bell Syst. Tech. J.* **1967**, 46, 1288-1295.
- [15] Jaswant S. Rathore, RajveerFandan, Shalini Srivastava, Krista R. Khiangte, Sudipta Das, Udayan Ganguly, Apurba Laha, Suddhasatta Mahapatra, ACS Appl. Electron. Mater. 2019, 1, 1852-1858.
- [16] G. Chakraborty, A. Sengupta, F. G. Requejo, C. K. Sarkar, J. Appl. Phys. 2011, 109, 064504.
- [17] Terry Tai-Jui Wang, Chang-Lung Chu, Ing-Jar Hsieh, Wen-Shou Tseng, *Appl. Phys. Lett.*2010, 97, 143507.
- [18] Ch. Sargentis, K. Giannakopoulos, A. Travlos, D. Tsamakis, *Physica E* **2007**, 38, 85-88.
- [19] S. A. Ng, K. A. Razak, K. Y. Cheong, K. C. Aw, *Thin Solid Films* **2016**, 615, 84-90.
- [20] C. W. Tseng, D. C. Huang, Y. T. Tao, ACS Appl. Mater. Interfaces 2013, 5, 9528-9536.
- [21] Seongmin Hong, Xiao Li, *Journal of Nanomaterials* **2013**, 2013, 790323.
- [22] Kevin G. Stamplecoskie, Juan C. Scaiano, Vidhu S. Tiwari, Hanan Anis, *J. Phys. Chem. C* **2011**, 115, 1403-1409.
- [23] V. S. Vendamani, S. V. S. Nageswara Rao, S. Venugopal Rao, D. Kanjilal, A. P. Pathak, *J. Appl. Phys.* **2018**, 123, 014301.
- [24] S. Chang, Z. A. Combs, M. K. Gupta, R. Davis, V. V. Tsukruk, *ACS Appl. Mater. Interfaces* **2010**, 2, 11, 3333-3339.
- [25] S. Horikoshi, N. Matsumoto, Y. Omata, T. Kato, J. Appl. Phys. **2014**, 115, 193506.
- [26] M. Mederos, S. N. M. Mestanza, R. Lang, I. Doi, J. A. Diniz, *Thin Solid Films* 2016, 611, 39-45.
- [27] Ch. Sargentis, K. Giannakopoulos, A. Travlos, D. Tsamakis, *Superlattices and Microstructures* **2008**, 44, 483-488.
- [28] Y. K. Mishra, S. Mohapatra, D. Kabiraj, B. Mohanta, N. P. Lalla, J. C. Pivin, D. K. Avasthi, *Scripta Materialia* **2007**, 56, 629-632.
- [29] S. Zhu, T. P. Chen, Y. C. Liu, S. F. Yu, Y. Liu, Electrochemical and Solid-State Letters

- **2010**, 13(12), K96-K99.
- [30] Y. K. Mishra, D. K. Avasthi, P. K. Kulriya, F. Singh, D. Kabiraj, A. Tripathi, J. C. Pivin, I. S. Bayer, A. Biswas, *Appl. Phys. Lett.* 2007, 90, 073110.
- [31] Raju Kumar Gupta, Damar Yoga Kusuma, P.S. Lee, M.P. Srinivasan, *ACS Appl. Mater. Interfaces* **2011**, 3, 4619-4625.
- [32] V. Mikhelashvili, B. Meyler, S. Yoffis, J. Salzman, M. Garbrecht, T. Cohen-Hyams, W. D. Kaplan, G. Eisenstein, *Appl. Phys. Lett.* **2009**, 95, 023104.
- [33] Xuan Feng, Shurong Dong, Hei Wong, Danqun Yu, K. L. Pey, K. Shubhakar, W. S. Lau, *Microelectronics Reliability* **2016**, 61, 78-81.
- [34] M. Dhanunjaya, S. A. Khan, A. P. Pathak, D. K. Avasthi, S. V. S. Nageswara Rao, *J. Phys. D: Appl. Phys.* **2017**, 50, 505301.
- [35] N. Manikanthababu, S. Vajandar, N. Arun, A. P. Pathak, K. Asokan, T. Osipowicz, T. Basu,S. V. S. Nageswara Rao, *Appl. Phys. Lett.* 2018, 112, 131601.
- [36] Arun Vinod, Mahendra Singh Rathore, Srinivasa Rao Nelamarri, *Superlattices and Microstructures* **2018**, 120, 616-628.
- [37] Nikolaos Kalfagiannis, AnastasiosSiozios, Dimitris V. Bellas, Dimosthenis Toliopoulos, Leon Bowen, Nikolaos Pliatsikas, Wayne M. Cranton, Constantinos Kosmidis, Demosthenes C. Koutsogeorgis, Elefterios Lidorikis, Panos Patsalas, *Nanoscale* **2016**, 8, 8236-8244.
- [38] L. Kastanis, J. L. Spear, Ch. Sargentis, N. Konofaos, D. Tsamakis, D. C. Koutsogeorgis, E.K. Evangelou, *Solid State Electronics* 2018, 148, 63-69.
- [39] A. Siozios, D. C. Koutsogeorgis, E. Lidorikis, G. P. Dimitrakopulos, Th. Kehagias, H. Zoubos, Ph. Komninou, W. M. Cranton, C. Kosmidis, P. Patsalas, *Nano Lett.* **2012**, 12(1), 259-63.
- [40] R. T. Wen, L. S. Wang, H. Z. Guo, Y. Chen, G. H. Yue, D. L.Peng, T. Hihara, K. Sumiyama, *Mater. Chem. Phys.* **2011**, 130, 823-826.
- [41] T.V. Perevalov, V. Sh. Aliev, V.A. Gritsenko, A.A. Saraev, V.V. Kaichev, *Microelectron*. *Eng.* **2013**, 109, 21-23.

- [42] M. Cyrankiewicz, T. Wybranowski, S. Kruszewski, *Journal of Physics: Conference Series* **2007**, 79, 1.
- [43] R. K. Chang and T. E. Furtak, "Surface Enhanced Raman Scattering", 315, Plenum, New York, USA, 1982.
- [44] L. Xia, J. Wang, S. Tong, G. Liu, J. Li, H. Zhang, *Vibrational Spectroscopy* **2008**, 47, 2, 124-128.
- [45] Y. Wang, H. Wei, B. Li, W. Ren, S. Guo, S. Dong, E. Wang, *Chemical Communications* **2007**, 48, 5220-5222.
- [46] S. Nie, S. R. Emory, *Science* **1997**, 275, 5303, 1102-1106.
- [47] J. Ni, R. J. Lipert, G. B. Dawson, M. D. Porter, Analytical Chemistry 1999, 71, 21, 4903-4908.
- [48] R. J. Dijkstra, W. J. J. M. Scheenen, N. Dam, E. W. Roubos, J. J. ter Meulen, *Journal of Neuro-science Methods* **2007**, 159, 1, 43-50.
- [49] M. Moskovits, *Nature* **2010**, 464, 7287, 357.
- [50] I. Mannelli, M. P. Marco, Analytical and Bioanalytical Chemistry **2010**, 398, 6, 2451-2469.
- [51] J. Kneipp, H. Kneipp, B. Wittig, K. Kneipp, *Nanomedicine* **2010**, 6, 2, 214-226.
- [52] T. Vo-Dinh, H. N. Wang, J. Scaffidi, *Journal of Biophotonics* **2010**, 3, 1-2, 89-102.
- [53] K. G. Stamplecoskie, J. C. Scaiano, V. S. Tiwari, H. Anis, *Journal of Physical Chemistry* C 2011, 115, 5, 1403-1409.
- [54] C. S. Seney, B. M. Gutzman, R. H. Goddard, *Journal of Physical Chemistry C* **2009**, 113, 1, 74-80.
- [55] P. K. Jain, X. Huang, I. H. El-Sayed, M. A. El-Sayed, *Plasmonics* **2007**, 2, 3, 107-118.
- [56] E. C. Le Ru, E. Blackie, M. Meyer, P. G. Etchegoin, J. Phys. Chem. C 2007, 111, 37, 13794-13803.
- [57] K. Y. Cheong, J. H. Moon, H. J. Kim, W. Bahng, Nam-Kyun Kim, J. Appl. Phys. 2008, 103, 084113.
- [58] J. C. Ranuarez, M. J. Deen, Chih-Hung Chen, *Microele. Reliab.* **2006**, 46(12), 1939-1956.

### Chapter-6

- [59] M. Lenzlinger, E. H. Snow, J. Appl. Phys. 1969, 40, 278-283.
- [60] Khairurrijal, W. Mizubayashi, S. Miyazaki, M. Hirose, J. Appl. Phys. 2000, 87, 3000.
- [61] A. Paskaleva, A. J. Bauer, M. Lemberger, S. Zucher, J. Appl. Phys. 2004, 95, 5583.

## **Conclusions and Scope of future work**

This chapter encapsulates the total work done in this thesis and provides the scope and outlook for the possible future investigations in this field.

### 7.1. Conclusions

In this thesis, the effects of electronic excitation induced by Gamma irradiation, Swift Heavy Ion (SHI) irradiation and Laser annealing on the structural and electrical properties of HfO<sub>2</sub> thin films have been studied. Further, an array of high density gold nanoparticles have been produced on the surface of HfO<sub>2</sub> thin films, without modifying the phase of HfO<sub>2</sub> using a non-thermal laser annealing technique.

Initially, the role of deposition time on HfO<sub>2</sub> thin-films synthesized on Semi-Insulating GaAs substrates using RF magnetron sputtering deposition technique were studied to synthesize reproducible HfO<sub>2</sub> thin films with good quality. It is observed that the film thickness and uniformity of the film increases with increasing deposition time. All the HfO<sub>2</sub> thin films grown at room temperature by varying deposition time are found to be amorphous in nature. Further, HfO<sub>2</sub> thin-films of optimized thickness were subjected to thermal annealing, gamma irradiation SHI irradiation. As expected, Introduction of crystalline phase of monoclinic HfO<sub>2</sub> has been observed when pristine amorphous films were subjected to thermal annealing which resulted in a significant increase in the tunneling current of the HfO2 based MOS structures. An orderly increase in tunneling current indicates the production of defects in HfO<sub>2</sub> thin films with increasing gamma irradiation dose. It is observed that the pristine HfO<sub>2</sub> thin film deposited on GaAs substrates consists of a smooth surface with uniform grains of average size around 9 nm. SHI irradiation resulted in a systematic growth in the grain size from 9 nm to 24 nm which may be attributed to possible agglomeration of grains. As-grown HfO2 thin films are amorphous in nature. Ion irradiation has introduced monoclinic and tetragonal phases in otherwise amorphous thin films of HfO<sub>2</sub>. The estimated track radius is found to be around 5-7 nm using thermal spike calculations from our previous studies. The leakage current conduction through the gate oxide has been studied using the Poole-Frenkel and Fowler-Nordheim tunneling mechanisms by examining the leakage current-voltage characteristics. The tunneling examinations shown the pre-existence of several type of defects in the as-deposited samples. The effect of PF tunneling was found to be decreasing up to the critical fluence (5 x 10<sup>12</sup> ions/cm<sup>2</sup>) which confirms the decrease in the density of defects/traps due to ion induced defect annealing. However, above the critical fluence, PF tunneling mechanism dominates which is attributed to increase of traps/defects which results in a rise in the tunneling current.

Furthermore, HfO<sub>2</sub> (30 nm)/GaO<sub>x</sub> (150 nm) bi-layered thin films were synthesized on Si. It is observed that as-grown films contain highly strained non-uniform large grains with average grain size of 34.5 nm. SHI irradiation resulted in a systematic decrease in the average size of grains from 34.5 nm to 13.8 nm and development of new grains which may be attributed to SHI induced grain fragmentation.

Thus, SHI irradiation induced grain agglomeration has been observed when thin films with smaller grains (< 10 nm) were subjected to SHI irradiation which resulted in an increase in the average grain size. Whereas, SHI irradiation induced grain fragmentation has been observed when thin films with larger grains (> 30 nm) were subjected to SHI irradiation which resulted in decrease in the average grain size. Ion induced defect annealing has been observed below the critical fluence ( $5 \times 10^{12}$  ions/cm<sup>2</sup>) which resulted in decrease of the tunneling current. However, ion induced defect formation and radiation damage have been observed above the critical fluence, which resulted in an orderly increase in the tunneling current.

An array of high density gold nanoparticles has been produced on the surface of HfO<sub>2</sub> thin films without modifying the phase of HfO<sub>2</sub> by subjecting the Au/HfO<sub>2</sub> bi-layers to laser annealing. It is observed that Au nanoparticles attain uniform spherical shape and the average size of the Au nanoparticles decreases with increasing laser pulses. These Au nanoparticles produced using laser annealing show considerable enhancement (~10<sup>7</sup>) in Raman scattering and improved storage capacity of the MOS capacitors. These studies suggest that an array of high density spherical Au nanoparticles may be created in the HfO<sub>2</sub> gate dielectric media using non-thermal laser annealing technique, which is useful in preparation of SERS substrates for molecular detection and in fabricating microelectronic compatible floating gate memory devices.

The influence of the electronic excitations induced by SHI, gamma and laser irradiation on the structural, optical and electrical properties of HfO<sub>2</sub> thin-films deposited on various technologically important semiconductor substrates has been studied in this thesis. The study indicates that these electronic excitations can anneal the defects below a critical fluence. Particularly, the energy released during the electron-hole recombination process can promote the migration of defects over the barriers within the solid [1-3]. However, at higher fluences the excessive production of defects can dominate this annealing phenomenon. This effect is observed in the present study in case of SHI irradiation and laser annealing/irradiation. However the lowest dose of gamma chosen in this

study seems to be high to observe such an effect. Our studies have clearly indicated that these methods can be used to improve the device performance by annealing the defects in the oxide layers with spatial selectivity and without affecting the phase of the oxide. Further, SHI irradiation has introduced crystalline phases in otherwise amorphous oxides above a critical fluence. Such phenomenon is not observed in case of gamma and laser annealing may be due to the longer relaxation times involved in these processes.

The electronic excitation induced by SHI irradiation results in grain agglomeration or grain fragmentation in HfO<sub>2</sub> thin films depending on the initial size of grains. SHI irradiation has introduced monoclinic and tetragonal phases in otherwise amorphous thin films of HfO<sub>2</sub>. Whereas, the phase of HfO<sub>2</sub> thin films remains same predominantly amorphous in nature, when these films are exposed to gamma irradiation and laser annealing. SHI induced defect annealing has been observed below the critical fluence (5x10<sup>12</sup> ions/cm<sup>2</sup>), and SHI induced defect formation and radiation damage have been observed above the critical fluence due to track overlap. Whereas, electronic excitation induced by gamma irradiation (2 KGy – 64 KGy) resulted only production of defects in HfO<sub>2</sub> thin films without any significant structural modifications. It is expected that gamma irradiation induced defect annealing may be possible for lower doses. The electronic excitation induced by laser annealing (100 – 2000 laser pulses) resulted only annealing of defects in HfO<sub>2</sub> thin films and formation of an array of high density spherical Au nanoparticles in Au/HfO<sub>2</sub> bi-layer films without modifying the phase of HfO<sub>2</sub>. In this study, a nanosecond laser (repetition rate ~ 10 Hz) was used to perform laser annealing experiments. The influence of the electronic excitation predominantly depends on the various coupling channels and the relaxation time. In the process of SHI irradiation, when an ion passes through the target material, it deposits a very huge amount of energy in short intervals leading to the well-known thermal spike in various materials. The relaxation time is in the order of 10<sup>-15</sup> s, whereas the relaxation time is quite longer in case of the nanosecond laser irradiation performed in this study. Hence, the electronic excitation induced non-equilibrium phase transformations are not observed. The electronic excitation induced by laser annealing/irradiation may result in crystallization and defect formation in HfO2 thin films by employing picosecond/femtosecond lasers.

This study will provide useful information for understanding the effects of electronic excitation on the structural modifications and subsequent effects on the electrical characteristics of HfO<sub>2</sub> thin films deposited on high mobility and/or wide bandgap semiconductors for fabricating tunable and radiation harsh electronic devices as HfO<sub>2</sub> based MOS structures are expected to be used in many devices in space and medical applications such as radiological treatment equipment and physics experiments associated with high energy such as nuclear power plants.

### 7.2. Future Scope

In this study, SHI induced phase transformations of HfO<sub>2</sub> thin-films such as introduction of monoclinic and tetragonal phases (mixed phase) in otherwise amorphous films have been observed. In-situ XRD studies would provide better understanding of SHI induced crystallization of HfO<sub>2</sub> thin-films. We have studied the effects of laser annealing (using KrF excimer laser of wavelength 248 nm) on the structural changes and subsequent effects on the electrical characteristics of HfO<sub>2</sub> thin films. This study can be extended by employing various lasers (picosecond, femtosecond etc.) for better understanding of laser annealing/irradiation induced effects on HfO<sub>2</sub> thin films. We have fabricated gold nanoparticles on the surface of HfO<sub>2</sub> thin films without modifying the phase of HfO<sub>2</sub> for SERS substrate and floating gate type memory device applications. Further, multilayers of Au and HfO<sub>2</sub> (HfO<sub>2</sub>/Au/HfO<sub>2</sub>, HfO<sub>2</sub>/Au/HfO<sub>2</sub>/Au/HfO<sub>2</sub> and HfO<sub>2</sub>/Au/HfO<sub>2</sub>/Au/HfO<sub>2</sub>) and other metals (Ag and Pt) may be subjected to laser annealing to produce embedded metal nanoparticles in HfO<sub>2</sub> dielectric media to improve the storage capacity of HfO<sub>2</sub> based MOS capacitors.

#### 7.3. References

- [1] G. D. Watkins, *Handbook of Semiconductor Technology* edited by K. A. Jackson and W. Schröter (Wiley-VCH, Weinheim), **2000**, 1, 121–165.
- [2] S.V.S. Nageswara Rao, S.K. Dixit, G. Lüpke, N.H. Tolk, L.C. Feldman, *Phys. Rev. B* **2007**, 75, 235202.
- [3] S.V.S. Nageswara Rao, S.K. Dixit, G. Lüpke, N.H. Tolk, L.C. Feldman, *Phys. Rev. B* **2011**, 83, 045204.

## List of Publications

- 1. **K. Vinod Kumar**, J. Pundareekam Goud, Kanaka Ravi Kumar, K. C. James Raju, S. V. S. Nageswara Rao, "Laser Annealing of Au/HfO<sub>2</sub> bi-layers to Fabricate Au Nanoparticles without altering the Phase of HfO<sub>2</sub> for Applications in SERS and Memory Devices", *Journal of Materials Science: Materials in Electronics* **2022**, 33, 6657-6669.
- 2. **K. Vinod Kumar**, N. Arun, A. Mangababu, Sunil Ojha, S. V. S. Nageswara Rao, A. P. Pathak "120 MeV Ag ion irradiation induced intermixing, grain fragmentation in HfO<sub>2</sub>/GaO<sub>x</sub> thin films and consequent effects on the electrical properties of HfO<sub>2</sub>/GaO<sub>x</sub>/Sibased MOS capacitors", *Rad. Eff. Deff. In Sol.* **2020**, 175 (1-2), 150-159.
- 3. **K. Vinod Kumar**, N. Arun, A. P. Pathak, S. V. S. Nageswara Rao, "Effects of Thermal Annealing and Gamma Irradiation on HfO<sub>2</sub> Thin Films deposited on GaAs", *AIP Conf. Proc.* **2019**, 2115, 030021-1–030021-4.
- 4. **K. Vinod Kumar**, N. Arun, A. Mangababu, Sunil Ojha, A. P. Pathak, S.V.S. Nageswara Rao, "Swift Heavy Ion irradiation induced modifications of HfO<sub>2</sub> thin films deposited on GaAs", (Submitted JMSE-D-22-01194).
- 5. N. Arun, L. D. Varma Sangani, **K. Vinod Kumar**, A. Mangababu, M. Ghanashyam Krishna, A. P. Pathak, and S.V.S. Nageswara Rao, "Effects of swift heavy ion irradiation on the performance of HfO<sub>2</sub>-based resistive random access memory devices", *J Mater Sci: Mater Electron*, **2022**, 32:2973–2986.
- A. Mangababu, N. Arun, K. Vinod Kumar, A. P. Pathak, S. V. S. Nageswara Rao, "Metal nanoparticles in dielectric media: Physical vapor deposited HfO<sub>2</sub> & Ag multilayers for MOS device and SPR applications", AIP Conf. Proc. 2020, 2265, 030271.
- 7. M. Dhanunjaya, **K. Vinod Kumar**, N. Manikanthababu, S.V.S. Nageswara Rao, A.P. Pathak, "Swift heavy ion irradiation assisted Si nanoparticle formation in HfSiO<sub>x</sub> nanocomposite thin films deposited by RF magnetron sputtering method", *Nuclear Inst. and Methods in Physics Research B* **2019**, 446, 37–42.

- 8. N. Arun, **K. Vinod Kumar**, A. Mangababu, S. V. S. Nageswara Rao, A. P. Pathak, "Influence of the bottom metal electrode and gamma irradiation effects on the performance of HfO<sub>2</sub>-based RRAM devices", *Rad. Eff. and Def. in Sol.* **2019**, 174 (1-2), 66-75.
- 9. N. Arun, J. Prabana, **K. Vinod Kumar**, A. P. Pathak, S. V. S. Nageswara Rao, "Fabrication of HfO<sub>2</sub> based MOS and RRAM devices: A study of Thermal Annealing Effects on these Devices", *AIP Conf. Proc.* **2019**, 2115, 030216-1–030216-4.
- 10. N. Arun, K. Vinod Kumar, A. P. Pathak, D. K. Avasthi, S. V. S. Nageswara Rao, "Hafnia based resistive switching devices for non-volatile memory applications and Effects of gamma irradiation on device performance", Rad. Eff. Def. In Sol. 2018, 173 (3-4), 239-249.

### List of Contributed/Attended Conferences/Workshops

- 1. **K. Vinod Kumar**, N. Arun, A. Mangababu, Sunil Ojha, A. P. Pathak, S.V.S. Nageswara Rao, "Effects of Swift Heavy Ion irradiation on the structural and electrical properties of HfO<sub>2</sub> thin-films deposited on GaAs", 25<sup>th</sup> International Conference (online) on Ion Beam Analysis (IBA & PIXE SIMS), 2021 (Poster presentation).
- 2. **K. Vinod Kumar**, N. Arun, A. Mangababu, Sunil Ojha, A. P. Pathak, S.V.S. Nageswara Rao, "Effects of Gamma and Swift Heavy Ion irradiation on the structural and electrical properties of HfO<sub>2</sub>/GaO<sub>x</sub>/Si based MOS structures", *International conference (online) on Ion Beams in Materials Engineering and Characterization (IBMEC)*, 2020 (Poster presentation).
- 3. **K. Vinod Kumar**, N. Arun, A. Mangababu, Sunil Ojha, A. P. Pathak, S.V.S. Nageswara Rao, "SHI irradiation induced grain fragmentation, crystallization of HfO<sub>2</sub> thin films and consequent effects on HfO<sub>2</sub>-GaAs based MOS devices", 5<sup>th</sup> International Conference on Nano-structuring by Ion Beams (ICNIB-2019), IGCAR, Kalpakkam (Poster presentation Best poster award).
- 4. **K. Vinod Kumar**, N. Arun, A. Mangababu, A. P. Pathak, S.V.S. Nageswara Rao, "Gamma irradiation Effects on HfO<sub>2</sub>/Ga<sub>2</sub>O<sub>3</sub>/Si and HfO<sub>2</sub>/Si based MOS devices", 5<sup>th</sup> International conference on Ion Beams in Materials Engineering and Characterizations (IBMEC-2018), IUAC, New Delhi (Poster presentation).
- 5. **K. Vinod Kumar**, N. Arun, A. P. Pathak, S.V.S. Nageswara Rao, "Effects of Thermal Annealing and Gamma Irradiation on HfO<sub>2</sub> Thin Films deposited on GaAs", 63<sup>rd</sup> DAE Solid State Physic Symposium (DAE-SSPS-2018), Guru Jambheswar University of Science & Technology, Hisar, Haryana (Poster presentation).
- 6. **K. Vinod Kumar**, N. Arun, A. P. Pathak, S.V.S. Nageswara Rao, "Effects of Thermal annealing and Gamma irradiation on HfO<sub>2</sub>/GaAs based MOS devices", *International Conference on Sculptured Thin Films (GLAD-2018), IIT Delhi, New delhi (Poster presentation)*.

- 7. **K. Vinod Kumar**, N. Arun, A. P. Pathak, S.V.S. Nageswara Rao, "Fabrication and characterization of HfO<sub>2</sub>-based high-k dielectric thin films on high mobility semiconductors for MOS device applications", *National Conference on Physics at Small Scales and Advanced Materials (NCPSSAM-2017), University of Hyderabad, Hyderabad. (Poster presentation).*
- 8. Participated in *Accelerated Particles in Physics (APP-2022)*, University of Hyderabad, Hyderabad.
- 9. Participated in *Pressing for Progress 2019*, University of Hyderabad, Hyderabad.
- 10. Participated in a Workshop on "Processing and Characterization of Thin films 2018, UGC-NRC, University of Hyderabad, Hyderabad
- 11. Participated in a Workshop on "Bringing The Nano world Together (BTNT-2017), Oxford Instruments Nanotechnology" December-2017, University of Hyderabad, Hyderabad
- 12. Participated in a Workshop on "Formulation and Development of Nanoparticles- 2017", HRDC-University of Hyderabad, Hyderabad
- 13. Participated in *Recent Advanced in Optical Sciences-II (RAOS-2016)*, University of Hyderabad, Hyderabad.
- 14. Participated in *Frontiers in Physics (FIP-2016)*, University of Hyderabad, Hyderabad.

### Plagiarism-free statement

This is to certify that the thesis title "Electronic Excitation Induced Effects on the Structural and Electrical Properties of HfO2 thin films" has been screened by the Turnitin Software at the Indira Gandhi Memorial Library of the University of Hyderabad. The software shows a 26% similarity index, out of which 18% came from the student's own publications related to this thesis, which are already published and available online. Thus the effective similarity index excluding his research articles is 26% - 18% = 8%, which is lower than the 10% stipulated by the university guidelines. Therefore, this thesis may be considered free from plagiarism as per guidelines.

S.V.S. Nogracion M. .
Prof. S. V. S. Nageswara Rao

12/04/2023.

(Supervisor)

Prof. S.V.S. NAGESWARA RAO School of Physics University of Hyderabad Hyderabad-500 046, INDIA.

# Electronic excitation induced effects on the structural and electrical properties of HfO2 thin films

by Karra Vinod Kumar

Submission date: 11-Apr-2022 03:31PM (UTC+0530)

Submission ID: 1807690430

File name: Karra\_Vinod\_Kumar.pdf (12.76M)

Word count: 38865

Character count: 202425

# Electronic excitation induced effects on the structural and electrical properties of HfO2 thin films

**ORIGINALITY REPORT** 

26%

14%

INTERNET SOURCES

25%

PUBLICATIONS

2%

STUDENT PAPERS

PRIMARY SOURCES

1

link.springer.com

Internet Source

SW 8%

2

K. Vinod Kumar, N. Arun, A. Mangababu, Sunil Ojha, S. V. S. Nageswara Rao, A. P. Pathak. "
120 MeV Ag ion irradiation induced intermixing, grain fragmentation in HfO /GaO thin films and consequent effects on the electrical properties of HfO /GaO /Si-based MOS capacitors ", Radiation Effects and Defects in Solids, 2020

Publication

3

K. Vinod Kumar, J. Pundareekam Goud, Kanaka Ravi Kumar, K. C. James Raju, S. V. S. Nageswara Rao. "Laser annealing of Au/HfO2 bi-layers to fabricate Au nanoparticles without altering the phase of HfO2 for applications in SERS and memory devices", Journal of Materials Science: Materials in Electronics, 2022 \* 2%

Publication

\* Student Publications in which he is the 1st author

Prof. S.V.S. NAGESWARA RAO School of Physics 104 W22. University of Hyderabad Hyderabad-500 046, INDIA.

| 4 | K. Vinod Kumar, N. Arun, A. P. Pathak, S. V. S. Nageswara Rao. "Effects of thermal annealing |
|---|--|
|   | and gamma irradiation on HfO2 thin films   |
|   | deposited on GaAs", AIP Publishing, 2019 Publication   |



N. Manikanthababu, M. Dhanunjaya, S.V.S. Nageswara Rao, A.P. Pathak. "SHI induced effects on the electrical and optical properties of HfO2 thin films deposited by RF sputtering", Nuclear Instruments and Methods in Physics Research Section B: Beam Interactions with Materials and Atoms, 2016 Publication

<1%

6 slib.tzc.edu.cn

<1%

Submitted to University of Hyderabad, Hyderabad

<1%

Student Paper

N. Manikanthababu, T.K. Chan, A.P. Pathak, G. Devaraju et al. "Ion beam studies of Hafnium based alternate high-k dielectric films deposited on silicon", Nuclear Instruments and Methods in Physics Research Section B: Beam Interactions with Materials and Atoms, 2014

Publication

\* Student's Publications in which he is the 1st author

Prof. S.V.S. NAGESWARA RAO School of Physics 204 7022. University of Hyderabad Hyderabad-500 046, INDIA.

| 9  | N. Manikanthababu, N. Arun, M. Dhanunjaya, S.V.S. Nageswara Rao, A. P. Pathak. "Gamma irradiation-induced effects on the electrical properties of HfO -based MOS devices", Radiation Effects and Defects in Solids, 2016  | <1% |
|----|---|-----|
| 10 | Thomas Henke, Martin Knaut, Marion Geidel, Felix Winkler, Matthias Albert, Johann W. Bartha. "Atomic layer deposition of tantalum oxide thin films using the precursor tert - butylimido-tris-ethylmethylamido-tantalum and water: Process characteristics and film properties", Thin Solid Films, 2017 | <1% |
| 11 | Submitted to IIT Delhi Student Paper  | <1% |
| 12 | "Semiconductor Physical Electronics",<br>Springer Science and Business Media LLC,<br>2006   | <1% |
|    | Publication   |     |

| 14 | annealing on the enhanced structural and electrical properties of amorphous and crystalline Ta[sub 2]O[sub 5] thin films for dynamic random access memory applications", Journal of Applied Physics, 1999 | <\  \  % |
|----|---|----------|
| 15 | www.science.gov Internet Source   | <1%      |
| 16 | B. Jayant Baliga. "Fundamentals of Power<br>Semiconductor Devices", Springer Science and<br>Business Media LLC, 2008<br>Publication   | <1%      |
| 17 | Arun Vinod, Mahendra Singh Rathore, N. Srinivasa Rao. "Effects of annealing on quality and stoichiometry of HfO 2 thin films grown by RF magnetron sputtering", Vacuum, 2018 Publication                  | <1%      |
| 18 | Liu Wen-Ting. "Influence of Radio-Frequecy<br>Power on Structural and Electrical Properties<br>of Sputtered Hafnium Dioxide Thin Films",<br>Chinese Physics Letters, 02/2010<br>Publication               | <1%      |
| 19 | N. Arun, K. Vinod Kumar, A. P. Pathak, D. K. Avasthi, S. V. S. Nageswara Rao. "Hafniabased resistive switching devices for non-   | <1%      |

volatile memory applications and effects of

### gamma irradiation on device performance", Radiation Effects and Defects in Solids, 2018

Publication

**Publication** 

A. Sudha, T.K. Maity, S.L. Sharma, A.N. Gupta. "An extensive study on the structural evolution and gamma radiation stability of TeO 2 thin films", Materials Science in Semiconductor Processing, 2018

<1%

GuruSampath Kumar A., Sofi Sarmash T.,
Obulapathi L., Jhansi Rani D., Subba Rao T.,
Asokan K.. "Structural, optical and electrical
properties of heavy ion irradiated CdZnO thin
films", Thin Solid Films, 2016
Publication

<1%

N. Manikanthababu, N. Arun, M. Dhanunjaya, V. Saikiran, S.V.S. Nageswara Rao, A.P. Pathak. "Synthesis, characterization and radiation damage studies of high-k dielectric (HfO) films for MOS device applications ", Radiation Effects and Defects in Solids, 2014

<1%

mail.cat.ernet.in
Internet Source

<1%

M Dhanunjaya, S A Khan, A P Pathak, D K Avasthi, S V S Nageswara Rao. "Ion induced crystallization and grain growth of hafnium oxide nano-particles in thin-films deposited by

<1%

## radio frequency magnetron sputtering", Journal of Physics D: Applied Physics, 2017

Publication

| 25 | Adolph Blicher. "Thyristor Physics", Springer Science and Business Media LLC, 1976 Publication   | <1% |
|----|--|-----|
| 26 | Senol Kaya, Aleksandar Jaksic, Ercan Yilmaz. "Co-60 gamma irradiation effects on electrical characteristics of HfO 2 MOSFETs and specification of basic radiation- induced degradation mechanism", Radiation Physics and Chemistry, 2018 Publication | <1% |
| 27 | www.freepatentsonline.com Internet Source  | <1% |
| 28 | "High Permittivity Gate Dielectric Materials", Springer Science and Business Media LLC, 2013 Publication   | <1% |
| 29 | idr.mnit.ac.in Internet Source   | <1% |
| 30 | "Ion Beam Modification of Solids", Springer<br>Science and Business Media LLC, 2016<br>Publication   | <1% |
| 31 | www.mdpi.com Internet Source   | <1% |

| 32 | leakage current density and the dielectric constant of Pt/(Ba,Sr)TiO[sub 3]/Pt capacitors by annealing under a N[sub 2] atmosphere", Journal of Applied Physics, 1999 Publication   | <1% |
|----|---|-----|
| 33 | Submitted to Universiti Sains Malaysia Student Paper  | <1% |
| 34 | D. K. Avasthi, G. K. Mehta. "Swift Heavy Ions<br>for Materials Engineering and<br>Nanostructuring", Springer Science and<br>Business Media LLC, 2011<br>Publication   | <1% |
| 35 | J. Udaya Bhanu, Mohammed Aminul Islam, P. Thangadurai. "Conduction mechanisms responsible for leakage currents in RF sputtered HfO2 high-k gate-oxide thin film MOS capacitors", Materials Science and Engineering: B, 2021 | <1% |
| 36 | Ahn, B.D "Structural, electrical and optical properties of GZO/HfO"2/GZO transparent MIM capacitors", Materials Science in Semiconductor Processing, 200612 Publication   | <1% |
| 37 | Prabath J. Binduhewa, Mike Barnes.  | <1% |

"Photovoltaic emulator", 2013 IEEE 8th

# International Conference on Industrial and Information Systems, 2013

Publication

| <b>I</b>  | <1%   |
|---|---|
| akyung Jeong, Dongjin Lee.<br>ne plasma treatment on sol–<br>2 thin films", Ceramics<br>17  | <1%   |
| iokhale, V.N. Bhoraskar.<br>r in c-Si induced by swift<br>fation Effects and Defects in   | <1%   |
| tw  | <1%   |
| 2. Zhu, M. Chang, Q. Fang,<br>ct of postdeposition<br>thermal stability and<br>teristics of sputtered HfO2<br>, Surface Science, 2005 | <1%   |
| .ac.uk  | <1%   |
| ıoradea.ro  |   |
|   | akyung Jeong, Dongjin Lee. Ine plasma treatment on sol- 2 thin films", Ceramics 17  Sokhale, V.N. Bhoraskar. In c-Si induced by swift Itation Effects and Defects in  tw  2. Zhu, M. Chang, Q. Fang, Interest of postdeposition Ithermal stability and Iteristics of sputtered HfO2 Iteristics of sputtered HfO2 Iteristics of science, 2005  Iteristics of science, 2005 |

| 45 | Kim, M.S "Modeling growth rate of HfO"2<br>thin films grown by metal-organic molecular<br>beam epitaxy", Microelectronics Journal,<br>200602<br>Publication   | <1% |
|----|---|-----|
| 46 | Sheng S. Li. "Semiconductor Physical Electronics", Springer Nature, 1993 Publication  | <1% |
| 47 | "Structure-Property Relationships in Surface-<br>Modified Ceramics", Springer Nature, 1989  | <1% |
| 48 | A. Nakao, Y. Suzuki, M. Kaibara, T. Tsukamoto, M. Iwaki. "Surface characterization of polymer modified by He-ion bombardment", Journal of Electron Spectroscopy and Related Phenomena, 1998 Publication | <1% |
| 49 | "Novel Aspects of Diamond", Springer Science and Business Media LLC, 2015 Publication   | <1% |
| 50 | Guo, H.Y "Electric characterization of HfO"2 thin films prepared by chemical solution deposition", Materials Science & Engineering B, 20050715 Publication  | <1% |
| 51 | Manoj Kumar Jaiswal, Rajesh Kumar, D.<br>Kanjilal. "Dense electronic excitation induced   | <1% |

# modification in TiO2 doped SnO2 nanocomposite films", Journal of Alloys and Compounds, 2014 Publication

| 52 | Rajesh Kumar, Vishnu Chauhan, N. Koratkar, Shalendra Kumar, Aditya Sharma, Keun-Hwa Chae, Sung Ok Won. "Influence of high energy ion irradiation on structural, morphological and optical properties of high-k dielectric hafnium oxide (HfO2) thin films grown by atomic layer deposition", Journal of Alloys and Compounds, 2020 Publication | <1% |
|----|--|-----|
| 53 | cyberleninka.org Internet Source   | <1% |
| 54 | d-nb.info<br>Internet Source   | <1% |
| 55 | Aída Serrano Rubio. "Modified Au-Based<br>Nanomaterials Studied by Surface Plasmon<br>Resonance Spectroscopy", Springer Science<br>and Business Media LLC, 2015<br>Publication   | <1% |
| 56 | dr.ntu.edu.sg Internet Source  | <1% |
| 57 | "Oxide Electronics", Wiley, 2021   | <1% |
|    |  |     |

M. Ramzan, M.F. Wasiq, A.M. Rana, S. Ali, M.Y. Nadeem. "Characterization of e-beam evaporated hafnium oxide thin films on post thermal annealing", Applied Surface Science, 2013

<1%

Publication

Mei Zhao, Xuewei Jia, Kewei Wu, Tao Yang et al. "Low Gain Avalanche Detectors with good time resolution developed by IHEP and IME for ATLAS HGTD project", Nuclear Instruments and Methods in Physics Research Section A: Accelerators, Spectrometers, Detectors and

Associated Equipment, 2022

<1%

Publication

N. Manikanthababu, K. Prajna, A. P. Pathak, S. V. S. Nageswara Rao. "120 MeV Ag ion induced effects in Au/HfO2/Si MOSCAPs", AIP Publishing, 2018

<1%

Publication

Xiao-Ying Zhang, Chia-Hsun Hsu, Yun-Shao Cho, Sam Zhang, Shui-Yang Lien, Wen-Zhang Zhu, Fei-Bing Xiong. "Rapid thermal processing of hafnium dioxide thin films by remote plasma atomic layer deposition as high-k dielectrics", Thin Solid Films, 2018

<1%

baadalsg.inflibnet.ac.in

| 63 | Zhao, Haoping Peng. "Effect on the Surface Anticorrosion and Corrosion Protection Mechanism of Integrated Rust Conversion Coating for Enhanced Corrosion Protection", ACS Omega, 2022 Publication   | < <b>1</b> % |
|----|---|--------------|
| 64 | Pragati Kumar, Nupur Saxena, Ramesh<br>Chandra, Kun Gao, Shengqiang Zhou, Avinash<br>Agarwal, Fouran Singh, Vinay Gupta, D.<br>Kanjilal. "SHI induced enhancement in green<br>emission from nanocrystalline CdS thin films<br>for photonic applications", Journal of<br>Luminescence, 2014<br>Publication | <1%          |
| 65 | Tarn, . "Physical Properties of Samarium, Sm", CRC Handbook of Metal Etchants, 1990.  Publication   | <1%          |
| 66 | Submitted to Texas Christian University Student Paper   | <1%          |
| 67 | Yu Chen, Jacob Bunch, Chao Jin, Chenghao Yang, Fanglin Chen. "Performance enhancement of Ni-YSZ electrode by impregnation of Mo0.1Ce0.9O2+δ", Journal of Power Sources, 2012  | <1%          |

Deepika Gupta, Vishnu Chauhan, Nikhil <1% 69 Koratkar, Fouran Singh, Ashok Kumar, Shalendra Kumar, Rajesh Kumar. "High energy (MeV) ion beam induced modifications in Al2O3-ZnO multilayers thin films grown by ALD and enhancement in photoluminescence, optical and structural properties", Vacuum, 2021 Publication Kumar, S.. "Swift heavy ion induced <1% 70 modifications in cobalt doped ZnO thin films: Structural and optical studies", Applied Surface Science, 20090630 Publication M. Dhanunjaya, N. Manikanthababu, S. Ojha, <1% 71 Soodkhet Pojprapai, A.P. Pathak, S.V.S. Nageswara Rao. " Effects of growth parameters on HfO thin-films deposited by RF Magnetron sputtering ", Radiation Effects and Defects in Solids, 2022 Publication Submitted to University of Sheffield <1% 72 Student Paper V. M. Jali, Basavaraj Angadi, M. T. Lagare, P. 73 Victor, Ravi Kumar, S. B. Krupanidhi. " High Energy Oxygen Ion Induced Modifications in

# Ferroelectric SrBi Ta O Thin Films ", Ferroelectrics, 2005 Publication

| 74 | boa.unimib.it Internet Source  | <1% |
|----|--|-----|
| 75 | Buiu, O "Investigation of optical and electronic properties of hafnium aluminate films deposited by Metal-Organic Chemical Vapour Deposition", Thin Solid Films, 20070226 Publication                | <1% |
| 76 | Li, C.L "Physical and electrochemical characterization of amorphous lithium lanthanum titanate solid electrolyte thin-film fabricated by e-beam evaporation", Thin Solid Films, 20061205 Publication | <1% |
| 77 | Y.B. Zheng, S.J. Wang, C.H.A. Huan. "Microstructure-dependent band structure of HfO2 thin films", Thin Solid Films, 2006 Publication   | <1% |
| 78 | scholar.lib.vt.edu<br>Internet Source  | <1% |
| 79 | Bibekananda Sahoo, Krutika L. Routray, K. Asokan, Dhrubananda Behera. "Study of fractal dimension and power spectral density analysis of superconductor/ferromagnetic                                | <1% |

bilayer", Nuclear Instruments and Methods in Physics Research Section B: Beam Interactions with Materials and Atoms, 2018

Submitted to Indian Institute of Technology, Kharagpure

<1%

Student Paper

J. Gao, G. He, B. Deng, D.Q. Xiao, M. Liu, P. Jin, C.Y. Zheng, Z.Q. Sun. "Microstructure, wettability, optical and electrical properties of HfO2 thin films: Effect of oxygen partial pressure", Journal of Alloys and Compounds, 2016

<1%

Publication

Junxue Fu. "Au nanoparticle based localized surface plasmon resonance substrates fabricated by dynamic shadowing growth", Nanotechnology, 04/30/2010

<1%

Publication

Submitted to Malaviya National Institute of Technology

<1%

Student Paper

P.M. Tirmali, Anil G. Khairnar, Bhavana N. Joshi, A.M. Mahajan. "Structural and electrical characteristics of RF-sputtered HfO2 high-k based MOS capacitors", Solid-State Electronics, 2011

<1%

Publication

| 85 | Preetam Singh, K. M. K. Srivatsa; Sourav Das. "Effect Of Substrate Temperature On Nanocrystalline CeO2 Thin Films Deposited On Si Substrate By RF Magnetron Sputtering", Advanced Materials Letters, 2015 Publication | <1% |
|----|---|-----|
| 86 | Promnimit, S "Growth of gold/zinc sulphide multilayer films using layer-by-layer assembly of colloidal nanoparticles", Physica E: Low-dimensional Systems and Nanostructures, 200812 Publication                      | <1% |
| 87 | Sharma, A.T "Barrier modification of Au/n-GaAs Schottky diode by swift heavy ion irradiation", Nuclear Inst. and Methods in Physics Research, B, 200710 Publication   | <1% |
| 88 | conservancy.umn.edu Internet Source   | <1% |
| 89 | digitalcommons.fiu.edu Internet Source  | <1% |
| 90 | eprints.hec.gov.pk Internet Source  | <1% |
| 91 | opus4.kobv.de Internet Source   | <1% |
|    |   |     |

- E. György. "Morphology evolution and local electric properties of Au nanoparticles on ZnO thin films", Journal of Applied Physics, 2005

  Publication
- <1%
- Kim, M.S.. "Characterization and process effects of HfO"2 thin films grown by metalorganic molecular beam epitaxy", Materials Science & Engineering B, 20051115
- <1%

- Liang, C.S.. "Electrical properties of W-doped (Ba"0"."5Sr"0"."5)TiO"3 thin films", Journal of Crystal Growth, 20050115
- <1%

Publication

Submitted to Nanyang Technological University

<1%

- Student Paper
- Submitted to National Chung Hsing University
  Student Paper

<1%

Sharma, A.T.. "Effects of swift heavy ion irradiation on the electrical characteristics of Au/n-GaAs Schottky diodes", Applied Surface Science, 20071115

<1%

Publication

99 aml.iaamonline.org

<1%

| 100 | apps.dtic.mil Internet Source   | <1% |
|-----|---|-----|
| 101 | repositorium.sdum.uminho.pt Internet Source   | <1% |
| 102 | repository.kaust.edu.sa Internet Source   | <1% |
| 103 | K.C. Das, S.P. Ghosh, N. Tripathy, D.H. Kim, T.I. Lee, J.M. Myoung, J.P. Kar. "Evolution of microstructural and electrical properties of sputtered HfO2 ceramic thin films with RF power and substrate temperature", Ceramics International, 2016 Publication | <1% |
| 104 | Qi He, Hui-bin Guo, Jun-jun Wei, S.J Askari,<br>Hong-bin Wang, Shu-yu Zhang, Hai Yang, Xiao-<br>ping Su, Fan-xiu Lu. "Deposition of HfO2 thin<br>films on ZnS substrates", Thin Solid Films,<br>2008<br>Publication   | <1% |
| 105 | Submitted to University of Newcastle upon Tyne Student Paper  | <1% |
| 106 | Y. Zhang, M.L. Crespillo, H. Xue, K. Jin, C.H. Chen, C.L. Fontana, J.T. Graham, W.J. Weber. "New ion beam materials laboratory for materials modification and irradiation effects research", Nuclear Instruments and Methods                                  | <1% |

### in Physics Research Section B: Beam Interactions with Materials and Atoms, 2014

Publication

| 107 | Fuminobu Hori. "Characterization of swift heavy ion-induced defects in Fe-Rh alloy by using positron beam technique", physica status solidi (c), 09/2007  Publication              | <1 % |
|-----|--|------|
| 108 | I.P. Jain, Garima Agarwal. "Ion beam induced surface and interface engineering", Surface Science Reports, 2011 Publication   | <1%  |
| 109 | Submitted to Indian Institute of Technology<br>Jodhpur<br>Student Paper  | <1%  |
| 110 | Submitted to Inter-University Accelerator Centre Student Paper   | <1 % |
| 111 | J.M. Khoshman, A. Khan, M.E. Kordesch.  "Amorphous hafnium oxide thin films for antireflection optical coatings", Surface and Coatings Technology, 2008  Publication               | <1%  |
| 112 | Jie Ni. "Influence of deposition temperature<br>on the structure and optical properties of<br>HfO2 thin films", Frontiers of Materials<br>Science in China, 12/2008<br>Publication | <1%  |



# Kadoshima, M.. "Rutile-type TiO"2 thin film for high-k gate insulator", Thin Solid Films, 20030131

<1%

Publication



Kyu-Jeong Choi. "Electrical properties of hafnium oxide gate dielectric deposited by plasma enhanced chemical vapor deposition", Integrated Ferroelectrics, 2001

<1%

Publication



Submitted to National Defense University
Student Paper



Exclude quotes

On

Exclude matches

< 14 words

Exclude bibliography